AAAS

Science

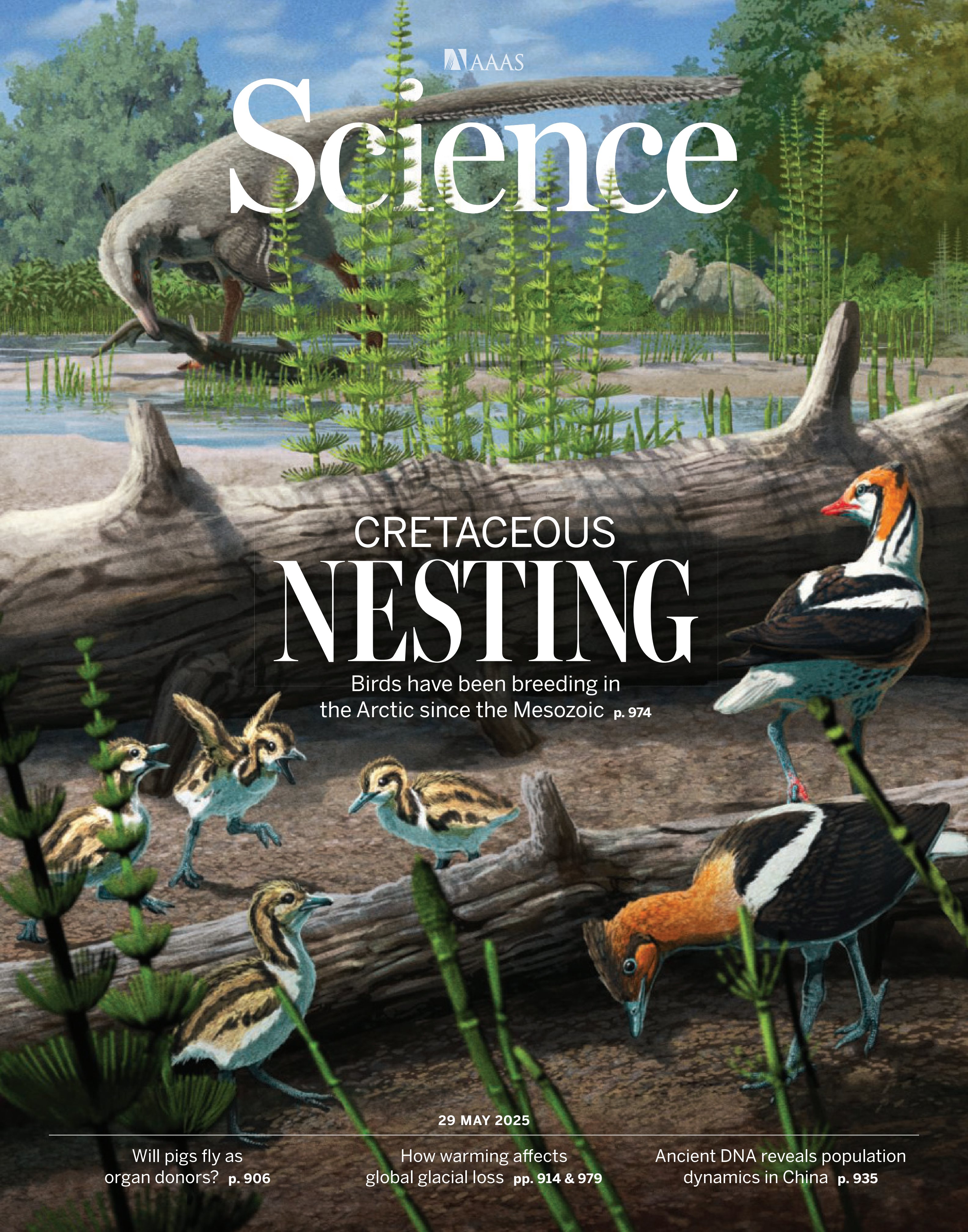

CRETACEOUS NESTING

Birds have been breeding in the Arctic since the Mesozoic **p. 974**

29 MAY 2025

Will pigs fly as organ donors? **p. 906**

How warming affects global glacial loss **pp. 914 & 979**

Ancient DNA reveals population dynamics in China **p. 935**

ASU Science

PRIZE FOR TRANSFORMATIONAL IMPACT

Apply now to the Arizona State University and *Science* Prize for Transformational Impact!

Arizona State University and *Science* have partnered to create the **ASU–*Science* Prize for Transformational Impact**. This prize recognizes transformational research that uses innovative methods and approaches to identify problems and develop solutions with impacts on policy and decision-making.

The grand prize winner will receive a prize of **US$30,000** and their prize-winning essay will be published in *Science* online and print. A runner-up will receive **US$10,000** and have their essay published in *Science* online.

APPLY BY **AUGUST 15, 2025**

www. Science.org/ASU

CONTENTS

29 MAY 2025 | VOLUME 388 | ISSUE 6750

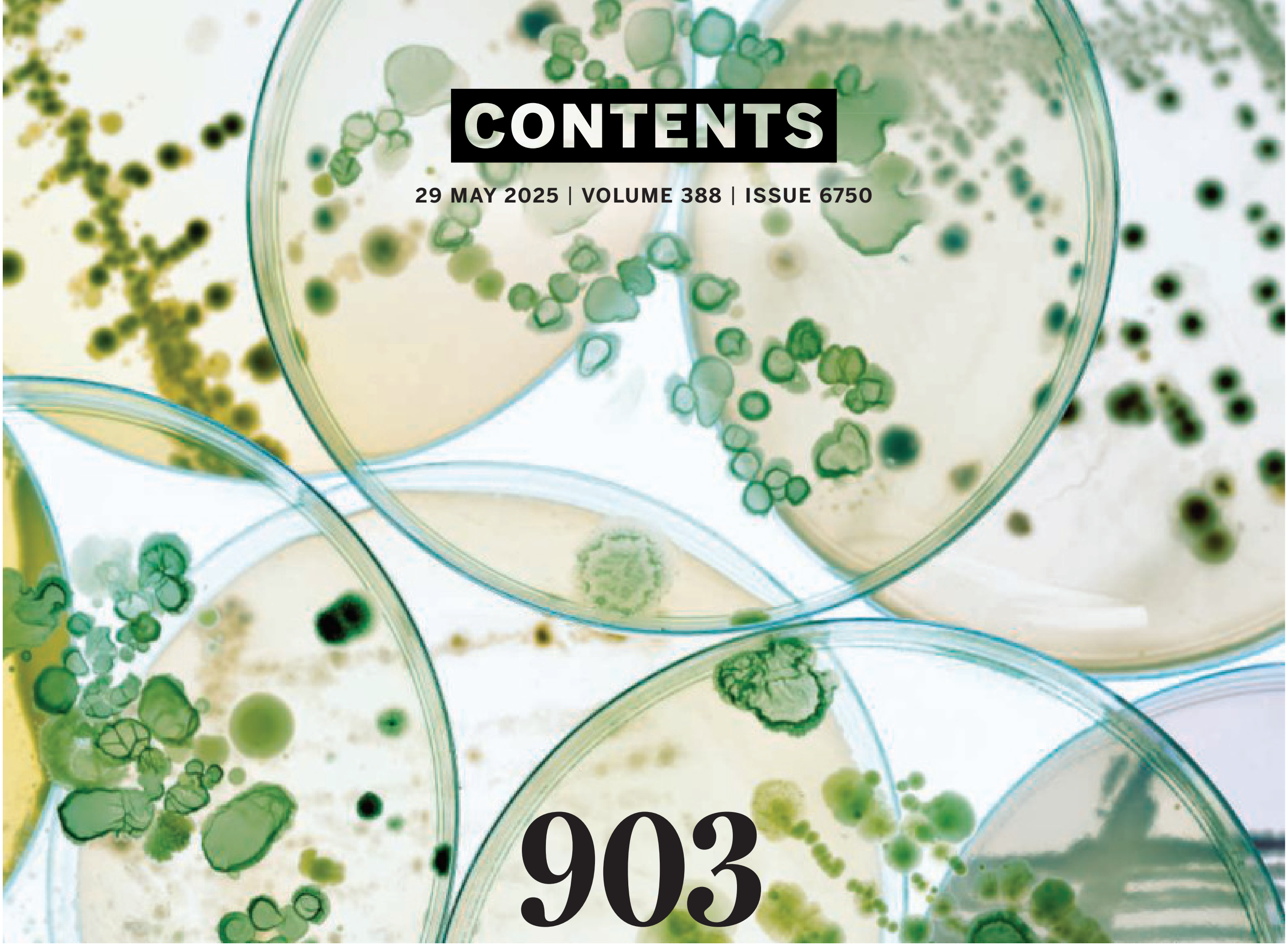

Microbial diversity should be protected, just like threatened animals and plants, scientists argue.

EDITORIAL

897 Critical statistical infrastructure
—N. Potok and E. L. Groshen

NEWS

898 Researchers question Abbott's rapid malaria tests
Reports of false negatives prompted a World Health Organization internal memo, but company denies problems —C. Offord

900 Leprosy was an American scourge long before Europeans arrived
Scientists find DNA from an enigmatic bacterium in 1000-year-old skeletons —M. Price

901 Studies making lasting paradigm shifts are on the rise
New metric identifying "persistently disruptive" papers offers a "bright spot" amid signs of declining innovation —J. Brainard

902 California hummingbirds are evolving fast—because of feeders
Beaks have grown longer and larger, and ranges have expanded to follow the feeders —R. Nuwer

904 A giant telescope shrouded in mystery
China is readying to build one of the world's largest telescopes—but only scant details have emerged —R. Stone

905 China sets out to sample an unusual asteroid
Kamoʻoalewa, a rare quasi-satellite of Earth, could be a chunk of the Moon —D. Normile

FEATURES

906 The organ farm
Gene-edited pig kidneys are finally moving the long-stymied field of xenotransplantation forward —J. Cohen

COMMENTARY

PERSPECTIVES

914 Social impacts of glacier loss
More than three-quarters of global glacier mass is projected to disappear under present-day conditions —C. Howe and D. Boyer
RESEARCH ARTICLE p. 979

916 Sleuthing out the symmetry of a superconductor
Experimental observations provide clues to understanding an enigmatic superconductor, uranium ditelluride —A. H. Nevidomskyy
RESEARCH ARTICLE p. 938

917 A wave of emotion
Sustained brainwide patterns of activity enable emotions to outlast their triggers —S. Karamihalev and N. Gogolla
RESEARCH SUMMARY p. 933

918 Growing anxious—Are preschoolers matched to their futures?
Evolutionary and developmental factors may contribute to anxiety in young people —M. A. Hanson and P. D. Gluckman

BOOKS ET AL.

920 The next best way to teach and learn
Technology always seems poised to revolutionize education—until it doesn't —J. Wai

921 Look beyond the longevity drips and supplements
There is a path to living longer and healthier that doesn't require reversing the aging process —E. J. Topol

PHOTO: WLADIMIR BULGAR/SCIENCE SOURCE

LETTERS

922 Philippine fisheries put food security at risk

—R. B. Cabral *et al.*

922 Remobilized metals threaten urban wetlands

—C. Li *et al.*

923 Scientific timidity enables oppression

—M. Omar

ANALYSIS

POLICY ARTICLE

924 What patents on AI-derived drugs reveal

Less in-depth, in vivo testing before patenting may affect overall research and development

—J. Freilich and A. K. Rai

REVIEWS

REVIEW SUMMARY

928 Ecology

Ecological and evolutionary consequences of changing seasonality

— D. Hernández-Carrasco *et al.*

RESEARCH

HIGHLIGHTS

929 From *Science* and other journals

RESEARCH SUMMARIES

932 Domestication

A single domestication origin of adzuki bean in Japan and the evolution of domestication genes

—C.-C. Chien *et al.*

933 Neuroscience

Conserved brain-wide emergence of emotional response from sensory experience in humans and mice

—I. Kauvar *et al.*

PERSPECTIVE p. 917

934 Signal transduction

BRAF oncogenic mutants evade autoinhibition through a common mechanism

—H. Lavoie *et al.*

935 Ancient DNA

Prehistoric genomes from Yunnan reveal ancestry related to Tibetans and Austroasiatic speakers

—T. Wang *et al.*

936 Diapause

Functional polymorphism of CYCLE underlies the diapause variation in moths

—S. Zheng *et al.*

937 Plague

Attenuation of virulence in *Yersinia pestis* across three plague pandemics

—R. K. Sidhu *et al.*

RESEARCH ARTICLES

938 Superconductivity

Pair wave function symmetry in UTe_2 from zero-energy surface state visualization —Q. Gu *et al.*

PERSPECTIVE p. 916

945 Atomic physics

Testing interelectronic interaction in lithium-like tin

—J. Morgner *et al.*

950 Nanomaterials

Resiliency, morphology, and entropic transformations in high-entropy oxide nanoribbons

—H. Shahbazi *et al.*

957 Solar cells

Vapor-assisted surface reconstruction enables outdoor-stable perovskite solar modules —X. Sun *et al.*

964 Solar cells

C_{60}-based ionic salt electron shuttle for high-performance inverted perovskite solar modules

—S. You *et al.*

969 Paleoproteomics

Enamel proteins reveal biological sex and genetic variability in southern African *Paranthropus*

—P. P. Madupe *et al.*

974 Paleontology

Arctic bird nesting traces back to the Cretaceous

—L. N. Wilson *et al.*

979 Glaciers

Glacier preservation doubled by limiting warming to 1.5°C versus 2.7°C —H. Zekollari *et al.*

PERSPECTIVE p. 914

984 Carbon cycling

Thermal acclimation of stem respiration implies a weaker carbon-climate feedback

—H. Zhang *et al.*

WORKING LIFE

994 Finding strength in sensitivity

—N. Stanojević

---

989 AAAS News & Notes

992 *Science* Careers

ON THE COVER

Science
NESTING

Newly hatched birds explore a 73-million-year-old Arctic environment. Modern birds breed in the Arctic to take advantage of abundant seasonal resources, but the evolutionary origins of this behavior remain elusive. Exceptional new fossils from northern Alaska reveal birds lived and nested alongside non-avian dinosaurs in Arctic Alaska long before the radiation of modern birds after the end-Cretaceous extinction. See page 974.
Illustration: Gabriel Ugueto

PHOTO: SIMONE BOCCACCIO/SOPA IMAGES/LIGHTROCKET/GETTY IMAGES

***Science* serves as a forum for discussion of important issues related to the advancement of science by publishing material on which a consensus has been reached as well as including the presentation of minority or conflicting points of view. Accordingly, all articles published in *Science*—including editorials, news, commentary, and book reviews—are signed and reflect the individual views of the authors and not official points of view adopted by AAAS or the institutions with which the authors are affiliated.** *Science* (ISSN 0036-8075) is published weekly on Thursday, except last week in December, by the American Association for the Advancement of Science, 1200 New York Avenue, NW, Washington, DC 20005. Periodicals mail postage (publication No. 484460) paid at Washington, DC, and additional mailing offices. Copyright © 2025 by the American Association for the Advancement of Science. The title *Science* is a registered trademark of the AAAS. Domestic individual membership, including subscription (12 months): $165 ($74 allocated to subscription). Domestic institutional subscription (51 issues): $2865; Foreign postage extra: Air assist delivery: $135. First class, airmail, student, and emeritus rates on request. Canadian rates with GST available upon request, GST #125488122. Publications Mail Agreement Number 1069624. **Printed in the U.S.A. Change of address:** Allow 4 weeks, giving old and new addresses and 8-digit account number. **Postmaster:** Send change of address to AAAS, P.O. Box 96178, Washington, DC 20090–6178. **Single-copy sales:** $15 each plus shipping and handling available from backissues.science.org; bulk rate on request. **Authorization to reproduce** material for internal or personal use under circumstances not falling within the fair use provisions of the Copyright Act can be obtained through the Copyright Clearance Center (CCC), www.copyright.com. The identification code for *Science* is 0036-8075. *Science* is indexed in the *Reader's Guide to Periodical Literature* and in several specialized indexes.

Fixing the US statistical infrastructure

Nancy Potok *and* **Erica L. Groshen**

Official government statistics are critical infrastructure for the information age. Reliable, relevant, statistical information helps businesses to invest and flourish; governments at the local, state, and national levels to make critical decisions on policy and public services; and individuals and families to invest in their futures. Yet surrounded by all manner of digitized data, one can still feel inadequately informed. A major driver of this disconnect in the US context is delayed modernization of the federal statistical system. The disconnect will likely worsen in coming months as the administration shrinks statistical agencies' staffing, terminates programs (notably for health and education statistics), and eliminates unpaid external advisory groups. Amid this upheaval, might the administration's appetite for disruption be harnessed to modernize federal statistics?

> “Trust…is an irreplaceable asset that must be protected…”

Federal statistics, one of the United States' premier public goods, differ from privately provided data because they are privacy protected, aggregated to address relevant questions for decision-makers, constructed transparently, and widely available without a subscription. The private sector cannot be expected to adequately supply such statistical infrastructure. Yes, some companies collect and aggregate some economic data, such as credit card purchases and payroll information. But without strong underpinnings of a modern, federal information infrastructure, there would be large gaps in nationally consistent, transparent, trustworthy data. Furthermore, most private providers rely on public statistics for their internal analytics, to improve their products. They are among the many data users asking for more from statistical agencies.

The US statistical system's innovative capacity is hampered by heavy reliance on methods developed during the past century. A bold effort is needed to modernize and coordinate the system, both to counter threats such as falling survey response rates and to take advantage of opportunities that arise from burgeoning “organic” digitized data and advances in hardware, software, and statistical methods. Continual improvement is a core principle of federal statistical agencies, and conditions that predate the current administration have introduced new imperatives.

A 2024 report by the Committee on National Statistics of the National Academies of Sciences, Engineering, and Medicine describes a 21st-century data infrastructure that would develop new data products that blend information from multiple sources. For example, job postings data could be combined with unemployment insurance claims to create timely measures of labor market dynamics.

Even prior to the upheaval of the past few months, agencies producing such statistics could only make slow, incremental improvements. Funding and staffing have been insufficient and not optimally distributed. Statistical agencies had been stretched to continue as is, squeezing out their ability to design new products. Also, the distributed structure of federal statistical agencies (13 principal agencies across almost as many federal departments, plus over 100 statistical programs) inhibits coordination, prioritization, and sharing data and resources.

Modern federal statistics require a consolidated system, as most other countries have. The US system stands out for its widely decentralized approach, a consequence of organic growth, not thoughtful planning. Previous presidents of both parties have proposed consolidation, to no avail, due to territoriality, lack of champions, and fears that it would not be done well.

We urge the administration to reorganize the statistical system, with particular care to improve agility by reducing barriers to sharing data and coordination while maintaining strong statutory privacy and confidentiality protections for statistical data; achieve economies of scale and scope across statistical agencies by sharing expertise, information technology, training, software, sample frames, and data standards; and increase public trust by ensuring that the consolidated system can design and execute statistical methods outside of policy and political influence while remaining responsive to policy-driven needs. Trust in the objectivity, transparency, and reliability of federal statistics is an irreplaceable asset that must be protected in any consolidation implementation.

As US statistical agencies' staff and resources dwindle and some civil service jobs may be made more like political appointments, a more centralized system with vigorous oversight and strongly enforced privacy protections can help ensure that data are used for statistical purposes only, in accordance with current laws and uses. The current decentralized approach, with fragmented oversight and investment, is more vulnerable to less responsible handling. We encourage the scientific community to support this long-overdue modernization. The alternative is to watch the federal statistical system deteriorate as individual units share the disconnected fates of their parent agencies. □

Nancy Potok is chief executive officer of NAPx Consulting, Beltsville, MD, USA and a senior fellow at the Center for Excellence in Public Leadership, George Washington University, Washington, DC, USA. nancy@napxconsulting.com **Erica L. Groshen** is senior economic adviser at the School of Industrial and Labor Relations, Cornell University, Ithaca, NY, USA and a research fellow at the Upjohn Institute for Employment Research, Kalamazoo, MI, USA. erica.groshen@cornell.edu

10.1126/science.ady6728

GLOBAL HEALTH

Researchers question Abbott's rapid malaria tests

Reports of false negatives prompted a World Health Organization internal memo, but company denies problems

CATHERINE OFFORD

The World Health Organization (WHO) has sent an internal memo about potential problems with a major company's malaria tests after scientists reported issues with test sensitivity and warned it could delay patients' access to critical treatment.

Abbott's Bioline rapid diagnostic tests (RDTs) for malaria are used by health workers around the world, particularly in remote areas where lab techniques such as microscopy and DNA detection aren't available. Investigations at several institutions in Southeast Asia suggest at least some of these RDTs fail to detect infections or show faint test lines for some positive cases.

Daniel Ngamije Madandi, director of WHO's Global Malaria Programme (GMP), issued the memo to WHO's six regional offices on 30 April. It lists 11 "affected" lots from two Abbott RDTs—Pf/Pv and Pf/Pan—that were associated with "faint lines and false negative results" in reports from "multiple research groups." The memo follows a public notice by WHO in March that warned of reports of faint lines in malaria RDTs without mentioning particular brands or products. In the new memo, GMP advises program leaders who received affected lots to report performance concerns to WHO and consider opening their own investigations. It does not say the tests shouldn't be used.

The information is "concerning," says Cristian Koepfli, an infectious disease researcher at the University of Notre Dame who has studied Abbott RDTs' performance and received funding from the manufacturer of a competitor brand. False negatives can deprive patients of potentially lifesaving therapies, hamper disease elimination efforts, and undermine trust in these diagnostics, he says.

Abbott did not answer specific questions from *Science*, but said in a statement that product quality and safety "are of the utmost priority to us." A thorough review has "confirmed that the product is performing as intended. Abbott also engaged a WHO-qualified lab to conduct additional tests." The company reminds customers that any line, however faint, "designates a positive result."

Malaria RDTs use a drop of blood and return a pink-purple line if they detect proteins from the *Plasmodium* parasites that cause malaria. WHO recommends a lower detection threshold of 200 parasites per microliter of blood, but many modern tests detect parasite densities below that. Companies often report sensitivities of 95% or higher, although factors including improper storage or use can compromise performance in the field.

A blood draw for a malaria test at a Shoklo Malaria Research Unit clinic in Thailand in 2013.

PHOTO: ZUMA PRESS/ALAMY STOCK PHOTO

Abbott's rapid tests have undergone extensive assessment, including by WHO. The organization includes Bioline malaria RDTs on its "prequalified diagnostics" list, which international agencies use to guide procurement of medical devices. Southeast Asia, for example, has millions of Abbott's malaria RDTs procured by the United Nations Office for Project Services with money from the Global Fund, a major international financer of efforts to eliminate malaria. (Supported primarily by donations from governments, the fund is reportedly seeking bigger investments from private donors amid recent uncertainty about U.S. and other nations' contributions.)

Malaria researcher François Nosten says he heard of problems with Abbott's tests in mid-2024. He heads the Shoklo Malaria Research Unit (SMRU) on the Thai border with Myanmar, part of the Mahidol Oxford Tropical Medicine Research Unit (MORU). Health workers told him of feverish patients in rural areas who tested negative with Abbott RDTs, sometimes repeatedly, only to test positive with another brand.

SMRU sent a team to investigate. Its reports, shared with WHO and viewed by *Science*, describe one screening of more than 70 patients in which Abbott RDTs identified just three positive cases, whereas another RDT brand and microscopy both flagged more than 10 times as many.

Such findings are worrying, particularly in areas where it's impractical to use more than one diagnostic, says Jaishree Raman, a principal medical scientist at South Africa's National Institute for Communicable Diseases who was not involved in the investigation. "You want to get a rapid, accurate test for a malaria patient so you can start treatment," she says. As well as being potentially lethal, an untreated case could start an outbreak in an area close to eliminating the disease.

In September 2024, Nosten wrote to collaborators saying his group wouldn't use or distribute Bioline RDTs it had obtained until the issue was resolved. "The amount of money that is involved is huge," Nosten tells *Science*. "What do we do with the [millions] of Abbott RDTs we have in store that we are not going to use?"

SMRU also mailed RDTs to other

labs and collaborators for additional evaluations. Using various protocols, one WHO-collaborating center in the Philippines concluded the RDTs successfully detected infections, but some test lines were faint; researchers at the Pasteur Institute of Cambodia found negative results at parasite densities of several thousand; and a University of Strasbourg lab sometimes found no line at parasite densities of up to about 370, and occasional faint lines at more than 1500. (A subsequent field test using the same lots in Madagascar did not reveal problems with test sensitivity, says Strasbourg malaria researcher Didier Ménard.)

Medical Action Myanmar, a nongovernmental organization in Myanmar that was co-founded by a researcher at MORU, submitted its own report about false negatives in the field, this one using RDTs that hadn't come from SMRU.

In January, Abbott and SMRU conducted a joint assessment of SMRU's RDTs as well as newly manufactured kits using fresh and frozen blood and a panel of parasite proteins. Reports of that assessment, viewed by *Science*, show Abbott's staff typically rated test lines' color intensity as stronger than SMRU's team did, though both recorded negatives for two frozen samples.

SMRU concluded that Abbott's RDTs had a "sensitivity issue" and were "not fit for purpose." But Abbott identified no quality issues, and noted its product instructions do not recommend testing frozen samples, which are frequently used for convenience in laboratory evaluations of RDTs. It highlighted a "reading variation" between Abbott and SMRU staff that could lead to "missed positive results in weak positive cases (faint lines)." It also noted issues with "sample volume collection method and visual [interpretation] of results" by SMRU. Nosten rejects any suggestion his team performed the tests incorrectly. He adds that if a test line "is so faint that 90% of people will say it's negative because there's 'no line' then you have a problem."

Raman and Koepfli, who reviewed the reports from the joint assessment and the lab evaluations obtained by *Science*, agree there are grounds for concern about test sensitivity. "RDTs are supposed to enable prompt, accurate diagnosis," Raman says. These reports suggest some Abbott RDTs "have challenges in achieving this."

Whether that's true worldwide isn't clear. False negatives may be less likely in countries where malaria transmission and parasite densities are higher, as in parts of Africa, says Nick White, a malaria researcher at MORU who is co-authoring an academic paper describing SMRU's findings.

The 30 April memo from GMP notes that reports of problems with Abbott's RDTs come from "diverse field settings and experienced users, suggesting the issue is not related to user error or test interpretation." It recommends programs that received any of the nine Pf/Pv and two Pf/Pan "affected" lots "seek information" about performance concerns and consider getting some boxes of tests evaluated.

In a statement, WHO says it takes reports of test issues seriously and is working with Abbott Diagnostics Korea, the subsidiary that makes the RDTs under scrutiny, to address concerns. It adds, "The manufacturer has committed to provide additional information on product usability and agreed to undergo a for-cause site inspection."

The April WHO memo will be "very important to support future purchases of alternative RDT brands," says Arjen Dondorp, chair of the steering committee for the Global Fund's Regional Artemisinin-resistance Initiative and deputy director at MORU. The Global Fund declined to comment on specific purchases, but said it remains "committed to supporting countries in the selection and procurement of effective tools" against malaria.

Raman says she understands WHO must avoid "making a statement without the proper and very strong evidence." Still, she says, "I would rather they had said: 'If you are using this Abbott kit, make sure that you get an alternative [or] add another diagnostic tool.' … Obviously, you don't want people with malaria not being detected or treated." ☐

This crab has headlights

Scuttling through Indo-Pacific mangrove forests, face-banded crabs (*Parasesarma eumolpe*) sometimes flash a dazzling green or blue light from a pair of bands on their heads. Researchers reported last week in *Ecology* that the bright light comes from the bands' unique shape, which focuses light into beams like the reflectors inside car headlights. Light hitting the bands at various angles tends to be reflected forward, the team found, in a beam that is especially bright between 5 and 50 centimeters away, the typical distance at which these crabs interact. Behavioral experiments showed the crabs are more interested in the light from same-sex individuals—males have blue bands, and females green—so it may be used to signal an intent to defend territory from rivals. *—Erik Stokstad*

PHOTO: PAVLIK LISITSYN/INATURALIST

TRUMP TRACKER

WHITE HOUSE REPORT DECRIES HEALTH OF U.S. KIDS Declaring today's children "the sickest generation in American history," President Donald Trump's administration last week released a 72-page report that identifies poor diet, environmental chemicals, sedentary lifestyles, and "overmedicalization" of youngsters as "potential" drivers of growing rates of youth obesity, diabetes, autism, and mental health diagnoses. The influence of Health and Human Services Secretary Robert F. Kennedy Jr., who chaired the commission of Cabinet secretaries that wrote the White House report, is clear in its pages. Kennedy has campaigned against childhood vaccines and pesticides and the report assails, for instance, alarming levels of some pesticides found in children's blood and urine. It also calls for research into "the links between vaccines and chronic disease." But the fingerprints of industry also dot the report, which declares the American food system "safe." The report does not mention the leading killer of U.S. children: gun violence. The commission will now begin work on an action plan that is due out in August.
—Meredith Wadman

PHOTO: PICTURE ALLIANCE/DPA/BRIDGEMAN IMAGES

INFECTIOUS DISEASES

Leprosy was an American scourge long before Europeans arrived

Scientists find DNA from an enigmatic bacterium in 1000-year-old skeletons

MICHAEL PRICE

For more than a century, scientists thought leprosy was an Old World disease with a single culprit. The bacterium *Mycobacterium leprae* had ravaged Europe, Asia, and Africa for thousands of years and was introduced to the Americas by European colonists and enslaved people from Africa about 500 years ago. But in 2008, researchers discovered a second species, *M. lepromatosis*, circulating in Mexico. Whether that, too, had arrived with Europeans or was native to the Americas was unclear.

Two later sightings of the same bacterium deepened the mystery. In 2016, veterinarians found *M. lepromatosis* in red squirrels with leprosylike lesions on the British Isles. Then in 2018, the pathogen popped up in the ancient DNA of an individual who lived 1000 years ago, centuries before Europeans arrived, in what today is Western Canada.

Now, a study online this week in *Science* charts the history of *M. lepromatosis*, confirming the enigmatic bacterium existed—and may have been widespread—in North and South America before European contact. "This is fascinating stuff," says Erwin Schurr at McGill University, who specializes in the genetics of leprosy.

Also known as Hansen disease, leprosy can cause disfiguring skin and skeletal lesions and extensive nerve damage, and often comes with social stigma. Researchers had never seen the skeletal lesions in ancient remains from the Americas, leading them to conclude it was unknown there before Europeans' arrival.

Pasteur Institute biologist Nicolás Rascovan and colleagues laid the groundwork for the new study with their 2018 finding. They had screened databases of ancient DNA, often from archeological sites, for the genetic signatures of pathogens. During a single fortuitous night, their search turned up an unknown strain of plague in a 5000-year-old Swedish tomb, as well as *M. lepromatosis* in a person who lived around 1000 C.E. near what today are the Lax Kw'alaams and Metlakatla First Nations, on the northern coast of British Columbia. "It was a really important night," Rascovan says.

His graduate student Maria Lopopolo screened additional ancient DNA databases from South America. "And then," he recalls, "she found it": *M. lepromatosis* in the skeletal remains from two sites in Argentina, both also dating to about 1000 years ago. By showing *M. lepromatis* was present in individuals

A leprosy patient receives treatment at a clinic in Marituba, Brazil, in 2013.

separated by more than 10,000 kilometers a millennium ago, the discovery suggests it may have been widespread in the Americas. (Rascovan notes that his team obtained permission from local tribal communities to use data from Indigenous ancient DNA. Joycelynn Mitchell, a treaty negotiator with the Metlakatla First Nation, is an author on the paper.)

Hoping to learn more about when *M. lepromatosis* emerged, Rascovan reached out to microbiologist Charlotte Avanzi at Colorado State University, whose lab investigated *M. lepromatosis* in British red squirrels. "It was really puzzling, because we had never found any *lepromatosis* in ancient DNA from Europe," she says. "We started to wonder whether it was something from the Americas."

Joining forces, the teams screened for the bacterium in 408 modern-day people, mostly leprosy patients, from the United States, Mexico, French Guiana, Brazil, and Paraguay. They detected *M. lepromatosis* in 34 individuals, most of them in Mexico. By estimating how long it would take various mutations to accumulate in the present-day bacterial genomes, as well as those of the ancient samples, the researchers conclude this version of the strain emerged about 9000 years ago, somewhere in the Americas. It diverged from the more common *M. leprae* about 1 million years ago.

It's not yet clear whether people migrating into North America across the Bering Land Bridge brought a predecessor of this *M. lepromatosis* strain with them or if they acquired it from animals already living on the continent. But the findings "clearly show the presence of *M. lepromatosis* in the Americas precontact," says Anne Stone, an anthropological geneticist at Arizona State University: "It highlights some of the surprises that ancient DNA can bring."

When Europeans arrived in the 15th century, the leprosy bacterium they brought with them, *M. leprae*, quickly became the dominant strain in the Americas as well. It remains a mystery why *M. lepromatosis* didn't, in turn, infect colonizing Europeans.

Another riddle: How exactly did *M. lepromatosis* end up in British red squirrels? The new study shows that the strain infecting them emerged within the past 300 years. One possibility is that rodents from the Americas—perhaps gray squirrels—can harbor the disease, and transmitted it to red squirrels after being transported across the Atlantic Ocean. But that's just a guess.

Rascovan notes that knowing more about the pathogen's strains and reservoirs will ultimately help scientists monitor and fight leprosy, which still affects thousands worldwide. "The first line in combating any disease is understanding its epidemiology," he says. ■

RESEARCH ON RESEARCH

Studies making lasting paradigm shifts are on the rise

New metric identifying "persistently disruptive" papers offers a "bright spot" amid signs of declining innovation

JEFFREY BRAINARD

There are signs that innovativeness has declined across many scientific fields, but a new study finds that groundbreaking scientific research with lasting impact is on the rise. The study found that the share of papers that are "persistently disruptive"—a new metric the authors developed—rose about fivefold from 1900 to 2019.

"It's a bright spot against the backdrop of lots of evidence suggesting innovation is getting harder," says Russell Funk, a sociologist at the University of Minnesota Twin Cities who co-authored a landmark 2023 study showing a decrease in papers' disruptiveness and co-wrote a commentary accompanying the new study. Understanding the common features of persistently disruptive research projects and the scientists who conduct them could shed light on "ways to really support scientists and ease some of the barriers to creating the most innovative work," he adds.

The new study, published last week in *Nature Computational Science,* builds on a nascent measure of scholarly innovativeness, dubbed "disruption," that measures how much a paper departs from a prior body of knowledge. A highly disruptive paper was originally defined as one that subsequent papers cite without also citing any of the works the original paper references—a sign the paper had broken with existing paradigms.

But An Zeng, a researcher in systems science at Beijing Normal University, was puzzled to see that the total number of citations to papers dubbed disruptive isn't always high, as one might expect if they contained bold, trailblazing ideas. In the new work, he and his colleagues sought to identify these truly groundbreaking papers using the new measure, persistent disruption, which relies on two criteria. First, a paper must be highly cited without the works it references—the same premise behind the original disruptiveness metric—but the new method takes a more fine-grained approach to better distinguish breakthroughs from incremental advances. Second, later papers that reference the citing papers must often cite the paper in question, a sign that it has staying power.

After looking at more than 100 million scholarly publications appearing from 1800 through 2019 and tracking citations for up to 10 years after a paper was published, the authors found some 3.6 million papers that scored highly on the twin dimensions—they disrupted their intellectual forebears but were not themselves disrupted by their successors. These papers received a whopping 1637 citations on average. "It's quite hard to get into this group" of persistent disrupters, Zeng says.

Such papers have doubled as a proportion of the literature since 2000, the researchers found. That result does not contradict previous findings that the share of papers that are disruptive has broadly declined, Zeng says. But, "For those papers that do disrupt previous work, they are more likely to be adopted by future work nowadays." A possible explanation is that the quality of the disruptive work may be improving, he suggests.

High persistent disruption scores are also correlated with other measures of originality, including recognition by Nobel Prizes, the authors found. The work of Chen-Ning Yang—who shared the 1957 Nobel Prize in Physics for a discovery that a physical law called the conservation of parity is violated during certain nuclear reactions—is a case in point. The older method of calculating disruptiveness ranks his work below that of another "typical" scientist who produced about as many papers (whom Zeng's paper did not name). But the new measure shows more of Yang's papers were persistently disruptive—less readily "overtaken by later developments" than this other scientist's works. The new study also found that large teams of scientists disproportionately produce persistently disruptive papers: Teams with 10 members produced them at twice the rate of teams with only three members.

The new paper is "elegant" and offers a new way to look at how scientific ideas evolve and some come to dominate a field, says Yiling Lin, a Ph.D. student in information science at the University of Pittsburgh who has studied disruptiveness. She cautions, though, that Zeng's measure may be biased, even more so than the original one, by the uneven distribution of citations, with some "star" papers drawing disproportionately many. What's more, Zeng's finding of a rising incidence of "persistently disruptive" papers may be explained not just by an increase in innovative ones, but by a rising tendency of papers citing them to build on or consolidate their findings, Lin says. "I think it's still at an early stage before we can come to the conclusion what is the best measure of disruption."

There's no formula for determining the optimal balance between disruptive research and work that builds incrementally on previous findings, Zeng says. For example, the discovery in 2016 of cosmic gravitational waves by researchers using the Laser Interferometer Gravitational-Wave Observatory confirmed elements of Albert Einstein's century-old general theory of relativity. The discovery was recognized by a Nobel Prize—and was a breakthrough even though it doesn't count as disruptive, Funk says. But to address challenging problems such as improving sustainability, adapting to climate change, and reducing income inequality, Funk says, "You might want much higher levels of disruption" than exist today. □

IN FOCUS

Forbidden photo?

The National Science Foundation (NSF) tried—and failed—to prevent staffers from gathering last week to snap a photo celebrating the besieged agency's 75th anniversary. There were no signs protesting moves by President Donald Trump's administration to terminate NSF grants, push out workers, and seek cuts to the agency's budget. "We just wanted to show our appreciation for [what] NSF has funded over the years," says one organizer, who requested anonymity. But NSF officials apparently saw it differently. "This is not an agency-supported event and we can't provide any resources," a senior NSF manager wrote to the organizers. Even so, more than 250 staffers gathered during their lunch break on 20 May to express support for an agency facing an uncertain future. —*Jeffrey Mervis*

PLANTS & ANIMALS

California hummingbirds are evolving fast—because of feeders

Beaks have grown longer and larger, and ranges have expanded to follow the feeders **RACHEL NUWER**

Hummingbird feeders are a beloved pastime for millions of backyard birders and a convenient dining spot for the birds. But for the Anna's hummingbird, a common species in the western United States, feeders have become a major evolutionary force. According to research published last week in *Global Change Biology*, artificial feeders have let the birds expand their range out of Southern California up to the state's northern end, while also driving a transformation of the birds themselves. Over just a few generations, their beaks have dramatically changed in size and shape.

"They seem to be moving where we go and changing quite rapidly to succeed in their new environments," says Nicolas Alexandre, a co–lead author who conducted the work when he was a graduate student at the University of California, Berkeley and is now a geneticist at Colossal Biosciences, a biotechnology company based in Dallas. "We can think of Anna's hummingbird as a commensal species, similar to pigeons."

Carleton University behaviorist Roslyn Dakin, who wasn't involved with the study, adds that the paper beautifully shows "evolution in action."

It's unclear when the earliest hummingbird feeders appeared. A 1928 *National Geographic* article provided instructions for DIY feeders to observe hummingbirds, but the technology likely existed earlier. What is clear, though, is that hummingbird feeders took off after World War II. When Alexandre and his colleagues mined the text of newspaper archives dating back to 1880, they found that ads for feeders proliferated after the first patented one appeared in 1947.

To test how Anna's hummingbirds responded to the uptick in feeders, the researchers turned to the Audubon Christmas Bird Count, an annual birding survey. Data from the survey showed which of California's 58 counties the bird inhabited from 1938 to 2019. U.S. Census records indicated human population density in these same areas, while newspaper ads for feeders served as a proxy for feeder density. In addition, the team analyzed hummingbird museum specimens in 2D and 3D to quantify changes to their beaks over time. Finally, they built a model

PHOTO: MATTHEW HERRON

As feeders proliferate, Anna's hummingbirds are evolving beaks that let them exploit the bounty.

PHOTO: ALAMY STOCK PHOTO

for predicting hummingbird range expansion that incorporated both artificial feeders and other factors, such as the locations of introduced eucalyptus trees, which can provide nectar throughout the year.

The researchers' findings suggest eucalyptus trees—which were planted en masse in California in the late 1800s—might have served as the first steppingstone for some populations of Anna's hummingbirds to expand their ranges. But hummingbird feeders played the biggest role in driving the hummingbird's northward population growth. "The feeders are what really make the difference here," says senior author Alejandro Rico-Guevara, an evolutionary biologist at the University of Washington.

The northward expansion of Anna's hummingbird was already known, says Catherine Graham, an ecologist at the Swiss Federal Institute for Forest, Snow and Landscape Research, but the exact mechanisms driving it weren't. She says the new paper stands out as "impressive" because of the detailed explanation it offers.

The researchers also found that as feeders proliferated, Anna's hummingbird beaks got longer and larger, which may reflect an adaptation to slurp up far more nectar than flowers can naturally provide. Developing a bigger beak to access feeders "is like having a large spoon to eat with," Rico-Guevara says.

This change was more pronounced in areas where feeders were dense. But in birds that lived in colder regions north of the species' historical range, the researchers spotted the opposite trend: Their beaks became shorter and smaller. This finding also makes sense: The researchers used an infrared camera to show for the first time that hummingbirds use their beaks to thermoregulate, by dissipating heat while they are perched. A smaller beak has less surface area—and would therefore help conserve heat.

It wasn't just the size and shape of beaks that changed. In areas where feeders are dense, male hummingbirds have also developed beaks that are pointier and sharper than usual. Pointy beaks in hummingbird species often indicate aggressiveness, and the researchers think male skirmishes over feeder control may have made these birds feistier. "Anyone who has a feeder knows that hummingbirds fight like crazy," Rico-Guevara says.

The most surprising finding, though, was how quickly these changes took place. By the 1950s, hummingbirds were noticeably different from those of the 1930s: a time span of only about 10 generations of birds, Alexandre says.

Dakin says the study adds nuance to our conception of humans as an evolutionary force. Often, researchers think of humans as exerting selective pressures through environmental damage or deliberate domestication. But as with Anna's hummingbird, "I think we're going to find more and more examples of contemporary and subtle changes," she says, "that we're shaping, indirectly, in many more species." □

Rachel Nuwer is a science writer in Brooklyn.

Q&A

KENT REDFORD

SPARE A THOUGHT FOR MICROBES

Could endangered bacteria such as *Bacillus coahuilensis*, found in the salt-rich lagoons in Mexico's Cuatro Ciénegas valley, one day be afforded the same protections as threatened animals and plants? That's the hope of a multidisciplinary group of scientists and conservationists who met at the Scripps Institution of Oceanography last week to discuss forming a microbe specialist group to advise the International Union for Conservation of Nature ahead of its World Conservation Congress in October. *Science* spoke with conservation biologist Kent Redford, who co-organized the meeting last week, about why conservation of microbes matters. The full interview is at https://scim.ag/RedfordQA.

Q: How do you conserve an individual species of a microbe?

A: I don't think you do that for individuals. Take the cryosphere—in the ice, snow, and under-the-sea ice. Unless we can change the trajectory the climate is on, we're going to lose most of life in the cryosphere. What we could do is create a bank that takes samples and preserves them for a time when we may be able to reverse the climate trajectory and we can reintroduce some of these.

Q: But microbe numbers are so vast. That's an enormous expense. Who is going to pay? Where are you going to store this stuff?

A: I don't know the answer, but there is the statement that has been made at this meeting that storing portions of microbe genomes digitally may be an important strategy. You don't have to keep something alive. This is a strategy that has not been thought about in the conservation world before, and it's super-interesting and exciting.

Q: What action do you want to see come out of the World Conservation Congress?

A: It would be wonderful to see this group develop a list of places that are valued for their microbes, like Cuatro Ciénegas, the hot springs of Yellowstone, and hydrothermal vents in the deep ocean. That would be a way of getting people to say, "Whoa, what?" *—Jon Cohen*

IN OTHER NEWS

SLEEPING EASIER
A new pill could allow some people with obstructive sleep apnea (OSA) to shed the cumbersome mask they must wear to bed. People with OSA stop breathing dozens or hundreds of times during the night, causing their blood oxygen to drop before they subconsciously awake, and the disorder comes with long-term risks including stroke, Alzheimer's disease, and sudden cardiac death. Many rely on burdensome continuous positive airway pressure machines that blow air into the throat to keep their airways open, but the results from a large clinical trial, released last week by the company Apnimed, suggest that a medicine called AD109 could also work. Participants who took the pill—a combination of the medications atomoxetine and aroxybutynin—nightly for 6 months experienced 56% fewer instances during sleep where their breathing grew shallow or ceased compared with those on a placebo, and 22% of the treated patients achieved complete control of the disease. Together, the medications stimulate the muscles critical to keeping the throat open. —*Meredith Wadman*

The Lenghu observatory in China's Qinghai province may soon be getting a big addition.

PHOTO: CHEN JIE/XINHUA NEWS AGENCY VIA REDUX

ASTRONOMY

A giant telescope shrouded in mystery

China is readying to build one of the world's largest telescopes—but only scant details have emerged

RICHARD STONE

High on the Tibetan Plateau, China appears to be laying the groundwork for what will be the largest optical telescope in the Northern Hemisphere—and perhaps briefly, in the world. But to the puzzlement of some astronomers, China has been keeping a tight lid on plans for its 14.5-meter Large Optical Telescope (LOT), with only glancing references in a handful of abstracts and Chinese media reports.

"As far as I can tell, it's real. And it will certainly put China in the big leagues," says Robert Kirshner, a cosmologist at Harvard University and executive director of the Thirty Meter Telescope, one of two massive U.S.-led optical telescopes undergoing design review and at least a decade away from first light.

The National Astronomical Observatories of China (NAOC) is racing to have the LOT up and running as early as 2030, according to a Chinese astronomer who requested anonymity because he is not authorized to speak about the project. It will be the crown jewel of NAOC's newest astronomical aerie: Saishiteng Mountain, a 4500-meter peak east of the town of Lenghu in Qinghai province that hosts other cutting-edge telescopes.

In November 2024, NAOC announced a $22 million contract to build the LOT's dome. But NAOC and the lead institute on the LOT, the Chinese Academy of Sciences's Nanjing Institute of Astronomical Optics and Technology, have not released details, for example, on the design of the mirror, other than that it will observe at both optical and infrared wavelengths.

Purchase orders on NAOC's website suggest the LOT will have a variety of instruments that would allow it to tackle a range of targets, much like the twin 10-meter W. M. Keck Observatory telescopes in Hawaii. With its larger aperture, LOT's discovery potential—its light-gathering power and spatial resolution—would be about four times that of the Keck telescopes, the largest in the United States.

The 39-meter Extremely Large Telescope (ELT) being built by the European Southern Observatory in Chile's Atacama desert will almost immediately eclipse the LOT in size. Originally slated for completion in 2018, the $1.5 billion ELT is now expected to see first light in March 2029, with scientific observations—which could include studies of Earth-like worlds around other stars—to commence at the end of 2030.

Still, Kirshner calls the LOT "a wake-up call for American science." With plans for giant telescopes moving slowly, he fears U.S. leadership in ground-based optical astronomy is slipping away. "I don't mean to scare people, but we really need to get moving," he says. ☐

With reporting by Dennis Normile and Bian Huihui.

SPACE SCIENCE

China sets out to sample an unusual asteroid

Kamoʻoalewa, a rare quasi-satellite of Earth, could be a chunk of the Moon **DENNIS NORMILE**

Following its successes retrieving lunar samples from both the near and far sides of the Moon, China is planning an encore, sending a probe to snatch material from a near-Earth asteroid.

The target of the Tianwen-2 mission, which is expected to launch this month, is 469219 Kamoʻoalewa. It is one of just seven asteroids that fall into a little-understood class known as quasi-satellites of Earth—and it could also be the first known asteroid comprised of lunar material. That hypothesis could be confirmed by laboratory studies of fragments collected by Tianwen-2, which are due to be returned to Earth about 2.5 years after launch.

“This is an ambitious mission to explore a fascinating object,” says astrophysicist Amy Mainzer of the University of California, Los Angeles.

Kamoʻoalewa was discovered in 2016 by the Pan-STARRS 1 telescope on Haleakala in Hawaii. It travels in a highly elliptical solar orbit and appears to terrestrial observers to be alternately leading and trailing Earth, giving the impression it orbits Earth. Kamoʻoalewa has been in its current orbit for about 100 years and will likely remain there for another 300, according to a study by brothers Raúl and Carlos de la Fuente Marcos, both of the Complutense University of Madrid. Shifting orbits are typical of quasi-satellites, and Kamoʻoalewa roughly means “oscillating celestial fragment” in Hawaiian.

China set its sights on Kamoʻoalewa because of its unusual orbit, unknown origin, and undetermined characteristics, planetary scientists Li Chunlai and Liu Jianjun of China’s National Astronomical Observatories wrote in an email. The mission “could potentially answer questions about the origin of Earth’s quasi-satellites and the evolution of their orbits,” they wrote.

After China announced the mission in 2019, further studies made Kamoʻoalewa even more interesting. When University of Arizona planetary scientist Benjamin Sharkey and colleagues observed the asteroid with the Large Binocular Telescope, located in Arizona, it detected a very atypical spectrum, or pattern of reflected light. It suggests Kamoʻoalewa is made up of silicates resembling those found in Apollo lunar samples. The asteroid might have been ejected from the Moon’s surface as the result of a collision with some object, Sharkey and his team wrote in *Communications Earth & Environment* in 2021.

Intrigued by that scenario, Tsinghua University planetary scientist Cheng Bin and colleagues ran simulations that indicated the Moon’s Giordano Bruno crater had the right location, size and age to have been a potential source, the group reported in *Nature Astronomy* in 2024. Models can’t prove a lunar origin, Sharkey says. But analyzing fragments in a lab could “settle the question definitively,” Mainzer says.

Getting samples will be a challenge. Kamoʻoalewa, which is 40 to 100 meters across, is far smaller than asteroids targeted by the three prior sample return missions—Japan’s two Hayabusa probes and NASA’s OSIRIS-Rex. It also rotates faster: every 28 minutes. Tianwen-2 will first hover over the asteroid and extend a robotic arm to probe surface conditions and collect weathered particles. Then it will deploy a pair of rotating brushes to sweep up fragments and use a stream of gas to blow them into a container. It might also attempt to extend three legs and land, using a claw to hold the asteroid while the sample collector does its job.

If Kamoʻoalewa does prove to be a Moon fragment, “it would let us test our knowledge of impact physics and ejection against a major cratering event,” Sharkey says. And even if it isn’t, the samples could reveal unforeseen secrets, Li and Liu say.

If all goes well, Tianwen-2’s mission won’t end at the asteroid. Next, it will head out on a 7-year voyage to comet 311P/PANSTARRS, where it will search for clues to the origins and evolution of the early Solar System. □

With reporting by Bian Huihui.

IN FOCUS

Invasive species rack up massive bill

The economic damage caused by the planet’s most notorious invasive species is 16 times greater than previously estimated, according to a study published this week in *Nature Ecology & Evolution*. Researchers gathered existing cost estimates for 162 invasive species—from plants that damage infrastructure to pests that destroy crops—then extrapolated the costs to other parts of the world where those species have been spotted but where damage hadn’t been calculated. By modeling the potential scope of the invasions and using economic indicators, the team estimates that these species have inflicted $2.2 trillion in damages over the past 6 decades. The European rabbit (pictured) was among the most economically destructive, costing $57 billion. *—Warren Cornwall*

PHOTO: KONRAD WOTHE/MINDEN

THE ORGAN FARM

Gene-edited pig kidneys are finally moving the long-stymied field of xenotransplantation forward

Surgeon Robert Montgomery holds the gene-edited pig kidney that Towana Looney received.

PHOTO: JOE CARROTTA/NYU LANGONE HEALTH

JON COHEN

On 8 January, a 66-year-old retiree in New Hampshire named Timothy Andrews sent a Facebook Messenger note to a 53-year-old stranger in New York City, Towana Looney, with an unusual question. He wanted to know how her new pig kidney was doing.

Six weeks earlier, surgeons at New York University (NYU) Langone Health had made international news when they gave Looney the organ from a pig genetically altered so its tissues would be less likely to be rejected by her body. Andrews himself was 2 weeks away from receiving a similar, engineered pig kidney. "There's one person on the planet that has one, and I'm going to talk to her," he told his doctors at Massachusetts General Hospital (MGH). "I was just curious if there was anything different, what she felt about it."

Andrews and Looney both had kidney failure and had relied on dialysis to cleanse their blood, a procedure that sustains life but stresses the heart. Human kidney transplants routinely free people from spending hours a week on dialysis machines. But the waiting lists for the organs are long, and for biological reasons both Looney and Andrews were poor candidates for a human kidney. In his Facebook message, the former supermarket manager commended Looney, a former cashier at a Dollar General discount store, for her bravery. Understanding her journey, he said, would help him with his own. They became fast friends and she eased his anxiety about the pig organ. “I learned it was working for her,” Andrews says.

Attempts to provide humans with animal organs—known as xenotransplantation—date back more than a century, a history marked by hype and dashed hopes. As surgeon Norman Shumway, who helped pioneer human-to-human heart transplants, quipped 2 decades ago, “Xenotransplantation is the future—and always will be.” But because of recent advances in gene editing, cloning, and immunosuppression, and major investor backing, many veteran researchers are increasingly confident that future is nearly here.

At the time Andrews reached out to her, Looney’s kidney was pumping out copious amounts of urine—a sign it was working—and her medically suppressed immune system appeared to be adjusting to the porcine guest. The NYU Langone doctors had released her from the hospital, but instead of returning to her home in Alabama, Looney stayed in a New York City apartment so they could closely monitor her health.

Andrews received his own kidney on 25 January, the same day the Associated Press celebrated a milestone for Looney: “The only person in the world with a functioning pig organ is thriving after a record 2 months,” the story read. Four other people had received kidneys or hearts from genetically modified pigs, and none had survived longer than 60 days.

On 13 February, Looney’s kidney was functioning well when *Science* met her in an Upper East Side apartment building. “I haven’t felt this good since high school,” she said, beaming. “My dream is when you walk into a dialysis clinic, I want a sign to say, ‘Have you ever thought about getting a xenotransplant?’”

That same month, the U.S. Food and Drug Administration (FDA) paved the way for Looney’s vision when it gave a green light to a bona fide clinical trial of xenotransplantation—a first—by United Therapeutics, the parent company of Revivicor, a biotech that created Looney’s kidney. After a series of one-off transplants like hers, the trial offers the company a regulatory path to prove the worth of its pig kidneys and then sell them. Later this year, eGenesis, which provided Andrews’s kidney, plans to seek FDA approval for its own trial. A Chinese company, ClonOrgan Biotechnology, also has an aggressive gene-editing program in pigs, and an unidentified 69-year-old woman received one of its kidneys in March.

Many leaders in the small xeno field say this is the year pig organs will demonstrate, convincingly, that they can help alleviate the dire shortage of human organs available for transplant. “We are at a tipping point now,” says MGH surgeon David Cooper, who began doing pig-to-baboon transplants in 1985 and has worked with both Revivicor and eGenesis. “What we need now is one or two patients, say, with a kidney transplant, who do well for several months or a year—or longer.”

The need is pressing. In the United States alone some 90,000 hoped to get kidneys last year, nearly 10,000 wanted livers, and another 3500 needed a donor heart. But among xeno researchers there remain conflicting ideas about the ideal pigs to use, the most important edits to make to their genomes, and the best way to prevent the human immune system from attacking its porcine interloper. “At this point, there are a lot of open questions that haven’t been answered,” says David Sachs, an immunologist at MGH and Columbia University whose interest in xenotransplantation dates back to 1971.

The field is also prone to showmanship and bad blood. Although many of the field’s researchers have collaborated, the intense media attention these bizarre-sounding experiments receive fuels enmities between star surgeons and can be unsettling for patients.

The latest twist illustrates how the field often takes two steps forward, one back. Not long after Looney spoke with *Science*, her pig kidney failed for reasons that are still unclear. Her surgeons removed it, and she’s once again on dialysis—although she remains a candidate for a second pig kidney. Andrews, for now, is still doing well with his foreign helper.

“WIZARD SURGEON PLANS RENEWING ALL VITAL ORGANS,” blared a *Chicago Tribune* headline on 20 June 1922. Serge Voronoff, the breathless report from Paris declared, had made “the startling discovery” that he could “rejuvenate” humans with transplanted “glands” from chimpanzees—these included testicles—and he was moving on to transferring every organ. “I can push back a man’s age 20 or 30 years, making his faculties more vigorous,” boasted Voronoff, a Russian who had relocated to France.

More than a decade earlier, two other surgeons in Europe had attempted to transplant monkey, goat, and pig kidneys to the arms and thighs of people who had chronic renal failure. Even earlier, physicians had experimented with tissue, bone, and cornea grafts from animals. But it was Voronoff who brought xenotransplantation world renown—and, as increasing numbers of doctors scrutinized his results and dismissed them as chicanery, ridicule.

Towana Looney’s xenotransplant functioned for 130 days, a new record.

PHOTO: JACKIE MOLLOY/*THE NEW YORK TIMES* VIA REDUX

Human-to-human organ transplants had a slower start. A Soviet surgeon performed the first one in 1933—but the kidney failed, and the patient quickly died. At the time, surgeons understood only dimly that a person’s immune system rejects organs from other people unless they’re a close genetic match to the recipient. But in the 1950s, Boston surgeon Joseph Murray and colleagues succeeded in transplanting one of a man’s kidneys to his identical twin, who was in renal failure. The brother went on to marry one of his nurses, have two children, and live for eight more years.

Few people needing a kidney have an identical twin. But because healthy donors can spare a kidney, surgeons gradually learned how to match many living donors to recipients, often seeking donations from siblings. They also found ways to dampen the immune responses that attack the organs.

In 1962, Murray showed that kidneys from a recently deceased person could also work, creating another, now routine, source of organs. He won a Nobel Prize in 1990 for his pioneering work. And as human kidney transplants became more successful, demand soon outstripped supply.

Xenotransplantation re-emerged as a possible solution to the shortages in 1963 when Keith Reemtsma, a Tulane University surgeon who had been experimenting with transferring organs between lab animals, began transplanting chimpanzee kidneys into people. (Chimps, an endangered species, are no longer used for any invasive biomedical research.) “I feel fine, practically good as new,” Reemtsma’s first xeno patient said at a press conference after his surgery. “I will outlive you all.” He died 3 weeks later. But one woman lived 9 months, even returning to work as a teacher. Joe Tector, a liver transplant surgeon at the University of Miami who has been doing xenotransplantation studies for 2 decades, says the transplant team got “lucky.”

As with other xenotransplant patients, Towana Looney required many medicines after surgery to stave off immune rejection of her new organ and infection from the immunosuppression.

PHOTO: JACKIE MOLLOY/*THE NEW YORK TIMES* VIA REDUX

Then in 1984 came one of the field’s highest profile, most scrutinized failures: the transfer of a baboon heart at Loma Linda University Medical Center to “Baby Fae.” Born with a deformed heart condition that is nearly always fatal within 1 month, Baby Fae lived with the baboon organ for 20 days, under the media spotlight the entire time. The experiment was assailed by animal rights activists, bioethicists concerned about the consent process, and legal scholars appalled by a minor being subjected to such a high-risk experiment. The surgeon, Leonard Bailey, was once advised to wear a bulletproof vest before giving a public talk about the operation.

Eight years later, Thomas Starzl at the University of Pittsburgh transplanted a baboon liver into a gravely ill 35-year-old man who had both HIV and hepatitis B infections and had been refused a human liver elsewhere. Starzl, famed for having pioneered human liver transplants, had decades before tried baboon kidneys in humans and failed. The man went into a coma shortly before the June 1992 xenotransplant, but in a hopeful sign, he was eating and walking 5 days later. Animal rights activists gathered outside the hospital and protested against “Dr. Frankenstarzl.”

The patient died 70 days after the surgery because of problems unrelated to organ rejection. Still, his death had long-lasting consequences. “The excitement around the future of xenotransplantation died with him,” wrote Richard Horton, editor-in-chief of *The Lancet*.

PART OF THE OPTIMISM that led Bailey and Starzl to attempt these high-risk xenotransplants came from powerful new immunosuppressive drugs, first cyclosporine and then tacrolimus. Indeed, after the introduction of cyclosporine, which FDA approved in 1983, rejections of human organ transplants plummeted, and they became so popular that the first major registries formed to match people in need with living and deceased donors.

The success of the drugs also attracted deep-pocketed pharmaceutical companies to xenotransplantation, despite the discouraging outcome of Starzl’s attempt. One Wall Street analyst predicted it would be a $6 billion market by 2010. At the same time, the field shifted away from using monkeys as the source of organs to pigs. Not only were swine far easier to breed and handle, but they also raised fewer ethical issues, and they cost less. Pig-to-monkey xenotransplants provided a helpful animal model to test ideas, too.

Firms started to genetically engineer pigs to prevent rejection and test their organs in monkeys in the 1990s. Still, progress was slow. “You have to be patient, patient, patient, patient, and you need guts,” says Bruno Reichart, a retired surgeon in Germany who started in the field 35 years ago and recently co-founded the company XTransplant. And then came a flashing red light. A 1997 report in *Nature Medicine* showed that remnants of ancient retroviruses that had colonized the pig genome could infect lab-grown human cells. The threat that a xenotransplant could infect humans with these porcine endogenous retroviruses (PERVs) sent the field into a tailspin. Attacks by animal rights groups, the growing alarm around mad cow disease, and opposition to genetically modified organisms (“Frankenswine”) also discouraged investors.

Immunologist Corinne Savill, who led a xeno program for Novartis, said the risks became too high for the company. “What if in doing this you basically started the world’s next pandemic?” she asks. Savill, now an executive at Cullinan Oncology, says there was a more formidable impediment still. “The immunology, the science, is just really hard, and it wasn’t as if at that time you had something that said, ‘Hey, it works.’”

IN THE WINTER, the winding road that leads to Revivicor’s main pig farm in rural Virginia has beautiful views of snow-covered hills. But imperceptible “black” ice can coat this scenic byway, making for a treacherous drive—not unlike the journey to practical xenotransplants.

This Blacksburg farm, which provided Looney’s kidney, helped reignite the field more than 2 decades ago when it belonged to a company called PPL Therapeutics, which famously helped clone Dolly the sheep in the United Kingdom. PPL had overcome a major impediment to xenotransplantation: In pig embryos, it knocked out the gene for an enzyme that creates the sugar molecule, or carbohydrate, known in shorthand as alpha-gal, and then cloned the offspring. Alpha-gal studs the surface of pig cells, but those of humans, other great apes, and old-world monkeys don’t make it because all the species have an inactivated gene for the enzyme. So when our immune system sees alpha-gal on a xenotransplant, it attacks. Within 24 hours, a massive antibody assault can lead to what’s called hyperacute rejection, the bête noire of the transplant field.

Knocking out alpha-gal solves that problem. But when researchers put alpha-gal knockout organs from pigs into monkeys, other hurdles popped up. “Once we’d inactivated the alpha-gal gene, it’s like peeling an onion—all of a sudden, you learn what else you need to do in order to modulate the animal to eliminate rejection,” says molecular geneticist David Ayares, who spun off Revivicor—and got the

Blacksburg farm—in 2003 when PPL was heading for bankruptcy. "It was taking too long for them to get a return on investment," Ayares says.

Revivicor would conclude that its ideal pig would need far more edits than the alpha-gal knockout, but it began to run out of money itself. In 2011, when Revivicor only had 2 months of funding left in the bank, United Therapeutics came to the rescue. Martine Rothblatt, an entrepreneurial lawyer who started Sirius Satellite radio in 1990, had originally launched the company to develop drugs to help her young daughter, Jenesis, survive a deadly pulmonary disease that can require a risky lung transplant. By 2001 Rothblatt had developed a new interest, xenotransplantation, even earning a Ph.D. on ethical issues surrounding it. With its purchase of Revivicor, "United Therapeutics saved the field," Ayares says. Revivicor's competitor, eGenesis, "never would have even started if Martine had not demonstrated that this was a viable endeavor."

Revivicor not only had ample funding, it could soon take advantage of a new gene-editing tool, CRISPR. Two decades ago, knocking out a gene was an inefficient, multistep process, but CRISPR now allows scientists to edit animal genes with relative ease. At the farm, Ayares picks up a 2-month-old piglet that has the same edits as the animal that supplied Looney's kidney. "This has 10 genetic modifications: four pig genes inactivated and the addition of six human genes to modulate immune rejection," he explains.

After identifying the alpha-gal problem, researchers discovered two other carbohydrates on pig cells that kick human immune systems into overdrive: an Sd antigen—named after a man named Sid, who supplied the antibody sample that found it—and one known in shorthand as Neu5Gc. Nearly every xeno strategy being pursued by companies today knocks out all three genes needed to produce these carbohydrates.

The fourth knockout in Revivicor's pigs cripples their growth hormone receptor. Without that modification, they could grow to 300-plus kilograms, and their organs—which are "harvested" when they're about 6 to 8 months old—might continue to grow in humans. In contrast, eGenesis,

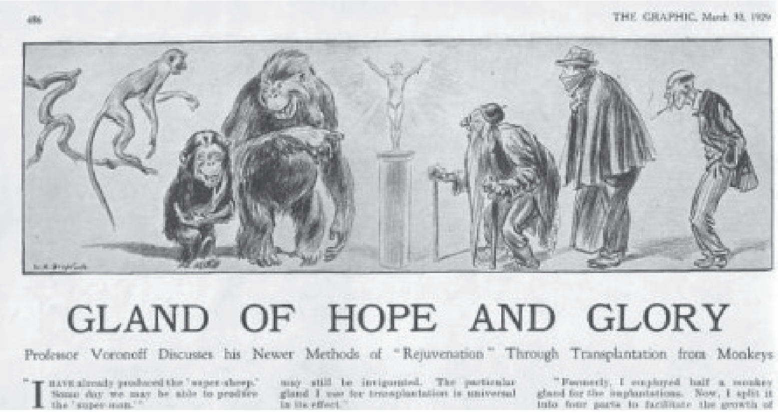

THE GRAPHIC, March 30, 1929

GLAND OF HOPE AND GLORY

Professor Voronoff Discusses his Newer Methods of "Rejuvenation" Through Transplantation from Monkeys

1929 Serge Voronoff popularizes transplanting monkey and chimp gonads.

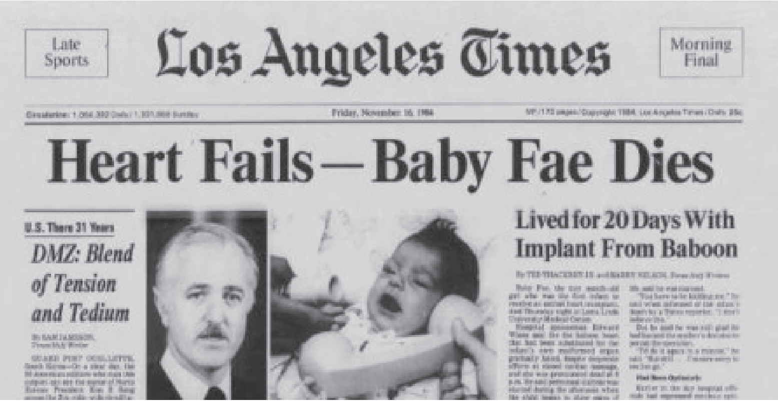

Late Sports

Los Angeles Times

Morning Final

Friday, November 16, 1984

Heart Fails—Baby Fae Dies

U.S. There 31 Years

DMZ: Blend of Tension and Tedium

Lived for 20 Days With Implant From Baboon

1984 Baby Fae survives 20 days after getting a baboon heart.

Xeno's checkered history

Efforts to transplant animal organs into people—xenotransplantation—date back more than a century, but have been marked by failure after failure. Progress in human-to-human transplants, coupled with improved immunosuppressive drugs and gene-editing advances, have prompted new enthusiasm for xeno. Still, success remains far from certain.

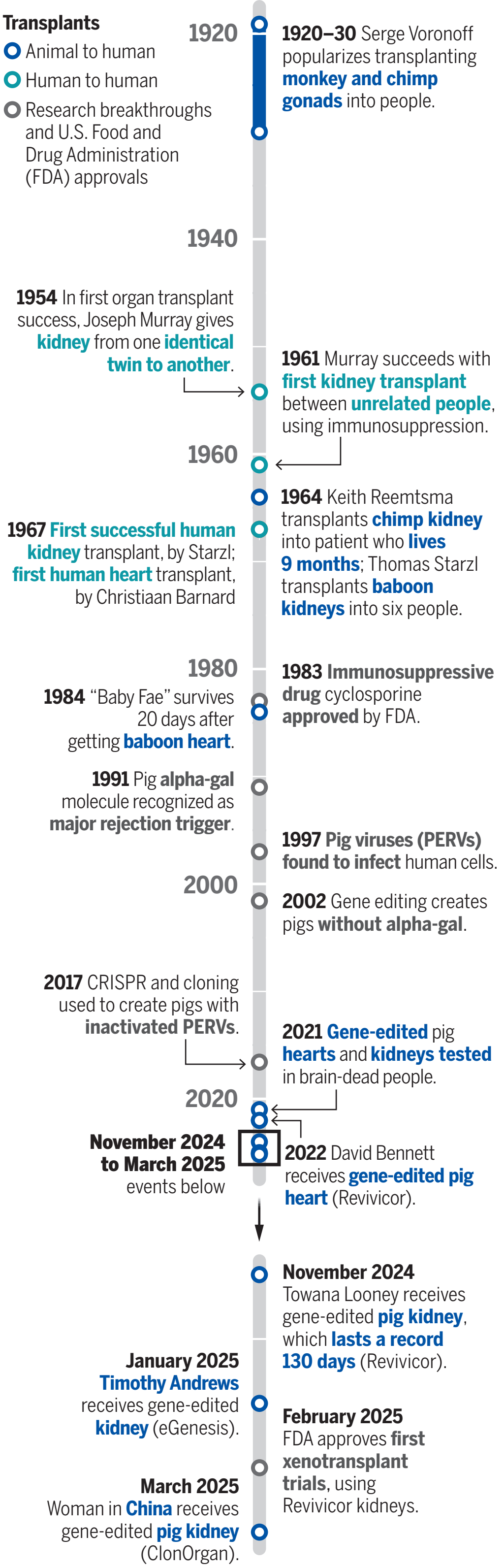
Transplants
○ Animal to human
○ Human to human
○ Research breakthroughs and U.S. Food and Drug Administration (FDA) approvals
1920
1940
1960
1980
2000
2020

1920–30 Serge Voronoff popularizes transplanting **monkey and chimp gonads** into people.

1954 In first organ transplant success, Joseph Murray gives **kidney** from one **identical twin to another**.

1961 Murray succeeds with **first kidney transplant** between **unrelated people**, using immunosuppression.

1964 Keith Reemtsma transplants **chimp kidney** into patient who **lives 9 months**; Thomas Starzl transplants **baboon kidneys** into six people.

1967 **First successful human kidney** transplant, by Starzl; **first human heart** transplant, by Christiaan Barnard

1983 **Immunosuppressive drug** cyclosporine **approved** by FDA.

1984 "Baby Fae" survives 20 days after getting **baboon heart**.

1991 Pig **alpha-gal** molecule recognized as **major rejection trigger**.

1997 **Pig viruses (PERVs) found to infect** human cells.

2002 Gene editing creates pigs **without alpha-gal**.

2017 CRISPR and cloning used to create pigs with **inactivated PERVs**.

2021 **Gene-edited** pig **hearts** and **kidneys tested** in brain-dead people.

2022 David Bennett receives **gene-edited pig heart** (Revivicor).

November 2024 to March 2025 events below

November 2024 Towana Looney receives gene-edited **pig kidney**, which **lasts a record 130 days** (Revivicor).

January 2025 **Timothy Andrews** receives gene-edited **kidney** (eGenesis).

February 2025 FDA approves **first xenotransplant trials**, using Revivicor kidneys.

March 2025 Woman in **China** receives gene-edited **pig kidney** (ClonOrgan).

CREDITS: (PHOTOS, TOP TO BOTTOM) *THE GRAPHIC: AN ILLUSTRATED WEEKLY NEWSPAPER* 20 MARCH 1929; *THE LOS ANGELES TIMES*, 16 NOVEMBER 1984; (GRAPHIC) V. PENNEY/*SCIENCE*

DO NOT USE THIS PEN

Revivicor's David Ayares holds a piglet with 10 edited genes (top); a company researcher removes DNA from a pig egg (bottom) as part of the cloning process used to breed the edited animals.

ClonOrgan, and XTransplant leave the growth hormone receptor intact and get around the growth problem by using miniature pig breeds.

The human genes that companies add to the pigs aim to dampen other immune responses (see table, p. 911). Two attempt to shut down the "complement cascade," in which proteins in the blood activate each other to crank up inflammation and other immune responses. Two others tame inflammation-triggered blood coagulation and thrombosis, one reduces inflammation itself, and one prevents the pig organs from sparking an "eat me" signal that instructs a person's phagocytes, a type of immune cell, to gobble foreigners.

No two xeno companies target the same set of genes, because nobody knows what will keep a pig organ healthy in a person. "There are so many other antigens in the pigs that we are not worried about at the minute that we *should* be worried about," Cooper cautions.

Xenotransplant teams are also still experimenting with different cocktails of immunosuppressive drugs that may be crucial to long-term success. Unlike Looney, Andrews has been receiving a monoclonal antibody that inhibits a human cell surface molecule known as CD154, which plays a central role in activating immune cells and may drive the gradual formation of human antibodies against pig antigens. "Anti-CD154 is the key drug," Cooper insists.

Transplants of edited pig organs into monkeys suggest all this tinkering will pay off—xenotransplant survival in these animals is now measured in years, not months. Still, Tector, who is engineering pigs with his own company, Makana Therapeutics, contends that "no one has the right pig yet." The many gene edits done to pigs so far only dampen rejection, he says, and do not lead to the real goal: full tolerance of the foreign organ. That, he says, will require another round of edits to eliminate what are known as swine leukocyte antigens, or SLAs, which stud all pig cells. SLAs allow a pig immune systems to distinguish self from nonself but can ramp up human immune rejection of transplanted organs.

Others, however, suspect further gene edits and various drug cocktails may not solve the tolerance riddle. "I am skeptical that all these latest genetic modifications are really needed," says Columbia University immunologist Megan Sykes, a longtime collaborator of Sachs, one of the field's most experienced researchers. "The only important one so far that I know of is the alpha-gal knockout, and that was done years ago."

Sachs and Sykes have recently shown that an organ with that gene edit alone can survive remarkably long if they add one other ingredient to the transplant: a pig thymus. This gland helps educate an animal's immune system—specifically, its maturing T cells—to recognize self. A little bit of pig thymus might tell human immune cells to leave the new organ alone, the pair theorized. "If you control the T cell response, that's the important thing," Sykes says.

At a transplantation meeting in 2023, they described putting an alpha-gal knockout "thymokidney"—a piece of the pig's thymus grafted onto a kidney—into baboons. It functioned for more than a year with minimal immunosuppressive drugs. Sachs doesn't claim full tolerance has been achieved, however, and he is now testing further gene edits with support from a company he co-founded, Choironex. (The company is funded by Pablo Legorreta, a pharma billionaire who has a child with kidney disease.) Choironex expects to seek FDA approval to test its pig kidneys in humans later this year.

As for the PERVs that spooked the field in 1997, only eGenesis attempts to engineer them out of their donor pigs. Using CRISPR, Harvard University geneticist George Church, a co-founder of the company, and his team made 59 more edits to the DNA of their pigs to inactivate PERV sequences. Other companies, including Revivicor, say they can vastly reduce the likelihood of potentially dangerous PERVs in their pigs through screening and breeding.

"There's never been a transmission to a human," Ayares stresses, whether to xenotransplant patients or to workers in pig slaughterhouses. But Mike Curtis, CEO of eGenesis, sees it differently. "If I was a patient and had the choice between a fully retrovirally inactivated porcine donor and one that might carry retroviral risk, I know which one I would take," he says.

AFTER A LONG HIATUS, the new era of xenotransplant experiments began in September 2021 with transplants of gene-edited pig kidneys into people who were brain-dead but whose bod-

PHOTOS: J. COHEN/*SCIENCE*

ies were volunteered by their families for tests of how the transplants would fare.

NYU Langone's Robert Montgomery, who has a transplanted human heart himself, was first, transplanting an alpha-gal knockout thymokidney, created by Revivicor based on the pig-to-monkey studies of Sykes and Sachs. Five days later, Jayme Locke at the University of Alabama at Birmingham (UAB) transplanted a 10-gene-edited kidney from another Revivicor pig. The two teams would do five more xenotransplants between them in brain-dead people, and other researchers in China and Pittsburgh have done similar decedent transplants of gene-edited pig kidneys and livers.

Some saw the experiments as macabre and pointless, but the researchers involved say they yielded valuable data on how the immune system rejects xenotransplants. MGH nephrologist Leonardo Riella, who cares for Andrews, says there was a sociological benefit as well. "We didn't know how the public would react about transplanting a pig kidney into humans," Riella says. "The way it was accepted, and how we saw patients actually very excited about the news, that was eye opening."

What's more, the UAB xenotransplantation program that did the decedent transplants helped pave the way for Looney's pig kidney. Launched in 2016 with $19.5 million from United Therapeutics, the program hired Tector as its director and other leaders in the field including Cooper. It built a new, "designated pathogen-free" pig facility nearby. And it was Locke who met Looney at the beginning of her search for a donor kidney.

After donating a kidney to her mother in 1991, Looney 25 years later suffered kidney failure herself and started dialysis. Her prospects for getting a donated human kidney turned out to be poor. She had high levels of antibodies against the tissue of most other people, a phenomenon sometimes seen in women who have had multiple pregnancies, resulting in prolonged exposure—via the fetuses—to antigens from the fathers. So that is how Looney moved to the front of the line for a pig kidney.

Administrative changes at UAB, ego clashes, and intellectual property concerns all combined to sink its xenotransplant program by 2021. "It was a terrible loss for Alabama," Cooper says, "because they could be dominant in the field now."

Instead, a team at the University of Maryland on 7 January 2022 was the first to transplant a gene-edited pig organ—a heart—into a living person. The man, David Bennett, was hospitalized for heart failure and required a machine to oxygenate his blood. He was told by several transplant centers that he wasn't a candidate for a human organ because he had a history of not complying with medical advice. "It was either die or do this transplant," Bennett said, the day before surgery, in which he received a heart from a Revivicor pig with its 10 edits. "I want to live. I know it's a shot in the dark, but it's my last choice." He lived 60 days before he died from heart failure, which his surgeons said may have in part been tied to inflammation from a pig cytomegalovirus inadvertently transmitted from the organ.

In September 2023, the team transplanted a second pig heart with the same edits to Laurence Faucette, who was ineligible for a human heart because of severe atherosclerosis and a recent gastrointestinal bleed. Faucette, who had been given little time to live if he did not get a new heart, died 6 weeks later. "You start with a great disadvantage with these patients," says Muhammad Mohiuddin, who co-led the surgical team for both xenotransplants and heads the International Xenotransplantation Association.

The first living patients to receive gene-edited pig kidneys similarly had complicated medical histories. In March 2024, MGH transplanted an eGenesis kidney into a man who had diabetes, hypertension, and previously received a human kidney that failed. A month later, NYU Langone gave a Revivicor thymokidney to a woman who also had a mechanical heart pump. Both died within 2 months, though doctors say the pig organs were still functioning.

Locke in May 2024 received FDA approval to do Looney's transplant at UAB. But with the demise of the xenotransplant program there, UAB would not let her proceed. Montgomery, who had been Locke's mentor, took over Looney's care at NYU Langone.

Her transplant, done with Locke's assistance, took place on 25 November 2024. On it rode not just her own hopes, but those of a burgeoning industry. By moving into healthier patients like Looney and Andrews, the xeno companies are hoping to finally have more success—and justify their expanding investment in a field that they contend will in the not-too-distant future produce enough organs for everyone in need.

IN A CHRISTIANSBURG, VIRGINIA, industrial park about 25 kilometers from the Revivicor farm, United Therapeutics last year built a $75 million facility dedicated to gene-edited pigs. From the outside the boxy building looks more like a drug manufacturing plant than a farm. If the company's vision becomes a reality and its pig organs receive FDA approval, they will, in effect, be drugs.

Brave new pigs

Various gene-editing strategies aim to create pigs whose organs will survive in a human body. Inactivating pig genes or adding human genes can limit immune rejection or keep organs small, for example.

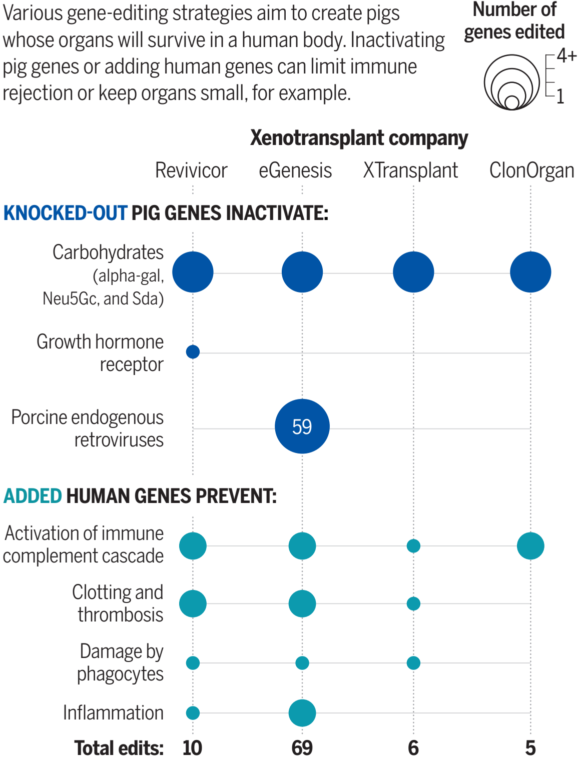

As with all drug manufacturing, sanitation is crucial: Pregnant sows from the Blacksburg farm are brought to an "introduction barn" at the Christiansburg site to give birth to their gene-edited piglets, which are carefully screened for viruses before they move into the pathogen-free facility. Humans who then work with the pigs wear personal protective equipment and must shower before and after entering. Elaborate systems eliminate waste, purify water, and constantly filter the air for the pigs. "They drink cleaner water and are in

CREDITS: (GRAPHIC) M. HERSHER/*SCIENCE*; (DATA) REVIVICOR; EGENESIS; XTRANSPLANT; CLONORGAN

> “I did it knowing that no matter what happened, I did something for humanity.
>
> **Timothy Andrews**

Timothy Andrews (right), leaving the hospital after his xenotransplant, thanks Tatsuo Kawai, who led the surgical team.

cleaner air than the employees,” says Aaron Orkin, who runs the facility.

The company is investing $200 million more to build similar pathogen-free facilities in Texas and Minnesota. “We are envisioning multiple facilities with an organ output of 2000 a year across the United States, Europe, and Asia,” Ayares says. eGenesis has two pig facilities of its own that it predicts can produce up to 1000 pigs a year.

Both companies still heavily rely on cloning to replicate animals with all the desired gene edits, because edits can be lost in conventional breeding. But cloning is slow and expensive. “It will be very difficult to produce several thousands of pigs” if you rely on cloning, says veterinarian and bioengineer Eckhard Wolf, the lead scientist at XTransplant, which is focusing on heart xenotransplants.

XTransplant and Choironex also clone their pigs to start but then rely on breeding the animals, which maintain gene edits better because they are so closely related. Similarly, ClonOrgan only breeds within its existing population of 500 gene-edited pigs, says its founder Dengke Pan. These pigs, he says, “can be used for mass production and supply of clinical xenotransplantation donor pigs, meeting the needs of hospitals in China.”

A test of whether these investments will pay off is imminent, as United Therapeutics moves ahead with clinical trials of Revivicor’s gene-edited pig kidneys at NYU Langone and Johns Hopkins University. If all goes well with the first six patients, the clinical trials can expand to 44 people at more sites. FDA has defined the “primary endpoint”—its criterion for success—as a kidney still working at 6 months, but it’s unclear what percent of trial participants will have to hit that mark to win the agency’s approval.

Beyond that hurdle lies the market. Curtis of eGenesis says the ultimate reception will depend on what the pig organs will cost—the companies haven’t released any public estimate, but the bill will surely be steep at first—and how much insurers and government health systems will cover. What patients and families consider a successful outcome will also be crucial. “We’re not convinced a 6-month end point is enough, but boy, it’s a great target for [regulatory] registration,” Curtis says. “Beyond that, I think you’re going to have to show some patients can go beyond 6 months.”

LOONEY, UNFORTUNATELY, didn’t make it that far. Seventeen days after the transplant, protein levels in her blood rose, and a biopsy revealed an antibody onslaught against the kidney. To solve the problem, her physicians repeatedly did a procedure called plasmapheresis that pulls blood from the body, separates the plasma and removes the antibodies, then returns clean plasma to the body. After plasmapheresis, Montgomery says, “the antibody never comes back.” But the immune system has myriad actors, and something else began to damage Looney’s new organ in late March.

On 4 April, Looney had her pig kidney removed. She had lived with the xenotransplant for 130 days. “This is really a victory,” Montgomery argues. “If you had asked me a couple of years ago whether we would be having this level of success, I probably wouldn’t have thought we would,” he said. Early indications suggest the kidney may have failed because an unrelated infection led doctors to reduce Looney’s immunosuppressive drug, but the ongoing studies should better clarify what went wrong.

At the time, Anderson was hospitalized with an infection unrelated to the xenotransplant. He since has recovered and returned home. “I know there are no guarantees, but it is sobering to see it happened,” he said about Looney’s xenostransplant ultimately failing. “Two things I live by now: It is what it is, and this is what we signed up for,” he said. “I was already committed to death with dialysis, so it wasn’t that hard of a leap for me,” Andrews added. “I did it knowing that no matter what happened, I did something for humanity.”

Six days after having her kidney removed, Looney was back home and having her hair dyed orange. Her hairdresser posted a video of them on Facebook in which she asked her client what’s the word for the day? “Blessed,” a smiling Looney said.

“And highly favored,” the hairdresser said.

“And highly favored,” Looney agreed.

PHOTO: KATE FLOCK/MASSACHUSETTS GENERAL HOSPITAL

eppendorf
& Science
PRIZE FOR
NEURO
BIOLOGY

2024 Winner
Laura Seeholzer, Ph.D.
University of California San Francisco,
School of Medicine, USA

For research on airway neuroendocrine cells responding to external threats

Application Deadline
June 15, 2025

Call for Entries 2025

Eppendorf & Science Prize for Neurobiology
The annual Eppendorf & Science Prize for Neurobiology is an international prize which honors young scientists for outstanding neurobiological research based on methods of molecular, cellular, systems, or organismic biology. If you are 35 years of age or younger and doing great research, now is the time to submit an entry for this prize.
It's easy to apply! Write a 1,000-word essay and tell the world about your work.

eppendorf.com/prize

As the winner, you could be next to receive
> Prize money of US$25,000
> Publication of your work in *Science*
> Full support to attend the Prize Ceremony held in conjunction with the Annual Meeting of the Society for Neuroscience in the USA
> 10-year AAAS membership and online subscription to *Science*
> Complimentary products worth US$1,000 from Eppendorf
> An invitation to visit Eppendorf in Hamburg, Germany

eppendorf

Science
AAAS

AAAS® and Science® are registered trademarks of the American Association for the Advancement of Science, USA. Eppendorf® and the Eppendorf Brand Design are registered trademarks of Eppendorf SE, Germany.
All rights reserved, including graphics and images. Copyright © 2025 by Eppendorf SE. Photography: Brian Carey, figMedia

COMMENTARY

PERSPECTIVES

CLIMATOLOGY

Social impacts of glacier loss

More than three-quarters of global glacier mass is projected to disappear under present-day policies

Cymene Howe[1,2] *and* **Dominic Boyer**[1,2]

It is no secret that melting glaciers are a signal of climate disruption. According to the Intergovernmental Panel on Climate Change, global ice loss is among the most certain indicators of warming conditions (*1*). Earth has now entered a new period in which glaciers are not simply retreating but are disappearing altogether. However, long-term glacier mass loss is largely unquantified owing to the lack of a comprehensive prediction model that accounts for all glaciers and constraints. On page 979 of this issue, Zekollari *et al.* (*2*) report the simulation of long-term glacier mass loss using eight glacier evolution models, which estimated that only 24% of glacier mass will remain under present climate policies. This finding underscores that short- and midterm glacier preservation efforts could affect changes in global glacier mass over many centuries.

Zekollari *et al.* predicted the fate of glaciers based on 80 future climate scenarios and global temperature increases above preindustrial levels. The authors estimated the global glacier mass and corresponding global mean sea-level rise at equilibration—a steady state in which glacier mass and geometry become stable. The results showed that under the Paris Agreement (global mean temperature does not rise more than 1.5°C above preindustrial levels), 53% of the present glacier mass could be preserved. Under existing climate policies, global mean temperature is on track to reach 2.7°C above preindustrial levels and 76% of global glacier mass is predicted to eventually disappear.

Although these metrics of melting glaciers may look abstract, the consequences of glacial loss have a variety of effects on natural and social environments on a planetary level. Melting raises sea levels (*3*), and affect water resources downstream (*4*) including their ecosystemic biodiversity (*5*). In addition, melting glaciers can compound other natural hazards such as increasing the formation of icebergs and accelerating permafrost erosion (*6*). They can also harm economic systems such as the tourism industry (*7*) and damage cultural heritage. As impacts to the cryosphere accelerate, so, too, do social repercussions. For example, the world's first funeral for a glacier was held in Iceland in 2019 for a little glacier called "Ok" (*8*), followed shortly thereafter by a memorial for Pizol Glacier in Switzerland and Ayoloco Glacier in Mexico. Since then, memorials for disappeared glaciers have increased across the world, illustrating the integral connection between loss in the natural world and human rituals of remembrance that are crucial for social cohesion.

The Global Glacier Casualty List (*9*), which is an online extension of these memorial acts, is a collaborative project between social scientists, glaciologists, and community members across six continents. This resource provides a global overview of melted glaciers as well as specific stories about them, featuring narratives and recollections that are important to the people who have lived near, worked with, and studied each of these now-vanished glaciers.

PHOTO: SIMONE BOCCACCIO/SOPA IMAGES/LIGHTROCKET/GETTY IMAGES

Melting of the ice cap on top of Africa's highest peak, Mount Kilimanjaro, affects local communities and ecosystems.

Whether a glacier is critically endangered (predicted to expire by 2050) or has ceased to be a glacier altogether, each entry in the list is geotagged on an interactive globe, indicating how glaciers are fundamental to both social and environmental processes.

Glacier loss causes stress on food chains and water supplies. For example, meltwater from Glisan Glacier in Oregon has changed Mount Hood's vibrant alpine ecosystem, putting surrounding orchards at risk (*10*). Ice loss from Glisan also threatens salmon and steelhead fisheries as well as the microbiomes created by springs throughout the region. The Quinault, one of eight Indigenous tribes living on Washington state's Olympic Peninsula, rely on glacial meltwater to sustain salmon populations for food as well as for cultural and economic purposes. The loss of Anderson Glacier in the Olympic Mountains further endangers local biodiversity. For Careser Glacier in Italy and the many glaciers that occupy the Icelandic Highlands, decreased water availability for hydroelectricity production will be one outcome of glacial loss, affecting industries that rely on renewable energy. This could cause some industries to turn to fossil fuels for power, accelerating the greenhouse gas emissions that are contributing to the loss of glaciers.

Glaciers are also important sites for undertaking scientific training, especially for the next generation of glaciologists whose expertise will undoubtedly be of great importance in an unpredictable future for ice. For instance, Santa Isabel Glacier in Colombia, which is predicted to disappear by 2030, has long been a key training area for glaciologists (*11*) and has the longest series of scientific measurements in the country. The snows of Kilimanjaro are among the most iconic in the world, and the glaciers atop the mountain form a key part of a United Nations Educational, Scientific, and Cultural Organization (UNESCO) World Heritage Site, which is also a source of tourism revenue. With less than 1 km^2 of glacial mass remaining, it is almost certain that Africa will be the first continent to entirely lose its glaciers because of global warming.

Beyond these impacts, glaciers are also repositories of cultural heritage and history. Yala Glacier in Nepal has been regarded as one of many sacred places for local people, but it is projected to vanish by 2040 (*12*). In May of 2025, a memorial was held for this glacier, with Buddhist monks in attendance. Venezuela lost its last remaining glacier in 2024. In a legend well known to the Indigenous people of the Venezuelan Andes, the five glaciated peaks of the region were home to five giant white eagles who settled atop the highest mountains in the land, long before colonization took hold. Now, the eagles and the ice survive only in story.

The close-knit relationship between the natural and social worlds illustrates the importance of complementing physical science with social science to understand how ritual and memory can create communities of purpose around climate mitigation. Policy alone may not achieve all the changes in energy and resource use that are required to accelerate decarbonization. Mass mediation (*13*) and mobilization, as well as collaborations across scientific disciplines, are needed (*14*).

This year, the United Nations is leading an initiative to draw attention to the world's disappearing glaciers by calling for their protection. The year 2025 is the United Nations' international year of glaciers' preservation (*15*). As Zekollari *et al.* underscores, the effectiveness of present and near-term climate policies will play a decisive role in the future of glaciers. If greenhouse gas emissions are reduced and global mean temperature is kept to 1.5°C above preindustrial levels, many of the world's glaciers can still be preserved. Consequently, glacier funerals will be fewer, and mournful stories of fallen glaciers can be reduced. In recognizing all that has been lost, focus now should turn to all that can be saved. □

REFERENCES AND NOTES

1. Intergovernmental Panel on Climate Change, *The Ocean and Cryosphere in a Changing Climate: Special Report of the Intergovernmental Panel on Climate Change*, H.-O. Pörtner *et al.*, Eds. (Cambridge Univ. Press, 2019).
2. H. Zekollari *et al.*, *Science* **388**, 979 (2025).
3. L. Jakob, N. Gourmelen, *Geophys. Res. Lett.* **50**, e2023GL102954 (2023).
4. M. Huss, R. Hock, *Nat. Clim. Change* **8**, 135 (2018).
5. J. B. Bosson *et al.*, *Nature* **620**, 562 (2023).
6. Y. Ding *et al.*, *Earth Sci. Rev.* **213**, 103500 (2021).
7. E. Salim, *Front. Hum. Dyn.* **5**, 1137551 (2023).
8. C. Howe, D. Boyer, *Soc. Anthropol.* **32**, 30 (2024).
9. D. Boyer, C. Howe, Global Glacier Casualty List; https://glaciercasualtylist.rice.edu/.
10. J. B. Miller, M. D. Frisbee, T. L. Hamilton, S. K. Murugapiran, *Environ. Res. Lett.* **16**, 064012 (2021).
11. J. L. Ceballos *et al.*, *Ann. Glaciol.* **43**, 194 (2006).
12. S. Sunako *et al.*, *J. Glaciol.* **69**, 425 (2023).
13. N. Oreskes *et al.*, *Regen. Environ. Art Culture* **1**, 1 (2025).
14. C. Howe, D. Boyer, *Nat. Cities* **1**, 330 (2024).
15. UNESCO, World Meteorological Organization, 2025 International Year of Glaciers' Preservation; https://www.un-glaciers.org/en.

ACKNOWLEDGMENTS

The authors acknowledge support from the National Science Foundation Office of Polar Programs, Arctic Social Sciences (award no. 2030474), The Rockefeller Foundation's Bellagio Center, and the scientific advisory board of the Global Glacier Casualty List.

10.1126/science.ady1688

---

[1]Department of Anthropology, Rice University, Houston, TX, USA. [2]Center for Coastal Futures and Adaptive Resilience, Rice University, Houston, TX, USA. Email: ach1@rice.edu

SUPERCONDUCTORS

Sleuthing out the symmetry of a superconductor

Experimental observations provide clues to understanding an enigmatic superconductor, uranium ditelluride

Andriy H. Nevidomskyy[1,2]

In the movie *Avatar*, mountains are hovering in the atmosphere because of a large deposit of a fictional rare-earth mineral, unobtanium, with room-temperature superconductivity (conducts electricity with zero resistance). In real life, superconductivity usually happens at cryogenic temperatures at which electrons in a material pair up to form so-called Cooper pairs, following the rules set by quantum mechanics. This creates a superconducting gap that describes the energy required to excite an electron from its paired (superconducting) state into an excited (resistive) state. A fundamental question about any superconductor is determining the symmetry of this gap. On page 938 of this issue, Gu *et al.* (*1*) report an experimental observation that is critical to understanding this symmetry in an enigmatic superconductor, uranium ditelluride. The finding should place constraints on how the superconducting state is modeled in this material for future studies.

Nearly all known superconducting materials belong to the spin-singlet class in which a Cooper pair consists of two electrons with opposite spins (net spin is zero). The most common ones are s-wave superconductors, which have Cooper pairs with a spatially symmetric wave function. In 1963, a different kind of superconducting state that is antisymmetric was proposed (*2*). In this case, the electrons form the Cooper pair in a spin-triplet configuration (net spin can be −1, 0, or 1), which was first observed in a superfluid helium-3. Since this discovery, a search for a solid-state superconducting analog of helium-3 has been underway, and a handful of potential materials has been proposed (*3*–*5*).

Probing the symmetry of superconducting gap

Scanning tunneling microscopy using a superconducting niobium tip can capture strong spectroscopic signatures of superconducting states of uranium ditelluride through Andreev reflection. This process allows the injection of an electron into a superconductor to form a Cooper pair by reflecting a hole.

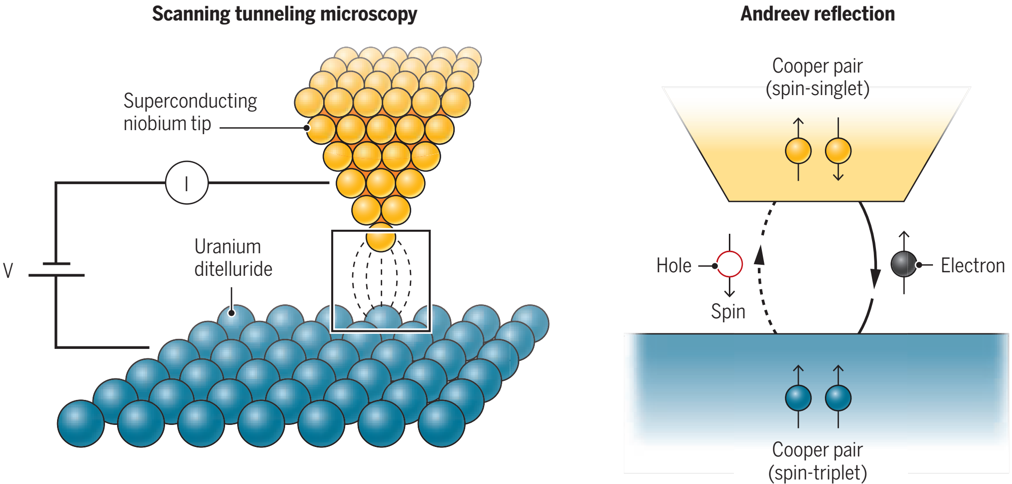
Scanning tunneling microscopy
Superconducting niobium tip
I
V
Uranium ditelluride
Andreev reflection
Cooper pair (spin-singlet)
Hole
Spin
Electron
Cooper pair (spin-triplet)

V; voltage, I; current.

GRAPHIC: K. HOLOSKI/*SCIENCE*

A candidate spin-triplet superconductor that has sparked much interest is uranium ditelluride (*6*, *7*). Intense research has been performed since the discovery of its superconducting properties in 2018 (*6*), but many puzzles remain to be solved. Perhaps the biggest question is the symmetry of electrons in the Cooper pair. The central challenge is whether the superconducting gap in uranium ditelluride is single- or multicomponent, with respect to the symmetry of its crystalline structure. Another closely related question is whether the Cooper pairs have a sense of chirality (being left- or right-handed).

Gu *et al.* used scanning tunneling microscopy to answer these questions. In this method, electrons pass through a potential energy barrier to be injected from an atomically sharp metal tip into a sample to image the atom-resolved topography of the sample surface. This quantum mechanical "tunneling" process is very sensitive to the availability of quantum states (number of different allowed modes) that the electrons can tunnel into. By changing the voltage between the tip and the sample surface, spectroscopic information about the material can be obtained.

A major challenge in characterizing uranium ditelluride is the low critical temperature for superconductivity, which is at most 2 K above absolute zero. In addition, Cooper pairing is reported to vanish along certain crystalline axes in uranium ditelluride. These two effects conspire to weaken the spectroscopic signature of superconductivity that is determined using the conventional metal tip. To overcome this, Gu *et al.* used another superconductor, niobium, as a tip for scanning tunneling microscopy. This approach allowed the authors to exploit a distinct quantum mechanical phenomenon, called Andreev reflection, at the tip–sample interface (see the figure). The technique has previously been used to study a high-temperature superconductor in the cuprate (copper-oxygen compound) family (*8*). Normally, injecting a single electron into a superconductor is prohibited by the gap in the tunneling current spectrum. The Andreev process enables the injection by reflecting a "hole" (absence of an electron), which is viewed as an antiparticle of an electron with the same mass but opposite electronic properties. This allows the electrons and holes to tunnel between the superconducting niobium tip and the surface of uranium ditelluride, manifesting as a peak in the spectrum at zero bias voltage (no voltage between tip and the sample).

Gu *et al.* observed that the shape of this peak in the spectrum was unaffected by the spatial position of the niobium tip relative to the sample surface, underscoring the robustness of the observed signal. The authors argued that the high-intensity Andreev peak at zero bias is direct evidence of the nodes in the superconducting gap of uranium ditelluride. They further examined whether the Cooper pairs had distinct handedness by observing how the spectra changed with the strength of the tunneling current. Theoretical analysis showed that a chiral superconductor should have a zero-bias Andreev peak that is unaffected by the strength of the tunneling current. However, the peak split into two satellites as the tunneling current increased, implying that the Cooper pairs had no distinct handedness.

The study of Gu *et al*. helps settle a long debate about the symmetry of the superconducting state in uranium ditelluride and contributes to theoretical modeling of superconductivity in this material. However, many questions remain unanswered. The properties of the nonsuperconducting state of uranium ditelluride are still poorly understood. Likewise, several measured quantities, such as specific heat and magnetic response, in a superconducting state depend on how the crystals were grown. In particular, the question of whether Cooper pairs are chiral has received contradictory answers from probing the change in polarization of light reflected off a uranium ditelluride crystal (*9*, *10*). Other reports have shown unusual vortices on the surface of uranium ditelluride under an applied magnetic field (*11, 12*) that suggest a nonchiral nature of the Cooper pairs, corroborating the conclusions of Gu *et al*. Further, a sharp zero-energy tunneling peak in the cores of these vortices may also imply a topological nature of superconductivity in uranium ditelluride (*12*).

What makes understanding uranium ditelluride more challenging is the pronounced variation in its superconducting properties under a strong applied magnetic field and pressure. This has led to a conjecture that there may be as many as four or five different superconducting phases in this material (*13*). Can some of these phases be chiral? Although this could be true under strong magnetic fields (*14*), further experimental and theoretical studies are needed to address this issue. The quest to understand the remaining puzzles surrounding the superconductivity of uranium ditelluride centers around two universal questions: What is the symmetry of the superconducting order parameter? And what is the "glue" that enables electrons to pair up? The study of Gu *et al*. may help answer the first question; at the same time, the nature of the pairing in uranium ditelluride remains as elusive as ever. ☐

REFERENCES AND NOTES

1. Q. Gu *et al*., *Science* **388**, 938 (2025).
2. R. Balian, N. R. Werthamer, *Phys. Rev.* **131**, 1553 (1963).
3. S. S. Saxena *et al*., *Nature* **406**, 587 (2000).
4. D. Aoki *et al*., *Nature* **413**, 613 (2001).
5. N. T. Huy *et al*., *Phys. Rev. Lett.* **99**, 067006 (2007).
6. S. Ran *et al*., *Science* **365**, 684 (2019).
7. D. Aoki *et al*., *J. Phys. Soc. Jpn.* **88**, 043702 (2019).
8. M. H. Hamidian *et al*., *Nature* **532**, 343 (2016).
9. I. M. Hayes *et al*., *Science* **373**, 797 (2021).
10. M. O. Ajeesh *et al*., *Phys. Rev. X* **13**, 041019 (2023).
11. R. Yin *et al*., arXiv:2503.21506 (2025).
12. N. Sharma *et al*., arXiv:2503.17450 (2025).
13. S. K. Lewin, C. E. Frank, S. Ran, J. Paglione, N. P. Butch, *Rep. Prog. Phys.* **86**, 114501 (2023).
14. S. K. Lewin *et al*., arXiv:2402.18564 (2024).

10.1126/science.ady3202

---

[1]Department of Physics and Astronomy, Rice University, Houston, TX, USA. [2]Rice Center for Quantum Materials and Advanced Materials Institute, Rice University, Houston, TX, USA. Email: andriy.nevidomskyy@rice.edu

NEUROSCIENCE

A wave of emotion

Sustained brainwide patterns of activity enable emotions to outlast their triggers

Stoyo Karamihalev *and* **Nadine Gogolla**

Emotions shape how individuals experience the world. Some emotions appear and fade away in seconds or minutes, whereas others linger for longer. Acute fear might dissipate quickly upon escape to safety or could transform into enduring anxiety. The grief caused by bereavement may persist for even longer, affecting an individual for many months. Whether fleeting or lasting, emotions influence perceptions, behavior, and decisions well beyond the experience that set them in motion. Yet very little is known about how the brain holds onto these internal states. Explaining the biological basis of their enduring nature is crucial for building a mechanistic understanding of emotion. On page 933 of this issue, Kauvar *et al*. (*1*) report an evolutionarily conserved brainwide response to an emotional stimulus that serves as the early-stage neural substrate of an emotion state. Thus, they identify a fundamental process that may help explain how emotions emerge.

A flash of light in the eye, a sudden noise, or a shooting pain can produce a neural response—a signature of the stimulus that bursts and disappears in milliseconds. However, the emotions that such stimuli can evoke are sustained at longer timescales, from seconds to minutes, and sometimes through to hours or even days (*2*). Not much is known about what facilitates the transformation of a brief stimulus-induced burst of activity into an enduring brainwide state. Kauvar *et al*. aimed to address this gap in knowledge. They shot puffs of air into the eyes of humans and mice to induce an aversive internal state. This precisely timed stimulus caused members of both species to squint their eyes reflexively. When the puff was over, the squint subsided, but did so slowly. The timing of this late-stage eye closure correlated with the negative emotional response reported by human participants. The authors also carried out intracranial electrophysiological recordings to measure brain activity during the task. The human participants underwent recordings as part of epilepsy treatment, so target brain regions were selected on the basis of clinical need but spanned the forebrain, with dense representation of areas such as the insular, premotor cortices and the hippocampus. In mice, recordings were collected from thousands of individual neurons across the whole brain.

The puffs of air caused a sudden burst of neural activity in humans and mice. These initial sharp responses were detected almost everywhere in the brain; however, they decayed within hundreds of milliseconds in areas that are involved early in the hierarchy of sensory processing, such as in parts of the midbrain and thalamus. Notably, Kauvar *et al*. also witnessed a slower wave of neuronal activity: Coordinated clusters of sustained activity echoed through the forebrain limbic and sensorimotor cortical areas over the following seconds. This slower wave of activity followed the dynamics of the nonreflexive eye closure, suggesting that it could be involved in the emotional experience. To test this possibility, the authors administered ketamine, a drug that can evoke a temporary state of dissociation and can flatten emotional responses (*3*). In this state of reduced emotionality, both mice and humans squinted, but not beyond the end of the stimulus. The reflex was there, but as was confirmed by the reports of the human participants, the longer-lasting aversive state didn't follow. And in the brains of both species, the short sharp neural response was observed, but the longer-lasting wave was absent.

Does the slower wave of activity observed by Kauvar *et al*. account for the persistence of emotions once the stimulus is no longer present? It may be a crucial prerequisite. At the fastest scale, neurons communicate with millisecond precision through fast neurotransmitter receptors. Such activity could be responsible for quickly broadcasting a sensory event. Ketamine, however, blocks a slow-acting neurotransmitter receptor that integrates bursts of neuronal activity that occur over tens to hundreds of milliseconds. With this receptor inactivated, many networks across the brain are incapable of persistent activity (*4*). The findings of Kauvar *et al.* indicate that this integration might be required for the initiation of an emotion state. Very little is known about how a global emotional context is maintained. In the mouse hypothalamus (an area of the brain involved in homeostatic control), a fear trigger causes neural activity that lasts for tens of seconds. That activity likely sustains itself by a combination of slow neurotransmission and even slower neuromodulatory input (*5*). The neural activity of a neighboring population of hypothalamic cells, which are involved in the expression of aggression in mice, shows stereotyped dynamics that unfold over tens of seconds to minutes. This network likely captures angry intent and its transformation into aggression (*6*, *7*).

More broadly, signals from one brain area to another can change the behavior of a brainwide neuronal network (*8*). For example, interventional experiments in mice show that, when performed at the correct frequency, manipulations of neuronal activity at the circuit-level have the power to extinguish or prolong an appetitive state of social engagement (*8*, *9*). At the brainwide level, activity across groups of brain regions, especially when constrained to particular frequencies, appears to show coherence and may become self-reinforcing at longer timescales (*10*). Some motivationally and emotionally charged states, such as hunger, thirst, or malaise, may persist because of their own dedicated molecular and circuit mechanisms. For example, two peptides involved in hunger and satiety (the feeling of fullness) were recently shown to dampen each other's impact, effectively preventing sudden fluctuations in the activity of the neurons responsible for the hunger state (*11*). This process works alongside what appears to be a dedicated molecular mechanism controlling the rate of satiation. Slow endocrine signaling and brain-body feedback loops could also play a key role, especially at the later stages of an emotional experience (*12*). For example, in mice, a stereotyped breathing pattern contributes to the maintenance of freezing in response to fear, perhaps reflecting a self-reinforcing physiological-behavioral loop (*13*).

Understanding what makes emotions last will require an integrative approach that draws on knowledge of the mechanisms that enable persistence at different timescales. The findings of Kauvar *et al.* improve the understanding of what happens in the brain in the first seconds during the formation of an emotion. Future work should investigate what information is carried on the observed wave of neural activity and its effects on how an emotion is maintained and changed. □

REFERENCES AND NOTES

1. I. Kauvar *et al.*, *Science* **388**, eadt3971 (2025).
2. P. Verduyn, S. Lavrijsen, *Motiv. Emot.* **39**, 119 (2015).
3. J. H. Krystal *et al.*, *Arch. Gen. Psychiatry* **51**, 199 (1994).
4. M. Wang *et al.*, *Neuron* **77**, 736 (2013).
5. A. Kennedy *et al.*, *Nature* **586**, 730 (2020).
6. A. Nair *et al.*, *Cell* **186**, 178 (2023).
7. A. Vinograd, A. Nair, J. H. Kim, S. W. Linderman, D. J. Anderson, *Nature* **634**, 910 (2024).
8. S. D. Mague *et al.*, *Neuron* **110**, 1728 (2022).
9. M. Murugan *et al.*, *Cell* **171**, 1663 (2017).
10. P. Fries, *Neuron* **88**, 220 (2015).
11. S. X. Zhang *et al.*, *Nature* **637**, 137 (2025).
12. M. Malezieux, A. S. Klein, N. Gogolla, *Annu. Rev. Neurosci.* **46**, 211 (2023).
13. S. Bagur *et al.*, *Nat. Commun.* **12**, 2605 (2021).

ACKNOWLEDGMENTS

The authors thank the Gogolla laboratory for feedback and acknowledge the Max Planck Society for support.

10.1126/science.adx8992

Emotion Research Department, Max Planck Institute of Psychiatry, Munich, Germany.
Email: stoyo_karamihalev@psych.mpg.de

HYPOTHESIS

Growing anxious—Are preschoolers matched to their futures?

Evolutionary and developmental factors may contribute to anxiety in young people

Mark A. Hanson[1] *and* **Peter D. Gluckman**[2,3]

Anxiety is an emotion that, in evolutionary terms, can have an adaptive role in ensuring alertness to potential danger. In animals, stresses such as population density, predators, and food availability can act, through maternal cues, on the prenatal and early postnatal development of stress responses in offspring (*1*). Such maternal and perinatal effects, which operate across a wide range of taxa, lead to predictive adaptive responses in offspring, promoting Darwinian fitness (*2*). Mechanistically, epigenetic changes in neural pathways have been implicated in explaining how environmental factors can affect gene expression and thus development (*3*). What if anticipated conditions do not match those that triggered a predictive adaptive response? For example, over- or inappropriate expression of anxiety later in human life can turn out to be maladaptive, reducing an individual's own or social functionality. Perhaps anxiety disorders can be understood as inappropriate socioemotional regulation in relation to actual, perceived, or anticipated challenges.

There is growing evidence that the incidence of anxiety disorders has risen considerably in recent years in adolescents (between 12 and 19 years old), particularly in developed countries (for example, the United States) (*4*). Although this trend is well documented in the years preceding the COVID-19 pandemic (*5*), there was only a small increase in the incidence of anxiety in children (younger than 12 years old) and adolescents during the pandemic by comparison (*6*). This suggests that contemporary stressful situations such as those operating during the pandemic do not fully explain a contemporaneous increase in anxiety in adolescents.

Environmental factors during the early years of development can have profound and lasting effects on a child's executive functions and emotional development, affecting socioemotional regulation, especially if these factors are deleterious and prolonged (*7*). But there are indications of more subtle effects on the development of executive functions, even in the prenatal and early postnatal periods (*8*). Such early life impacts could contribute to the increased prevalence of anxiety later in life, triggered by current social and environmental challenges.

Executive functions in humans depend on the development of fronto-thalamic and limbic systems in the brain, which are the critical foundations for socioemotional and attentional regulation. Much of this neural substrate develops in the first 4 years after conception, but there are also prenatal and postnatal modifications of these neural systems that occur in response to environmental cues (*9*). Although maturation of the prefrontal cortex is not complete until late in adolescence, its foundations and plasticity are greatest in the early years. Thus, early modifications may affect how an individual responds to later stressor challenges, making resilience or anxiety more or less likely to be exhibited and, consequently, whether the expression of anxiety states is likely to be adaptive or maladaptive.

Maternal stress during pregnancy has been shown to affect offspring executive functions, as measured with functional, electrophysiological, and imaging techniques, and the incidence of mild to moderate maternal stress in pregnancy is estimated to exceed 40% in high-income countries (*10*). Such stresses are attributed to a range of factors, including relationship dynamics, cost of living, conflict, labor opportunities, and childcare costs. Furthermore, these effects of maternal stress on offspring may operate across generations through mechanisms beyond genetic inheritance. For example, girls who develop higher levels of anxiety may become more stressed during their own pregnancies, with potential effects on their subsequent children.

The nature of caregiver-infant interactions in the first 2 years of life has been shown to influence executive function development (*11*). Limited availability of high-quality care for children in their early postnatal years may limit the types of adult-infant interactions that foster healthy neurodevelopment. And it is possible that "technoference" in caregiving through the use of digital devices exacerbates such effects on early childhood development of executive functions either directly or by reducing interactive time with caregivers (*12*).

> **...predictive adaptive responses could hypersensitize the individual to triggering cues... leading to a mismatch between the emotional response and the actual challenge faced.**

Can these maternal and developmental cues of stress trigger regulatory changes in anticipation of stressful challenges to be met in future adolescent and adult years? Such predictive adaptive responses could hypersensitize the individual to triggering cues that otherwise would not induce such intense responses, leading to a mismatch between the emotional response and the actual challenge faced. Adolescent anxiety thus may arise in part because the developmental plasticity in executive functions has been affected during the early years by environmental cues interpreted as predicting a dangerous or stressful world, irrespective of whether this turns out to be the case. If one considers that social changes have led to greater chances of exposure to such priming cues, then it is possible that as the child grows, they could exhibit inappropriate levels of anxiety relative to the actual levels of stress present.

The predictive adaptive-maladaptive nature of this developmental mismatch model is distinct from the diathesis-stress model (*13*), which posits a "two-hit" pathophysiological paradigm—that is, a predisposition to anxiety combined with stress. Given the current rapid changes in the societal environment, such as in digital technologies, the mismatch model offers a possible contributing factor to the recent rapid rise in anxiety disorders in young people. The developmental mismatch is similar to that described for cardiometabolic phenotypes that developed in early life in response to signals of inadequate nutrition and the contemporary lifestyles of overnutrition widely adopted later (*2*).

The informational and sociocultural environments also constitute an evolutionary novelty in their nature, scale, and speed of change. Thus, people may now be required to cope with societal and technological environments more complex than humans have evolved to inhabit. The resulting evolutionary mismatch makes more likely hypersensitivity to the challenges that contemporary environments pose, especially during a prolonged adolescence, which in itself is a relatively recent developmental period in evolutionary terms. Both evolutionary and developmental mismatches have been suggested to play a role in the origins of the epidemic of noncommunicable disease in humans in the Anthropocene (*2*). Childhood and adolescent anxiety could be considered similarly.

Without appropriately formed executive functions in the preschool years (ages 3 to 5 years old), long-term adverse consequences for both individuals and society are likely. The long-term prognosis of these mismatches is of concern, not only in terms of managing the burden of mental health conditions but also in terms of effects on social cohesion and productivity. For example, anxiety and fear have been proposed to be associated with a preference for strong leadership (*14*). The recent decline in young people's participation in democratic processes (*15*) might be a reaction to the parlous state of democratic politics but also a manifestation of a desire for more autocratic, stronger leadership to inspire a sense of security. Autocratic leaders in turn understand the need to create a sense of uncertainty or even fear. Today's young people may be particularly susceptible to such influences.

Societies face an emerging burden of mental health issues, especially in young people. Although appropriate interventions are needed to help those already affected, preventative approaches are also critical. Solutions will need to adopt a life-course perspective, involving more cohesive thinking about parental and caregiver support and the early childhood years by policy-makers across health, education, and social welfare. The quality of the emotional environment in which young children develop, including active adult-infant interactions both within and outside the home, is essential. Education policies alone cannot meet this challenge because they do not generally focus on the preschool years. Health and social care policies will need to address the increasing prevalence of stress and mental health problems in women before and during pregnancy, and their partners, if repeating cycles of such problems across generations are to be prevented. The cost to society of not refreshing our thinking and actions about young people's emotional development may well be enormous. □

REFERENCES AND NOTES

1. M. J. Sheriff, C. J. Krebs, R. Boonstra, *Ecology* **91**, 2983 (2010).
2. P. D. Gluckman, M. A. Hanson, F. M. Low, *Philos. Trans. R Soc. Lond. B Biol. Sci.* **374**, 20180109 (2019).
3. T. Y. Zhang, B. Labonté, X. L. Wen, G. Turecki, M. J. Meaney, *Neuropsychopharmacology* **38**, 111 (2013).
4. R. H. Bitsko *et al.*, *MMWR* **71**, 1 (2022).
5. J. Piao *et al.*, *Child Adolescent Psych.* **31**, 1827 (2022).
6. S. Madigan *et al.*, *JAMA Pediatr.* **177**, 567 (2023).
7. M. Wade *et al.*, *Dev. Sci.* **27**, e13517 (2024).
8. A. Rifkin-Graboi *et al.*, *Biologic. Psych* **74**, 837 (2013).
9. D. S. Valcan, H. Davis, D. Pino-Pasternak, *Ed. Psychol. Rev.* **30**, 607 (2018).
10. M. J. Meaney, *Am. J. Psychiatry* **175**, 1084 (2018).
11. J. A. Mortensen, M. A. Barnett, *Early Ed. Dev.* **26**, 209 (2015)
12. J. Komanchuk *et al.*, *Cyberpsychol. Behav. Soc. Netw.* **26**, 579 (2023).
13. K. Salomon, A. Jin, in *Encyclopedia of Behavioral Medicine* (Springer, 2020), pp. 655–657.
14. W. Davies, *Nervous States: Democracy and the Decline of Reason* (Norton, 2019).
15. T. Deželan, "Young people's participation in European democratic processes: How to improve and facilitate youth involvement" (Eurpoean Union, 2023).

ACKNOWLEDGMENTS

The authors acknowledge philanthropic support from G. Hart and R. Hart. We thank F. Low for assistance in preparing the manuscript and to anonymous reviewers for helpful comments.

10.1126/science.adp3764

---

[1]Institute for Developmental Sciences, University of Southampton, Southampton, UK. [2]Koi Tū Centre for Informed Futures, Auckland, New Zealand. [3]A*STAR Institute for Human Development and Potential, Singapore. Email: m.hanson@soton.ac.uk; pd.gluckman@auckland.ac.nz

BOOKS ET AL.

EDUCATION

The next best way to teach and learn

Technology always seems poised to revolutionize education—until it doesn't **Jonathan Wai**

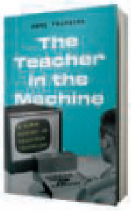

The Teacher in the Machine: A Human History of Education Technology
Anne Trumbore
Princeton University Press, 2025. 240 pp.

Are technological advancements new solutions to old problems, reflections of what we already know, or amplifiers of who we already are? Ann Trumbore's *The Teacher in the Machine* explores a history of educational technology ("edtech") in the United States to shed light on these questions.

Trumbore examines two periods of educational entrepreneurship: the 1960s and 1970s and a more recent era that began in 2012. She chose these two periods because—like other aspects of education history—in her opinion, they have largely (and mistakenly) been ignored (*1*).

More than a century ago, Sidney Pressey invented a device called a "teaching machine" that presented to students a multiple-choice test that would not advance until they got the answer correct. Pressey believed that such machines could offer a more customized learning experience. As B. F. Skinner explained in 1958: "Even in a small classroom the teacher usually knows that he is moving too slowly for some students and too fast for others. Those who could go faster are penalized, and those who should go slower are poorly taught and unnecessarily punished by criticism and failure. Machine instruction would permit each student to proceed at his own rate" (*2*).

Part 1 of *The Teacher in the Machine* focuses largely on three scholars and their ideas for improving US education. Stanford University philosophy professor Patrick Suppes dreamed of an "individual Aristotle," or tutor for every child, who would help each student learn at their own pace. University of Illinois electrical engineering professor Don Bitzer created a sophisticated computer-based educational platform in the 1960s known as PLATO, which "could support up to one thousand students around the world doing coursework, playing early versions of video games, and chatting with their friends on message boards simultaneously." MIT applied math and education professor Seymour Papert led the "One Laptop per Child" initiative, which delivered laptops to millions of children around the world. His ideas influenced the "maker movement" of the 2010s and popular programming languages such as Scratch.

In the second half of the book, Trumbore examines the rise of edtech as part of the business of higher education—and in particular the role of the internet in distributing education beyond the college classroom. Venture capitalists and "disruptors" smelled possible profits in distance learning ventures led by elite universities at the beginning of the 21st century, she notes. These included MIT, which decided in 2001 to give away all its course materials (*3*). And in 2012, Udacity—led by computer scientist Sebastian Thrun—raised $5 million in venture capital with the promise that "eventually, recruiters and corporations worldwide would pay to recruit from its pool of talented learners educated through their courses." Then there was the massive open online course (MOOC) frenzy, in which edtech leaders claimed that there was a tsunami of free online coursework coming to subsume higher education, pushing universities to jump on the bandwagon. Ultimately, however, universities proved quite resistant to change. Venture capital for edtech peaked at $21 billion in 2021 and has since cratered by about 90%.

On the topic of artificial intelligence, Trumbore notes that "generative AI seems poised to fundamentally alter teaching and learning, but it's unclear how universities can profit from it, beyond selling online courses on the topic." Scholars have expressed concerns about how to get students to master basic skills related to AI and to use it responsibly (*4*). Science fiction writer Ted Chiang articulates the problem this way: "Using ChatGPT to complete assignments is like bringing a forklift into the weight room; you will never improve your cognitive fitness that way" (*5*).

This brings us back to a question Trumbore presciently asks after reviewing the history of edtech: "Why are we so eager to turn to technology to solve educational problems for which the one reliably proven solution is more person-to-person connection?" Maybe the answer is that there really are only so many ideas under the Sun, and it is too easy to forget the lessons of the past. □

REFERENCES AND NOTES

1. D. Tyack, L. Cuban, *Tinkering Toward Utopia: A Century of Public School Reform* (Harvard Univ. Press, 1995).
2. B. F. Skinner, *Science* **128**, 969 (1958).
3. MIT OpenCourseWare; https://ocw.mit.edu/.
4. C. T. Bergstrom, J. D. West, "Lesson 11: Transforming education?," Modern-Day Oracles or Bullshit Machines? How to thrive in a ChatGPT world (2025); https://thebullshitmachines.com/lesson-11-transforming-education/index.html.
5. T. Chiang, "Why A.I. isn't going to make art," *New Yorker*, 31 August 2024; https://www.newyorker.com/culture/the-weekend-essay/why-ai-isnt-going-to-make-art.

10.1126/science.adx4571

The reviewer is at the Department of Education Reform and Department of Psychology, University of Arkansas, Fayetteville, AR, USA. Email: jwai@uark.edu

PHOTO: STOCKPLANETS/ISTOCK PHOTO

AGING

Look beyond the longevity drips and supplements

There is a path to living longer and healthier that doesn't require reversing the aging process

Eric J. Topol

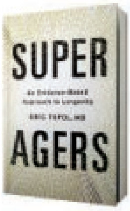

Eric Topol
Simon & Schuster,
2025. 464 pp.

SUPER AGERS | Have you visited the longevity lifespan circus lately? There are eight hundred longevity clinics in the United States—even at the prestigious Mayo Clinic—so they are hard to miss. Some charge up to $50,000 per week. There are longevity vacations with intravenous drips; "Rejuvenation Olympics"; a Fountain Life "country club for precision diagnostics"; fitness centers with intravenous antiaging drips; an X-Prize costing over $100 million to restore at least a decade's worth of muscle, brain, and immune function in older adults; and stem cell clinics for longevity. There are carnival barker scientists making false claims and hawking supplements as well as longevity leader lists for what dose of rapamycin they are taking to extend their lifespan. There's an outspoken forty-seven-year-old centimillionaire taking over 110 supplement pills a day, monitoring his organs (which includes a penile-ring erection sensor) with a staff of thirty medical specialists, spending more than $2 million for food each year for a precise daily intake of 1,977 calories, who has received plasma infusions from his teenage son, along with gene therapy.

Then there are the many hundreds of companies developing drugs or interventions to promote lifespan or selling biomarkers to track one's biological age. Many high-profile billionaires, such as Jeff Bezos, Sam Altman, Yuri Milner, and Peter Thiel, are betting big on some of these companies. I don't claim to have any special access to the motivations of these successful businesspeople, but I am reminded of a line from Venki Ramakrishnan in *Why We Die*: "When they were young they wanted to be rich, and now that they're rich they want to be young." These entrepreneurial investments aren't likely to settle down anytime soon because we're seeing some real progress in understanding the science of the aging process. Unfortunately, that has led to irrational exuberance in many dimensions.

It is true that we are in the midst of changing our perception of what "old age" means. For a start, there are simply more centenarians around. There were 120,000 people aged one hundred and older in the United States in 2024, and that number is expected to rise to about 600,000 by 2060. But there's little evidence we've conquered frailty—we seem to be as vulnerable to age-associated decline as ever. In fact, more so. The result of more people getting older with multiple chronic conditions.

According to the World Health Organization, the average American celebrates just one healthy birthday after the age of sixty-five. That seems bleak, but another way to express this acceleration of morbidity with older age is by the number of chronic conditions. For Americans aged sixty years and above, 95 percent have at least one chronic disease, such as heart disease or diabetes, and 79 percent have at least two chronic conditions. Life expectancy in the United States is starting to come back with a small increase after the COVID pandemic but is still below its peak a decade ago, and well below many peer countries in western Europe and Asia.

Life expectancy (LE) and health-adjusted life expectancy (known as HALE) are quite different. LE is the average number of years that a person at a given age is expected to live. In contrast, HALE is the average number of years spent in good health, and there's a wide spectrum of conditions that are considered to detract from "good health."

Over time, the gap between LE and HALE is getting larger, with chronic illnesses on the rise in the United States. That's why the notion that slowing down aging for one year, a small increase in LE, would be worth $38 trillion, and by ten years $367 trillion in United States is far-fetched. If health span is not increased and the gap closed, we'd be adding to the economic burden of long lives with chronic diseases, not reducing it. The only way we might accomplish closing the gap is to slow the aging process, ideally at the whole-body level. If we reduce heart disease but increase the prevalence of Alzheimer's disease, we're into competing interests and a Whac-A-Mole model of expanding health span. A longer lifespan gives more chance for all the diseases of biological aging to manifest. People just don't fall off a cliff healthy. Slowing the whole-body aging process is the only way to bridge the gap. ☐

ACKNOWLEDGMENTS

This article has been adapted from Eric Topol's latest book, *Super Agers: An Evidence-Based Approach to Longevity* (https://www.simonandschuster.com/books/Super-Agers/Eric-Topol/9781668067666).

SUPER AGERS: An Evidence-Based Approach to Longevity by Eric Topol, MD. Copyright © 2025 Reprinted by permission of Simon & Schuster, LLC.

10.1126/science.adw7640

The author is at Scripps Research Translational Institute, Scripps Research, La Jolla, CA, USA. Email: etopol@scripps.edu

PHOTO: LJUBAPHOTO/ISTOCK PHOTO

PODCAST

Maintaining social interactions and an active lifestyle can contribute to healthy aging.

SCIENCE OF DEATH

Immortality, for now, remains out of reach. But just how elastic is the human life span? This week on the *Science* podcast, Venki Ramakrishnan, author of **Why We Die**, separates longevity facts from fiction and offers insights into how to live well longer.

10.1126/science.ady6762

https://scim.ag/WhyWeDie

Edited by
Jennifer Sills

For decades, the Philippines has given small-scale fishers priority over commercial fishers in municipal waters.

PHOTO: RHIA GONZALES/MERF-FRMP PROJECT

Philippine fisheries put food security at risk

On 19 August 2024, the Philippine Supreme Court upheld a Regional Trial Court's decision (*1*) allowing commercial fishing in municipal waters, which extend 15 km from the shore. This decision is inconsistent with the provisions of the Philippine Fisheries Code, which grants small-scale fishers preferential access to municipal waters (*2*), as well as the Local Government Code of 1991 (*3*) and the 1987 Philippine Constitution (*4*), which include protections for small-scale fishers. The country's food security and livelihoods are at risk as a result. A motion for reconsideration has already been filed by the country's Bureau of Fisheries and Aquatic Resources (*5*). The government should continue to seek legal remedies that uphold the rights of small-scale fishers.

Allowing commercial fishing in municipal waters threatens both fishers and fish stocks. More than 80% of the 1.4 million Filipino fishers belong to small-scale fisheries, accounting for half the Philippines' 1.8 million–ton annual marine fish harvest (*6*, *7*). Filipino fishers are the country's poorest sector, with one third below the poverty line (*6*). Moreover, major Philippine fisheries have been overfished since 1990 (*8*), and fish catch has been declining (*6*, *7*). Reef fish biomass in fished areas has dropped to less than 10% of its unexploited level (*8*). Illegal fishing is prevalent, and commercial fishing intrusion into municipal waters has been identified as a top threat (*8*, *9*).

Bioeconomic models predict that without substantial investments in fisheries management, increasing commercial fishers' access to shared fish stocks will increase their catch and profit in the short term but accelerate fisheries' decline (*10*). Thus, small-scale fishers' catch and profit are expected to decrease in the short and long term (*10*).

The Philippine Fisheries Code prioritizes food security in fishery resources decisions (*2*). If the Supreme Court's decision stands, the Philippines should closely monitor the early impacts of the policy on nearshore fish stocks and prioritize bioeconomic models that predict long-term impacts over empirical observations. Delayed assessment can be costly given that fish stocks typically take a decade or more to recover from overexploitation (*11*).

Many nations grant preferential access to small-scale fishers in nearshore areas (*12*) to safeguard marginalized communities' food security. Rather than allowing commercial fishing in municipal waters, the Philippines should improve aquatic food security by focusing on conservation and sustainable marine aquaculture (*7*). The precautionary principle, which precludes implementing a potentially harmful policy, should guide the Philippines' fisheries decisions.

Reniel B. Cabral[1], Richard N. Muallil[2], Samuel S. Mamauag[3], Michael P. Atrigenio[4]

[1]Centre for Sustainable Tropical Fisheries and Aquaculture, College of Science and Engineering, James Cook University, QLD, Australia. [2]Mindanao State University—Tawi-Tawi College of Technology and Oceanography, Bongao, Tawi-Tawi, Philippines. [3]Department of Biology, College of Science, De La Salle University, Manila, Philippines. [4]The Marine Science Institute, University of the Philippines Diliman, Quezon City, Philippines. Email: reniel.cabral@jcu.edu.au

REFERENCES AND NOTES

1. The Philippine Supreme Court First Division Notice of Resolution dated 19 August 2024; https://karagatanpatrol.org/atin_ang_kinse/.
2. The Philippine Fisheries Code of 1998 (Republic Act 8550, amended by Republic Act 10654 in 2015); https://www.bfar.da.gov.ph/wp-content/uploads/2021/02/Philippine-Fisheries-Code-of-1998.pdf.
3. The Local Government Code of 1991, Section 16; https://www.officialgazette.gov.ph/1991/10/10/republic-act-no-7160.
4. 1987 Philippine Constitution Article XIII, Section 7; https://www.officialgazette.gov.ph/constitutions/1987-constitution.
5. Philippine Department of Agriculture (DA), "DA appeals SC ruling allowing commercial fishing in municipal waters," (DA Press Office, 2025); https://www.da.gov.ph/da-appeals-sc-ruling-allowing-commercial-fishing-in-municipal-waters.
6. Philippine Bureau of Fisheries and Aquatic Resources (BFAR), "Philippine Fisheries Profile 2022" (BFAR, 2023); https://www.bfar.da.gov.ph/wp-content/uploads/2024/02/2022-Philippine-Fisheries-Profile.pdf.
7. R. B. Cabral *et al.*, *Philippine J. Fish.* **30**, 298 (2023).
8. S. J. Green *et al.*, "Philippine fisheries in crisis: A framework for management" (Coastal Resource Management Project of the Department of Environment and Natural Resources, 2003); https://oneocean.org/download/db_files/philippine_fisheries_in_crisis.pdf.
9. R. N. Muallil *et al.*, *Mar. Policy* **44**, 212 (2014).
10. D. J. Kaczan *et al.*, "Towards higher performing fisheries: Options for sustainable and productive fisheries in Indonesia" (The World Bank, 2024); http://documents.worldbank.org/curated/en/099060724065528790/P1664661a669900ba1a5c11ae922d5dfeb2.
11. P. Neubauer *et al.*, *Science* **340**, 347 (2013).
12. X. Basurto *et al.*, *npj Ocean Sustain.* **3**, 56 (2024).

10.1126/science.adv7145

Remobilized metals threaten urban wetlands

Urban wetland restoration is gaining international momentum (*1*, *2*). This strategy alleviates biodiversity loss by providing pivotal habitats for local wildlife and migratory birds in urban areas (*1*). Although urban wetland restoration provides substantial ecological benefits, these projects may inadvertently remobilize legacy metal contaminants (LMCs), including harmful chemicals such as mercury, that were produced by anthropogenic activities and have since accumulated in urban soils and sediments. Project planners must work to prevent or mitigate the damage that LMCs could cause.

Urban wetland projects often include resubmergence in water and revegetation of degraded wetlands, each of which can release LMCs from the soil, increase their mobility and bioavailability, and intensify their bioaccumulation along wetland food chains (*3*, *4*). Although LMCs such as mercury are less toxic than recently discharged chemicals (*5*), their remobilization threatens local wildlife and migratory species. For example, the concentration of mercury in urban wetland fish in the US is 111.7% of the concentration in their offshore migratory counterparts (*6*), putting both the fish and their predators, including endangered wetland birds and mammals, at risk of adverse health effects such as reproductive failure and neurological impairment (*7*).

Climate change could further exacerbate the remobilization of LMCs (*8*). For example, in forest wetlands, rising summer temperatures stimulate the activity of mercury-methylating microorganisms, leading to a 300% increase in the conversion of less toxic inorganic mercury to neurotoxic methylmercury (*9*). Furthermore, elevated carbon dioxide leads to a 27.6% increase in cadmium bioavailability in wetland soil owing to decreased soil pH (*10*). These changes could eventually trigger massive fluxes of remobilized LMCs into wetland food webs, posing a looming threat to biodiversity and, if they enter the human food chain, public health (*11*).

Urban wetland restoration projects must include robust risk mitigation strategies for LMC remobilization. Rigorous scientific evaluation and continuous monitoring of microbes and their functional changes can determine how they contribute to the remobilization of LMCs under both human interventions and climate-change scenarios. Once key microbes have been identified and hotspots of LMC release induced by urban wetland restoration have been located, project managers can implement nature-based solutions, such as planting vegetation that accumulates metals (*12*), to remove remobilized LMCs and prevent their accumulation in food chains. Such strategies should be integrated into all future urban wetland restoration projects as well as existing multilateral environmental agreements such as the Convention on Biological Diversity.

Chengjun Li[1,2], Shouying Li[3], Qinghua Zhou[4], Wenli Tang[3], Huan Zhong[4]
[1]Institute of Environmental Research at Greater Bay Area, Guangzhou University, Guangzhou, China. [2]Nanjing Institute of Environmental Sciences, Ministry of Ecology and Environment, Nanjing, China. [3]School of Environment, Nanjing University, Nanjing, China. [4]College of Resources, Sichuan Agricultural University, Chengdu, China. Email: zhonghuan@nju.edu.cn

COMPETING INTERESTS

H.Z. serves as a roster expert of the Minamata Convention on Mercury's Open-ended Scientific Group.

REFERENCES AND NOTES

1. F. Cheng *et al.*, *Nature* **588**, 625 (2020).
2. Q. He *et al.*, *Nat. Rev. Biodivers.* **1**, 50 (2025).
3. M. Speelmans *et al.*, *Sci. Total Environ.* **380**, 144 (2007).
4. H. Su *et al.*, *Int. J. Environ. Sci. Tech.* **16**, 853 (2019).
5. E. Peruzzi *et al.*, *Ecol. Eng.* **37**, 771 (2011).
6. B. K. Greenfield *et al.*, *Environ. Pollut.* **158**, 2716 (2010).
7. B. Kushawaha *et al.*, *J. Trace Elem. Med. Biol.* **87**, 127598 (2025).
8. K. Timmis *et al.*, *Microb. Biotechnol.* **10**, 984 (2017).
9. P. Selvendiran *et al.*, *Environ. Pollut.* **154**, 46 (2008).
10. Y. B. Wang *et al.*, *Environ. Pollut.* **324**, 121396 (2023).
11. F. Coppola *et al.*, *Ecotoxicol. Environ. Saf.* **147**, 954 (2018).
12. W. Yuan *et al.*, *Eco-Environ. Health* **3**, 260 (2024).

10.1126/science.adw8981

Scientific timidity enables oppression

The US scientific enterprise is facing an unprecedented assault. The current administration is working to cap indirect research costs at 15% (*1*), halt National Institutes of Health (NIH) grant reviews (*2*), slash the 2026 NIH budget by 44% (*3*), cut the National Oceanic and Atmospheric Administration (NOAA) budget by 27% (*4*), and cancel 20% of funding for the Environmental Protection Agency (EPA) (*5*). Executive orders have forced agencies to remove terms such as "gender" from public health research (*6*); erase climate-related terms from government websites (*6*, *7*); and eliminate diversity, equity, and inclusion (DEI) programs (*8*). The scientific community must protest these policies with a strong and united voice.

So far, the response from the scientific community has been defensive and fragmented. In the absence of a convincing public challenge to the censorship of terms such as "climate change" and "diversity," some scientists and institutions have quietly removed those keywords from project descriptions (*9*). Such defensive concessions may preserve individual projects in the short term, but omitting terms to appease politicians normalizes a paradigm in which science must seek permission to tell the truth.

The scientific community's efforts have also lacked unity. Researchers have objected to cuts affecting their own fields, but these groups often operate without coordination. Fragmentation dilutes the protests' impact and allows the administration to play fields against each other. The lack of a united front also undermines scientists' ability to convey their message to the public and to policy-makers.

As history shows (*10*), silencing science is a tool of tyranny. Even in democracies, the consequences of scientific silence can be dire. When evidence on climate change is stifled or ignored, vulnerable communities suffer the worst impacts of unchecked pollution and global warming. When public health officials are forced to downplay a pandemic, people die needlessly (*11*, *12*). When those who understand the evidence do not loudly defend it, those in power face no obstacle to perpetuating harmful lies.

Scientists need not abandon objectivity to publicly speak out with clarity and conviction when science is misrepresented or ignored. Universities and scientific organizations should issue unambiguous statements against political censorship of research, provide legal and moral support to those who come under fire, and lobby for the protection of scientific integrity. Individual scientists must engage with the public and the media to counter misinformation directly rather than hoping that peer-reviewed papers alone will correct false narratives. Researchers can write op-eds, march in peaceful protests, and form advocacy groups. Building solidarity with educators, journalists, and the public will amplify this message. Scientists cannot win this fight alone, but they can lead by example.

Mohamed Omar
Cedars-Sinai Medical Center, Los Angeles, CA, USA. Email: mohamed.omar@cshs.org
Opinions are the author's and do not reflect the official views of his institution.

REFERENCES AND NOTES

1. B. M. Seminera, "Universities are facing big cuts to research funding. At Duke, it's a time for 'damage control,'" *The Telegraph*, 8 March 2025.
2. M. M. Chen, A. Usha Lee McFarling, "Graduate student admissions paused and cut back as universities react to Trump orders on research," *STAT*, 19 February 2025.
3. M. Wadman, "Trump proposes massive NIH budget cut and reorganization," *Science* 10.1126/science.zaomfqe (2025).
4. A. Gaffney, "White House plan calls for NOAA research programs to be dismantled," *New York Times*, 11 April 2025.
5. US EPA, "EPA Administrator Lee Zeldin Cancels 400+ Grants in 4th Round of Cuts with DOGE, Saving Americans More than $1.7B" (EPA, 2025).
6. J. Steenhuysen, "Trump recall of CDC research puts scientific papers in limbo," *Reuters*, 7 February 2025.
7. K. Yoder, "In Trump's new purge of climate language, even 'resilience' isn't safe," *Grist*, 11 March 2025.
8. D. J. Trump, "Ending radical and wasteful government DEI programs and preferencing" (White House, 2025).
9. U. L. McFarling, A. Chen, S. Owermohle, "Growing number of federal health agencies are combing grants for taboo words, unnerving researchers," *STAT*, 13 February 2025.
10. K. L. Lerner, "The disastrous effects of Lysenkoism on Soviet agriculture," *Encyclopedia.com*, 5 May 2025.
11. D. Diamond, "Trump officials interfered with CDC reports on Covid-19," *Politico*, 12 September 2020.
12. A. Cancryn, "Birx: Trump adviser squeezed out health officials to downplay seriousness of Covid-19," *Politico*, 26 October 2021.

10.1126/science.adx4667

POLICY ARTICLE

DRUG DEVELOPMENT

What patents on AI-derived drugs reveal

Less in-depth, in vivo testing before patenting may affect overall research and development

Janet Freilich[1] *and* **Arti K. Rai**[2]

Proponents of the use of artificial intelligence (AI) in drug discovery predict that it is likely to make drug discovery and development faster and cheaper, particularly in preclinical stages before patents are filed (*1*). But AI use may also create tendencies to file “compound” patents on molecules that disclose little evidence of real-world testing, exacerbating an issue already of concern in more traditional (even if also computer-aided) drug development and patenting. Our preliminary analyses of an original dataset of compound patents on small-molecule drugs suggest that, compared with more traditional drug developers, “AI-native” developers perform less in vivo, in-depth testing before patenting. In light of the potential for such early patenting to dampen overall drug research and development, it is worth considering policies that encourage disclosure of more evidence for securing a patent and provide incentives for research on disclosed but unpatented structures.

> **...AI-native firms are indeed obtaining patents without in vivo experiments at higher rates compared with controls...**

Although computer-assisted drug discovery has been improving for years, AI’s creation of new, potentially less-interpretable paths for in silico discovery and development accentuates existing concerns. AI applications relevant to drug discovery include analysis of knowledge graphs to identify potential drug targets, the AlphaFold models predicting protein folding that won its developers a Nobel Prize in 2024, and systems that can produce and sift through a universe of chemical compounds many orders of magnitude larger than the 10 million or so that have historically been used by pharmaceutical firms. But in the highly patent-sensitive biopharmaceutical industry, the quality of patent disclosure is an issue of considerable interest: A molecule patent granted too early, to a firm with a speculative idea but no plan to test the molecule, may dampen interest from others able to do the work of vetting for safety and efficacy. Additionally, even if speculative molecular structures are not the subject of a patent claim, a cursory disclosure could preclude patenting by others (*2*).

Prior empirical studies of AI use in drug discovery and development, principally authored by Jayatunga *et al.* (*3*, *4*), have focused on the novelty of targets on which AI-based firms focus and on early-phase clinical trial success rates associated with molecules that have entered trials. Although these studies are important, they do not get at the question of whether premature patenting and/or disclosure could result in abandoned molecules. Another possibility for investigating how much preclinical testing has been done on the compounds—examining information provided to the Food and Drug Administration (FDA) by sponsors seeking to enter clinical trials—is unavailable because these submissions are kept secret.

It is possible, however, to examine the quality of disclosure in patents filed on molecules identified using AI techniques. Although FDA submissions contain more information, both because they generally occur a few years after patent filing (*3*) and because firms know that information submitted to the FDA will be kept secret, patent disclosure may still provide some insight on preclinical vetting of compounds.

FINDING PATENTS FROM AI DRUG DEVELOPMENT

To assemble our dataset of AI-derived patents, we could not rely on information in the patents themselves. Patents do not generally contain information about the discovery process (*5*), a point that our manual review confirmed for our dataset. Instead, we developed the dataset indirectly, by using a combination of sources that had previously worked on such identification. Details of our methodology are provided in the supplementary materials. Briefly, we first retrieved a large list of more than 500 firms identified as using AI-powered drug discovery by the global capital market research database PitchBook. On the basis of our independent analysis of public-facing marketing materials available from these PitchBook firms, we determined that the majority used multiple different modes of discovery. We therefore narrowed the list to those firms with marketing materials that indicated the firms’ predominant reliance on AI for therapeutic outputs. We then supplemented this AI-native list by adding additional firms specifically identified as AI-native by Jayatunga *et al.* of the Boston Consulting Group (*3*, *4*). The total number of firms identified was 116.

Next, we used US Patent and Trademark Office (USPTO) databases to identify all granted US patents held by these firms. Although we study only US patents, our findings are internationally applicable because many jurisdictions have disclosure requirements comparable to those in the US, many pharmaceutical patents are filed with the same disclosure in the US and multiple other countries, and information disclosed in patents anywhere is accessible everywhere. We then read the patents to identify the subset that represented the first US compound patent on a given small molecule. We excluded patents on biologic compounds as well as patents on machine learning methods and manufacturing processes.

More AI, less in vivo experimentation

In total, 77 compound patents for small-molecule drugs granted to AI-native firms were analyzed. Compared with 77 matched control firms, AI-native firms obtained patents without in vivo experiments at a higher rate.

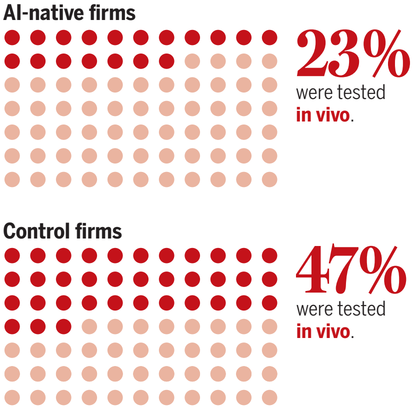

We also assembled a “control” set of patents. We assembled the control set by using the patent analytics database Questel Orbit Intelligence to match each AI-derived patent with a random small-molecule compound patent filed by the same law firm, from a company in the same USPTO size classification, and with a priority date (when the first patent in the family was filed) within ±2 years. Matching on applicant size, law firm, and priority filing year controls for applicant- and law firm–specific drafting choices, applicant resources, and the evolution of technology. Additionally, none of the control patents was assigned to an AI-native firm. In the small number of cases where no control patent was available, we dropped the treatment patent. Moreover, because a number of AI-native firms had no granted patents, our final dataset contained 77 treatment patents and 77 control patents. Further details regarding assembly of the treatment set and of the matching exercise used to assemble the control set are provided in the supplementary materials.

As noted, our treatment patents did not contain information on how AI methods were used to identify the molecules in question. Additionally, as discussed further below, if AI methods were used to test the molecules, they were not disclosed. Accordingly, we could not assess the quality of these methods. We also could not assess the quality of any methods used to identify molecules in the control set. Instead, our metrics of research progress and disclosure quality focused on the compounds and experiments disclosed in the patent. We manually coded the number of specific compounds disclosed, the number and characteristics of experiments testing those compounds, as well as several additional metrics of disclosure volume—number of words, pages, and images in the patent. More detail is provided in the supplementary materials. Statistical significance for continuous variables was calculated using the Mann-Whitney U test and significance for binary variables with the Fisher’s exact test.

ARE AI-NATIVE FIRMS PATENTING TOO EARLY?

In many jurisdictions, patents can be obtained with minimal or no physical evidence that a molecule (or any invention) is safe or effective, as long as the invention does not seem implausible (*6*). Early-obtained patents on drugs that were never tested properly or that fail later trials may dissuade others from trying to study the drugs—whether for the first time or in different diseases or populations—because the patent on the molecule belongs to another. This problem may be particularly acute for patents obtained on drugs studied only in silico. AI-native firms may scoop up patents solely on the basis of preliminary computer output, perhaps preventing large numbers of compounds from ever being tested properly.

As a metric of in-depth preclinical testing, we use animal in vivo experiments. Although such experiments have substantial limitations, testing through alternatives—for example, through organ-on-a-chip systems or high-quality AI models—is only now beginning to be considered an appropriate alternative to in vivo testing. Accordingly, for the purposes of our data, which cover scientific research conducted no later than 2022, we focus on in vivo testing. In any event, to the extent that AI-native firms in our data used AI alternatives to in vivo testing, they did not disclose such testing in their patents.

We find that AI-native firms are indeed obtaining patents without in vivo experiments at higher rates compared with controls, and where in vivo experiments are present, patents from AI-native firms have fewer such experiments. In our sample, only 23% of AI patents have any in vivo experiments compared with 47% of control patents ($P < 0.01$) (see the figure). AI patents also tested a mean of 0.8 compounds in vivo (yielding, on a per-patent basis, a mean of 3.0% of the compounds disclosed in any given patent being tested) as compared with a mean of 3.1 compounds tested in vivo for controls (mean of 6.4% of compounds disclosed in a given patent) ($P < 0.01$). As we report below, many AI and control patents disclose hundreds of compounds, so both groups test only a small fraction of disclosed compounds in vivo. AI-native firms also file patents with less of the testing and development necessary to proceed to human trials: 12% of AI patents have in vivo ADMET (absorption, distribution, metabolism, excretion, toxicology) experiments compared with 26% of control patents ($P < 0.05$), and 1% of AI patents disclose a specific formulation for their drug compared with 14% of control patents ($P < 0.01$).

Other measures of the quantity of experimentation and disclosure are not significantly different between treatment and control patents, including the number of images and pages, the length of the description, whether the patent discloses any in vitro testing, and the median number of nonsynthesis working examples (see the supplementary materials for detailed results).

Overall, the data indicate that both types of firms are conducting in vitro tests on large numbers of compounds but that traditional drug developers do more in-depth tests before filing a patent. We cannot measure the extent to which traditional drug developers are relying partially on AI or on other computationally intensive technology, nor whether our results are attributable to AI use itself or to the way that AI is integrated into other parts of the drug development process. Nonetheless, patents from AI-native firms look different. If AI models are good predictors of drug safety and efficacy in humans, this may be an efficiency gain; if not, it may bog down drug discovery. Depending on the quality of the AI model, patents on molecules never tested in vivo may be less likely to be developed.

WILL AI-GENERATED MOLECULES BLOCK PATENTING AND INVESTMENT?

Fears abound that AI methods will be used to generate countless new molecules, which, when published, will prevent others from patenting those molecules, thereby diminishing incentives for further research (*7*, *8*). Patents are only available for novel, never-before-disclosed molecules, so a published AI-generated molecule (“prior art” in the patent law lexicon) can block others from patenting those molecules, even if the AI user did not study the molecule any further. Moreover, because pharmaceutical companies are reluctant to invest in research on molecules that are not patentable, promising drugs may never reach clinical trials. Although AI-generated molecules can be published in any format, patents are

GRAPHIC: M. HERSHER/*SCIENCE*

> ...it is worth considering raising the evidentiary bar for securing a patent.

the most common source of prior art reviewed at the USPTO and therefore are a good place to test whether AI-generated prior art should be feared.

We find that AI-native firms do not disclose more molecules than their non-AI counterparts {median 101 [interquartile range (IQR), 44 to 266] [mean 276, 95% confidence interval (CI): 173 to 379] for AI-native patents; median 90 (IQR, 25 to 215) (mean 242, 95% CI: 141 to 344) for non-AI controls}. (A bootstrapped CI check on medians similarly yielded largely overlapping 95% CIs for medians of 78 to 146 for AI-native treatment and 73 to 128 for non-AI controls.) These data suggest that AI-native firms are not disclosing orders-of-magnitude more molecules than their non-AI counterparts. But this conclusion is not entirely optimistic because non-AI firms also disclose hundreds, sometimes thousands, of molecules per patent.

Additionally, our sample concludes with patent applications with a priority filing date of 2022—before any substantial use of large language models (LLMs) to assist in drafting patent applications. It is possible that once LLM use accelerated in 2023, AI-native firms not only used AI tools in their scientific research but that they encouraged their legal representatives to use AI tools in drafting patent applications, with one potential result being that AI-native applications filed after 2022 could disclose more molecules.

A PATH FORWARD FOR DRUG DEVELOPMENT

Although our analyses suggest that AI firms are filing patents with limited in vivo evidence, we urge caution with respect to prescription. Caution is warranted given our small sample size, the quickly evolving nature of the field, and our inability to fully assess the causal role of AI use.

Nonetheless, the dearth of in vivo experiments in patents that appear to be developed primarily using AI is worrying, even if one believes the AI optimist's view that the models produce drug candidates more likely to succeed in clinical trials. Given that compound patents as a whole do not provide disclosure regarding how they were discovered, and that AI-native patents in particular also do not discuss AI use in testing (*5*), it is not possible to know whether the in silico discovery and testing was sufficiently superior to traditional methods to obviate the need for in vivo testing before securing a patent. Further, AI-native firms claim to be generating particularly novel drugs, which might require more disclosure. Highly novel molecules that are patented without testing may never be developed—other firms avoid molecules for which they cannot obtain the first patent, and, although the original patent on the molecule could in theory be licensed, such licensing may be difficult because firms, at least at present, prefer to license patents or assets that have been derisked through substantial real-world testing (*9*). Accordingly, it is worth considering raising the evidentiary bar for securing a patent.

Additionally, although the number of molecules disclosed in patents filed by AI-native firms is similar to the number disclosed in non-AI controls, the volume of disclosure is large and likely to increase—risking situations where disclosure of molecules blocks others from patenting those molecules. Disclosure of novel molecules is beneficial, as long as it does not hamper later development of those molecules. To encourage disclosure while avoiding its downside, we suggest permitting others to obtain patents even where the molecule has been previously disclosed but not otherwise tested. Policy-makers could also strengthen regulatory exclusivity (the period during which marketers of approved drugs can enjoy exclusive rights to distribute the drugs) for new compounds that are taken through clinical trials, which provides an incentive that is not linked to earlier disclosures. Finally, to the extent that, going forward, AI-native firms (or other firms for that matter) do use high-quality AI models as an alternative to in vivo testing, they should disclose such testing in patents. Such disclosure would enhance confidence that AI-native firms are using AI not to patent too early but instead to move beyond in vivo testing.

Notably, these changes could benefit AI-native firms. Their early patenting of molecules, before much testing, means that further vetting must take place while the patent term is running—a potential disadvantage. If firms patent early to avoid the possibility that others disclose or patent first, they may welcome policy changes that make delay safer.

As AI develops, there may come a time when its predictions are, by themselves, sufficiently reliable to meet a higher evidentiary bar. Regardless, both for the present moment and the future, our proposed changes would preserve the value of disclosure (*10*) while reducing the risk to innovation for both AI-native and traditional drug development. □

REFERENCES AND NOTES

1. BCG and Wellcome Trust, "Unlocking the potential of AI in Drug Discovery: Current status, barriers and future opportunities" (2023); https://cms.wellcome.org/sites/default/files/2023-06/unlocking-the-potential-of-AI-in-drug-discovery_report.pdf.
2. J. Freilich, L. L. Ouellette, *Science* **364**, 1036 (2019).
3. M. K. P. Jayatunga, W. Xie, L. Ruder, U. Schulze, C. Meier, *Nat. Rev. Drug Discov*. **21**, 175 (2022).
4. M. K. P. Jayatunga, M. Ayers, L. Bruens, D. Jayanth, C. Meier, *Drug Discov. Today* **29**, 104009 (2024).
5. A. K. Rai, "The reliability response to patent law's AI challenges" (2025); https://papers.ssrn.com/sol3/papers.cfm?abstract_id=5247266.
6. J. Freilich, *UC Davis Law Rev.* **53**, 663 (2019).
7. Department of Commerce, USPTO, "Request for comments regarding the impact of the proliferation of artificial intelligence on prior art, the knowledge of a person having ordinary skill in the art, and determinations of patentability in view of the foregoing," 89 FR 24217 (2024).
8. W. D. Heaven, "AI is dreaming up drugs that no one has ever seen. Now we've got to see if they work," *MIT Technology Review*, 15 February 2023.
9. J. P. Morgan, "2024 biopharma industry insights: Investment trends, M&A activity, and market dynamics" (2025); https://www.jpmorgan.com/content/dam/jpmorgan/documents/cb/insights/outlook/jpm-biopharma-deck-q4-2024-final-ada.pdf.
10. S. Graham, D. Hegde, *Science* **347**, 236 (2015).
11. J. Freilich, A. K. Rai, Data and code for "Testing the black box: What patents on AI-derived drugs reveal," Dataverse (2025); https://doi.org/10.7910/DVN/LP.

ACKNOWLEDGMENTS

The authors thank B. Sampat and M. Meurer for suggestions and J. Baggett, C. Gilman, and B. Genaw for research assistance. All data and code used in this paper can be found on Dataverse (*11*).

SUPPLEMENTARY MATERIALS

science.org/doi/10.1126/science.adw1972

10.1126/science.adw1972

---

[1]School of Law, Boston University, Boston, MA, USA. [2]School of Law, Center for Innovation Policy, and Duke-Margolis Institute for Health Policy, Duke University, Durham, NC, USA. Email: rai@law.duke.edu

Science
Webinars
AAAS

Science Webinars help you keep pace with emerging scientific fields!

Stay informed about scientific breakthroughs and discoveries.

Gain insights into current research from top scientists.

Take the opportunity to ask questions during live broadcasts.

Get alerts about upcoming free webinars.

Sign up at: scim.ag/wcfq2023

REVIEW SUMMARY

ECOLOGY

Ecological and evolutionary consequences of changing seasonality

Daniel Hernández-Carrasco*, Jason M. Tylianakis, David A. Lytle, Jonathan D. Tonkin*

Full article and list of author affiliations:
https://doi.org/10.1126/science.ads4880

BACKGROUND: Climate change is rapidly altering seasonal regimes in terrestrial, freshwater, and marine realms, disrupting the natural rhythm of ecological processes. Seasonality is so fundamental to ecosystems that these shifts threaten the maintenance of biodiversity and its contributions to society. Recent advances across several fields in ecology and evolution have identified links between environmental seasonality and processes affecting natural systems at different levels, from the genetic structure of populations to whole ecosystem functions. These connections reveal unexplored pathways through which changes in seasonality could affect biodiversity and propagate across multiple levels of ecological complexity. At the same time, ecological and evolutionary processes governed by seasonality can determine species' ability to adapt to changing seasonal patterns. Yet, despite the potential pervasive consequences for biological systems, changing environmental seasonality remains a largely overlooked dimension of climate change. We explore the diverse ways in which altered seasonal patterns can produce cross-level ecological responses. Given the prospect of further seasonal shifts over the next decades, it is imperative to identify and quantify the mechanisms that underpin biological responses to seasonal regimes and the potential for species to adapt.

ADVANCES: We synthesize theoretical and empirical evidence to identify two broad pathways through which altered seasonality affects living systems: the demographic response to the experienced environment, and adaptations that allow the synchronization with environmental fluctuations. The former is closely linked to the physiological constraints and adaptations determining populations' demographic rates in different environmental conditions, whereas the latter depends on plastic, life-history, and behavioral traits that allow organisms to track seasonal fluctuations. We show that both pathways can propagate the effects of changes in the amplitude, timing, and predictability of seasonality, though the mechanisms may depend on the average conditions of the environment. This interplay provides a means for climate change to affect ecological processes linked to seasonality, including population phenology and species interactions, even when other attributes of seasonality remain unchanged. Furthermore, previous adaptations to seasonality, such as the use of environmental cues, could limit species' tracking of environmental changes through evolutionary adaptation and latitudinal range shifts. Recent developments in modeling enable the inclusion of complex interactions among processes operating at different levels. Such models can predict emergent properties such as biodiversity change by allowing the propagation of known effects across levels—an area ripe for advancement in the context of changing seasonality.

OUTLOOK: The pervasive effects of seasonality and the interactions between processes operating at multiple levels increase uncertainty around the future of biodiversity in the face of global disruptions to seasonality. A deeper understanding of the effects of altered seasonality will help build tools to forecast ecological dynamics into a no-analog future. Empirical work is thus necessary to uncover and quantify these effects, but consensus between applied and theoretical studies is paramount. Such consensus can be achieved by using more ecologically informative measures of seasonality that incorporate the critical components to which biodiversity responds. The resulting theoretical knowledge can be used to inform mechanistic models that allow the propagation of effects across levels of ecological organization. Although part of the information required to build fully mechanistic models might currently be lacking, our synthesis suggests that including species' phenology and their demographic response to the environment can already improve current predictions. Understanding the mechanisms that allow the propagation of impacts opens new avenues for improving conservation planning, invasive species management, large-scale restoration, and biodiversity forecasting. ☐

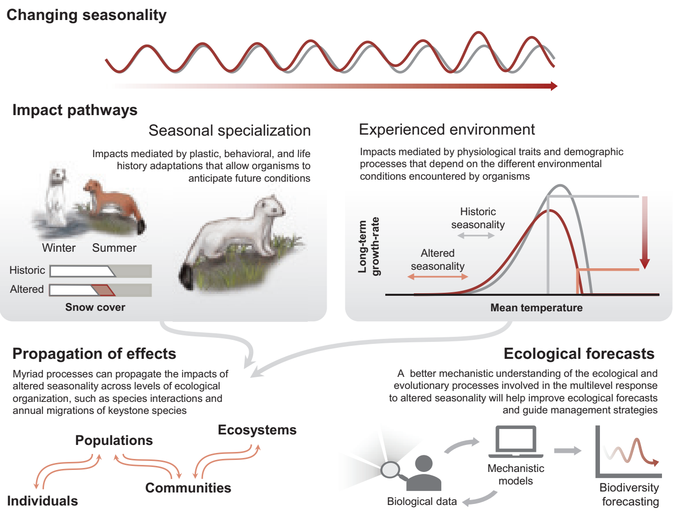
Changing seasonality
Impact pathways
Seasonal specialization
Impacts mediated by plastic, behavioral, and life history adaptations that allow organisms to anticipate future conditions
Winter
Summer
Historic
Altered
Snow cover
Experienced environment
Impacts mediated by physiological traits and demographic processes that depend on the different environmental conditions encountered by organisms
Long-term growth-rate
Historic seasonality
Altered seasonality
Mean temperature
Propagation of effects
Myriad processes can propagate the impacts of altered seasonality across levels of ecological organization, such as species interactions and annual migrations of keystone species
Populations
Ecosystems
Individuals
Communities
Ecological forecasts
A better mechanistic understanding of the ecological and evolutionary processes involved in the multilevel response to altered seasonality will help improve ecological forecasts and guide management strategies
Mechanistic models
Biological data
Biodiversity forecasting

Rapidly changing seasonal patterns can generate complex ecological impacts. These impacts arise through (i) adaptations that allow a proactive response to periodic shifts in the environment (e.g., coat color changes with environmental cues) and (ii) individual performance under conditions experienced throughout the year (e.g., temperature-dependent growth). Such impacts propagate across levels of organization, often producing nonlinear responses, which require mechanistic approaches to anticipate.

STOAT IMAGE CREDIT: IMAGEBROKER.COM/SHUTTERSTOCK.COM

---

*Corresponding author. Email: daniel.hernandezcarrasco@pg.canterbury.ac.nz (D.H.-C.) jonathan.tonkin@canterbury.ac.nz (J.D.T.) Cite this article as D. Hernández-Carrasco *et al.*, *Science* **388**, eads4880 (2025). DOI: 10.1126/science.ads4880

RESEARCH

IN *SCIENCE* JOURNALS

Edited by **Michael Funk**

CARBON CYCLING

Plants can take the heat

Plant respiration contributes several times the amount of carbon emissions to the atmosphere as anthropogenic sources. Respiration also increases with temperature, leading to a positive feedback loop. However, plants can acclimatize to warmer temperatures and reduce their respiration rate. Using a model based on ecological-evolutionary optimality principles, Zhang *et al*. predicted the rate of respiration acclimation to warming driven by decreasing water viscosity within the plant. They then tested these predictions using a dataset of stem respiration measurements from 186 woody plant species collected in the field and laboratory. Incorporating thermal acclimation into emissions projections reduced the predicted terrestrial carbon emissions estimate by nearly one third. —Bianca Lopez

Science p. 984, 10.1126/science.adr9978

Respiration in woody tissues, such as the trunk of this maritime pine (*Pinus pinaster*), acclimates to higher temperatures, potentially reducing one climate change feedback mechanism.

PHOTO: TETIANA KOLUBAI/GETTY IMAGES

SOLAR CELLS

Surviving summer days and nights

Vapor deposition of a polydentate ligand stabilizes perovskite surfaces by blocking iodide migration into the charge transport layer and reducing surface defects. Sun *et al*. treated preformed formamidinium lead iodide films with a terpyridine molecule to cap defective octahedra on the surface, which helped to reduce ion migration driven by light-dark cycles. Large-area perovskite solar modules (areas of ~0.8 square meters) had a power conversion efficiency of ~19% and maintained this power output after 45 days of summer outdoor operation. —Phil Szuromi

Science p. 957, 10.1126/science.adv4280

CANCER

Targeting tumors

Chimeric antigen receptor (CAR) T cells have not proven as successful for solid tumors as they have for blood cancers, in part due to a lack of true tumor-specific targets. Some targets may be enriched on tumor cells, but their expression on healthy tissue raises the concern of on-target off-tumor toxicity. Greco *et al.* applied a rational workflow considering both target expression and localization on healthy and tumor cells for antigen identification. They found that the expression of Cadherin 17 is enriched in colorectal cancer tumors (CRCs) compared with healthy tissue, including CRC liver metastases. Moreover, although Cadherin 17 is homogeneously expressed on the surface of CRC cells, as determined in patient samples, its expression is restricted to cell-to-cell junctions in healthy colon tissue, a site inaccessible to CAR T cells. These data, coupled with preclinical studies screening a panel of CARs in models of efficacy and toxicity, support the further clinical development of Cadherin 17 CAR T cells. —Courtney Malo

Sci. Transl. Med. (2025)
10.1126/scitranslmed.adr1928

PALEOPROTEOMICS

Telling ancient hominin tales

It is now well known that the early hominin fauna was species rich, with many overlapping lineages existing in the African Pleistocene. However, our knowledge of diversity within many of these lineages has been limited because current ancient DNA technologies have not been able to reveal genetic sequences older than around 0.2 million years. Madupe *et al*. examined protein sequences from approximately 2-million-year-old *Paranthropus robustus* teeth that were particularly well preserved. Using proteomics approaches, the authors were able to assign the individual teeth to sex and to identify patterns of diversity suggesting the existence of multiple populations. —Sacha Vignieri

Science p. 969, 10.1126/science.adt9539

PALEONTOLOGY

Cretaceous birds in the Arctic

In the modern world, birds represent key components of polar ecosystems. This is true even in the face of the extreme seasonal changes that occur in these regions. Although the Cretaceous world was considerably warmer than ours, the polar regions still experienced months of near total darkness, suggesting that this was a challenging environment to colonize even when it didn't experience extreme cold. Wilson *et al*. report on a fossil assemblage of birds from the late Cretaceous Arctic. This assemblage includes both chicks and adults of multiple species, suggesting that birds began breeding in Arctic regions early on in their evolution. —Sacha Vignieri

Science p. 974, 10.1126/science.adt5189

NANOMATERIALS

Robust high-entropy oxides

High temperature and corrosion stability, as well as high wear resistance and stiffness, have now been shown for oxides containing five transition metals. Shahbazi *et al*. prevented phase segregation of the metals by oxidizing metal sulfide precursors. The resulting metal oxide nanoribbons were stable in strong acids and bases, at temperatures up to 1000°C, and at pressures up to 12 gigapascals. Above 30 gigapascals, they underwent a reversible amorphization transition. —Phil Szuromi

Science p. 950, 10.1126/science.adr5604

ATOMIC PHYSICS

Testing quantum electrodynamics

Lithium-like ions, those having three electrons orbiting the nucleus, can be used to test the predictions of quantum electrodynamics (QED). Such tests are more stringent than those possible with hydrogen-like ions because of interelectron interactions present in lithium-like systems. A discrepancy that had existed between theory and experiment for the g-factor of lithium-like silicon and calcium was recently resolved, but testing this resolution using a heavier lithium-like ion has remained challenging. Morgner *et al*. performed a high-precision g-factor measurement of the much heavier lithium-like tin ion and compared it with their QED calculations. The agreement they found provides confidence in theoretical calculations in a previously unexplored regime. —Jelena Stajic

Science p. 945, 10.1126/science.adn5981

CHEMISTRY

Smaller, better, faster

Machine learning relies on accurate, well-annotated, and well-distributed training data to generate accurate predictions. High-throughput methods offer a means of generating very large training datasets. Götz *et al*. developed an on-demand miniaturized and automated synthesis platform based on a three-component reaction that produces drug-like molecules. Equipped with a dataset based on 50,000 distinct microscale reactions, the authors used machine learning to develop accurate predictions for reactions with unseen reactants. This dataset is large enough to critically evaluate emerging machine learning approaches to chemical reactivity. —Dennis Hall

Sci. Adv. (2025)
10.1126/sciadv.adw6047

IN OTHER JOURNALS

Edited by **Corinne Simonti** *and* **Jesse Smith**

ANIMAL BEHAVIOR

Fighting or flirting?

In animal societies, groups often fight over resources, and success depends on members contributing to collective efforts. However, individual fitness incentives can undermine group performance. Green *et al.* studied banded mongooses to understand how intergroup conflict outcomes relate to reproductive success. They found that groups with females in heat were more likely to win fights, but surprisingly, winning groups often lost paternity to rival males, suggesting that rivals prioritized mating over fighting. Younger males benefited disproportionately from outgroup matings. These findings reveal a conflict between individual and group interests, challenging assumptions that collective success always aligns with fitness gains and highlighting how personal incentives can shape group dynamics in animal societies. —Di Jiang

Anim. Behav. (2025)
10.1016/j.anbehav.2025.123194

IMMUNOLOGY

Give-and-take during lung infection

Cross-talk between immune cells helps balance control of infection with tissue damage in the lung. Cembellin-Prieto *et al.* found that acetylcholine, which is synthesized by choline acetyltransferase and secreted by B cells, signaled to macrophages to decrease their production of the proinflammatory cytokine tumor necrosis factor. When choline acetyltransferase was deleted in B cells, mice had lower levels of influenza virus the day after infection

Banded mongoose (*Mungos mungo*) males that lose in competitions for resources often prioritize reproduction, contributing more to the next generation.

but more inflammation at later stages, along with indicators of damaged airway tissues. Although B cells may restrain the activity of macrophages and restrict viral control initially, this may act as a regulatory mechanism to prevent more serious consequences after infection. —Sarah H. Ross

Nat. Immunol. (2025) 10.1038/s41590-025-02124-8

ANTIBIOTIC RESISTANCE

Slow, quick, slow

How bacteria evolve in the dynamic environments provided by the human body is obscure. Crow *et al.* cultured *Escherichia coli* facing changes in antibiotic exposure. If antibiotic levels were continuously increased, then the bacteria evolved a series of point mutations to tune an efflux pump called AcrB. With sudden, large antibiotic doses, a nimbler strategy was required. High doses were followed by transposon insertions, which derepressed the alternative defense of last resort, the efflux pump TetA, the expression of which is toxic. There remains the challenge of understanding what such dynamics mean at a population scale. Emons *et al.* analyzed the trajectories of antibiotic resistance for eight bacterial species from more than 3 million samples taken between 1998 and 2019. Resistance did not reach fixation for many drugs, instead attaining a lower stable equilibrium depending on the amount of antibiotics consumed in a country. —Caroline Ash

ISME J. (2025) 10.1093/ismejo/wraf082; *PLOS Pathog.* (2025) 10.1371/journal.ppat.1012945

ELECTROCATALYSTS

Role of hydrogen coverage in hydrogenation

Electrochemical hydrogenation (ECH), a promising sustainable approach for organic synthesis, is typically performed in alkaline media to minimize extensive hydrogen evolution. An ideal ECH catalyst should not only promote water dissociation, but also retain hydrogen atoms in a configuration that effectively hydrogenates organic substrates. By combining computational calculations with experimental verification, Ciotti *et al.* uncovered the critical role of moderate hydrogen-binding strength and well-dispersed surface hydrogen coverage on the catalyst, leading to the discovery of copper, gold, and silver as cost-effective catalysts for the ECH of acetophenone. Notably, copper achieved moderate to excellent conversion rates and chemoselectivities toward the ECH of a wide range of unsaturated compounds featuring C=O, C=C, C≡C, and C≡N bonds. —Jack Huang

J. Am. Chem. Soc. (2025) 10.1021/jacs.4c15821

STEM EDUCATION

Brilliance as a double-edged sword

First-generation (FG) students (the first in their family to go to college) represent a large population of potential scientists, yet they remain underrepresented in STEM fields. Hernandez *et al.* collected data from faculty and undergraduate researchers at three universities to determine whether faculty research mentors' beliefs that brilliance leads to great science (and scientists) were associated with student researchers' science identity. The results showed that faculty with strong brilliance beliefs were associated with higher levels of brilliance beliefs among FG students, but not among continuing generation students. Greater brilliance beliefs among students subsequently predicted lower levels of science identity 3 months later, particularly among FG students. Conversely, the less faculty believed that brilliance was required to succeed in STEM, the less FG researchers incorporated brilliance beliefs themselves and the more they identified as scientists over time. —Melissa McCartney

Commun. Psychol. (2025) 10.1038/s44271-025-00223-8

QUANTUM OPTICS

Photon correlation sensing goes wide-field

In optics, the ability to determine correlations between photons from an emitter can provide information on the nature of the emitter, be it a classical or quantum process. Such correlations also have practical use across a range of fields such as spectroscopy, sensing, secure communication, and imaging. Key to measuring these correlations are the photon detectors, with much of the work limited to just two or a few single photon detectors. Using a large 500 × 500 single-photon detector array, Elmalem *et al.* showed that correlation measurements could be extended to the wide-field. Demonstrating the ability to image multiple quantum emitters with super-resolution and wide-field emitter counting, they claim that such single-photon detector arrays could be used to accelerate the performance of quantum sensing and imaging technologies by orders of magnitude. —Ian S. Osborne

Optica (2025) 10.1364/OPTICA.550498

PHOTO: JUERGEN & CHRISTINE SOHNS/MIDEN

RESEARCH ARTICLE SUMMARY

DOMESTICATION

A single domestication origin of adzuki bean in Japan and the evolution of domestication genes

Chih-Cheng Chien, Takashi Seiko, Chiaki Muto, Hirotaka Ariga, Yen-Chiao Wang, Chuan-Hsin Chang, Hiroaki Sakai, Ken Naito*, Cheng-Ruei Lee*

Full article and list of author affiliations:
https://doi.org/10.1126/science.ads2871

INTRODUCTION AND RATIONALE: The adzuki bean (*Vigna angularis*), with its characteristic red seed coat color, is a crucial legume of East Asian culinary culture. Although archaeological records suggest the earliest traces of cultivation in Japan, previous genetic evidence identified the highest genetic variation in central Chinese cultigens. Because the hunter-gatherer-fisher Jomon populations inhabited the Japanese archipelago before the arrival of the rice-growing Yayoi populations about three thousand years ago (3 kya), the spatiotemporal origin of adzuki domestication remains debated. Furthermore, the evolution of some domestication traits (e.g., pod shattering and seed coat color) cannot be traced by archaeological records, requiring input from genetics studies.

RESULTS: We investigated about 700 adzuki accessions, covering wild and cultigen populations across the species range. The wild populations of this species likely originated near the Himalayas and naturally spread to central China and Japan. We identified genetic evidence of domestication 3 to 5 kya in Japan, with subsequent cultigen expansion back to China, followed by hybridization with Chinese wild populations and generation of admixed cultigen population in southern China. This complex demography likely thwarted previous attempts to trace adzuki domestication origin, and our results explain previous archaeological and genetic observations.

Wild adzuki seed coats have mottled black pigment spots on a pale background, and most cultigens have a characteristic uniform red background without black spots. We identified one major effect gene for each of the two traits. The gain of red background was caused by an amino acid mutation in the anthocyanidin reductase gene *VaANR1*. Our molecular characterization of the wild and cultigen alleles confirmed that this amino acid mutation altered enzyme function, disrupting the processing of anthocyanidins and the accumulation of downstream colorless proanthocyanidins. For the locus conferring mottled black pigment spots, the wild-progenitor haplotype contained three homologous MYB transcription factor genes, and only the central copy, *VaPAP1*, expressed during seed development. In cultigens, nonallelic homologous recombination likely happened between the two flanking copies, deleting *VaPAP1* and resulting in a chimeric copy not expressed during seed development.

We modeled their evolutionary trajectories with another gene, *VaMYB26*, whose frameshift mutation was previously shown to cause pod nonshattering in cultigens. Because all three traits have a Mendelian genetic basis, the time-course mutant allele frequency reflects the domestication phenotype evolution in this predominately self-fertilizing species. Mutant frequency of the three genes increased much earlier than 5 kya, suggesting that weak selection existed before the inferred wild-cultigen divergence time.

CONCLUSION: In this study, we resolved the complex demography of adzuki domestication, identified and validated key genes for domestication traits, and inferred the evolutionary trajectory of these traits, which could not be directly observed from archaeological records. These results complement the growing archaeological evidence that Jomons were not exclusively hunter-gatherer-fishers from the genetics perspective and support the recent archaeobotanical view that weak selection may have existed in local populations thousands of years before clear traces of sophisticated agricultural activities. □

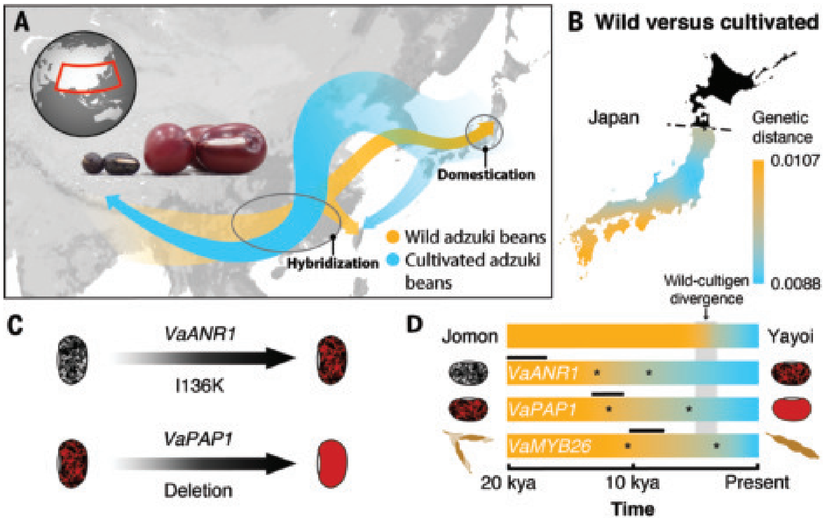

The domestication of adzuki bean. (**A**) The expansion route of wild and cultivated adzuki. [Map based on data from Stadia Maps; inset globe adapted from FreeVectorMaps.com] (**B**) Central Japanese wild accessions as the most likely progenitor of adzuki cultigens. (**C**) The two-step evolution from wild to cultivated adzuki and associated genetic changes. (**D**) The timeline of Japanese human demography and adzuki trait evolution. Horizontal black bars indicate mutation age; asterisks mark timing of initial mutant frequency increase and when frequency reached 0.1; gray band marks wild-cultigen divergence.

---

*Corresponding author. Email: chengrueilee@ntu.edu.tw (C.-R.L.); naito.ken988@naro.go.jp (K.N.) Cite this article as C.-C. Chien *et al.*, *Science* **388**, eads2871 (2025). DOI: 10.1126/science.ads2871

RESEARCH ARTICLE SUMMARY

NEUROSCIENCE

Conserved brain-wide emergence of emotional response from sensory experience in humans and mice

Isaac Kauvar†, Ethan B. Richman†, Tony X. Liu† *et al.*

Full article and list of author affiliations:
https://doi.org/10.1126/science.adt3971

INTRODUCTION: Emotional states are central to the human condition in health and disease, yet the neural processes by which emotions emerge from experience remain mysterious. In mammals, lasting emotional responses may serve to integrate external and internal information spread across the brain, to guide contextually appropriate behaviors. We hypothesized that common structural and functional constraints on sensory integration into emotional states in the mammalian lineage could yield conserved dynamical principles governing the establishment and maintenance of emotional responses.

RATIONALE: To identify broadly conserved patterns of neural activity, we first developed unbiased brain-wide activity screens spanning widely divergent mammalian species. Specifically, we explored when, where, and how emotional states emerge, using high-speed, invasive, and global methods in human and mouse subjects carrying out the same task. While recognizing and leveraging the value of obtaining verbal descriptions of subjective emotional experience from human subjects for this question, we also explicitly bridged human and mouse systems with temporally precise affective behavioral measures, clinically compatible pharmacological interventions, and deep brain-spanning intracranial electrophysiological readouts, designed to be similarly carried out in parallel in both human and mouse subjects, to investigate conserved principles underlying the emergence of lasting emotional states from brief sensory input.

RESULTS: We determined that sequences of air puffs, directed at the cornea of human or mouse subjects, elicit both fast/reflexive and sustained/affective eye closure behaviors; the latter (in both species) is characterized by negative valence, persistence, generalization, and ablation by the dissociative agent ketamine. We performed a brain-wide neural activity screen of this temporally precise behavioral response, using intracranial stereo-electroencephalography (iEEG) in humans and multiprobe Neuropixels single-unit electrophysiology in mice. This brain-wide screen revealed a biphasic process in which emotionally salient sensory signals are swiftly broadcast throughout the mammalian brain and directly followed by a slower and widely distributed persistent signal. We discovered that the persistent signal could be selectively and similarly blocked by ketamine while preserving the fast sensory broadcast in both species, and that emergence of a behaviorally defined emotional state could be selectively blocked by this intervention. We found that the accumulation and decay pattern of persistent population neural activity was consistent with first-order system dynamics, and that the dose-dependent pharmacological impact on the emotional response could be well-modeled by varying a single decay timescale parameter, with emotion-blunting dissociative drugs accelerating the decay. We furthermore found (in both humans and mice) that ketamine accelerated the intrinsic timescale of baseline spontaneous activity and reduced brain-wide population coupling in networks with puff-triggered persistent activity. Control experiments in mice with a neutral auditory stimulus (while operating on faster timescales than emotionally salient stimuli) revealed that the pharmacological effect of sharpening response dynamics and reducing capacity to maintain persistent information across the brain was generalizable, highlighting the importance of signal persistence in the establishment of brain-wide responses.

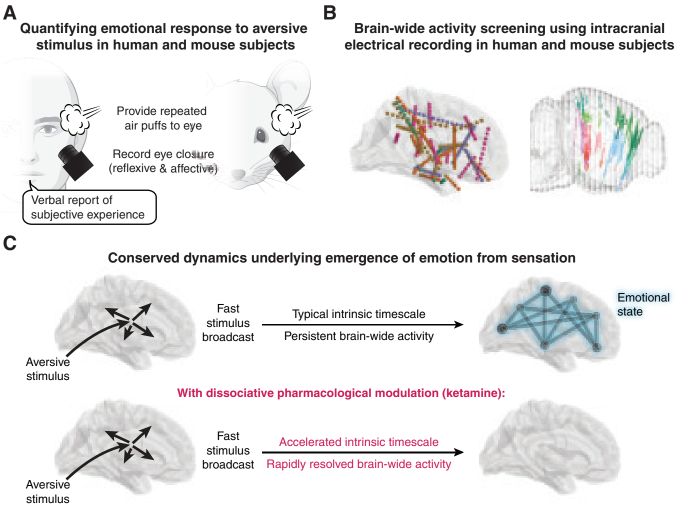
A
Quantifying emotional response to aversive stimulus in human and mouse subjects
Provide repeated air puffs to eye
Record eye closure (reflexive & affective)
Verbal report of subjective experience
B
Brain-wide activity screening using intracranial electrical recording in human and mouse subjects
C
Conserved dynamics underlying emergence of emotion from sensation
Aversive stimulus
Fast stimulus broadcast
Typical intrinsic timescale
Persistent brain-wide activity
Emotional state
With dissociative pharmacological modulation (ketamine):
Aversive stimulus
Fast stimulus broadcast
Accelerated intrinsic timescale
Rapidly resolved brain-wide activity

Brain-wide emergence of emotional response in humans and mice. (**A**) A repeatable, temporally precise, and cross-species measure of emotional response. (**B**) Broad, fast, and spatially resolved neural activity mapping across species with intracranial electrical recording. (**C**) The aversive stimulus signal is rapidly and widely broadcast, and from this, a sustained and distributed emotional state emerges. Ketamine selectively blocks the sustained response by accelerating the decay rate of system dynamics.

CONCLUSION: We find that mammalian emotional states, in a conserved pattern spanning divergent species, are integrated from sensory experiences through persistent activity dynamics that can be shaped by a global and tunable intrinsic timescale, akin to the action of a piano sustain pedal. Functioning as a distributed neural context, adaptive emotional states appear to depend upon brain-wide mechanisms of signal persistence in specific networks. Furthermore, consistent with our measurements of intrinsic timescale modulation by clinically relevant intervention, aspects of the etiology and treatment of certain neuropsychiatric disorders may be governed by altered stability of brain states linked to maladaptively fast or slow intrinsic timescales. ☐

Corresponding authors: Karl Deisseroth (deissero@stanford.edu); Vivek Buch (vpbuch@stanford.edu); Carolyn Rodriguez (cr2163@stanford.edu); Paul Nuyujukian (23sciencemag@pn.stanford.edu) †These authors contributed equally to this work. **Cite this article as I. Kauvar *et al.*, *Science* 388, eadt3971 (2025). DOI 10.1126/science.adt3971**

RESEARCH ARTICLE SUMMARY

SIGNAL TRANSDUCTION

BRAF oncogenic mutants evade autoinhibition through a common mechanism

Hugo Lavoie†, Ting Jin†, Driss Lajoie†, Marion Decossas, Patrick Gendron, Bing Wang, Frantisek Filandr, Malha Sahmi, Chang Hwa Jo, Sandra Weber, Geneviève Arseneault, Sasmita Tripathy, Pierre Beaulieu, Doris A. Schuetz, David C. Schriemer, Anne Marinier, William J. Rice, Pierre Maisonneuve, Marc Therrien*

Full article and list of author affiliations: https://doi.org/10.1126/science.adp2742

INTRODUCTION: Cells utilize a complex network of signaling pathways to integrate and respond to external cues. The rat sarcoma (RAS)–extracellular signal–regulated kinase (ERK) signaling pathway regulates cell proliferation and differentiation. Upon activation by receptors on the cell surface, the small guanosine triphosphatase RAS recruits and activates kinases from the rapidly accelerated fibrosarcoma (RAF) family. These kinases initiate a phosphorylation cascade, ultimately modulating numerous target proteins that drive specific cellular responses. One prominent member of the RAF family, BRAF, is frequently activated by mutations in human cancers.

RATIONALE: Under quiescent conditions, wild-type (WT) BRAF is maintained in a monomeric autoinhibited state, stabilized by interactions between its cysteine-rich domain (CRD) and kinase domain (KD; CRD-in conformation). Upon growth factor stimulation, BRAF undergoes activation through KD dimerization. The most prevalent class of BRAF mutations (Class 1) appear to induce constitutive activation independently of RAS activity and bypass the requirement for KD dimerization. However, the structural basis for these properties has remained speculative. We used cryo–electron microscopy (cryo-EM) to determine the three-dimensional (3D) structures of oncogenic BRAF variants and compared them to those of WT BRAF. This revealed the alterations caused by the mutations, offering insights into the molecular mechanisms underlying BRAF oncogenic activation.

RESULTS: The 3D structure of monomeric BRAF V600E, encoded by the most prevalent Class 1 oncogenic mutation in the *BRAF* gene, revealed features characteristic of an active dimer despite the monomeric state. The inhibitory interaction between the CRD and the KD was disrupted (CRD-out conformation), and the KD adopted an active-like orientation, resembling the conformation of a single BRAF molecule in an active dimer. The inward positioning of helix αC within the KD was consistent with the active state. This inward movement of helix αC, driven by the V600E mutation, was shown to be the main mechanism underlying the structural reorganization of BRAF. By using small-molecule inhibitors that stabilize either the inward (active) or outward (inactive) position of helix αC, we demonstrated that this conformational shift is central to the activation mechanism induced by the V600E mutation. We also solved the 3D structures of representative class 2 and 3 oncogenic BRAF variants. These variants exhibited the same global reorganization of the KD observed in BRAF V600E, including the disruption of autoinhibitory interactions. Our findings are consistent with a common mechanism by which oncogenic BRAF mutations induce kinase activation through the release of autoinhibition and the adoption of an active-like KD conformation driven by helix αC inward movement.

CONCLUSION: This study establishes a structural and mechanistic framework that unifies the mode of action of diverse oncogenic BRAF mutations, providing crucial insights into their common activation mechanisms and potential opportunities for targeted therapeutic intervention. The active-like conformation adopted by these oncogenic variants resembles a hybrid state between the autoinhibited monomer and active dimer configurations observed in WT BRAF. This similarity suggests that the oncogenic variants may mimic a transition state that WT BRAF undergoes during its shift from an inactive monomer to an active dimer. ☐

---

*Corresponding author. Email: marc.therrien@umontreal.ca †These authors contributed equally to this work. **Cite this article as H. Lavoie *et al.*, *Science* 388, eadp2742 (2025). DOI: 10.1126/science.adp2742**

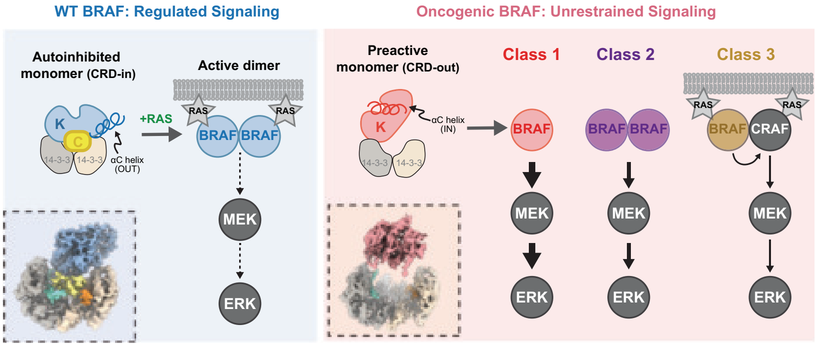

Cryo-EM structural analysis of oncogenic BRAF variants (red shading) compared with WT BRAF (blue shading), leading to their unrestrained activity. WT BRAF adopts a stable, autoinhibited monomeric state in which its CRD (C) forms inhibitory contacts with the KD (K), stabilized by a 14-3-3 protein dimer (CRD-in). Upon binding to activated RAS at the plasma membrane, WT BRAF forms a catalytically active dimer, enabling downstream signaling to mitogen-activated protein kinase kinase (MEK) and ERK. Oncogenic BRAF mutations induce an inward shift of the KD's helix αC, disrupting CRD-KD interactions and repositioning the KD into a preactive conformation (CRD-out). Class 1 mutants are constitutively active as stable monomers, independent of dimerization. Class 2 mutants also form CRD-out monomers but require dimerization for full activation. Class 3 mutants, which are catalytically impaired, adopt a CRD-out monomeric state that enhances RAS binding and facilitates dimerization and transactivation of another catalytically competent RAF protein, such as CRAF.

RESEARCH ARTICLE SUMMARY

ANCIENT DNA

Prehistoric genomes from Yunnan reveal ancestry related to Tibetans and Austroasiatic speakers

Tianyi Wang *et al.*

Full article and list of author affiliations:
https://doi.org/10.1126/science.adq9792

INTRODUCTION: In East and Southeast Asia, a long history of population movement, replacement, and mixture has heavily influenced the genetic composition of humans up to the present day. For example, early populations found across this region that diversified before 40,000 years ago carrying Basal Asian ancestries have largely been replaced by a single lineage that diversified into the ancestries found in most present-day East and Southeast Asians. However, these ancestries sampled to date have yet to explain the genetic diversity observed across all present-day East and Southeast Asians, with ancestries still uncharacterized in many populations, including in Tibetans and Austroasiatic speakers.

RATIONALE: Sequencing of 127 ancient human genomes dating to 7100 to 1500 years ago from Yunnan province in southwestern China may help to further clarify human population history in East and Southeast Asia. Yunnan is at the intersection of the Tibetan Plateau, Southeast Asia, and southern China and is home to the highest ethnic and linguistic diversity in China today. Thus, genomic sampling of ancient populations from this region provides an opportunity to capture the migration, interaction, and change over time in prehistoric populations of East and Southeast Asia.

RESULTS: Analysis of a 7100-year-old individual from the Xingyi archaeological site in central Yunnan revealed a previously unsampled Basal Asian ancestry that is deeply diverged from East Asian ancestries and persisted in southern East Asia into the mid-Holocene. This Basal Asian Xingyi ancestry is also related to deeply diverged ghost ancestry found in Tibetan Plateau populations, providing new information for studying the origin of Tibetan Plateau populations. The 5500- to 1500-year-old populations from central Yunnan do not show Basal Asian Xingyi ancestry, but carry an East Asian ancestry distinct from northern and southern East Asian ancestries previously characterized, denoted here as Central Yunnan ancestry. This distinct East Asian ancestry can be found across present-day Austroasiatic speakers, indicating that these ancient populations in central Yunnan were likely a proto-Austroasiatic population. By contrast, 3800- to 1700-year-old populations from western Yunnan primarily have northern East Asian ancestry, whereas a 3400-year-old population from eastern Yunnan shows a mixture of southern East Asian and Central Yunnan ancestries. Collectively, these patterns indicate that multiple diverse East Asian ancestries coexisted in Bronze Age Yunnan populations.

CONCLUSION: Sampling ancient humans from Yunnan province, we discovered a new Basal Asian ancestry that is closely related to a “ghost” ancestry that influenced populations who lived on the Tibetan Plateau. In addition, we found a distinct East Asian ancestry that sheds light on the origin of Austroasiatic populations. Multiple East Asian ancestries in Yunnan during the Bronze Age reveal high human genetic diversity and dynamic population movements across East and Southeast Asia. ☐

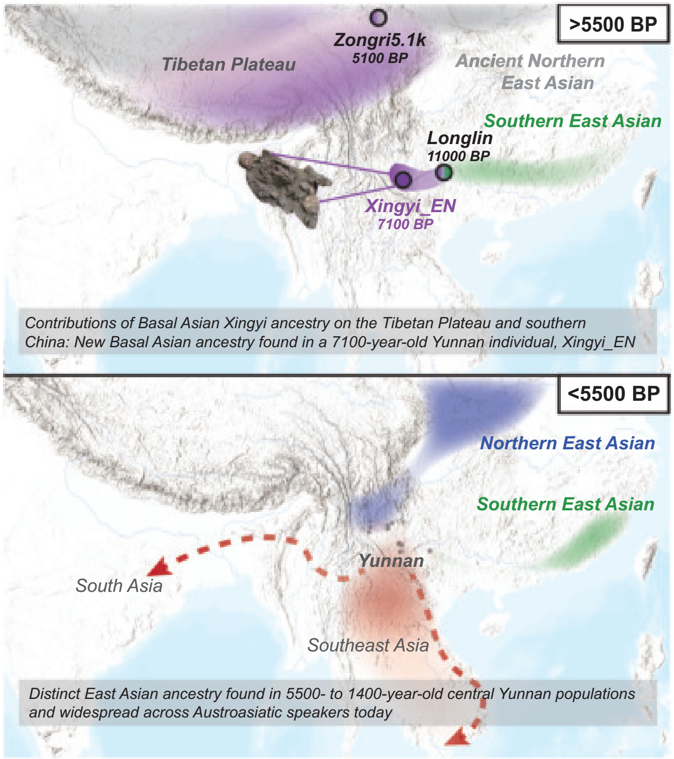

Contributions of Basal Asian Xingyi ancestry on the Tibetan Plateau and southern China: New Basal Asian ancestry found in a 7100-year-old Yunnan individual, Xingyi_EN

Distinct East Asian ancestry found in 5500- to 1400-year-old central Yunnan populations and widespread across Austroasiatic speakers today

Population migration, replacement, and the preservation of deeply diverged ancestry in southern East Asia. A 7100-year-old individual from Yunnan shows a Basal Asian ancestry that is related to a deeply diverged ghost ancestry contributing to Tibetan Plateau populations. After 5500 years before present (BP), populations in Yunnan exhibited diverse ancestries, including contributions from northern East Asia in western Yunnan, coastal southern East Asia in eastern Yunnan, and a newly identified East Asian lineage in central Yunnan that later contributed to present-day Austroasiatic speakers.

Corresponding author: Qiaomei Fu (fuqiaomei@ivpp.ac.cn) Cite this article as T. Wang *et al.*, *Science* **388**, eadq9792 (2025). DOI: 10.1126/science.adq9792

RESEARCH ARTICLE SUMMARY

DIAPAUSE

Functional polymorphism of CYCLE underlies the diapause variation in moths

Shirui Zheng†, Yaohui Wang†, Guiyun Li†, Sheng Qin, Zhi Dong, Xu Yang, Xiaomiao Xu, Gangqi Fang, Muwang Li, Shuai Zhan*

Full article and list of author affiliations:
https://doi.org/10.1126/science.ado2129

INTRODUCTION: Seasonal adaptation is crucial for the survival of natural animals. As a specific form of dormancy, diapause halts development to endure unfavorable seasons and commonly serves as a seasonal adaptative strategy in insects. Diapause traits vary pronouncedly within and among species, contributing to life history diversification in response to latitude and climate changes. Elucidating the genetic basis of diapause variation enhances our understanding of how insects rapidly adapt to changing environments for speciation and range expansion and allows for prediction of their further adaptation under global climate change. Despite broad interest, the molecular bases underlying the diversity of diapause traits and annual timing remain largely unexplored in insects, particularly for specified causal alleles in nonmodel species.

RATIONALE: The domestic silk moth (*Bombyx mori*) exhibits characteristic diapause phenotypes across strains. To synchronize their life cycles with human activities, most domestic strains produce one or two generations a year through embryonic diapause (univoltinism or bivoltinism), depending on the perception of environmental cues in the maternal generation. By contrast, local strains originating from the tropics do not enter diapause regardless of environmental conditions (polyvoltinism). The rich variety of resources and well-documented phenotypes enable in-depth studies in this species to characterize the molecular mechanisms underlying diapause traits in Lepidoptera (moths and butterflies). We aimed to combine canonical genetic approaches and high-throughput genome-wide investigations to (i) identify causal loci responsible for the diapause variation in *B. mori* and (ii) test whether these identified loci have analogous effects in other species of Lepidoptera.

RESULTS: We generated cross-mapping progeny between a facultative diapause bivoltine strain and a nondiapause polyvoltine strain of silk moths that mapped the major locus responsible for diapause variation on chromosome Z. By integrating with genome-wide association of 255 parental strains exhibiting diapause polymorphism, we localized the most effecting locus to the 5′ region of a central clock gene, C*ycle* (an insect homolog of BMAL1 in vertebrates). We identified a 1–base pair deletion exclusive to nondiapause strains as the key causal allele that disrupts one specific isoform of CYC (CYC-C), while preserving the complete copies of alternative isoforms (CYC-A/B). Multidimensional lines of evidence supported the involvement of CYC-C in controlling diapause in the silk moth, linking it with multiple functional modules potentially related to diapause modulation, and showed that CYC-A/B may play the native role of CYC as a fundamental component of circadian regulation. We further showed that the expression of alternative CYC transcripts is subject to independent regulation and that this functional diversity has been reserved across a wide range of Lepidoptera taxa. On the basis of isoform-specific mutagenesis, we validated the effect of CYC-C in initiating larval diapause in the Asian corn borer (*Ostrinia furnacalis*) that diverged with the silk moth approximately 100 million years ago.

CONCLUSION: In this study, we defined the additional function of the circadian protein CYC, through one of its alternative isoforms, in controlling the entry into diapause in Lepidoptera, and identified a newly derived mutation in this isoform, arising along with the domestication in tropical regions, which is responsible for the diapause variation in silk moths. The potential functional diversity of CYC is widespread in Lepidoptera, which may reconcile the flexibility of seasonal adaptation with the functional constraint on fundamental circadian regulation. Combined with previously documented examples in TIMELESS (TIM) and PERIOD (PER) in *Drosophila*, the diverse isoforms of central clock genes may serve as common targets of selection for seasonal adaptation in insects. ☐

---

*Corresponding author. Email: szhan@sibs.ac.cn †These authors contributed equally to this work. **Cite this article as S. Zheng *et al.*, *Science* 388, eado2129 (2025). DOI: 10.1126/science.ado2129**

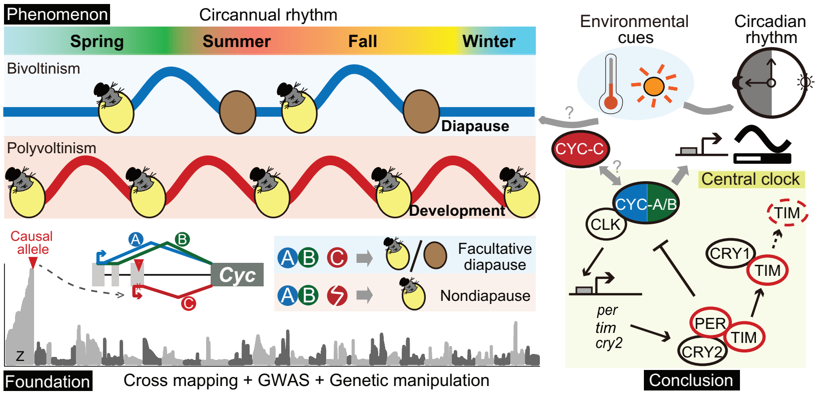

A tale of two roles: Central clock genes maintain circadian rhythm and confer variable seasonal timing of diapause. Genetic analyses identify a causal deletion that disrupts an isoform of CYC (C), thereby affecting diapause incidence in domestic silk moths (the brown unhatched eggs). The isoform-based functional complexity of clock genes may widely contribute to seasonal adaptation in insects, supported by previously documented similar cases involving TIM and PER in *Drosophila* (circled in red). GWAS, genome-wide association study (a detailed explanation of this model is available in fig. S21).

RESEARCH ARTICLE SUMMARY

PLAGUE

Attenuation of virulence in *Yersinia pestis* across three plague pandemics

Ravneet Kaur Sidhu† and Guillem Mas Fiol† *et al.*

Full article and list of author affiliations:
https://doi.org/10.1126/science.adt3880

INTRODUCTION: The Plague of Justinian and the Black Death represent two of the greatest mortality events in recorded human history and are herald waves of the first and second plague pandemics. Genomes of the plague bacterium *Yersinia pestis*, reconstructed from ancient human remains from about a century into each pandemic, show evidence of a depletion in the copy number of the virulence gene *pla*, which resides on the high–copy number plasmid (pPCP1) and encodes a plasminogen activator (Pla) protease that is responsible for virulence and pathogenicity in bubonic and pneumonic models of plague.

RATIONALE: To determine the effects of the *pla* depletion on virulence in mice, we tested modern (third pandemic) strains of *Y. pestis* from Vietnam that contain the same depletion as ancient strains using models of bubonic, pneumonic, and septicemic plague. We also investigated the genomes of the ancient and modern *Y. pestis* strains to characterize the molecular basis of the *pla* depletion.

RESULTS: De novo reconstruction of the ancient and modern strains of *Y. pestis* that contain lower–copy number *pla* show transfer from the high–copy number plasmid (pPCP1) to single-copy genomic features in the modern (pCD1) and ancient (chromosome) strains. A common *pla* deletion mechanism is likely mediated by *xrs* sites present in pPCP1. Depletion in *pla* copy number led to an attenuation of virulence in bubonic models of plague (but not pneumonic or septicemic models), with lowered overall mortality (100 to 85%) and a longer time to death (by ~2 days).

CONCLUSION: We hypothesize that natural selection for *pla*-reduced strains reflects the metapopulation structure of rat populations, supporting epidemiological models in which pathogen attenuation enables disease persistence in small and fragmented populations through frequent, reinitiated epidemics after population recovery. The massive rat mortality that presumably occurred during the first and second pandemics likely led to suppressed rodent densities. By increasing population fragmentation, this created an environment that favored *pla*-reduced, attenuated strains of *Y. pestis* over their more virulent wild-type *pla* relatives. Specifically, a decreased mortality rate and longer time to host death would allow for the continued movement of rodents between existing populations, now more distantly spaced than early in the pandemic, allowing for the continued persistence, and hence increased transmission, of *Y. pestis* and the slow continual burn of the epidemic. □

Corresponding authors: Ravneet Kaur Sidhu (sidhur5@mcmaster.ca); Javier Pizarro-Cerdá (javier.pizarro-cerda@pasteur.fr); Hendrik N. Poinar (poinarh@mcmaster.ca) †These authors contributed equally to this work. **Cite this article as** R. K. Sidhu *et al.*, *Science* **388**, eadt3880 (2025). DOI: 10.1126/science.adt3880

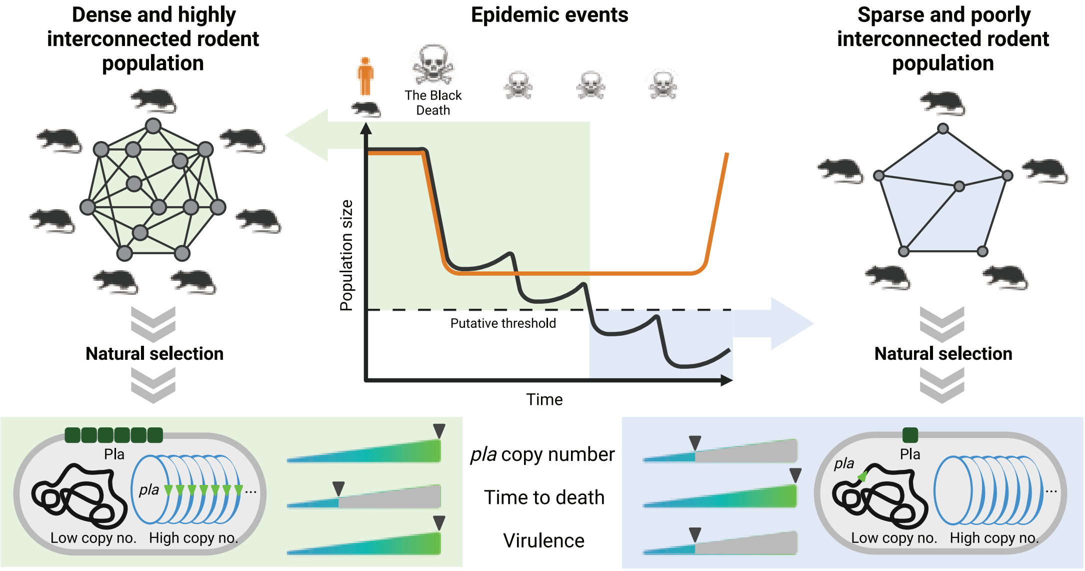

Graphical representation of our working hypothesis. Rodent metapopulation structure and size are critical selective pressures for virulence attenuation in the plague bacterium *Y. pestis*. The Black Death and subsequent epidemics of the second pandemic continually suppressed population sizes of key amplifying hosts (black rats), eventually reaching a threshold at which depletion in the virulence gene *pla* swept across most European strains. Depletion of the *pla* gene lowers overall mortality in bubonic models of plague and increases the time to death, allowing for the more sparsely populated rats to reach new hosts that are now more distantly spaced. [Figure created with BioRender.com]

RESEARCH ARTICLES

SUPERCONDUCTIVITY

Pair wave function symmetry in UTe_2 from zero-energy surface state visualization

Qiangqiang Gu[1]*†, Shuqiu Wang[1,2,3]†, Joseph P. Carroll[1,4]†, Kuanysh Zhussupbekov[1,4]†, Christopher Broyles[5], Sheng Ran[5], Nicholas P. Butch[6,7], Jarryd A. Horn[6], Shanta Saha[6], Johnpierre Paglione[6,8], Xiaolong Liu[1,9,10], J. C. Séamus Davis[1,2,4,11]*, Dung-Hai Lee[12,13]*

Although nodal spin-triplet topological superconductivity appears probable in uranium ditelluride (UTe_2), its superconductive order parameter $\Delta_{\mathbf{k}}$ remains unestablished. In theory, a distinctive identifier would be the existence of a superconductive topological surface band, which could facilitate zero-energy Andreev tunneling to an s-wave superconductor and also distinguish a chiral from a nonchiral $\Delta_{\mathbf{k}}$ through enhanced s-wave proximity. In this study, we used s-wave superconductive scan tips and detected intense zero-energy Andreev conductance at the UTe_2 (0-11) termination surface. Imaging revealed subgap quasiparticle scattering interference signatures with *a*-axis orientation. The observed zero-energy Andreev peak splitting with enhanced s-wave proximity signifies that $\Delta_{\mathbf{k}}$ of UTe_2 is a nonchiral state: B_{1u}, B_{2u}, or B_{3u}. However, if the quasiparticle scattering along the *a* axis is internodal, then a nonchiral B_{3u} state is the most consistent for UTe_2.

The internal symmetry of electron-pair wave functions in nontrivial superconductors (*1*) is represented by the momentum $\mathbf{p} = \hbar\mathbf{k}$ dependence of the electron-pairing order parameter $\Delta_{\mathbf{k}}$, where $\hbar$ is the reduced Planck constant. For spin-triplet superconductors, where electron pairs have three spin-1 eigenstates $(|\uparrow\uparrow\rangle, |\downarrow\downarrow\rangle, |\uparrow\downarrow + \downarrow\uparrow\rangle)$, $\Delta_{\mathbf{k}}$ is a 2×2 matrix: $\Delta_{\mathbf{k}} = \begin{pmatrix} \Delta_{\mathbf{k}\uparrow\uparrow} & \Delta_{\mathbf{k}\uparrow\downarrow} \\ \Delta_{\mathbf{k}\downarrow\uparrow} & \Delta_{\mathbf{k}\downarrow\downarrow} \end{pmatrix}$ with $\Delta^{\mathrm{T}}_{-\mathbf{k}} = -\Delta_{\mathbf{k}}$ and $\Delta_{\mathbf{k}} = \Delta^{\mathrm{T}}_{\mathbf{k}}$ (*1–5*). This may also be represented in the $\mathbf{d}$-vector notation as $\Delta_{\mathbf{k}} \equiv \Delta_0(\mathbf{d}\cdot\boldsymbol{\sigma})i\sigma_2$ where σ_i are the Pauli matrices. Many such systems should be intrinsic topological superconductors (ITSs), where a bulk superconducting energy gap with nontrivial topology coexists with a symmetry-protected topological surface band (TSB) of Bogoliubov quasiparticles within that energy gap. Unlike proximitized topological insulators or semiconductors, when three-dimensional (3D) superconductors are topological (*6*), it is not because of electronic band structure topology but rather because $\Delta_{\mathbf{k}}$ exhibits topologically nontrivial properties (*7*). The prototypical example would be a 3D spin-triplet nodal superconductor (*1–6*), and the search for such ITSs that are also technologically viable is a forefront of quantum matter research (*8*).

Three-dimensional spin-triplet superconductors are complex states of quantum matter (*1*, *4*, *5*). Thus, for pedagogical purposes, we describe a nodal spin-triplet superconductor using a spherical Fermi surface within a cubic 3D Brillouin zone (Fig. 1A). The zeros of $\Delta_{\mathbf{k}}$ are then represented by red points at $\pm\mathbf{k}_n$. The Bogoliubov–de Gennes (BdG) Hamiltonian is given by

$$H = \sum_{k_x} \sum_{\mathbf{k}_\perp} \psi^{+}(k_x, \mathbf{k}_\perp) h(k_x, \mathbf{k}_\perp) \psi(k_x, \mathbf{k}_\perp) \quad (1)$$

Here $\psi^T(\mathbf{k}) = \left(c_{\mathbf{k}\uparrow}, c_{\mathbf{k}\downarrow}, c^{+}_{-\mathbf{k}\uparrow}, c^{+}_{-\mathbf{k}\downarrow}\right)$ and $h(k_x, \mathbf{k}_\perp)$ is a 4×4 matrix, containing both band structure and $\Delta_{\mathbf{k}}$. We distinguish $\mathbf{k} = (k_x, \mathbf{k}_\perp)$ because they play different roles in the following didactic presentation. Considering one particular 2D slice of the 3D Brillouin zone with a fixed k_x: Its Hamiltonian $h(k_x, \mathbf{k}_\perp)$ is that of a 2D superconductor within a 2D Brillouin zone spanned by $\mathbf{k}_\perp$. The 2D states $|k_x| < |\mathbf{k}_n|$ (Fig. 1A, blue) are topological and those $|k_x| > |\mathbf{k}_n|$ (Fig. 1A, green) are nontopological. The essential signature of such physics is a superconductive TSB [or Andreev bound state (ABS) (*7*)] on the edges of each 2D slice for $|k_x| < |\mathbf{k}_n|$, and its absence when $|k_x| > |\mathbf{k}_n|$. The 2D Brillouin zone of any crystal surface parallel to the nodal axis of $\Delta_{\mathbf{k}}$ is shown in Fig. 1B along with the quasiparticle dispersion $\mathbf{k}(E)$ of a single TSB. The equatorial circle in Fig. 1B is the $k_x - k_y$ contour satisfying $\epsilon(k_x, k_y, 0) = 0$ with $\epsilon(k)$ being the quasiparticle band dispersion. A line of zero-energy TSB states then connects the two projections of the nodal wave vectors $\pm\mathbf{k}_n$ onto this 2D zone (this is often called a "Fermi arc," although it is actually a twofold degenerate Majorana arc of charge-neutral Bogoliubov quasiparticles). Calculation of the density of such TSB quasiparticle states $N(E)$ from $\mathbf{k}(E)$ in Fig. 1B yields a continuum in the range $-\Delta_0 \le E \le \Delta_0$, with a sharp central peak at $E = 0$ due to this arc (Fig. 1C). Thus, 3D nodal spin-triplet superconductors should exhibit a TSB on any surface parallel to their nodal axis, and such TSBs exhibit a zero-energy peak in $N(E)$ [see supplementary text section 1 of (*9*)]. The conceptual phenomena presented in Fig. 1, A to C, depend solely on whether the symmetry protecting the TSB is broken, and not on material details. Hence, the presence or absence of a gapless TSB on a given surface of a 3D superconductor, of a zero-energy peak in $N(E)$ from its Majorana arcs, and of the response of the TSB to breaking specific symmetries can reveal the symmetry and topology of $\Delta_{\mathbf{k}}$.

Pair wave function symmetry in UTe_2

UTe_2 is now the leading candidate 3D nodal spin-triplet superconductor (*10*, *11*). Its crystal symmetry point group is D_{2h} and the space group is *Immm* [section 2 of (*9*)]. Associated with the three basis vectors **a**, **b**, and **c** are the three orthogonal **k**-space axes k_x, k_y, k_z. Within D_{2h} there are four possible odd-parity order parameter symmetries designated A_u, B_{1u}, B_{2u}, and B_{3u} [section 2 of (*9*)]. All preserve time-reversal symmetry: A_u is fully gapped, whereas B_{1u}, B_{2u}, and B_{3u} have zeros (point nodes) in $\Delta_{\mathbf{k}}$, whose axial alignment is along **c**, **b**, or **a**, respectively [section 2 of (*9*)]. Linear combinations of A_u, B_{1u}, B_{2u}, and B_{3u} are also possible, which break point-group and time-reversal symmetries, resulting in a chiral TSB (*7*, *8*). For UTe_2, there are two chiral states of particular interest with $\Delta_{\mathbf{k}}$ nodes aligned with the crystal *c* axis, and two with nodes aligned with the *a* axis [section 2 of (*9*)]. Although identifying which (if any) of these superconductive states exists in UTe_2 is key to its fundamental physics, this objective has proven extraordinarily difficult to achieve (*12*).

Identifying the $\Delta_{\mathbf{k}}$ symmetry of UTe_2 using macroscopic experiments has been problematic because, depending on the sample preparation method, the UTe_2 samples appear to have various degrees of heterogeneity. Samples grown by chemical vapor transport (CVT) exhibit small residual resistivity ratios (RRRs) (~35) and transition temperatures $T_c \approx$ 1.6 to 2 K (*13–15*), whereas samples grown by the molten flux method (MFM) have larger RRRs (~1000) and higher transition temperatures ($T_c \approx 2$ K) (*16*). From macroscopic studies, the status $\Delta_{\mathbf{k}}$ for UTe_2 remains indeterminate (*17–27*) [section 3 of (*9*)]. To date, $\Delta_{\mathbf{k}}$ symmetry of UTe_2

---

[1]Lab of Atomic and Solid State Physics (LASSP), Department of Physics, Cornell University, Ithaca, NY, USA. [2]Clarendon Laboratory, University of Oxford, Oxford, UK. [3]H. H. Wills Physics Laboratory, University of Bristol, Bristol, UK. [4]Department of Physics, University College Cork, Cork, Ireland. [5]Department of Physics, Washington University in St. Louis, St. Louis, MO, USA. [6]Maryland Quantum Materials Center, University of Maryland, College Park, MD, USA. [7]NIST Center for Neutron Research, Gaithersburg, MD, USA. [8]Canadian Institute for Advanced Research, Toronto, Ontario, Canada. [9]Department of Physics and Astronomy, University of Notre Dame, Notre Dame, IN, USA. [10]Stavropoulos Center for Complex Quantum Matter, University of Notre Dame, Notre Dame, IN, USA. [11]Max-Planck Institute for Chemical Physics of Solids, Dresden, Germany. [12]Department of Physics, University of California, Berkeley, Berkeley, CA, USA. [13]Materials Sciences Division, Lawrence Berkeley National Laboratory, Berkeley, CA, USA. ***Corresponding author. Email: qiangqianggu2016@gmail.com (Q.G.); jcseamusdavis@gmail.com (J.C.S.D.); dunghai@berkeley.edu (D.-H.L.)** †These authors contributed equally to this work.

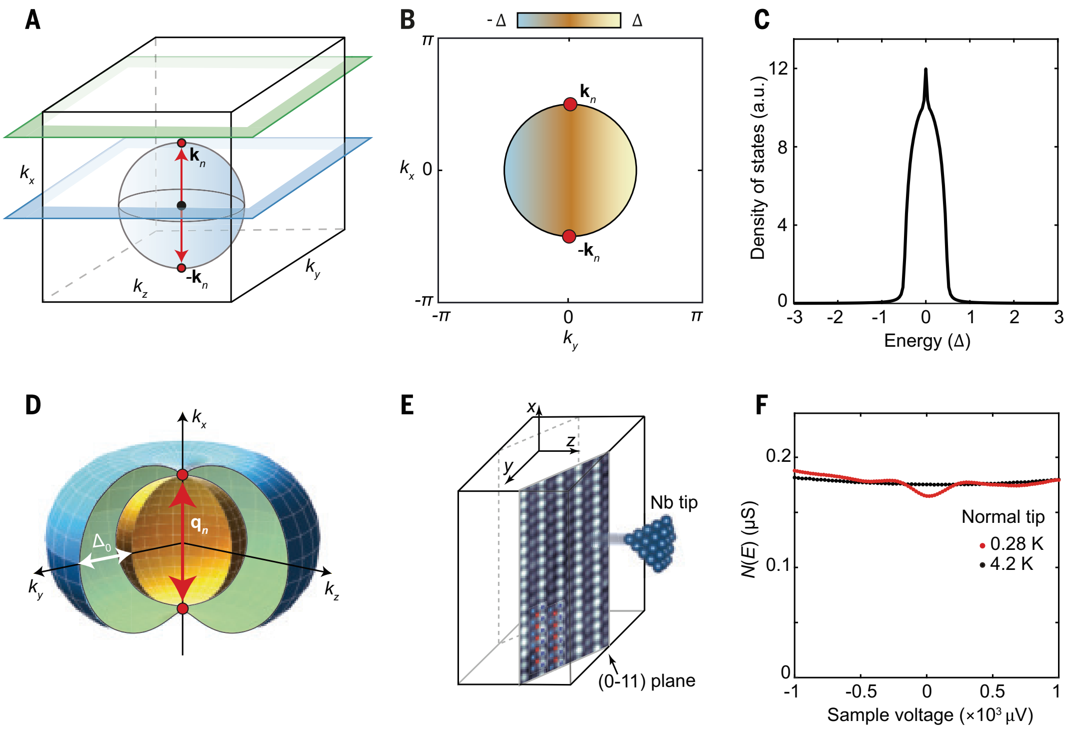

Fig. 1. Pair wave function symmetry in UTe$_2$. (**A**) Pedagogical model of a nodal spin-triplet superconductor with order parameter $\Delta_\mathbf{k}$ having *a*-axis nodes identified by red dots; the red arrow labels the internodal scattering wave vector. The 2D states $|k_x| < |\mathbf{k}_n|$ indicated for example by a blue plane are topological, whereas those $|k_x| > |\mathbf{k}_n|$, indicated by a green plane, are nontopological. (**B**) The 2D Brillouin zone of the crystal surface parallel to the $\Delta_\mathbf{k}$ nodal axis, namely, the *a*-*b* plane, showing a single TSB dispersion $\mathbf{k}(E)$ with color code for E. A line of zero-energy TSB states dubbed the Fermi arc connects the two points representing the projections of the 3D $\Delta_\mathbf{k}$ nodal wave vectors $\pm\mathbf{k}_n(E)$ onto this 2D zone. The equatorial circle in this plot is the $k_x - k_y$ contour satisfying $\epsilon(k_x,k_y,0) = 0$ where $\epsilon(k_x,k_y,k_z)$ is the band dispersion used in the model. (**C**) The density of TSB quasiparticle states $N(E)$ calculated from (B) exhibits a continuum $|E| \leq \Delta_0$ with a sharp peak at $E = 0$ owing to the TSB Fermi arc. a.u., arbitrary units. (**D**) Schematic symmetry of a possible UTe$_2$ order parameter $\Delta_\mathbf{k}$ that has two *a*-axis nodes. The *a* axis–oriented internodal scattering $\mathbf{q}_n$ is indicated by a red arrow. (**E**) Schematic of (0-11) cleave surface of UTe$_2$ shown in relative orientation to the STM tip tunneling direction and $\Delta_\mathbf{k}$ in (D). (**F**) Measured $N(E)$ of normal ($T = 4.2$ K) and superconducting ($T = 280$ mK) states of UTe$_2$ using a nonsuperconducting STM tip at the (0-11) cleave surface as seen in (E). At the UTe$_2$ surface, virtually all states $|E| \leq \Delta_0$ are ungapped.

has been conjectured as nonchiral A_u (*17*, *20*), B_{1u} (*24*), B_{3u} (*18*, *24*), chiral $A_u + iB_{3u}$ (*21*), $B_{2u} + iB_{3u}$ (*22*), $A_u + iB_{1u}$ (*22*), and $B_{1u} + iB_{2u}$ (*26*). Notably, however, no tunneling spectroscopic measurements of $\Delta_\mathbf{k}$, which could differentiate directly between these scenarios, have been reported.

Tunneling between s-wave and topological p-wave superconductors

An efficient tunneling spectroscopic technique for establishing $\Delta_\mathbf{k}$ in unconventional superconductors (*28*–*33*) is quasiparticle interference imaging (QPI); but this has proven ineffective for unraveling the conundra of UTe$_2$. This is because conventional single-electron tunneling spectroscopy of UTe$_2$, even at $T = 280$ mK ($T/T_c \lesssim 1/6$), yields a typical quasiparticle density-of-states spectrum $N(E \leq \Delta_0)$ that is essentially metallic, with only tenuous hints of opening the bulk superconductive energy gap (Fig. 1F) (*34*, *35*). Further, UTe$_2$ surface impedance measurements detect a nonsuperconductive component of surface conductivity $\sigma_1(\omega,T)$ deep in the superconductive phase (*36*). Yet the classic QPI signature (*37*) of a bulk superconductive $\Delta_\mathbf{k}$ has been impossible to detect, apparently because the high $N(E \leq \Delta_0)$ overwhelms any tunneling conductance signal from the 3D quasiparticles. Given these challenges to determining the symmetry of $\Delta_\mathbf{k}$ using a normal scan tip, we explored the possibility of using a superconductive scan tip [(*38*–*43*) and section 4 of (*9*)]. Theoretically, we consider two primary channels for conduction from the fully gapped s-wave superconductive tip to a nodal spin-triplet superconductor. The first is single-electron tunneling, for which the minimum voltage required is $V = \Delta_{\text{tip}}/e$. The second, is Andreev reflection of pairs of subgap quasiparticles [section 4 of (*9*)] transferring charge $2e$ across the junction: This occurs because creating or annihilating Cooper pairs costs no energy in a superconductor. Conceptually, therefore, there are notable advantages to using scanned Andreev tunneling spectroscopy for ITS studies, including that TSB quasiparticles within the interface predominate the Andreev process, that the order parameter symmetry difference between sample and tip does not preclude the resulting zero-bias Andreev conductance, and that the enhanced zero-energy conductance peak due to the TSB can be detected simply and directly in this way.

To explore this opportunity, we have developed a general guiding theoretical model to describe an s-wave superconducting tip [e.g., niobium (Nb)] connected by tunneling to a nodal p-wave superconductor (e.g., UTe$_2$), which sustains a TSB within the interface. We refer to this throughout as the SIP model. To simplify computational complexity, we consider a planar interface shown schematically in Fig. 2A with in-plane momenta as good quantum numbers. The BdG Hamiltonian of this SIP model has three elements: $H = H_{\text{Nb}} + H_{\text{UTe}_2} + H_{\text{T}}$. Here, H_{Nb} is the Hamiltonian for an ordinary s-wave superconductor given by $H_{\text{Nb}}(\mathbf{k}) = \begin{pmatrix} \epsilon_{\text{Nb}}(\mathbf{k})\sigma_0 & \Delta_{\text{Nb}}(i\sigma_2) \\ \Delta^*_{\text{Nb}}(-i\sigma_2) & -\epsilon_{\text{Nb}}(-\mathbf{k})\sigma_0 \end{pmatrix}$; $\epsilon_{\text{Nb}}(\mathbf{k})$ is the band structure model for Nb, and Δ_{Nb} is the Nb superconducting order parameter. H_{UTe_2} is the Hamiltonian of the putative p-wave superconductor with $\begin{pmatrix} \epsilon_{\text{UTe}_2}(\mathbf{k})\sigma_0 & \Delta_{\text{UTe}_2}(\mathbf{k}) \\ \Delta^+_{\text{UTe}_2}(\mathbf{k}) & -\epsilon_{\text{UTe}_2}(-\mathbf{k})\sigma_0 \end{pmatrix}$; $\epsilon_{\text{UTe}_2}(\mathbf{k})$ is the band structure, and $\Delta_{\text{UTe}_2}(\mathbf{k})$ is a 2×2 spin-triplet pairing matrix given by $\Delta_{\text{UTe}_2}(\mathbf{k}) \equiv \Delta_{\text{UTe}_2} i(\mathbf{d}\cdot\boldsymbol{\sigma})\sigma_2$. H_{T} is the tunneling Hamiltonian between the

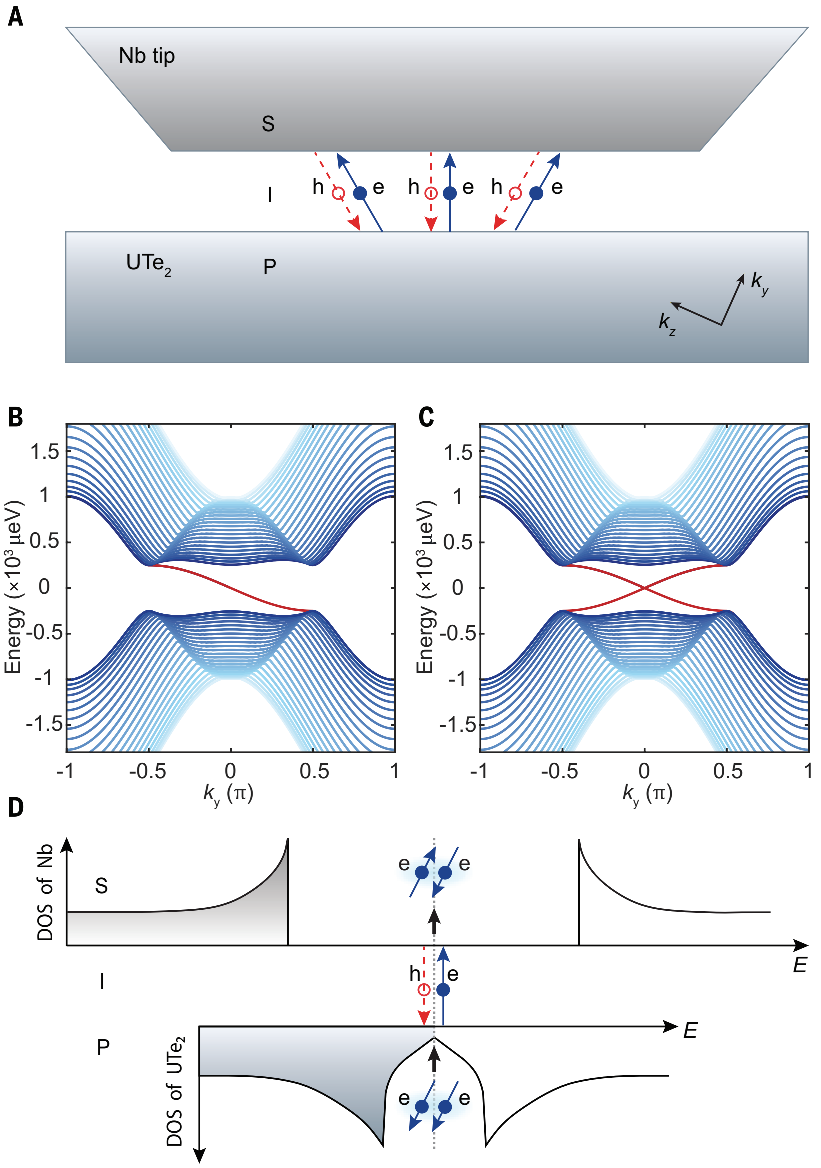

Fig. 2. SIP model: Interfacial quasiparticle TSB between p-wave and s-wave electrodes. (**A**) Schematic SIP model for interface between an s-wave electrode ("S") and a p-wave superconductor ("P") separated by an interface ("I"), containing the TSB on the surface of the p-wave superconductor. There is a variable tunneling matrix element $|M|$ between them, where $|M| \sim 1/R$ and R is the junction resistance. This model is designed to characterize a tunnel junction between superconductive Nb (S) scan tip and UTe$_2$ surface (P). Any superconductive TSB quasiparticles existing within the interface undergo Andreev scattering between s-wave and p-wave electrodes. (**B**) Calculated quasiparticle bands within the SIP interface for a chiral, time-reversal symmetry–breaking, p-wave order parameter with $A_u + iB_{3u}$ symmetry (table S2). The Nb electrode has trivial s-wave symmetry. For this plot, k_x is set to zero. Throughout all the calculated band dispersions, the red dispersion lines denote the superconductive TSB. The shading of the blue dispersion lines is used to highlight the low-energy band structure phenomena, which are central to the tunneling process within the SIP interface. (**C**) Calculated quasiparticle bands within the SIP interface for a nonchiral, time-reversal symmetry–conserving, p-wave order parameter with B_{3u} symmetry (table S1). Here the gapless TSB is protected by time-reversal symmetry. The value of k_x in this plot is set to zero. (**D**) Schematic of the zero-energy differential Andreev tunneling conductance $a(V) \equiv dI/dV|_{\mathrm{SIP}}$ to the s-wave electrode. The magnitude of this zero-bias peak in $a(V)$ is determined by the density $N(0)$ of TSB quasiparticle states within the SIP interface, through a two-quasiparticle Andreev scattering process as shown. DOS, density of states.

two superconductors $H_{\mathrm{T}} = -|M|\sum_{\mathbf{k}_\parallel}\left[\psi^*_{\mathrm{Nb},\mathbf{k}_\parallel}\sigma_3 \otimes \sigma_0 \psi_{\mathrm{UTe}_2,\mathbf{k}_\parallel}(\mathbf{k}) + \mathrm{h.c.}\right]$. Further, $\mathbf{k}_\parallel$ is the momentum in the plane parallel to the interface, ψ is the four-component fermion field (eq. S2) localizing on the adjacent planes of the s-wave and p-wave superconductors, and $|M|$ is the tunneling matrix element. To simplify the SIP calculation, $\epsilon_{\mathrm{Nb}}(\mathbf{k})$ and $\epsilon_{\mathrm{UTe}_2}(\mathbf{k})$ are approximated as single bands [section 4 of (*9*)], yet this alters neither the fundamental characteristics of the TSB nor the symmetry properties of the problem, both of which are controlled primarily by the symmetry and topology of $\Delta_{\mathbf{k}}$ [section 4 of (*9*)]. Finally, our simple band structure model $\epsilon_{\mathrm{UTe}_2}(\mathbf{k})$ represents a closed 3D Fermi surface [section 11 of (*9*)] upon which depends the nontrivial topology of $\Delta_{\mathbf{k}}$.

For H_{UTe_2}, we consider two scenarios: (i) chiral pairing state $A_u + iB_{3u}$ with $\mathbf{d}(\mathbf{k}) = \left(0, k_y + ik_z, ik_y + k_z\right)$ and (ii) nonchiral pairing state B_{3u} with $\mathbf{d}(\mathbf{k}) = \left(0, k_z, k_y\right)$. In both examples, the two nodes of $\Delta_{\mathbf{k}}$ lie along the *a* axis, as in Fig. 1A, and we use $\Delta_{\mathrm{UTe}_2} = \frac{1}{5}\Delta_{\mathrm{Nb}}$. First, for $|M| = 0$, we solve the spectrum of H_{UTe_2} exactly. Figure 2B shows the quasiparticle eigenstates $E(k_x = 0, k_y)$ plotted versus k_y for the chiral order

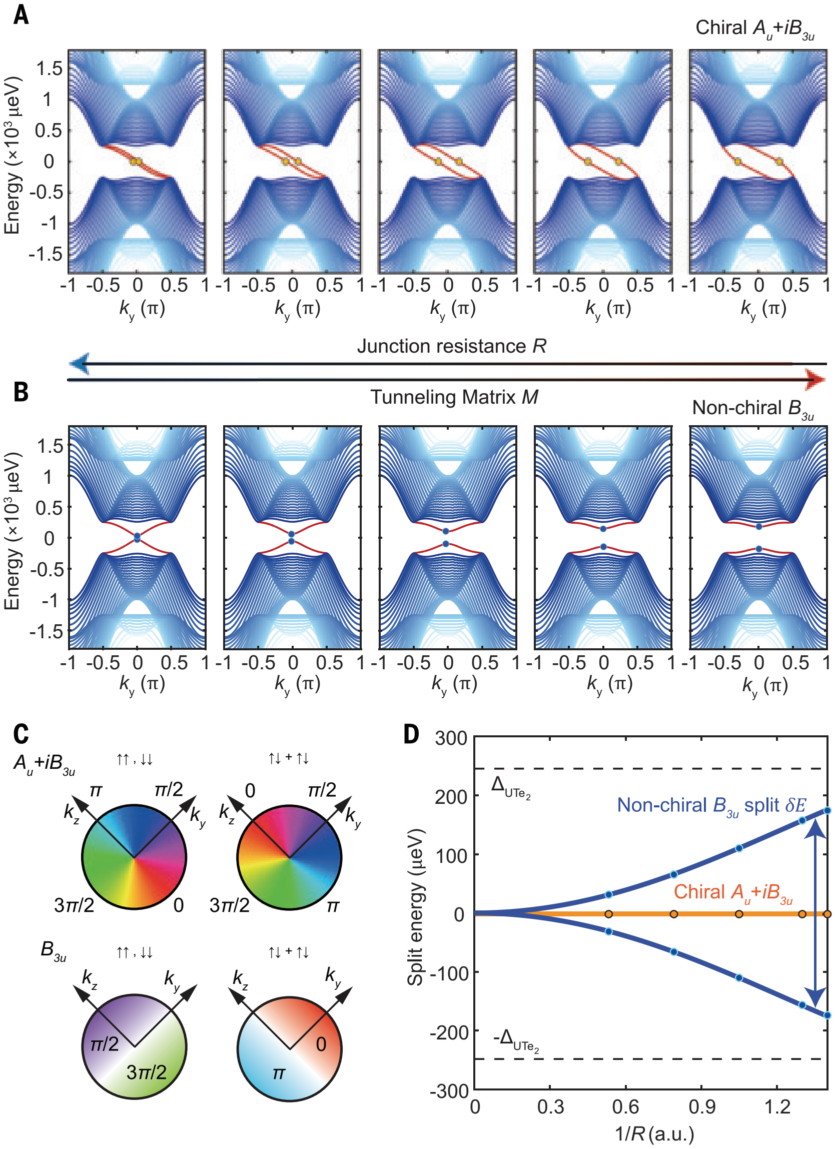

Fig. 3. Order parameter–specific TSB effects with enhanced tunneling. (**A**) Calculated quasiparticle bands within the SIP interface between Nb and UTe_2 with $\delta\phi = \pi/2$ as a function of tunneling matrix element $|M|$. Here the chiral order parameter has $A_u + iB_{3u}$ symmetry. As $|M|\rightarrow 0$ and $R\rightarrow\infty$, the chiral TSB crosses $E = 0$. With increasing $|M|$ (diminishing R), the effect of the s-wave electrode in the SIP model generates two chiral TSBs inside the UTe_2 superconducting gap for all $E < \Delta_{UTe_2}$, meaning that the zero-energy $dI/dV|_{SIP}$ peak will be virtually unperturbed (the points where the TSB crosses $E = 0$ are indicated by orange circles). (**B**) As in (A), but with a nonchiral TSB that also crosses $E = 0$. With increasing $|M|$ (diminishing R), the effect of the s-wave electrode splits the quasiparticle bands into two (the split is indicated by blue circles), neither of which crosses $E = 0$. This key observation means that the zero-energy $a(0) = dI/dV|_{SIP}$ Andreev conductance peak must split into two particle-hole symmetric maxima separating as $|M|$ is increased. (**C**) Examples of possible order parameter **k**-space phase evolution for UTe_2 as used in (A) and (B). Top panel shows the equatorial ($k_x = 0$) complex phase values of $\Delta_{\mathbf{k}}$ and spin-triplet configurations for chiral order parameter $A_u + iB_{3u}$ (table S2). Bottom panel shows the equatorial ($k_x = 0$) values of $\Delta_{\mathbf{k}}$ and spin-triplet configurations for nonchiral order parameter B_{3u} (table S1). The chiral $A_u + iB_{3u}$ order parameter has a continuous phase winding, in contrast to the discontinuous phase change in the B_{3u} order parameter. (**D**) Calculated energy splitting δE of the zero-energy $a(0) = dI/dV|_{SIP}$ Andreev conductance peak as a function of tunneling matrix element $|M| \sim 1/R$. The δE is zero for $A_u + iB_{3u}$ (orange) at all tunneling matrices $|M|$. However, δE increases as a function of $|M| \sim 1/R$ for a B_{3u} (blue) order parameter, within the SIP model shown in Fig. 2A. The orange circles correspond to the predicted TSB crossing points in (A). The blue circles correspond to the predicted TSB termination points in (B).

parameter with $A_u + iB_{3u}$ symmetry: A chiral TSB spans the full energy range $-\Delta_{UTe_2} \le E \le \Delta_{UTe_2}$, crossing the Fermi level ($E = 0$) and generating a finite density of quasiparticle states $N\left(|E| < \Delta_{UTe_2}\right)$. Similarly, Fig. 2C shows the quasiparticle spectrum versus k_y at $k_x = 0$ for a nonchiral order parameter with B_{3u} symmetry: two nonchiral TSBs span $-\Delta_{UTe_2} \le E \le \Delta_{UTe_2}$, and feature $E = 0$ states generating a finite $N\left(|E| < \Delta_{UTe_2}\right)$. Although these TSBs have dispersion in both the positive and negative k_y directions and can backscatter, their gaplessness is protected by time-reversal symmetry with $T^2 = -I$. Hence, solely on the basis of $N\left(|E| < \Delta_{UTe_2}\right)$ of the TSB, one cannot discriminate between the two symmetries of $\Delta_{\mathbf{k}}$.

Instead, we explored how to distinguish a chiral from a nonchiral $\Delta_{\mathbf{k}}$ by using scanned Andreev tunneling microscopy and spectroscopy. Specifically, within the SIP model, we calculated the Andreev conductance $a(V) = dI/dV|_{SIP}$ between Nb and UTe_2 using the nonchiral TSB and demonstrated that a sharp $a(V)$ peak should occur surrounding zero bias [section 7 of (9)]. Because the TSB quasiparticles subtending this peak are protected by time-reversal symmetry and because Andreev reflection of TSB quasiparticles allows efficient transfer of charge $2e$ across the junction, the peak's sharpness is robust. This makes scanned Andreev tunneling spectroscopy an ideal approach for studying superconductive topological surface bands in ITS.

Depending on whether UTe_2 is hypothesized as a chiral or nonchiral superconductor, the TSB quasiparticles are themselves chiral (Fig. 2B) or nonchiral (Fig. 2C). As the tunneling matrix element to the s-wave electrode $|M| \rightarrow 0$, these phenomena are indistinguishable, but as $|M|$ increases, the wave functions of Nb overlap those of UTe_2, allowing detection of the TSB quasiparticles at the s-wave electrode. Figure 3A shows the predicted quasiparticle bands within the SIP interface for $A_u + iB_{3u}$ symmetry (Fig. 3C) versus increasing $|M|$ [sections 4 and 5 of (9)]. With increasing $|M| \sim 1/R$, where R is the SIP tunnel junction resistance, the proximity effect of the s-wave electrode generates two chiral TSBs for all $|E| < \Delta_{UTe_2}$, both of which cross $E = 0$. Hence, for the chiral $\Delta_{\mathbf{k}}$, the zero-energy $N(E)$ will be virtually unperturbed by increasing $|M|$. Equivalently, Fig. 3B presents the TSB of quasiparticles within the SIP interface as a function of $|M|$ for the nonchiral order parameter with B_{3u} symmetry (Fig. 3C). When $|M| \rightarrow 0$, the nonchiral TSB crosses $E = 0$. But with increasing $|M| \sim 1/R$, time-reversal symmetry breaking due to the s-wave electrode splits the TSB of the quasiparticles into two, neither of which cross $E = 0$. This reveals that the $N(0)$ peak must split as the zero-energy quasiparticles of the TSB disappear, generating two particle-hole symmetric $N(E)$ maxima at finite energy. The pivotal concept is thus: Whereas the chiral TSB in Fig. 2B requires no symmetry to protect it, the nonchiral TSB of

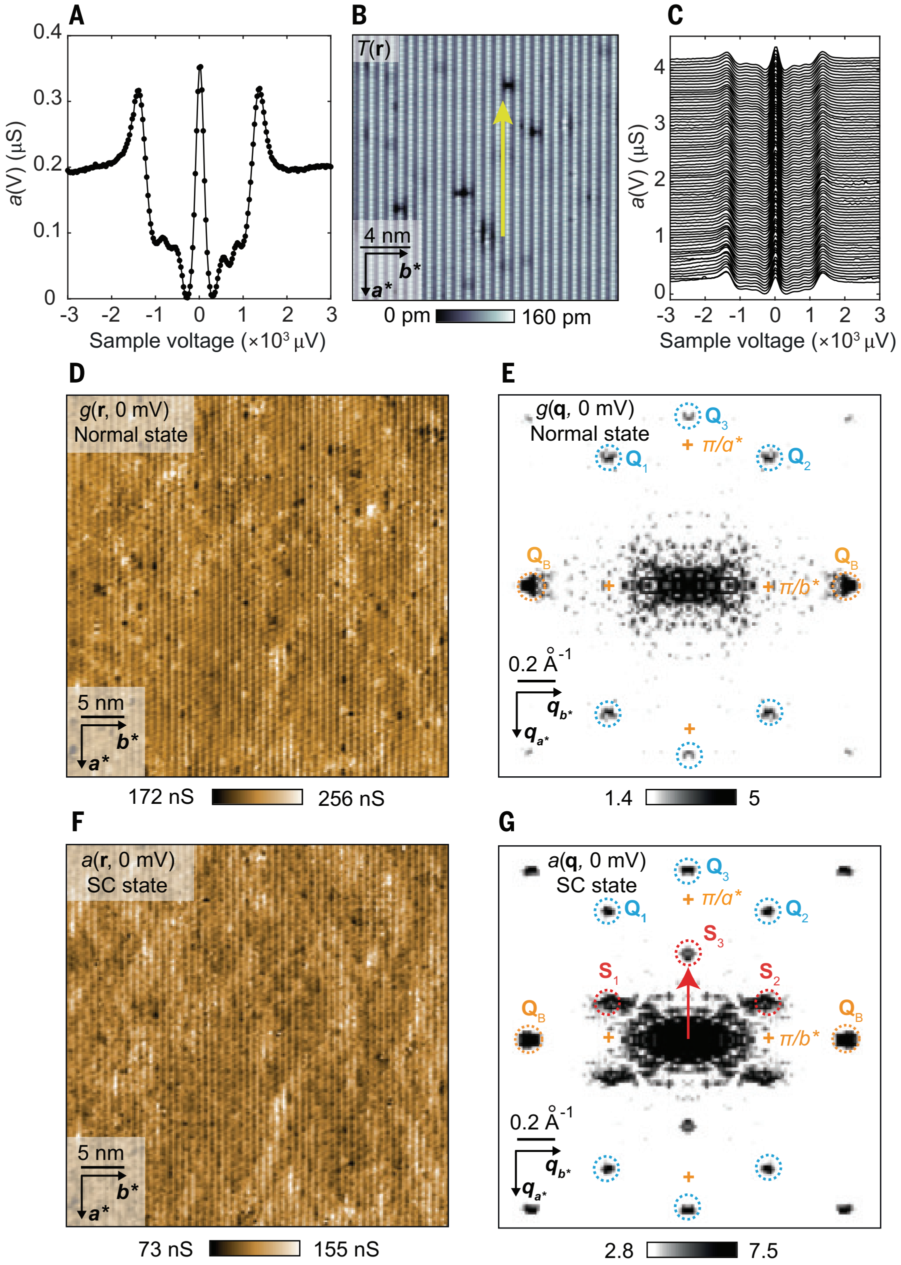

Fig. 4. Discovery of Andreev conductance spectrum $a(V)$ for Nb/UTe_2 tunneling. (**A**) Typical SIP Andreev conductance spectrum $a(V) \equiv dI/dV|_{SIP}$ measured with a Nb scan tip on UTe_2 (0-11) surface for junction resistance $R = 6$ megohms and $T = 280$ mK. A high-intensity zero-bias $dI/dV|_{SIP}$ peak is detected. (**B**) Typical topographic image $T(\mathbf{r})$ of (0-11) surface ($I_s = 0.2$ nA, $V_s = 5$ mV). (**C**) Evolution of measured $a(\mathbf{r}, V)$ across the (0-11) surface of UTe_2 indicated by the yellow arrow in (B) for junction resistance $R = 6$ megohms and $T = 280$ mK. The zero-bias $dI/dV|_{SIP}$ peaks are universal and robust, indicating that the zero-energy ABS is omnipresent. (**D**) Measured $g(\mathbf{r}, 0)$ at $T = 4.2$ K in the normal state of UTe_2. (**E**) Measured $g(\mathbf{q}, 0)$ is the Fourier transform of $g(\mathbf{r}, 0)$ in (D). (**F**) Superconductive tip–measured $a(\mathbf{r}, 0)$ at $T = 280$ mK in the UTe_2 superconducting state. This image introduces visualization of the spatial configurations of a zero-energy TSB at the surface of UTe_2. (**G**) Superconductive tip–measured $a(\mathbf{q}, 0)$ at $T = 280$ mK in UTe_2: the Fourier transform of $a(\mathbf{r}, 0)$ in (F). Three specific new incommensurate scattering wave vectors, $\mathbf{S}_1$, $\mathbf{S}_2$, and $\mathbf{S}_3$, are indicated by red circles.

Fig. 2C will open a gap if time-reversal symmetry is broken. This occurs because the SIP model for a nonchiral $\Delta_{\mathbf{k}}$ (Fig. 2C) predicts strong $|M|$ locking of the relative phase $\delta\phi$ between the two superconductors at $\delta\phi = \pi/2$ to minimize the total energy of the SIP junction [sections 4 and 5 of (*9*)], thus breaking time-reversal symmetry. Conversely, the value of $\delta\phi$ is irrelevant for a chiral $\Delta_{\mathbf{k}}$ (Fig. 2B) because the TSB at the interface remains gapless for any $\delta\phi$ (i.e., the chiral TSB requires no symmetry to protect it). Figure 3D shows the quantitatively predicted splitting of $N(0)$ into two particle-hole symmetric $N(E)$ maxima as a function of $|M|$ for a chiral $\Delta_{\mathbf{k}}$ (orange) and for a nonchiral $\Delta_{\mathbf{k}}$ (blue), within the SIP model of Fig. 2A [sections 4 and 5 of (*9*)]. The decisive fact revealed by this SIP model for Andreev tunneling between an s-wave electrode and a p-wave topological superconductor through the latter's TSB, is that a nonchiral pairing state can be clearly distinguished from a chiral pairing state.

Zero-energy Andreev conductance peak in UTe$_2$

To search for such phenomena, UTe$_2$ samples were introduced to a superconductive-tip (*38*–*43*) scanning tunneling microscope, cleaved at 4.2 K in cryogenic ultrahigh vacuum, inserted to the scan head, and cooled to $T = 280$ mK. A typical topographic image $T(\mathbf{r})$ of the (0-11) cleave surface as measured by a superconductive Nb tip is shown in section 8 of (*9*) with atomic periodicities defined by vectors $\mathbf{a}^*$, $\mathbf{b}^*$, where $\mathbf{a}^* = \mathbf{a} = 4.16$ Å is the $\hat{x}$-axis unit-cell vector and $\mathbf{b}^* = 7.62$ Å is a vector in the $\hat{y}:\hat{z}$ plane. As the temperature is reduced, several peaks appear within the overall energy gap; these are clear characteristics of the UTe$_2$ surface states because when the tip is traversed across an adsorbed (non-UTe$_2$) metal cluster, the subgap peaks disappear [section 8 of (*9*)]. Most notably, for Nb scan tips on the atomically homogeneous (0-11) UTe$_2$ surface, a sharp zero-energy peak appears in the spectrum as shown in Fig. 4A. This robust zero-bias $dI/dV|_{\mathrm{SIP}}$ peak is observed universally, as exemplified, for example, by Fig. 4, B and C. These phenomena are not due to Josephson tunneling, because the zero-bias conductance $a(0)$ of Nb/UTe$_2$ is orders of magnitude larger than it could possibly be owing to Josephson currents through the same junction, and because $a(0)$ grows linearly with falling R before diminishing steeply as R is further reduced, whereas $g(0)$, because of Josephson currents, should grow continuously as $1/R^2$ [section 8 of (*9*)]. Moreover, the SIP model predicts quantitatively that such an intense $a(0)$ peak should occur if UTe$_2$ $\Delta_{\mathbf{k}}$ supports a TSB within the interface (Fig. 2A) and because Andreev transport, owing to its quasiparticles, allows zero-bias conductance to the Nb electrode [Fig. 2D and section 7 of (*9*)].

This discovery provides an excellent opportunity to explore the TSB quasiparticles of a nodal odd-parity superconductor. To do so, we focused on a 44 nm by 44 nm field of view (FOV) and, for comparison, first imaged conventional differential conductance at zero-bias $g(\mathbf{r}, 0)$ at $T = 4.2$ K in the normal state of UTe$_2$ as shown in Fig. 4D. The normal-state QPI signature $g(\mathbf{q}, 0)$ shown in Fig. 4E, is found from Fourier transform of $g(\mathbf{r}, 0)$ in Fig. 4D. Next, Andreev differential conductance $a(\mathbf{r}, V) \equiv dI/dV|_{\mathrm{SIP}}(\mathbf{r}, V)$ measurements using a superconductive Nb tip were carried out in the identical FOV at $T = 280$ mK, deep in the UTe$_2$ superconducting state [Fig. 4F and section 10 of (*9*)]. Note that $a(\mathbf{r}, V)$ represents a two-electron process and is thus not simply proportional to the density of TSB quasiparticle states $N(\mathbf{r}, E)$ but, instead, to the Andreev conductance. Our $a(\mathbf{r}, 0)$ imaging was then carried out in bias-voltage range $V = 0 \pm 150$ μV inside the $dI/dV|_{\mathrm{SIP}}$ peak (Fig. 4A). Such images introduce atomic-scale visualization of zero-energy quasiparticles of a superconductive TSB. The Andreev QPI signature $a(\mathbf{q}, 0)$ of these zero-energy quasiparticles is shown in Fig. 4G. Here, three new scattering wave vectors—$\mathbf{S}_1$, $\mathbf{S}_2$, and $\mathbf{S}_3$—are indicated by red circles. Because $\mathbf{S}_3$ exists only in the superconducting state and only for $|E| \lesssim 150$ μeV, it cannot be attributed to any new charge-ordered state [section 10 of (*9*)] but is generated by TSB quasiparticles. And,

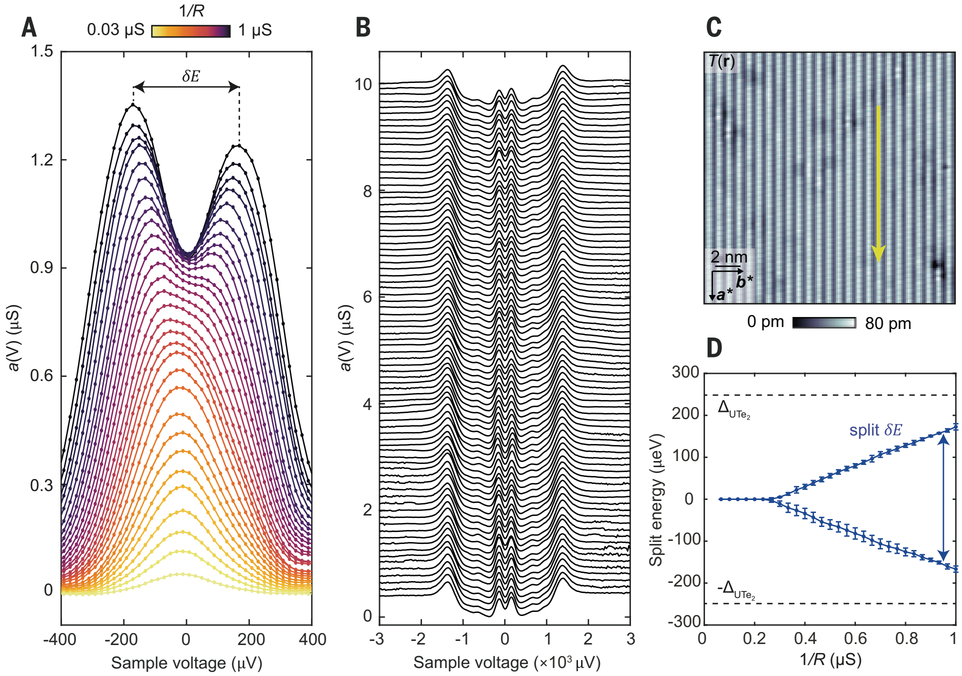

Fig. 5. Evolution and splitting of *a*(*V*) peak with enhanced s-wave hybridization. (**A**) Measured evolution of $a(V) \equiv dI/dV|_{\mathrm{SIP}}$ at $T = 280$ mK in UTe$_2$ as a function of decreasing junction resistance R (i.e., decreasing the tip-sample distance) and thus increasing tunneling matrix element $|M| \sim 1/R$. The $a(V)$ spectra start to split when the junction resistance falls below $R \sim 5$ megohms. (**B**) Evolution of measured $a(\mathbf{r}, V)$ splitting across the (0-11) surface of UTe$_2$ along the yellow arrow indicated in (C), at junction resistance $R = 3$ megohms and $T = 280$ mK, demonstrating that $a(\mathbf{r}, V)$ split peaks are pervasive at low junction resistance R and high tunneling matrix $|M|$. (**C**) Topographic image $T(\mathbf{r})$ of (0-11) surface ($I_s = 0.2$ nA, $V_s = 3$ mV, $T = 280$ mK) showing the trajectory of the $a(\mathbf{r}, V)$ spectra that demonstrate the universality of $a(V)$ splitting in (B). (**D**) Measured energy splitting of $a(V)$ at $T = 280$ mK in UTe$_2$ versus $1/R$. These data may be compared with predictions of $a(V)$ splitting within the SIP model for $A_u + iB_{3u}$ and B_{3u} order parameters of UTe$_2$ (Fig. 3D).

because a closed Fermi surface has been hypothesized for UTe_2 from both angle-resolved photoemission and quantum oscillation research (*44*–*46*), $\mathbf{S}_3$ is not inconsistent with an a-axis internodal scattering wave vector on such a Fermi surface.

Nature of the UTe_2 superconductive order parameter $\Delta_\mathbf{k}$

Finally, to determine spectroscopically whether the UTe_2 order parameter is chiral, we measured the evolution of Andreev conductance $a(V)$ at $T = 280$ mK as a function of decreasing junction resistance R or equivalently increasing tunneling matrix element $|M|$. Figure 5A shows clearly the strong energy splitting δE observable in $a(V)$, which first appears and then evolves with increasing $1/R$. Figure 5B shows the measured $a(\mathbf{r}, V)$ splitting across the (0-11) surface of UTe_2 along the yellow arrow indicated in Fig. 5C for $R = 3$ megohms, demonstrating that $a(\mathbf{r}, V)$ split peaks are pervasive. Decisively, from measurements in Fig. 5A, we plotted in Fig. 5D the measured δE between peaks in $a(\mathbf{r}, V)$ at $T = 280$ mK versus $1/R$. On the basis of predictions for energy splitting δE within the SIP model presented in Fig. 3D for chiral $\Delta_\mathbf{k}$ (Fig. 3A) and nonchiral $\Delta_\mathbf{k}$ (Fig. 3B), a chiral $\Delta_\mathbf{k}$ appears to be ruled out. However, here we note that the SIP model assumes a planar junction with translational invariance parallel to the interface: This implies mirror symmetry ($k_x \rightarrow -k_x$), which the STM tip could break, compromising the protection of the nonchiral state and splitting a zero-bias peak [section 6 of (*9*)]. Nonetheless, as a chiral TSB is symmetry independent, our conclusion holds: Splitting of the zero-bias Andreev conductance peak indicates nonchiral pairing in UTe_2.

Thus, the chiral order parameters $A_u + iB_{1u}$ and $B_{3u} + iB_{2u}$ proposed for UTe_2 seem inapplicable because of the observed Andreev conductance $a(0)$ splitting (Fig. 5A). Within the four possible odd-parity time-reversal–preserving symmetries, A_u, B_{1u}, B_{2u}, and B_{3u}, the isotropic A_u order parameter appears insupportable because its TSB is a Majorana cone of Bogoliubons with zero density of states at zero energy (*7*), meaning that Andreev conductance $a(0)$ would be highly suppressed. Among the remaining three possible order parameters, B_{1u}, B_{2u}, and B_{3u}, all should exhibit the Andreev conductance $a(0)$ splitting that is observed. However, if the $\mathbf{S}_3$ modulations are due to a-axis internodal scattering, then the B_{3u} state is favored because its nodes occur along the a axis.

Discussion and outlook

Modeling Andreev conductance from an s-wave superconductor through the intervening TSB of an intrinsic topological superconductor reveals a zero-energy Andreev conductance maximum at surfaces parallel to the nodal axis. Further, splitting of this Andreev conductance peak owing to proximity of an s-wave superconductor signifies a 3D ITS, with $\Delta_\mathbf{k}$ preserving time-reversal symmetry. Although the B_{1u}, B_{2u}, or B_{3u} states could all be consistent with such a phenomenology, should the $a(\mathbf{r}, 0)$ modulations at wave vector $\mathbf{S}_3$ result from a axis–oriented energy-gap nodes, then the complete experimental data imply that $\Delta_\mathbf{k}$ of UTe_2 is in the B_{3u} state. Future experiments using energy-resolved quasiparticle interference imaging of the TSB may explore this premise even more directly. Most generally, use of SIP Andreev conductance spectroscopy for quasiparticle surface band detection and $\Delta_\mathbf{k}$ symmetry determination opens new avenues for discovery and exploration of 3D intrinsic topological superconductors.

REFERENCES AND NOTES

1. M. R. Norman, *Science* **332**, 196–200 (2011).
2. P. W. Anderson, P. Morel, *Phys. Rev.* **123**, 1911–1934 (1961).
3. R. Balian, N. R. Werthamer, *Phys. Rev.* **131**, 1553–1564 (1963).
4. D. Vollhardt, P. Woelfle, *The Superfluid Phases of Helium 3* (Taylor & Francis, 1990).
5. A. J. Leggett, *Quantum Liquids: Bose Condensation and Cooper Pairing in Condensed-Matter Systems* (Oxford Univ. Press, 2006).
6. A. P. Schnyder, S. Ryu, A. Furusaki, A. W. W. Ludwig, *Phys. Rev. B* **78**, 195125 (2008).
7. A. P. Schnyder, P. M. R. Brydon, *J. Phys. Condens. Matter* **27**, 243201 (2015).
8. C. Kallin, J. Berlinsky, *Rep. Prog. Phys.* **79**, 054502 (2016).
9. Supplementary materials.
10. D. Aoki *et al.*, *J. Phys. Soc. Jpn.* **88**, 043702 (2019).
11. S. Ran *et al.*, *Science* **365**, 684–687 (2019).
12. D. Aoki *et al.*, *J. Phys. Condens. Matter* **34**, 243002 (2022).
13. P. F. S. Rosa *et al.*, *Commun. Mater.* **3**, 33 (2022).
14. Y. Tokunaga *et al.*, *J. Phys. Soc. Jpn.* **88**, 073701 (2019).
15. G. Nakamine *et al.*, *J. Phys. Soc. Jpn.* **88**, 113703 (2019).
16. H. Sakai *et al.*, *Phys. Rev. Mater.* **6**, 073401 (2022).
17. H. Matsumara *et al.*, *J. Phys. Soc. Jpn.* **92**, 063701 (2023).
18. H. Fujibayashi *et al.*, *J. Phys. Soc. Jpn.* **91**, 043705 (2022).
19. T. Metz *et al.*, *Phys. Rev. B* **100**, 220504(R) (2019).
20. S. Suetsugu *et al.*, *Sci. Adv.* **10**, eadk3772 (2024).
21. S. Kittaka *et al.*, *Phys. Rev. Res.* **2**, 032014(R) (2020).
22. I. M. Hayes *et al.*, *Science* **373**, 797–801 (2021).
23. L. P. Cairns, C. R. Stevens, C. D. O'Neill, A. Huxley, *J. Phys. Condens. Matter* **32**, 415602 (2020).
24. Y. Iguchi *et al.*, *Phys. Rev. Lett.* **130**, 196003 (2023).
25. K. Ishihara *et al.*, *Nat. Commun.* **14**, 2966 (2023).
26. L. Jiao *et al.*, *Nature* **579**, 523–527 (2020).
27. M. O. Ajeesh *et al.*, *Phys. Rev. X* **13**, 041019 (2023).
28. J. E. Hoffman *et al.*, *Science* **297**, 1148–1151 (2002).
29. T. Hanaguri *et al.*, *Physica C* **460**, 954–955 (2007).
30. M. P. Allan *et al.*, *Nat. Phys.* **9**, 468–473 (2013).
31. M. P. Allan *et al.*, *Science* **336**, 563–567 (2012).
32. P. O. Sprau *et al.*, *Science* **357**, 75–80 (2017).
33. R. Sharma *et al.*, *Proc. Natl. Acad. Sci. U.S.A.* **117**, 5222–5227 (2020).
34. Q. Gu *et al.*, *Nature* **618**, 921–927 (2023).
35. A. Aishwarya *et al.*, *Nature* **618**, 928–933 (2023).
36. S. Bae *et al.*, *Nat. Commun.* **12**, 2644 (2021).
37. Q. H. Wang, D. H. Lee, *Phys. Rev. B* **67**, 020511(R) (2003).
38. M. H. Hamidian *et al.*, *Nature* **532**, 343–347 (2016).
39. D. Cho, K. M. Bastiaans, D. Chatzopoulos, G. D. Gu, M. P. Allan, *Nature* **571**, 541–545 (2019).
40. X. Liu, Y. X. Chong, R. Sharma, J. C. Davis, *Science* **372**, 1447–1452 (2021).
41. X. Liu, Y. X. Chong, R. Sharma, J. C. S. Davis, *Nat. Mater.* **20**, 1480–1484 (2021).
42. S. M. O'Mahony *et al.*, *Proc. Natl. Acad. Sci. U.S.A.* **119**, e2207449119 (2022).
43. W. Chen *et al.*, *Proc. Natl. Acad. Sci. U.S.A.* **119**, e2206481119 (2022).
44. S. Fujimori *et al.*, *J. Phys. Soc. Jpn.* **88**, 103701 (2019).
45. L. Miao *et al.*, *Phys. Rev. Lett.* **124**, 076401 (2020).
46. C. Broyles *et al.*, *Phys. Rev. Lett.* **131**, 036501 (2023).
47. Q. Gu, Pair Wave Function Symmetry in UTe_2 from Zero-Energy Surface State Visualization [Data set], version 2, Zenodo (2025); https://doi.org/10.5281/zenodo.15021425.

ACKNOWLEDGMENTS

We acknowledge and thank M. Aprili, C. Bena, J. E. Hoffman, E.-A. Kim, S. Kivelson, A. P. Mackenzie, V. Madhavan, and C. Pepin for key discussions and guidance. **Funding:** Research at the University of Maryland was supported by the US Department of Energy award DE-SC-0019154 (sample characterization), the Gordon and Betty Moore Foundation's EPiQS Initiative through grant GBMF9071 (materials synthesis), NIST, and the Maryland Quantum Materials Center. Research at Washington University in St. Louis was supported by National Science Foundation (NSF) Division of Materials Research award DMR-2236528. S.W. and J.C.S.D. acknowledge support from the European Research Council (ERC) under award DLV-788932. X.L. acknowledges support from the Department of Energy (DE-SC0025021). Q.G., S.W., J.P.C., and J.C.S.D. acknowledge support from the Moore Foundation's EPiQS Initiative through grant GBMF9457. J.C.S.D. acknowledges support from the Royal Society under award R64897. J.P.C., K.Z., and J.C.S.D. acknowledge support from Science Foundation Ireland under award SFI 17/RP/5445. D.-H.L. was supported by the US Department of Energy, Office of Science, Basic Energy Sciences, Materials Sciences and Engineering Division, contract DE-AC02-05-CH11231, within the Quantum Materials Program (KC2202). **Author contributions:** D.-H.L. and J.C.S.D. conceived of and supervised the project. S.R., C.B., S.S., J.A.H., N.P.B., and J.P. developed, synthesized, and characterized materials; D.-H.L. provided the theoretical motivation and the SIP model; Q.G., S.W., J.P.C., K.Z., and X.L. carried out the experiments; Q.G., S.W., K.Z., and J.P.C. developed and implemented the analysis. J.C.S.D. and D.-H.L. wrote the paper, with key contributions from S.W., Q.G., K.Z., J.P.C., and X.L. The paper reflects contributions and ideas of all authors. Conceptualization: J.C.S.D., D.-H.L., Q.G.; Methodology: J.C.S.D., D.-H.L., Q.G.; Materials: S.R., C.B., S.S., J.A.H., N.P.B., J.P.; Investigation: Q.G., S.W., J.P.C., K.Z.; Visualization: Q.G., S.W., J.P.C., K.Z.; Funding acquisition: J.C.S.D., J.P., D.H.L.; Project administration: J.C.S.D.; Supervision: J.C.S.D., D.H.L.; Writing – original draft: J.C.S.D., D.-H.L.; Writing – review & editing: J.C.S.D., D.-H.L., S.W., K.Z., J.P.C., X.L., Q.G. **Competing interests:** The authors declare that they have no competing interests. **Data and materials availability:** All data are available in the main text, the supplementary materials, and in Zenodo (*47*). **License information:** Copyright © 2025 the authors, some rights reserved; exclusive licensee American Association for the Advancement of Science. No claim to original US government works. https://www.science.org/about/science-licenses-journal-article-reuse

SUPPLEMENTARY MATERIALS

science.org/doi/10.1126/science.adk7219
Materials and Methods; Supplementary Text; Figs. S1 to S8; Tables S1 and S2;
References (*48*–*54*)

Submitted 15 September 2023; resubmitted 1 February 2024; accepted 2 April 2025

10.1126/science.adk7219

Testing interelectronic interaction in lithium-like tin

Jonathan Morgner*, Vladimir A. Yerokhin, Charlotte M. König, Fabian Heiße, Bingsheng Tu†, Tim Sailer, Bastian Sikora, Zoltán Harman, José R. Crespo López-Urrutia, Christoph H. Keitel, Sven Sturm, Klaus Blaum

Magnetic moments of bound-electron systems are a sensitive tool for testing fundamental interactions. The g factors of lithium-like ions have been rigorously studied in recent years, enabling insights into the relativistic interelectronic effects. In this work, we present the g-factor measurement of lithium-like tin, accurate to 0.5 parts per billion, as well as ab initio theoretical calculations that include an advanced treatment of the interelectronic interaction. We further improved the prediction by using the experimental result for the hydrogen-like tin g factor, inferring from it the unknown higher-order quantum electrodynamic (QED) effects. The observed agreement independently confirms the revised theory at a previously inaccessible high atomic number Z of 50, where QED effects are considerably larger.

Quantum electrodynamics (QED) is the fundamental theory describing the electromagnetic interaction of charged particles by exchange of photons. It includes nonclassical effects such as vacuum polarization and the electron's self-energy. Such effects have been studied in a wide variety of systems (*1–6*), subjecting the QED framework to rigorous scrutiny. Recently, the magnetic properties of lithium-like ions have raised interest both in experimental (*7–11*) and theoretical research (*12–16*). These ions are in many respects similar to hydrogen-like systems but are substantially richer because of the interaction not only between the electron and the nucleus but also among the electrons. Nonetheless, their configuration is still simple, with a single 2s electron above a tightly bound $1s^2$ shell. This makes the electron-electron interaction tractable within the QED theory so that theoretical predictions can still challenge experiments to match their precision. Even more advantageous is to measure both the lithium-like and the hydrogen-like charge states of the same element, which allows the theory to be enhanced further by eliminating unknown contributions that are correlated in different electronic configurations. As a result, the comparison of theory and experiment for a combination of the lithium-like and the hydrogen-like charge states is capable of yielding enhanced tests of bound-state QED (*17*) and possibly, in the future, an improved determination of the fine-structure constant (*18*), as well as placing stringent bounds on the coupling constants of beyond Standard Model interactions (*19*).

Ab initio QED calculations of the g factor of lithium-like ions are very cumbersome and have proved to be problematic in the past. In particular, several advanced QED calculations (*13*, *14*, *20*) reported up to five standard deviations from the experimental data on lithium-like silicon (atomic number $Z = 14$) and calcium ($Z = 20$). Recently, a careful reanalysis of the interelectronic QED effects in (*15*) found agreement with the calcium experiment and a deviation of only 1.5σ for silicon. However, it will remain unclear whether the problem was fully resolved until a test of theory with a new measurement, ideally on a lithium-like ion with a higher Z, is accomplished.

In this work, we report on a high-precision g-factor measurement of the much heavier lithium-like system $^{118}\mathrm{Sn}^{47+}$, accompanied with its ab initio QED calculation. The nuclear charge of tin with $Z = 50$ and, correspondingly, the nuclear electric field are much higher than in the previous g-factor measurements, testing the QED theory of bound states in a very different regime.

QED theory of the lithium-like tin g factor

In ab initio bound-state QED theory, the g factor of the lithium-like ion arises in the zeroth order from the interaction of the spin of the 2s valence electron with the external magnetic field. This explains why it is numerically close to that of the free electron g_e, which is known with great accuracy both experimentally and theoretically (*5*, *21*). Therefore, we focused here on the so-called binding effects, which result from the interaction with the nucleus and other electrons in the atom. The largest binding contribution follows from the Dirac equation and was analytically described for the point nucleus (pnt) by G. Breit in 1928 (*22*):

$$\delta g_{\mathrm{D}}(\mathrm{pnt}) = \frac{2}{3}\left[\sqrt{2\left(1+\sqrt{1-(Z\alpha)^2}\right)}-2\right] \tag{1}$$

where Z is the atomic number and α is the fine-structure constant. In addition, the g factor receives numerous smaller corrections from QED, the electron-electron interaction, and finite nuclear size (FNS) and mass. The contributions are summarized in Table 1, and the main Feynman diagrams are shown in Fig. 1.

For convenience, we considered two classes of binding effects separately: one-electron contributions induced exclusively by the valence 2s electron and the many-electron corrections caused by the interaction with the other bound electrons. The dominant one-electron QED corrections induced by the one-loop electron self-energy and vacuum polarization have been extensively studied and can be calculated very accurately (*12*, *23*, *24*). The effects of the FNS and mass are also well under control (*25*, *26*). However, the two-loop QED corrections are far more challenging. Despite much attention in recent years (*27–32*), a large part of the two-loop QED effects is calculated only within the $Z\alpha$ expansion. For tin with $Z\alpha \approx 50/137 \approx 0.36$, the expansion is poorly converging and the uncertainty on the two-loop QED contribution is therefore rather large. However, in a previous investigation (*33*), the missing two-loop effects for the 1s state of hydrogen-like tin were isolated experimentally. This allowed us to use the rescaled experimental two-loop QED correction to reduce the uncertainty of the theoretical prediction for the lithium-like ion.

What makes the calculations of the g factor of a lithium-like ion truly challenging is the presence of multiple electrons. An accurate theory of the interelectronic effects in the atomic g factor requires a systematic treatment of the nonlocal electron-electron interaction, which is possible only within QED. The QED perturbation expansion is formulated in terms of Feynman diagrams containing the exchange of one, two, three, and so on virtual photons between the electrons. The resulting multitude of diagrams is divided into two classes: those without radiative loops, called electron-structure corrections, and those with self-energy or vacuum-polarization loops, called QED-screening corrections (see Fig. 1). Rigorous calculations of the two-photon electron-structure and one-photon QED screening diagrams have recently become possible and were carried out without any expansion in the parameter $Z\alpha$ (*13–15*, *20*, *34*). In this work, we refined that approach, leading to improved accuracy. In particular, the numerical precision for the self-energy screening correction for $Z = 14$ and 20 (*15*) has been improved by a factor of 10, which removed one of the dominant errors in the theoretical predictions (see supplementary materials). This improvement was made possible by using a highly

---

Max-Planck-Institut für Kernphysik, Heidelberg, Germany. ***Corresponding author. Email: jonathan.morgner@mpi-hd.mpg.de** †Present address: Institute of Modern Physics, Fudan University, Shanghai, China.

Table 1. Theoretical values. Shown are the binding corrections to the *g* factor of $^{118}\text{Sn}^{47+}$ along with the total theoretical values, with and without the "enhancement" by the experimentally measured two-loop effects (see text).

Effect	Value ($\times\ 10^{-6}$)
Dirac, point nucleus	−23,181.721
Dirac, FNS	2.040(3)
Electron structure	1,192.179 (7)
One-loop QED	23.977(1)
Two-loop QED	−0.107(33)
Two-loop QED , enhanced	−0.080(6)
QED screening	−1.076(8)
Nuclear recoil	0.172(1)
g_e(*5, 21*)	2,002,319.304361
g_{theo}	1,980,354.769(35)
g_{theo} (enh)	1,980,354.797(12)

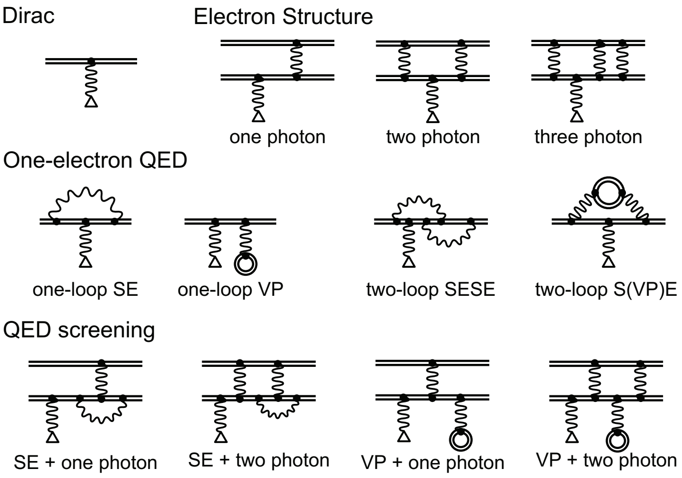

Fig. 1. Main Feynman diagrams describing the *g* factor of a few-electron ion. The double lines denote the bound electrons, the wavy lines represent the virtual photon exchange, and the wavy lines terminated by a triangle indicate the interaction with the external magnetic field. SE, self-energy; VP, vacuum polarization.

accurate Green-function representation of electron propagators and including in it 2.5 times more partial waves than in the previous computation.

With the leading electron structure and QED screening effects accurately calculated, the source of theoretical uncertainty shifts to higher-order interelectronic effects, which presently cannot be calculated rigorously to all orders in $Z\alpha$. The magnitude of these effects has previously been underestimated. These effects were responsible for the deviations of theory and experiment for silicon and calcium (*13*, *14*, *20*), as argued in (*15*), where they applied recursive perturbation theory (*35*) and obtained approximate results for the corresponding corrections for silicon and calcium. In this work, we used the nonrelativistic QED (NRQED) approach to evaluate them to the leading order in $Z\alpha$ with a very high numerical accuracy (supplementary materials).

The crucial point now is to estimate the theoretical uncertainty stemming from the omitted higher-order in $Z\alpha$ interelectronic effects. We did this by varying the zeroth-order approximation, namely by including the so-called screening potential (approximately describing the interaction with core electrons) in the zeroth-order Dirac equation. Our uncertainty estimates are based on the spread of results obtained with different screening potentials; see supplementary text for details.

Adding all the binding effects and the well-established value of the free-electron *g* factor (*5*, *21*), we obtained the total theoretical prediction for the *g* factor of $^{118}\text{Sn}^{47+}$ as

$$g_{\text{theo}} = 1.980\ 354\ 769(35) \tag{2}$$

As can be seen from Table 1, in our calculations we were able to compute the interelectronic effects with the absolute error of 8×10^{-9} so that the dominant theoretical uncertainty now comes from the one-electron two-loop QED effects. This is in sharp contrast to previous measurements of lighter lithium-like ions (*7*, *20*), where the theoretical predictions were limited by the electron-structure effects.

The ab initio prediction (Eq. 2) can be further improved if we use the two-loop QED contribution extracted from the recent measurement of the *g* factor in hydrogen-like tin (*33*) and scale it to the lithium-like electron case. This procedure is similar to the specific difference used to reduce uncertainties from nuclear-size contributions that behave similarly in different charge states of the same element (*36*). Performing the scaling conversion (supplementary materials), we obtained an "experimentally enhanced" theoretical prediction

$$g_{\text{theo}}(\text{enh}) = 1.980\ 354\ 797(12) \tag{3}$$

with three times smaller uncertainty than the purely theoretical value (Eq. 2). Because the problematic higher-order two-loop QED effects are about eight times smaller for the lithium-like ions than for the corresponding hydrogen-like configuration, we achieved in total a relative prediction accuracy of 6×10^{-9}, a 25-fold improvement over the hydrogen-like case.

Experimental measurement of the *g* factor

For the high-precision measurement, the ions are produced externally in an electron beam ion trap, where electrons are stripped from the nucleus by electron impact ionization. The highly charged ions are transported into the ALPHATRAP Penning trap apparatus through a room-temperature beamline. In this case, hydrogen-like tin was captured, and subsequent charge exchange, specifically double electron capture, resulted in lithium-like tin. In the Penning trap, a strong magnetic field $B_0 \approx 4$ T in the ALPHATRAP apparatus confines a single ion to a cyclotron orbit, allowing us to perform nondestructive Penning trap spectroscopy (*37*). The gyromagnetic ratio, or *g* factor of the spin 1/2 particle, is determined by measuring its Larmor precession frequency v_{L} together with B_0; the two quantities are connected by the relation

$$\nu_{\text{L}} = \frac{g}{4\pi}\frac{e}{m_e}B_0 \tag{4}$$

where $\frac{e}{m_e}$ is the electron charge-to-mass ratio. B_0 is measured via the cyclotron frequency $\nu_c = \frac{1}{2\pi}\frac{q}{M}B_0$, where $\frac{q}{M}$ is the charge-to-mass ratio of the ion. Combined, this results in

$$g = 2\,\frac{\nu_{\text{L}}}{\nu_{\text{c}}}\frac{q}{e}\frac{m_e}{M} \tag{5}$$

Therefore, to determine the *g* factor we measured the ratio $\frac{\nu_{\text{L}}}{\nu_c} = \Gamma_0$ and combined it with the literature values for the other parameters (*33*, *38*).

In addition to the magnetic radial confinement, an electrostatic field traps the ion in the axial direction (see Fig. 2A). As a result of the optimized electrode geometry, the ion motion can be described by a close-to-perfect harmonic oscillator within a large region of the trap. Along the magnetic field lines, the ion oscillates with an axial frequency v_z. The $\mathbf{E}\times\mathbf{B}$ drift caused by the applied electric field slightly

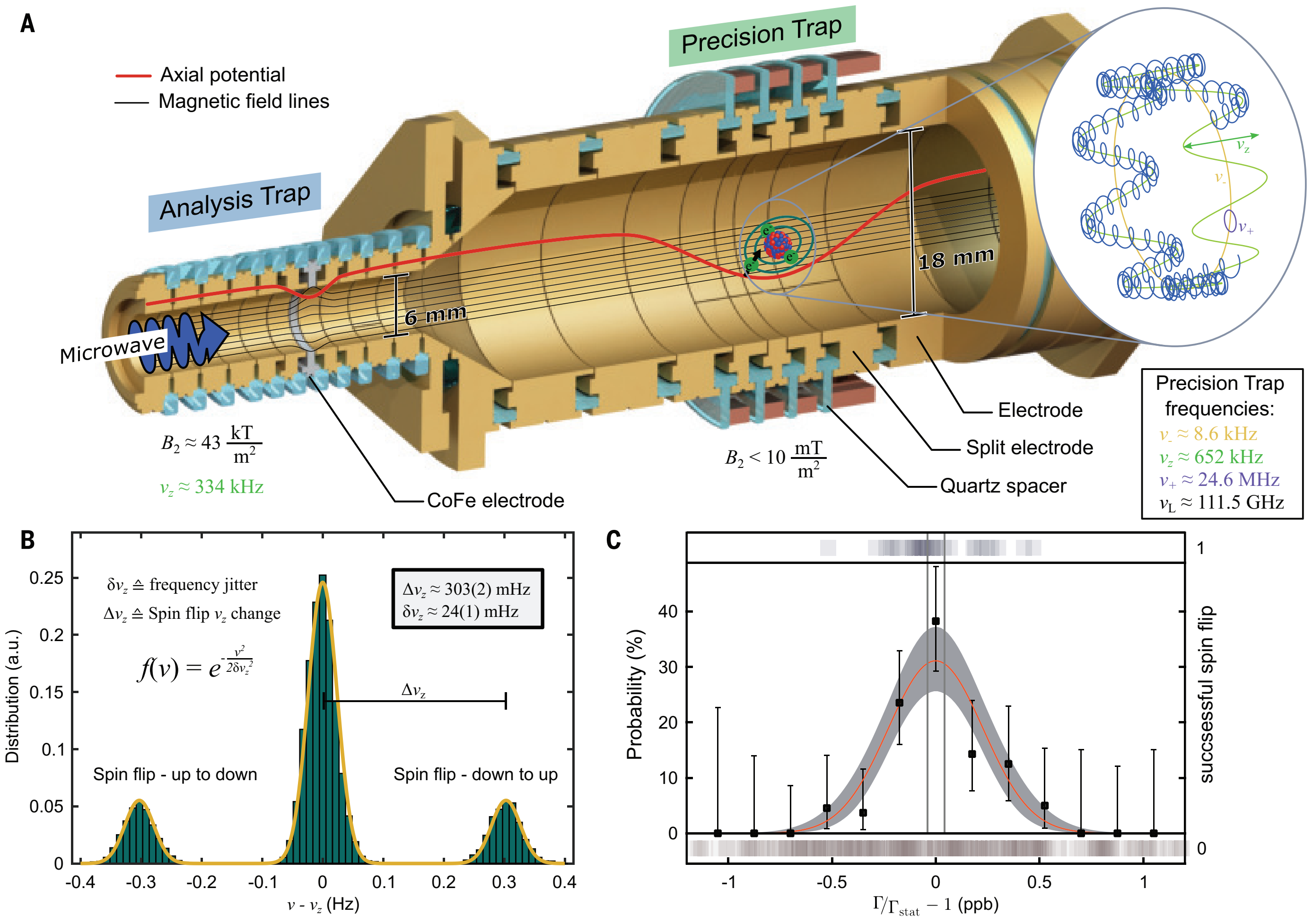
A
Precision Trap
Axial potential
Magnetic field lines
Analysis Trap
Microwave
6 mm
18 mm
ν_z
ν_-
ν_+
$B_2 \approx 43\,\frac{\mathrm{kT}}{\mathrm{m}^2}$
$\nu_z \approx 334$ kHz
CoFe electrode
$B_2 < 10\,\frac{\mathrm{mT}}{\mathrm{m}^2}$
Electrode
Split electrode
Quartz spacer
Precision Trap frequencies:
$\nu_- \approx 8.6$ kHz
$\nu_z \approx 652$ kHz
$\nu_+ \approx 24.6$ MHz
$\nu_L \approx 111.5$ GHz
B
$\delta\nu_z \triangleq$ frequency jitter
$\Delta\nu_z \triangleq$ Spin flip ν_z change
$f(\nu) = e^{-\frac{\nu^2}{2\delta\nu_z^2}}$
$\Delta\nu_z \approx 303(2)$ mHz
$\delta\nu_z \approx 24(1)$ mHz
$\Delta\nu_z$
Spin flip - up to down
Spin flip - down to up
Distribution (a.u.)
0.25
0.2
0.15
0.1
0.05
0
-0.4
-0.3
-0.2
-0.1
0
0.1
0.2
0.3
0.4
$\nu - \nu_z$ (Hz)
C
Probability (%)
40
30
20
10
0
-1
-0.5
0
0.5
1
$\Gamma/\Gamma_{\mathrm{stat}} - 1$ (ppb)
successful spin flip
1
0

Fig. 2. Schematic and results of the experiment. (**A**) The precision measurement takes place in two separate traps, between which the ion is shuttled by adiabatic transport. In the precision trap, the electric field is extremely harmonic and the magnetic field is as homogeneous as possible, which are optimal conditions for precision spectroscopy. In the analysis trap, the center electrode is made of a ferromagnetic material that produces a large magnetic field inhomogeneity, allowing nondestructive detection of the spin state (*40*). (**B**) The frequency data taken in the analysis trap during the *g*-factor measurement. Because the likelihood to drive a spin flip (see main text) is only 50%, no frequency change is observed half of the time. When a spin flip occurs, the frequency is 300 mHz larger or smaller, corresponding to the distributions at +300 mHz and −300 mHz. Based on the direction of the change, the current (and prior) spin orientation is determined. a.u., arbitrary units. (**C**) Fit to the recorded spin-flip data. The resonance consists of 330 individual measurement points, shown at the top and bottom for successful and unsuccessful attempts, respectively. The black scattered dots are a binned set of the data, shown for better visualization. The red line is the fitted curve, and the gray band shows its 1σ confidence interval. The gray vertical lines show the 1σ confidence intervals of Γ_{stat}. ppb, parts per billion.

modifies the frequency of the cyclotron motion, and an additional magnetron motion with frequency v_- appears. The resulting particle trajectory is shown in the inset of Fig. 2A. The three eigenmodes—modified cyclotron, axial, and magnetron—are related to the free-space cyclotron frequency by the invariance theorem, which shows that errors caused by misalignment of the electric and magnetic fields are cancelled, and the motions are connected via the equation $v_c^2 = v_+^2 + v_z^2 + v_-^2$ (*39*). The axial frequency is measured via the femtoampere image current induced in the surrounding electrodes. It is transformed into a measurable voltage by a superconducting tank circuit that interacts with the ions when in resonance, resulting in energy exchange and, consequently, thermalization of the axial motion to the temperature of the detector at 5.7(2) K. In this case, the Fourier spectrum of the detector signal shows a distinct dip at the mode frequency, which can then be determined from fitting. The cyclotron and magnetron frequencies are measured with the same detector using radio-frequency quadrupole fields, which couple the modes. As the frequency hierarchy in a Penning trap is typically $\nu_- \ll \nu_z \ll \nu_+$, v_c is mostly dependent on the frequency v_+ of the modified cyclotron motion. Frequencies of the $^{118}\mathrm{Sn}^{47+}$ ion are shown in Fig. 2A. To determine the ratio of Larmor to cyclotron frequency Γ_0, we measured v_+ and simultaneously irradiated a microwave. When the ratio of the irradiated microwave frequency v_{MW} and the measured v_c are in resonance with Γ_0, the transition is driven, and the electron spin can change its orientation. To detect such a spin flip nondestructively, we used the continuous Stern-Gerlach effect (*40*). In the nearby analysis trap, a large magnetic bottle field exerts a force on the magnetic moment of the ion. Depending on the spin orientation with respect to the magnetic field, the ion becomes "low-field seeking" or "high-field seeking." Thus, a spin flip results in a shift of the axial frequency (see Fig. 2B):

$$\Delta\nu_z \approx \frac{B_2 \hbar q}{4\pi^2 M^2 \nu_z} \Gamma_0 \Delta m_s \tag{6}$$

where $\hbar$ is the reduced Planck's constant. The magnetic bottle strength, $B_2 \approx 43\ \frac{\mathrm{kT}}{\mathrm{m}^2}$, is the second-order magnetic field coefficient $B(z) = B_0 + B_2 z^2 + \ldots$ in the analysis trap; in this trap, the axial frequency is $\nu_z \approx 334$ kHz; and the change of the spin magnetic quantum number $\Delta m_s = \pm 1$ depends on the initial spin orientation. Figure 2A highlights the magnetic field lines in the analysis trap, where a direct high-precision measurement of Γ_0 is not possible because of the magnetic field inhomogeneity. Therefore, we measured Γ_0 in the precision trap using the double-trap technique (*41*). The magnetic field in this trap is much more homogeneous. Combined with an excellent harmonicity of the electrostatic trapping field, systematic effects in this trap are quite small and under better control (supplementary materials). The double-trap setup for the measurement is shown in Fig. 2A; the microwaves are injected through a millimeter waveguide into the setup, irradiating all traps with the electromagnetic wave.

The measurement sequence of Γ_0 follows the one presented in (*33*). The particle is continuously shuttled between the two traps. First, we determined its spin state in the analysis trap. To achieve this with high fidelity, we set the axial oscillation frequency in resonance with the detector circuit by changing the voltage applied to the electrodes. We then measured the motional frequency, followed by irradiation of a high-power microwave to try to change the spin state. This drive quickly loses coherence and has a roughly 50% chance of flipping the spin in the analysis trap. The axial frequency is measured again to detect a possible spin flip, observable as a jump in frequency after the microwave irradiation. We used a phase-sensitive technique to measure the axial frequency jump as described in (*42*), which allowed the spin state to be read quickly. Figure 2B shows the frequency readings of the spin-state detection during the measurement run with a measured shot-to-shot stability of about 24(1) mHz. A spin flip shifts the frequency by about 300 mHz (Eq. 6). This, together with averaging over four phase measurements, results in extremely low error rates in state detection. After state determination, the sequence continues in the precision trap, where the motional eigenfrequencies are measured. During the ν_+ measurement, the microwave field at frequency ν_{MW} is applied, chosen with a random offset to the expected Larmor frequency. We then checked in the analysis trap whether the spin state was flipped by this drive. Repeating the cycle, which takes on average 20 min, at different ratios Γ results in a probability histogram, shown in Fig. 2C. A total of 330 Γ ratios were probed, and 31 resulted in successful spin flips. Using a maximum-likelihood analysis, we determined the center to be $\Gamma_{\mathrm{stat}} = 4526.89426668(20)$. Correcting this for systematic effects as shown in Table 2, we extracted a measured value for the frequency ratio:

$$\Gamma_0 = 4526.894\,265\,905(191)_{\mathrm{stat}}(107)_{\mathrm{sys}} \tag{7}$$

The treatment of systematic effects is summarized in the supplementary materials. This follows the full discussion as given in (*33*), which uses very similar trap parameters, resulting in nearly identical systematic shifts and effects. Using Eq. 5, the literature value of the electron mass (*38*), and the ion mass reported in (*33*), corrected by the two additional electrons and binding energies (*43*), we determined the *g* factor of the lithium-like tin ion as

$$g_{\mathrm{exp}} = 1.980\,354\,799\,750(84)_{\mathrm{stat}}(47)_{\mathrm{sys}}(944)_{\mathrm{ext}} \tag{8}$$

The numbers in parentheses are the 1σ confidence intervals of the statistical, systematic, and external uncertainties, respectively. The external uncertainties are dominated by the ion mass uncertainty, which presently limits the experimental accuracy. It is also feasible to improve the precision of the mass value by more than an order of magnitude and consequently enhance the precision of the measured *g* factor (*44*–*46*).

Table 2. Error budget of Γ_0 and *g*. Following (*33*), additional shifts and uncertainties are smaller than 1 parts per trillion (ppt), and thus insignificant here. Blank cells indicate the contributions without an associated shift.

Parameter	Shift (ppt)	Uncertainty (ppt)
$\Gamma = \nu_L/\nu_c$ error budget:		
ν_- measurement		4.2
Relativistic shift (*49*)	21.8	4.4
Image-charge shift (*50*)	148	7.5
ν_z line shape		22
Statistical uncertainty		42
g−factor error budget:		
Total Γ uncertainty		44
Electron mass (*38, 51*)		29
$^{118}\mathrm{Sn}^{47+}$ mass (*33, 43*)		475

Discussion and outlook

Experimental data were blinded at the time of the theory evaluation. The observed agreement between experiment and theory (Eqs. 2, 3, and 8) is an important step forward because it consolidates the improvement of the most recent *g*-factor calculations over previous theoretical studies, which repeatedly reported results inconsistent with measured values (*13*–*15*, *20*). Our results provide a crucial test of sophisticated many-body QED calculations performed for a much higher nuclear charge *Z* than previously accomplished, thus probing the nontrivial bound-state QED effects scaling as Z^4 to a markedly greater extent. Furthermore, the agreement of the enhanced theoretical value (Eq. 3) with the experiment implicitly checks the consistency of the experiments on hydrogen-like and lithium-like tin and their theory.

The improved precision of the theoretical prediction allowed us to clearly resolve the electron-structure and QED screening effects and to test the advanced calculations in the so-far-unexplored regime of medium- to high-*Z* ions. In the future, measurements of heavier lithium-like systems such as $^{208}\mathrm{Pb}^{79+}$ and the expected progress in two-loop QED calculations will explore with even higher precision the regime of the strong electric fields reachable with highly charged ions. The advanced theoretical methods developed in this work for the description of interelectronic QED effects can be applied to calculations of *g* factors of more complex ions [boron-like, carbon-like (*9*, *47*)], parity-nonconserving transition amplitudes in neutral atoms, and other effects (*48*).

REFERENCES AND NOTES

1. I. Beltrami *et al.*, *Nucl. Phys. A.* **451**, 679–700 (1986).
2. P. Beiersdorfer, H. Chen, D. B. Thorn, E. Träbert, *Phys. Rev. Lett.* **95**, 233003 (2005).
3. S. Sturm *et al.*, *Phys. Rev. Lett.* **107**, 023002 (2011).
4. S. Kraft-Bermuth *et al.*, *Atoms* **6**, 59 (2018).
5. X. Fan, T. G. Myers, B. A. D. Sukra, G. Gabrielse, *Phys. Rev. Lett.* **130**, 071801 (2023).
6. T. Sailer *et al.*, *Nature* **606**, 479–483 (2022).
7. A. Wagner *et al.*, *Phys. Rev. Lett.* **110**, 033003 (2013).
8. F. Köhler *et al.*, *Nat. Commun.* **7**, 10246 (2016).
9. J. Ullmann *et al.*, *Nat. Commun.* **8**, 15484 (2017).
10. V. Hannen *et al.*, *J. Phys. At. Mol. Opt. Phys.* **52**, 085003 (2019).
11. P. Micke *et al.*, *Nature* **578**, 60–65 (2020).
12. V. A. Yerokhin, Z. Harman, *Phys. Rev. A* **95**, 060501 (2017).
13. V. A. Yerokhin, K. Pachucki, M. Puchalski, C. H. Keitel, Z. Harman, *Phys. Rev. A* **102**, 022815 (2020).
14. V. A. Yerokhin, C. H. Keitel, Z. Harman, *Phys. Rev. A* **104**, 022814 (2021).
15. V. P. Kosheleva, A. V. Volotka, D. A. Glazov, D. V. Zinenko, S. Fritzsche, *Phys. Rev. Lett.* **128**, 103001 (2022).
16. D. V. Zinenko, D. A. Glazov, V. P. Kosheleva, A. V. Volotka, S. Fritzsche, *Phys. Rev. A* **107**, 032815 (2023).
17. V. M. Shabaev *et al.*, *Phys. Rev. A* **65**, 062104 (2002).

18. V. A. Yerokhin, E. Berseneva, Z. Harman, I. I. Tupitsyn, C. H. Keitel, *Phys. Rev. Lett.* **116**, 100801 (2016).
19. V. Debierre, C. H. Keitel, Z. Harman, *Phys. Lett. B* **807**, 135527 (2020).
20. D. A. Glazov *et al.*, *Phys. Rev. Lett.* **123**, 173001 (2019).
21. T. Aoyama, T. Kinoshita, M. Nio, *Phys. Rev. D* **97**, 036001 (2018).
22. G. Breit, *Nature* **122**, 649 (1928).
23. V. A. Yerokhin, P. Indelicato, V. M. Shabaev, *Phys. Rev. A* **69**, 052503 (2004).
24. V. A. Yerokhin, U. D. Jentschura, *Phys. Rev. Lett.* **100**, 163001 (2008).
25. V. M. Shabaev, V. A. Yerokhin, *Phys. Rev. Lett.* **88**, 091801 (2002).
26. V. M. Shabaev, D. A. Glazov, A. V. Malyshev, I. I. Tupitsyn, *Phys. Rev. Lett.* **119**, 263001 (2017).
27. K. Pachucki, A. Czarnecki, U. D. Jentschura, V. A. Yerokhin, *Phys. Rev. A* **72**, 022108 (2005).
28. V. A. Yerokhin, Z. Harman, *Phys. Rev. A* **88**, 042502 (2013).
29. A. Czarnecki, R. Szafron, *Phys. Rev. A* **94**, 060501 (2016).
30. A. Czarnecki, M. Dowling, J. Piclum, R. Szafron, *Phys. Rev. Lett.* **120**, 043203 (2018).
31. A. Czarnecki, J. Piclum, R. Szafron, *Phys. Rev. A* **102**, 050801 (2020).
32. B. Sikora *et al.*, *Phys. Rev. Res.* **2**, 012002 (2020).
33. J. Morgner *et al.*, *Nature* **622**, 53–57 (2023).
34. A. V. Volotka, D. A. Glazov, V. M. Shabaev, I. I. Tupitsyn, G. Plunien, *Phys. Rev. Lett.* **112**, 253004 (2014).
35. D. A. Glazov *et al.*, *Nucl. Inst. Meth. Phys. Res. Sect. B* **408**, 46–49 (2017).
36. V. M. Shabaev *et al.*, *Phys. Rev. Lett.* **96**, 253002 (2006).
37. S. Sturm *et al.*, *Eur. Phys. J. Spec. Top.* **227**, 1425–1491 (2019).
38. E. Tiesinga, P. J. Mohr, D. B. Newell, B. N. Taylor, *Rev. Mod. Phys.* **93**, 025010 (2021).
39. L. S. Brown, G. Gabrielse, *Rev. Mod. Phys.* **58**, 233–311 (1986).
40. H. Dehmelt, *Proc. Natl. Acad. Sci. U.S.A.* **83**, 2291–2294 (1986).
41. H. Häffner, T. Beier, S. Djekić, *Eur. Phys. J. D* **22**, 163–182 (2003).
42. S. Stahl *et al.*, *J. Phys. At. Mol. Opt. Phys.* **38**, 297–304 (2005).
43. A. Kramida, Y. Ralchenko, J. Reader, NIST ASD Team, NIST Atomic Spectra Database (version 5.9) (National Institute of Standards and Technology, 2021).
44. A. Rischka *et al.*, *Phys. Rev. Lett.* **124**, 113001 (2020).
45. K. Kromer *et al.*, *Eur. Phys. J. A* **58**, 202 (2022).
46. F. Heiße *et al.*, *Phys. Rev. Lett.* **131**, 253002 (2023).
47. I. Arapoglou *et al.*, *Phys. Rev. Lett.* **122**, 253001 (2019).
48. M. S. Safronova *et al.*, *Rev. Mod. Phys.* **90**, 025008 (2018).
49. J. Ketter *et al.*, *Int. J. Mass Spectrom.* **361**, 34–40 (2014).
50. M. Schuh *et al.*, *Phys. Rev. A* **100**, 023411 (2019).
51. S. Sturm *et al.*, *Nature* **506**, 467–470 (2014).
52. J. Morgner, Measurement data for the lithium-like tin-118 Gamma determination at ALPHATRAP. Edmond, V1 (2024); https://doi.org/10.17617/3.ACSYZF.
53. V. A. Yerokhin, Dataset for the evaluation of the bound-electron g factor of lithium-like tin. Edmond, V1 (2025); https://doi.org/10.17617/3.URUI57.

ACKNOWLEDGMENTS

Funding: This work was supported by the Max Planck Society (MPG); the International Max Planck Research School for Quantum Dynamics in Physics, Chemistry and Biology (IMPRS-QD); the German Research Foundation (DFG) Collaborative Research Centre SFB 1225 (ISOQUANT); and the Max Planck PTB RIKEN Center for Time, Constants, and Fundamental Symmetries. This project has received funding from the European Research Council (ERC) under the European Union's Horizon 2020 research and innovation program under grant agreement number 832848 FunI. This work comprises parts of the PhD thesis work of J.M. to be submitted to Heidelberg University, Germany. **Author contributions:** The experiment was maintained and performed by J.M., C.M.K., T.S., B.T., F.H., and S.S. The data were analyzed by J.M., F.H., and B.T. Theoretical calculations were performed by V.A.Y., B.S., and Z.H. J.M. and V.A.Y. contributed to the writing of the manuscript, which was edited by S.S., Z.H., J.R.C.L.-U., C.H.K., and K.B. All authors discussed and approved the data as well as the manuscript. **Competing interests:** The authors declare no competing interests. **Data and materials availability:** All data needed to evaluate the conclusions in the paper are present in the paper and/or the supplementary materials. Experimental data are publicly available in Edmond (*52*). Theoretical data and code generated for the presented study are publicly available in Edmond (*53*). **License information:** Copyright © 2025 the authors, some rights reserved; exclusive licensee American Association for the Advancement of Science. No claim to original US government works. https://www.science.org/about/science-licenses-journal-article-reuse. This research was funded in whole or in part by the European Research Council (ERC) (grant no. 832848), a cOAlition S organization. The author will make the Author Accepted Manuscript (AAM) version available under a CC BY public copyright license.

SUPPLEMENTARY MATERIALS

science.org/doi/10.1126/science.adn5981
Supplementary Text; Tables S1 to S3; References (*54*–*69*)

Submitted 23 December 2023; accepted 28 March 2025

10.1126/science.adn5981

NANOMATERIALS

Resiliency, morphology, and entropic transformations in high-entropy oxide nanoribbons

Hessam Shahbazi[1], Pardis Seraji[1], Husam Farraj[2], Taimin Yang[3], Allen Kim[4], Seyyedfaridoddin Fattahpour[5], Ilias Papailias[1,6], Matthew Diamond[7]†, Shahriar Namvar[1], Alireza Ahmadiparidari[1], Shuxi Wang[1,8], Zhenxian Liu[7], Shihui Feng[3], Khagesh Kumar[2], Muhtar Ahart[7], Jordi Cabana[2], Sara Kadkhodaei[5], Junlan Wang[4], Zhehao Huang[3,9]*, Russell J. Hemley[2,7,10]*, Amin Salehi-Khojin[1,6]*

We present the successful synthesis and characterization of a one-dimensional high-entropy oxide (1D-HEO) exhibiting nanoribbon morphology. These 1D-HEO nanoribbons exhibit high structural stability at elevated temperatures (to 1000°C), elevated pressures (to 12 gigapascals), and long exposure to harsh acid or base chemical environments. Moreover, they exhibit notable mechanical properties, with an excellent modulus of resilience reaching 40 megajoules per cubic meter. High-pressure experiments reveal an intriguing transformation of the 1D-HEO nanoribbons from orthorhombic to cubic structures at 15 gigapascals followed by the formation of fully amorphous HEOs above 30 gigapascals, which are recoverable to ambient conditions. These transformations introduce additional entropy (structural disorder) besides configurational entropy. This finding offers a way to create low-dimensional, resilient, and high-entropy materials.

High-entropy alloys (HEAs), which contain five or more metallic elements, can exhibit superior wear resistance, thermal stability, and mechanical strength (*1*–*5*) compared with conventional alloys, and since their discovery, high-entropy carbides (*6*–*11*), nitrides (*12*), sulfides (*13*, *14*), and oxides (HEOs) have been developed (*15*–*18*). The latter feature complex compositions of multiple metal cations and oxygen anions in equimolar fractions for stability (*19*, *20*). Stabilizing such multicomponent structures is challenging because it requires sufficient temperature (T) and entropy (S) contributions (-TdS) to counteract the enthalpy contributions (dH) and achieve favorable free energy (*21*).

To date, only a limited range of single-phase HEOs has been synthesized; most materials undergo compositional segregation into multiple phases driven by variations in element size, electronegativity, and complex oxidation state (*16*, *22*–*30*). This segregation can cause structural instability, especially under extreme conditions, such as high temperature, high pressure, harsh chemical environments, and mechanical wear (*27*, *31*). Various synthesis techniques have been explored for HEOs, including mechanical milling to synthesize pyrochlore phase $(La_{0.2}Nd_{0.2}Sm_{0.2}Eu_{0.2}Gd_{0.2})_2Zr_2O_7$ (*32*, *33*), carbothermal shock to synthesize rocksalt (Co,Cu,Mg,Ni,Zn)O (*34*, *35*), flame spray pyrolysis to synthesize spinel $(Mn,Fe,Ni,Cu,Zn)_3O_4$ (*19*, *36*), chemical solution deposition to synthesize orthorhombic $(Bi_{3.25}La_{0.75})(Ti_{3-3x}Zr_xHf_xSn_x)O_{12}$ (*37*), and sol-gel to synthesize perovskite $Sr(La_{0.2}Pr_{0.2}Nd_{0.2}Sm_{0.2}Sr_{0.2}Mn)O_{3-\delta}$ (*38*). All of these methods yield single-phase nanoparticle morphology, though phase stability was often unexamined, and some showed segregation at high temperatures (*39*–*41*).

In this work, we report an approach for synthesizing $(MoWNbTaV)O_3$ HEO material that has a characteristic one-dimensional (1D) nanoribbon morphology (hereafter referred to as 1D-HEO) and investigating these dimensionally confined HEO nanostructures. We attained precise control over the HEO ribbon width and fine-tuned it across two orders of magnitude (from 60.0 ± 15.3 nm to 15.0 ± 2.6 μm). These nanoribbons exhibit outstanding resilience under extreme conditions and remarkable mechanical properties. Notably, they exhibit a pressure-induced transformation from orthorhombic to cubic followed by the formation of fully amorphous HEOs at elevated pressures (above 30 GPa), which are recoverable to ambient conditions. These transformations introduce structural disorders, adding to the system's configurational entropy.

There is currently no established benchmark for the performance of HEOs under extreme conditions, which would greatly benefit other studies in evaluating these materials for various applications. Our material shows excellent resistance to extreme temperatures, extreme pressures, and harsh chemical environments. Potential applications for this material include settings where heat resistance, pressure tolerance, durability under mechanical loads, and resilience in corrosive environments are critical; additional implications are described in the supplementary materials, section S1.

Synthesis and characterization

A multielement equimolar 2D sulfide, serving as both the reactant and substrate for the growth of 1D-HEO nanoribbons, was selected from groups V and VI because of their similar atomic characteristics and positive mixing enthalpy (*13*). Figure 1A shows the scanning electron microscopy (SEM) image of the multielement sulfide precursor, $(MoWNbTaV)S_2$, with hexagonal-shaped morphology (see the supplementary materials, section S3, for the synthesis and table S1 for details on the crystal structure information). The energy-dispersive spectroscopy (EDS) mapping confirmed a homogeneous distribution of all elements shown in fig. S1. We did not observe any signs of preferential segregation in samples. Transmission electron microscopy (TEM) results, shown in fig. S2, further confirmed that a single-phase solid solution hexagonal structure of $(MoWNbTaV)S_2$ formed with the space group of $P6_3/mmc$) $P\text{-}3m1$.

Figure 1B illustrates the schematic of the temperature profile for synthesizing 1D-HEO in air through the oxidation of 2D sulfide precursors. The precursor was placed inside a ceramic crucible within an open-ended tube furnace with the temperature profile consisting of three steps, including a heating ramp rate of 2°C/min from room temperature (RT) to 900°C, an isothermal step at 900°C for 3 hours, and a final cooling ramp of 5°C/min to RT. This process differs from all the reported multielement oxides, which typically use mixtures of unary oxides as the precursor. Figure 1C shows the SEM image and corresponding EDS mapping of the synthesized nanoribbon 1D-HEO morphology. The atomic percentage of each transition metal element and oxygen for the synthesized 1D-HEO, measured by x-ray photoelectron spectroscopy (XPS), was Mo: 4.49, W: 6.60, Nb: 5.29, Ta: 5.40, V: 4.11, and O: 73.86, representing all of the transition metal elemental peaks in the spectra to be in a nearly equimolar ratio and agreement with

---

[1]Department of Mechanical and Industrial Engineering, University of Illinois Chicago, Chicago, IL, USA. [2]Department of Chemistry, University of Illinois Chicago, Chicago, IL, USA. [3]Department of Materials and Environmental Chemistry, Stockholm University, Stockholm, Sweden. [4]Department of Mechanical Engineering, University of Washington, Seattle, WA, USA. [5]Department of Civil, Materials, and Environmental Engineering, University of Illinois Chicago, Chicago, IL, USA. [6]Department of Mechanical Engineering, Southern Methodist University, Dallas, TX, USA. [7]Department of Physics, University of Illinois Chicago, Chicago, IL, USA. [8]MOE Key Laboratory for Nonequilibrium Synthesis and Modulation of Condensed Matter, School of Physics, Xi'an Jiaotong University, Xi'an, China. [9]School of Emergent Soft Matter, Center for Electron Microscopy, Guangdong Basic Research Center of Excellence for Energy and Information Polymer Materials, South China University of Technology, Guangzhou, China. [10]Department of Earth and Environmental Sciences, University of Illinois Chicago, Chicago, IL, USA. ***Corresponding author. Email: asalehikhojin@smu.edu (A.S.-K.); rhemley@uic.edu (R.J.H.); zhehao.huang@mmk.su.se (Z.H.)** †Present address: X-ray Science Division, Advanced Photon Source, Argonne National Laboratory, Lemont, IL, USA.

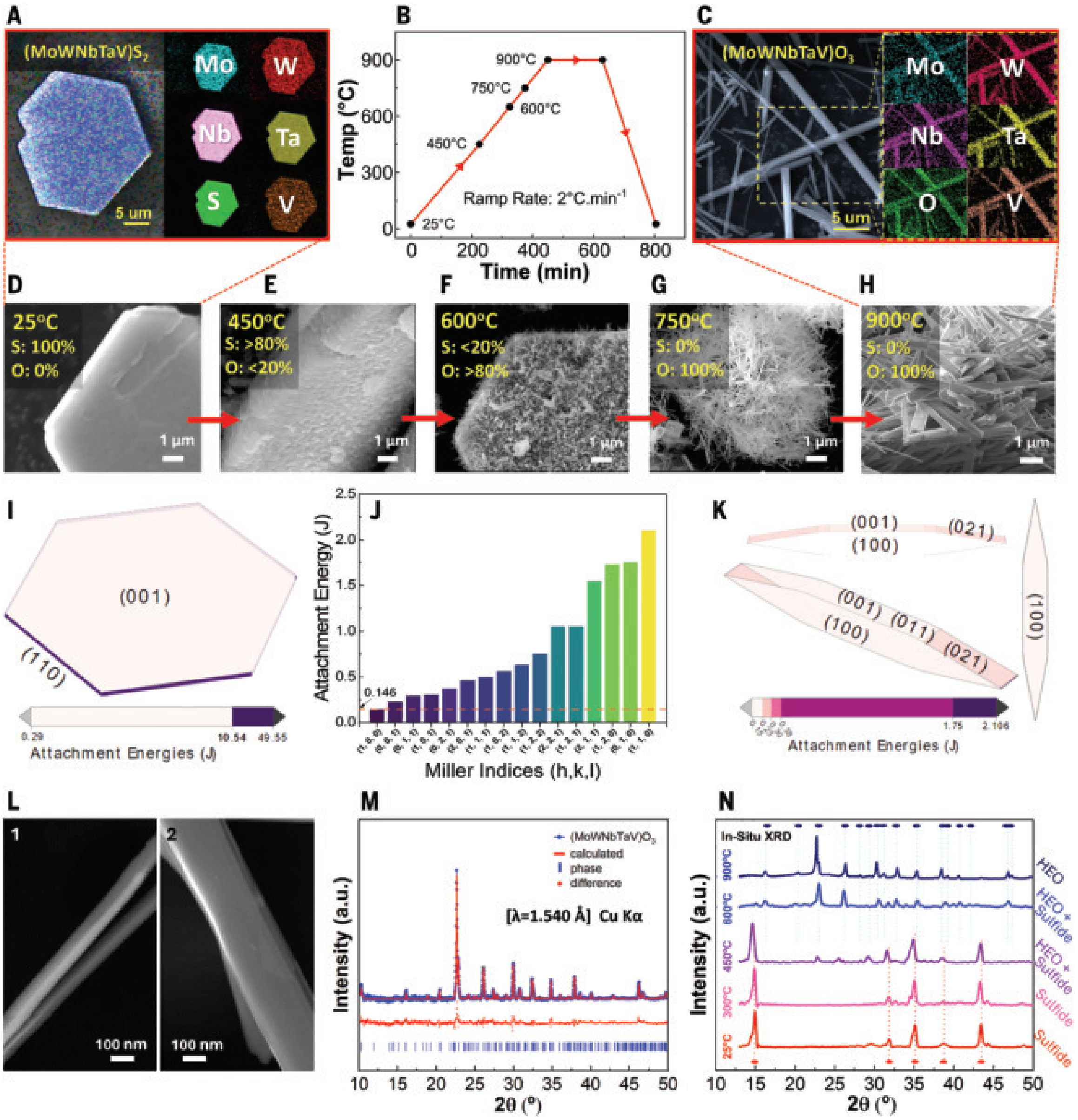

Fig. 1. Transformation pathway from 2D precursor to 1D-HEO. (**A**) SEM-EDS of the precursor material: 2D sulfide precursor (MoWNbTaV)S_2. (**B**) Synthesis temperature profile. (**C**) SEM-EDS of the as-synthesized material: 1D-HEO (MoWNbTaV)O_3. The EDS mapping region in the SEM image is outlined by a yellow dashed line. (**D** to **H**) SEM images of 1D-HEO at different temperatures showing the grains formation and vertical growth of 1D-HEO on top of 2D sulfide precursor flakes. (**I**) The Wulff shape constructed from the attachment energies for the 2D sulfide precursor with hexagonal crystal shape, color-coded by the attachment energies. (**J**) The attachment energies for the 1D-HEO crystal, color-coded by the attachment energies. (**K**) The Wulff shape constructed from the attachment energies for the 1D-HEO crystal, color-coded by the attachment energies. (**L**) SEM images from the side and the top of the 1D-HEO, showing the nanoribbon morphology. (**M**) Powder diffraction pattern of as-synthesized 1D-HEO at ambient temperature with fit to the orthorhombic $P2_12_12$ space group. Blue dots display the measured data, the red line is the refinement model fit, and tick marks (teal short vertical lines) represent the model peak positions that correspond to the *hkl* indexing. a.u., arbitrary units. (**N**) In situ XRD at different temperature stages during the transition from the 2D sulfide precursor to 1D-HEO.

EDS results (detailed results provided in the supplementary materials, section S3; figs. S7 and S8; and table S4).

Growth control

Experiments were conducted to elucidate the morphological evolution during synthesis, revealing detailed information about the growth mechanism of the nanoribbons. The synthesis process was set at isothermal steps of 450°, 600°, 750°, and 900°C (denoted by the black dots in Fig. 1B) followed by natural quenching to RT in an air atmosphere. The SEM results showed that after heating to 450°C (Fig. 1E), the 2D sulfide precursor acted as both substrate and precursor for the growth of (MoWNbTaV)O_3. The process began with the formation of honeycomb-shaped grains on top of the hexagonal planes of the 2D sulfide precursor (see lower-magnification SEM images in the supplementary materials, section S3, and figs. S12 and S13). At 600°C (Fig. 1F), these honeycomb grains acted as nucleation sites to initiate vertical growth of the 1D-HEO.

At 750°C (Fig. 1G), the 2D sulfide precursor was consumed, resulting in a mat of 1D nanoribbons, and by 900°C (Fig. 1H), layered stacks of nanoribbons had grown together (Fig. 1, D to H). We performed an

EDS analysis to determine the O/S ratio during the transition from 2D sulfide precursor to 1D-HEO. As the temperature increased from 25° to 450°C, 20% of the S atoms in the structure were replaced by O atoms. After the temperature reached 600°C, the oxidation accelerated, and >80% of S had been replaced by O. Finally, at and above 750°C, all S atoms were substituted by O atoms (100%). The nanoribbon morphology is clearly observed in Fig. 1L, where the SEM images of the side and top of the 1D-HEO are presented.

We used the Wulff construction to predict the crystal shape of the HEO and sulfide precursor (more details are provided in the supplementary materials, section S4). The surface energy (SE) crystal predicted the shape of the sulfide precursor as a relatively thick polygon (fig. S37C). By contrast, the attachment energy (AE) crystal shape was a much thinner hexagonal disk (Fig. 1I), consistent with the results of Fig. 1A. However, as shown in Fig. 1K, the AE crystal shape of HEO was elongated in one direction, which is in good agreement with the SEM images shown in Fig. 1C.

By contrast, the SE predicted a crystal shape that was less elongated (fig. S37A). Notably, facets such as (1,2,1), (1,2,0), and (1,0,1) that form a large area of the SE crystal shape disappeared from the AE crystal shape, whereas the (1,0,0) facet increased to form >50% of the SE crystallite shape area, as shown in fig. S38 (supplementary materials). This difference was caused by the (1,0,0) facet exhibiting the lowest AE of 0.146 J while also having the lowest SE of 0.193 J/m^2 among other facets (Fig. 1J and fig. S38, A and B), which implies a strong preference for nucleation and growth of the facet. The (0,0,1) facet, although having SE as small as that of (1,0,0), had a larger AE, which hindered its growth, resulting in a decrease of its area fraction from SE to AE (fig. S39, A and B). A facet such as (1,2,1) had an SE value near that of the lowest SE facet; however, its AE was much higher, completely suppressing its growth, and thus it disappeared in the AE crystal shape. Thus, the AE crystal shape prediction, which included growth kinetic factors, effectively and accurately replicated the ribbonlike shape of the HEO crystallites observed in the SEM images.

The x-ray diffraction (XRD) result of the HEO in ambient conditions is shown in Fig. 1M. We performed Le Bail refinement, revealing an orthorhombic $P2_12_12$ space group with lattice parameters $a = 12.2078(3)$ Å, $b = 36.504(1)$ Å, $c = 3.9393(2)$ Å, and $V = 1755.5(1)$ [where the last digit in parentheses indicates the standard uncertainty (±) in the last digit], with an R factor of 0.0964 and a goodness of fit of 1.08. The structure was similar to the tungsten bronze-type, as reported for $Nb_{16}W_{18}O_{94}$ (*42*). The green lines in the figure illustrate the region selected for the temperature-variable in situ XRD (Fig. 1N). The characteristic diffraction peaks of 2D sulfide precursor were observed at 2θ degrees of 6.75°, 14.5°, 16.25°, 17.7°, and 20.1°, represented by red dots at the bottom of the plot. The corresponding $(MoWNbTaV)O_3$ peaks appeared at 7.6°, 9.5°, 10.75°, 11.75°, 12.5°, 14.1°, 14.6°, 14.9°, 16.25°, 17.1°, 17.3°, 19.5°, 21.25°, and 22°, represented by blue dots at the top of the plot (Fig. 1M). The 2D sulfide precursor's XRD peaks remained up to 300°C. As the temperature increased to 450°C, small peaks correlated with the 1D-HEO crystal start to stand out. By increasing the temperature to 600°C, 1D-HEO peaks became more dominant, and at 900°C, the 2D sulfide precursor peaks disappeared. These results verified a complete transition from 2D sulfide to 1D-HEO.

Figure 2, A to C, demonstrates approximately two orders of magnitude of control over the width of nanoribbons (from 60.0 ± 15.3 nm to 15.0 ± 2.6 μm) by altering the isothermal step temperature and heating ramp rate. For these experiments, two different isothermal temperatures (900° and 1200°C) and two different heating ramp rates (2° and 5°C/min) were chosen. To rule out the effect of the cooling rate, all samples were cooled down at the same rate of 5°C/min. Analysis of 50 individual ribbons of each synthesis condition indicated that increasing the isothermal temperature from 750° to 1200°C with a heating ramp of 2°C/min resulted in width increase from the nanometer scale (60 nm) to the micrometer scale (1 μm), reaching tens of micrometers (15 μm) at 1200°C. However, increasing the ramp rate from 2° to 5°C/min with the same isothermal temperature of 900°C reduced the width from the micrometer scale (1 μm) down to 280 nm. Also, our results (shown in fig. S5) indicated that as the holding temperature increased from 750° to 900° and 1200°C, the ribbon lengths grew from the nanometer scale (69 nm) to tens of micrometers (12.9 μm) and eventually to hundreds of micrometers (138.9 μm), respectively. Increasing the heating rate from 2° to 5°C/min at 900°C resulted in a length increase from a median of ~4.7 μm to ~12.9 μm.

Figure 2D shows that the width and thickness of one single nanoribbon isolated through mechanical exfoliation process were 150 nm and 80 nm, respectively. The TEM image and electron diffraction pattern in Fig. 2E confirmed that the material had a ribbonlike morphology and that the growth direction of the nanoribbon was along the *c* axis. The scanning transmission electron microscopy (STEM)–EDS spectrum (figs. S15 and S16) showed that the material contains W, Ta, Nb, Mo, and V with uniform distribution at the atomic scale. To determine the crystal structure, a three-dimensional electron diffraction (3DED) combined with atomic-resolution STEM image was acquired. From the 3DED data, the 3D reciprocal lattice (Fig. 2G) was reconstructed to obtain the unit cell of the crystal. The unit cell parameters were $a = 12.26(9)$ Å, $b = 36.66(26)$ Å, and $c = 3.94(3)$ Å. This structure was reported by Sleight *et al.* (*42*) but only for a subset of these elements. The space group $P2_12_12$ was deduced from the systematic absence viewed from the slice of lattice planes (Fig. 2G). The high-angle annular dark-field (HAADF)–STEM image was acquired along the [101] zone axis (Fig. 2F), revealing a flat [010] exposed surface of our nanoribbons. The magnified HAADF image shows the arrangement of atomic columns with the same direction, which corresponded well with the structure model determined by 3DED (see fig. S17 for enhanced visualization).

We also conducted 3DED experiments after oxidation to evaluate the structure of 1D-HEO at both RT and 700°C. By analyzing the data using least squares refinement (table S6), we identified a small amount of oxygen vacancies in the structure, as indicated by the red circles in fig. S23. The oxygen occupancy was found to be 0.88(17) at 25°C and 0.71(9) at 700°C. Considering that the total molecular weight of atoms in the unit cell is 5551.09, and only four oxygen atoms experienced a decrease in occupancy from 0.88 to 0.71, it showed a total weight loss of <0.3%, consistent with the thermal stability tests of the material.

The structure was composed of six coordinated metal atoms as well as five coordinated metal atoms that resulted from oxygen deficiency. From the structure, we also obtained the stoichiometry for this material, which is $M_{10}O_{26}$ (where M = W, Ta, Nb, Mo, or V). This value was consistent with the XPS results discussed above. Figure 2H shows the visualization of the structure obtained from the crystallographic information file (CIF). Figure 2H also illustrates the oxide crystal structure with partial occupancies at metal sites, as approximated by the virtual crystal approximation (VCA). The crystal unit cell consisted of 128 atoms, with metal atoms occupying the 32c and 2b Wyckoff positions and oxygen at the 2b and 92c Wyckoff sites. Figure S3 is a similar illustration of the 2D sulfide precursor crystal structure for comparison. The crystal unit cell consisted of 48 atoms, with metal atoms occupying the 16d Wyckoff positions and sulfur at the 32f Wyckoff sites.

Material properties

We studied the thermal and chemical stability as well as the mechanical properties of the synthesized 1D-HEO. The thermal stability of the 1D-HEO nanoribbons was first examined using thermogravimetric analysis (TGA) in the air atmosphere with a heating ramp of 10°C/min from RT to 1000°C (supplementary materials, section S2). The results presented in Fig. 3A indicate the absence of noticeable volatile content or sharp weight loss up to 1000°C and confirmed the material's thermal stability with negligible weight loss (<1%). These results aligned

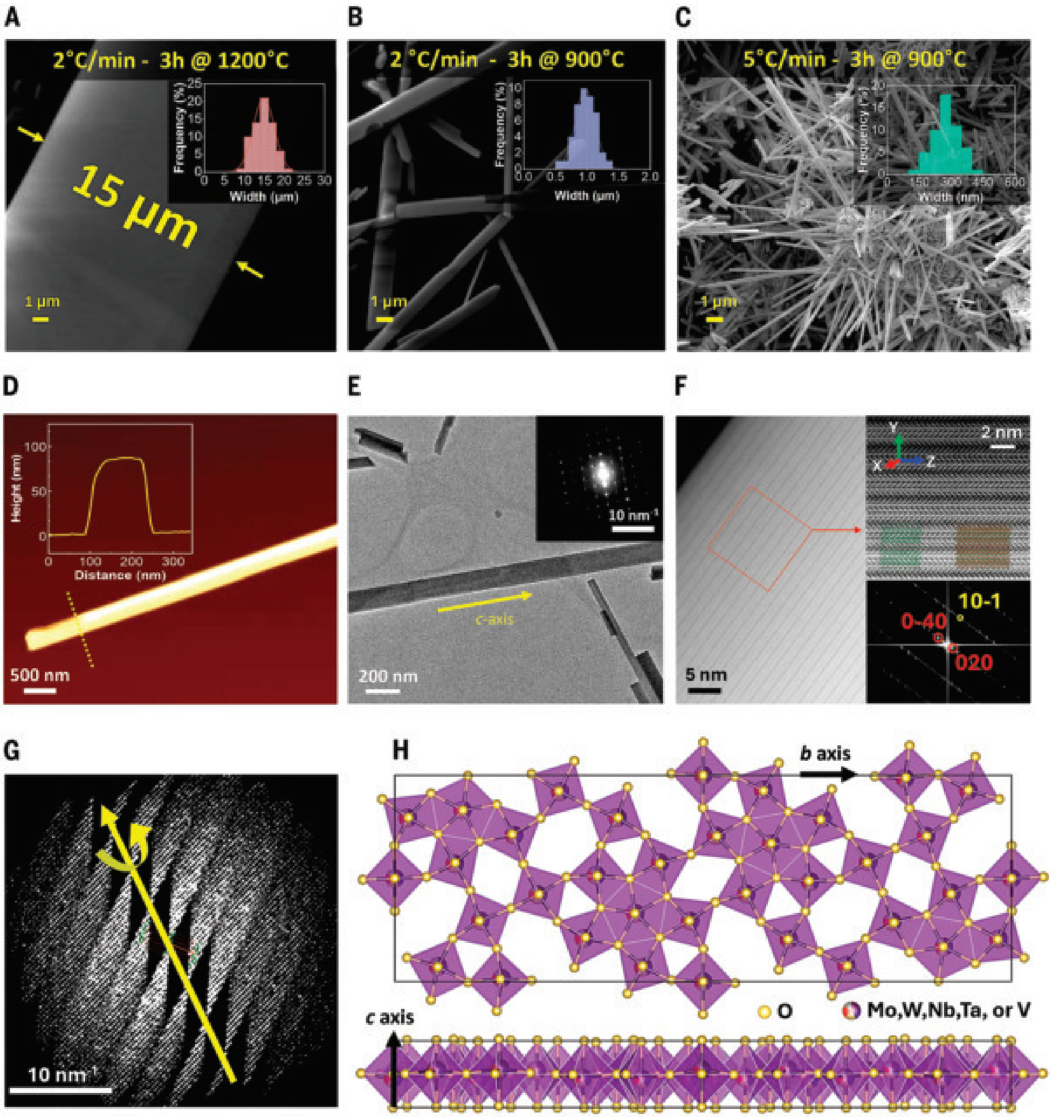

Fig. 2. Growth control and structural characterization of 1D-HEO. (**A** to **C**) SEM images showing the overall morphologies of the sample synthesized at 1200°C (A) and 900°C (B) with the ramp rate of 2°C/min and the morphology of the sample synthesized at 900°C with the ramp rate of 5°C/min (C) (inset plots show width distributions). (**D**) Atomic force microscopy (AFM) image and size measurement plot of single nanoribbon $(MoWNbTaV)O_3$. (**E**) TEM image showing the overall morphologies of the sample. The inset shows the corresponding diffraction pattern. (**F**) HAADF-STEM images taken along the [101] direction, with the corresponding fast Fourier transform (FFT) displayed in the bottom right inset. Top right inset shows a magnified HAADF image, aligned well with structure model. (**G**) Reconstructed 3D reciprocal space of 1D-HEO. (**H**) Visualization of the 1D-HEO structure along the *c* and *b* axes.

with the TEM results in Fig. 2 that there was no evidence of phase segregation or the formation of minor phases. Furthermore, powder XRD and SEM-EDS analyses in Fig. 1 confirm the presence of only a single detected phase, with no indication of side reactions. No new phase formation or decomposition was detected, consistent with the high thermal stability of 1D-HEO described earlier. This stability was also consistent with the TGA results in air (Fig. 3A).

Additionally, high-temperature in situ TEM experiment results indicated that the electron diffraction patterns at 700°C (the highest achievable temperature in the TEM chamber) were similar to those collected at RT (Fig. 3C). We also obtained 3DED data at 450° and 600°C. From the reconstructed 3D reciprocal lattice, the unit cell parameters were a = 12.38 Å, b = 36.64 Å, c = 3.91 Å, α = 89.77°, β = 90.97°, and γ = 90.38° for 450°C and a = 12.41 Å, b = 36.77 Å, c = 3.92 Å, α = 90.03°, β = 90.24°, and γ = 90.88° for 600°C. Compared with the unit cell parameters of a = 12.38 Å, b = 36.62 Å, c = 3.88 Å, α = 90.04°, β = 89.99°, and γ = 90.07° at 25°C, the differences are within the systematic error of the measurement. In addition, the reflection conditions at each temperature were deduced to be the same (figs. S18 to S21). Thus, it can be concluded that the structure of the 1D-HEO remained the same during the annealing process. Also, the unit cell, space group, and atomic coordinates at high temperatures remain the same as those obtained at RT (table S6). Details are provided in the supplementary materials, section S3.

To assess the resilience of the 1D-HEO material under chemically harsh conditions, we performed XRD and XPS analyses before and after placing the samples in acidic media (5 mM H_2SO_4, pH = 2.3) and basic media (0.1M NaOH, pH = 13) for 7 days. XRD results shown in fig. S24 indicated that no new phases form after 7 days. SEM-EDS of the samples shown in Fig. 3D demonstrated no elemental distribution change or morphological transformation either. The XPS results also verified that the chemical composition of 1D-HEO remained nearly

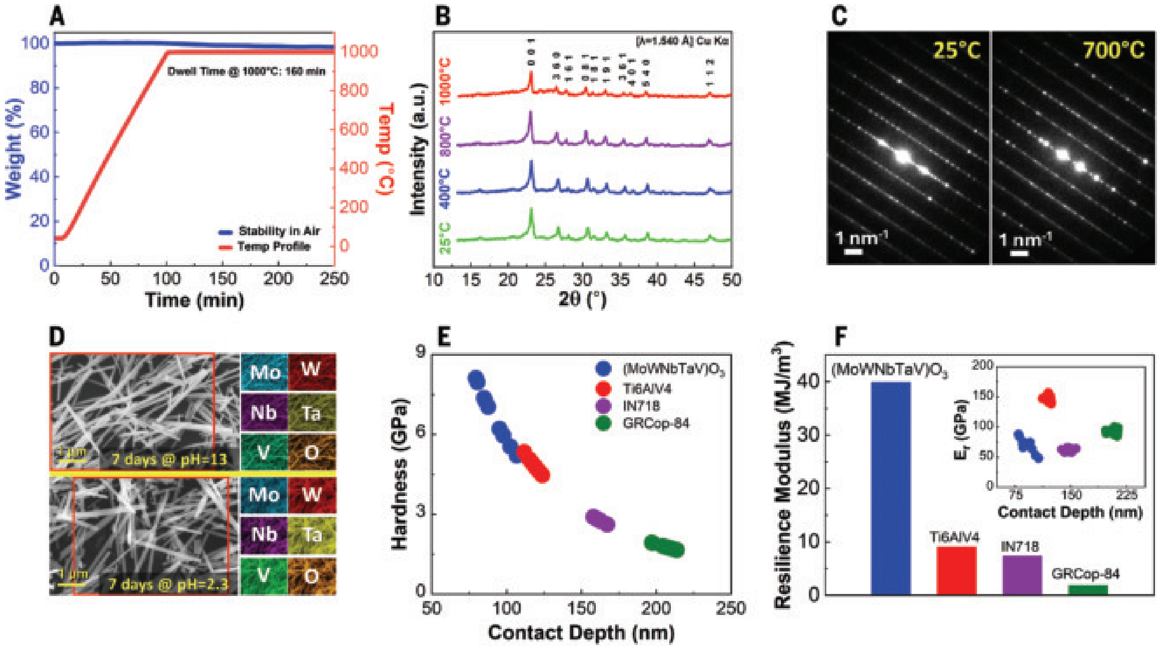

Fig. 3. Thermal, mechanical, and chemical stability of 1D-HEO. (**A**) TGA data of 1D-HEO sample at the temperature range of 25° to 1000°C. The blue line shows stability in the air, and the red line illustrates the temperature profile throughout the experiment. (**B**) High-temperature XRD data showing the stability of 1D-HEO between 25° and 1000°C. (**C**) Electron diffraction patterns collected at RT and 700°C. (**D**) Morphological and chemical stability after remaining in basic media (pH = 13, 0.1 M NaOH) and acidic media (pH = 2.3, 5 mM H_2SO_4) for 7 days. The EDS mapping region in the SEM image is outlined by red lines. (**E** and **F**) Hardness versus contact depth comparing 1D $(MoWNbTaV)O_3$ with IN718, Ti6AlV4, and GPCop-84 (E) and reduced modulus (inset) and resilience modulus of 1D $(MoWNbTaV)O_3$ compared with IN718, Ti6AlV4, and GPCop-84 (F).

unchanged upon long exposure to acidic and basic chemical environments (table S4 and figs. S8 to S10).

To further verify the stability results, inductively coupled plasma mass spectrometry (ICP-MS) measurements were performed after 1, 3, 5, and 7 days in the acidic and basic media (results presented in tables S8 and S9, respectively) before and after each experiment, and only traces of metals were detected [<5 parts per million (ppm) for acidic and <13 ppm for basic media] (supplementary materials, section S3). To elaborate on the source of HEO stability in highly corrosive environments, STEM results (Fig. 2F) indicated that the exposed surface of the HEO nanoribbon was super flat at the atomic scale, indicating the absence of surface defects. Also, the atomic-resolution STEM image agreed perfectly with the structural model solved from 3DED, further confirming large areas without defects (Fig. 2F, insets).

We performed nanoindentation experiments to determine the mechanical properties (hardness and elastic modulus) of the 1D-HEO. For comparison, three additional additively manufactured aerospace high-temperature alloys of GRCop-84, Inconel 718, and Ti-6Al-4V were tested under the same ambient conditions and an indentation load of 3000 μN. Figure 3E shows the hardness values for the tested samples as a function of contact depth. Measured hardness for the HEO ranges from 8.3 GPa at 75 nm to 6.89 GPa at 100 nm of indentation depth for 1D-HEO, and average values of 1.74, 2.79, and 4.76 GPa for the GRCop-84, IN718, and Ti-6Al-4V alloys, respectively. The inset of Fig. 3F shows the reduced modulus results as a function of contact depth, with average values of 70.3 GPa for 1D-HEO and 62.2, 91.9, and 146.7 GPa, respectively, for the IN718, GRCop-84, and Ti-6Al-4V.

Hardness measures resistance to permanent and localized plastic deformation, and the reduced modulus represents the stiffness of a material in response to an applied load. Our 1D-HEO single nanoribbon displayed markedly high hardness compared with the three aerospace alloys tested under identical conditions, indicating strong resistance to plastic deformation (supplementary materials, section S3). This high hardness would make it ideal for wear resistance by preventing abrasion and cutting action, which otherwise lead to material loss (*43*).

Also, the combination of high hardness and moderate modulus properties suggested that these materials would have a high modulus of resilience, which is a measure of materials' capacity to absorb energy and recover from deformation without permanent failure (*44*). As shown in Fig. 3F, the modulus of resilience was 40 MJ/m^3 for 1D-HEO, whereas for GRCop-84, IN718, and Ti-6Al-4V, the values were 1.95, 7.43, and 9.14 MJ/m^3, respectively. The 1D-HEO showed a notably high modulus of resilience compared with the three high-temperature aerospace alloys (20 times as high as GRCop-84, 5 times as high as Inconel 718, and 4 times as high as Ti-6Al-4V) (supplementary materials, section S3). We also performed bond length, charge density distribution, and electron localization function (ELF) calculations using density functional theory (DFT). These calculations suggest that the high mechanical hardness of the HEO stems from its complex, heterogeneous (mixed ionic-covalent) bonding environment (supplementary materials, section S4).

To further understand the thermodynamic properties and stability of the material, we performed a series of high-pressure experiments using diamond-anvil cells (DACs) to >30 GPa. High-pressure synchrotron XRD was performed on 1D-HEO samples loaded in DACs with and without a pressure-transmitting medium. The RT diffraction patterns of the 1D-HEO samples changed with increasing pressure. At lower pressures, high-quality XRD patterns were readily measured with samples of an Ar pressure medium, and data could fit with the initial $P2_12_12$ orthorhombic structure. Pressure-volume (*P-V*) relations revealed pressure-induced first-order structural transitions with a large volume discontinuity at 15 GPa and gradual disordering leading to an amorphous HEO above 30 GPa (Fig. 4A). The intensities of the low-angle peaks ($2\theta < 3°$) decreased, broadened, and were lost by 15 GPa (Fig. 4, B and C). The remaining peaks broadened with pressure, becoming diffused and indistinct at the highest pressure of the experiments (fig. S30).

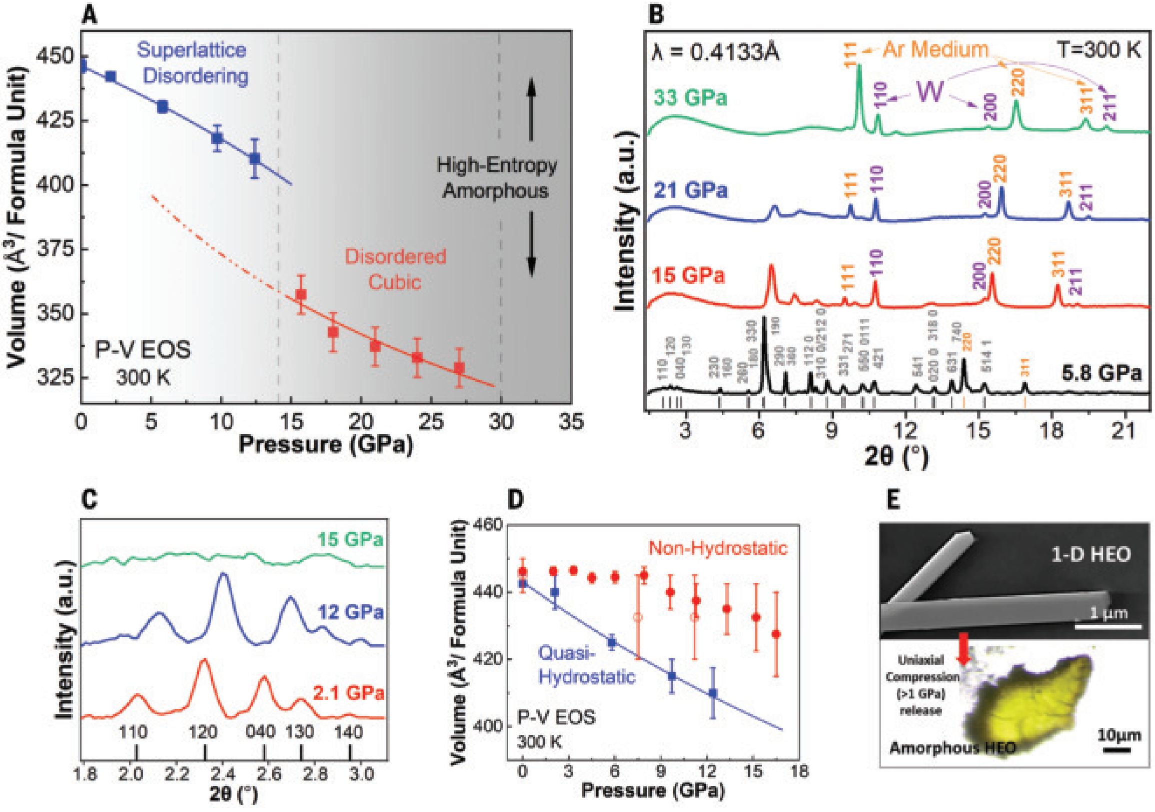

Fig. 4. High-pressure experiments on the 1D-HEO. (**A**) *P-V* EOS obtained from XRD of a 1D-HEO sample in an Ar medium at 300 K. The results show the pressure-induced first-order structural transition from the orthorhombic to the disordered cubic phase at 15 GPa and the transition to an x-ray amorphous phase above 30 GPa. The lines show the results of Vinet *et al*. (*51*) EOS fits to ambient pressure-volume (V_0), bulk modulus (K_0), and bulk modulus pressure derivative (K_0'). Notably, the EOS of the initial phase shows an unusual negative curvature, with best-fit values of $V_0 = 446(1)$ Å^3/formula unit, $K_0 = 177(15)$ GPa, and a $K_0' = -5(2)$ for the initial phase. The EOS fit for the high-pressure cubic phase gave $V_0 = 862$ Å^3/formula unit (fixed), $K_0 = 47(17)$ GPa, and a $K_0' = 5(3)$, where the errors are larger because of the use of a fictitious reference volume at ambient pressure. (**B**) Examples of in situ XRD for 1D-HEO in an Ar medium. The 5.8-GPa pattern shows the Le Bail model fit to an orthorhombic structure with $P2_12_12$ space group consistent with the ambient pressure results; the results show the broadening and loss of 1D-HEO peaks, in contrast to the Ar (pressure medium) and W gasket peaks, which persist to the highest pressures (orange and purple indices). (**C**) Details of (B), showing loss of low-angle peaks at 15 GPa on compression of the 1D-HEO in an Ar medium. We associate this pressure-induced disordering and gradual loss of superlattice reflections along *b* with the strongly negative value of the K_0'. (**D**) *P-V* data obtained from XRD with (blue) and without (red) pressure-transmitting medium. Decompression data (hollow red) are reported for the nonhydrostatic experiments. In the data without a pressure medium, compression of the unit cell is not observed until ~7 GPa [the stress measured at the anvil surface by Raman scattering (*52*)], at which point the porosity of the sample disappears and the strong HEO ribbons begin to deform and compact. (**E**) A stress-quenched sample that had been uniaxially compressed shows evidence of grain compaction (becoming transparent and developing the ability to fracture) owing to uniaxial stress.

The quasihydrostatic, nonhydrostatic, and direct uniaxial compression experiments thus provide insight into the material performance and mechanical response (Fig. 4, B and D). The nonhydrostatic and uniaxial compression experiments produced plastic deformation in the samples, which increased entropy in this already high-entropy material. The deformation characterized by an initial loss of long-range crystalline order (Fig. 4C) followed by further structural disorder, indicated that the building blocks of the wolfram bronze structure, which can be a 1 × 9 × 3 superlattice of the structural unit of the wolfram bronze (*45*), ultimately broke down at pressures of 30 GPa. Altogether, the results indicate that compression introduces additional entropy in the 1D-HEO—i.e., the structural disorder in the oxide in addition to the configurational entropy arising from the disorder of the metal cations resulting in the formation of amorphous HEO material.

These compression measurements on 1D-HEO thus reveal notable results, beginning with the disordering of the Sleight structure, consistent with the anomalous equation of state (EOS) with its negative K_0'. This disordering was followed by a first-order transition to a cubic phase, akin to structures found in other complex oxides, occurring near 15 GPa. The large volume change together with the changes in unit cell size and lattice parameters documented by the XRD indicated that the transition is first order and reconstructive. For such pressure-induced transitions, the mechanism would be nucleation and growth (*46*). This cubic phase further disordered on compression, ultimately leading to the formation of a fully x-ray amorphous HEO around 30 GPa (*45*, *47*). Notably, this behavior differs substantially from what has been reported with other HEOs under pressure (*48*, *49*).

We also note that the XRD data obtained for the 1D-HEO with and without a pressure medium appeared to follow a completely different trend, which is the stress measured at the anvil-sample interface and not that experienced by the bulk of the material, which was not compacted. This difference between hydrostatic and nonhydrostatic data (Fig. 4C) arose from the collapse of void space in the highly porous needlelike sample (i.e., without the pressure medium). The difference between the two curves is a measure of the compressive strength of the 1D-HEO material, which is indeed high (e.g., >5 GPa, where the sample begins to compress in Fig. 4C). The results are consistent with the hardness values obtained above (6.89 GPa). This conclusion was supported by the optical microscopy of a sample in Fig. 4E that showed the ribbonlike texture of the 1D-HEO transformed into a consolidated mass of material when subjected to uniaxial compression. Moreover, the state of the material persisted in recovery to ambient pressure at RT (Fig. 4E).

Loss of crystalline order was also observed in the sample without a pressure medium. At the highest pressures of these experiments (16 GPa), a broad amorphous band developed below the sample diffraction peaks. This sample also exhibited amorphization in the side concentric region, first observed at 11 GPa and remaining during subsequent compression and decompression. The appearance of the amorphous features in the x-ray data coincided with the onset of partial optical transparency viewed with backlit illumination between 12 and 16 GPa from a stereo microscope (fig. S31). Although the ambient sample appeared dark and optically opaque, these images showed a brown irislike glassy region that grew with increasing pressure before darkening. The results were consistent with higher compaction of the sample in the higher-pressure radial region of the sample.

To examine the optical properties, including possible changes in bandgap and potential metallization under pressure, we also measured the infrared absorption of the 1D-HEO in DACs using synchrotron radiation (*50*). These measurements showed that despite the opaque appearance of the material (figs. S31, S35, and S36), there is no evidence for bandgap closure at ambient or the pressure range investigated. In fact, the changes in the optical properties of the material described above were not intrinsic to the material but arose from substantial changes in light scattering owing to pressure-induced changes in sample texture and porosity.

Discussion

We successfully synthesized and comprehensively characterized (MoWNbTaV)O_3, a 1D-HEO with nanoribbon morphology. The 1D-HEO demonstrates notably high structural stability up to 1000°C, 12-GPa pressure, and harsh chemical environments (pH = 2.3 and 13 for 7 days). It also exhibits notable wear resistance and mechanical properties, with a resilience modulus of 40 MJ/m^3 and a hardness of 6.89 GPa. High-pressure experiments reveal a transformation near 15 GPa, forming a cubic HEO, and further transition to amorphous HEO at higher pressures, suggesting a previously unknown class of high-entropy materials. This combination of high hardness and high modulus of resilience would make our 1D-HEO an ideal candidate for applications that require high wear resistance, high energy absorption, and shock resistance. These findings also offer a way to create resilient materials for diverse applications in challenging environments.

REFERENCES AND NOTES

1. B. Gludovatz *et al.*, *Science* **345**, 1153–1158 (2014).
2. A. Gali, E. P. George, *Intermetallics* **39**, 74–78 (2013).
3. J. W. Yeh *et al.*, *Adv. Eng. Mater.* **6**, 299–303 (2004).
4. Q. Ding *et al.*, *Nature* **574**, 223–227 (2019).
5. H. Wang *et al.*, *Sci. Adv.* **7**, eabe3105 (2021).
6. J. Hu *et al.*, *Nat. Commun.* **14**, 5717 (2023).
7. L. Feng, W. Chen, W. G. Fahrenholtz, G. E. Hilmas, *J. Am. Ceram. Soc.* **104**, 419–427 (2021).
8. P. Sarker *et al.*, *Nat. Commun.* **9**, 4980 (2018).
9. A. Calzolari *et al.*, *Nat. Commun.* **13**, 5993 (2022).
10. M. Esters *et al.*, *Nat. Commun.* **12**, 5747 (2021).
11. B. Ye, T. Wen, K. Huang, C. Wang, Y. Chu, *J. Am. Ceram. Soc.* **102**, 4344–4352 (2019).
12. T. Jin *et al.*, *Adv. Mater.* **30**, e1707512 (2018).
13. J. Cavin *et al.*, *Adv. Mater.* **33**, e2100347 (2021).
14. M. Cui *et al.*, *Adv. Energy Mater.* **11**, 2002887 (2021).
15. Y. Li *et al.*, *Nat. Commun.* **14**, 3171 (2023).
16. C. M. Rost *et al.*, *Nat. Commun.* **6**, 8485 (2015).
17. W. Wang *et al.*, *Nano Energy* **124**, 109482 (2024).
18. H. Gao *et al.*, *Adv. Energy Mater.* **14**, 2304529 (2024).
19. A. Sarkar *et al.*, *J. Eur. Ceram. Soc.* **37**, 747–754 (2017).
20. C. R. McCormick, R. E. Schaak, *J. Am. Chem. Soc.* **143**, 1017–1023 (2021).
21. Y. Ikeda, B. Grabowski, F. Körmann, *Mater. Charact.* **147**, 464–511 (2019).
22. S. Wei *et al.*, *Nat. Mater.* **19**, 1175–1181 (2020).
23. V. R. Naganaboina, M. Anandkumar, A. S. Deshpande, S. G. Singh, *ACS Appl. Nano Mater.* **5**, 4524–4536 (2022).
24. G. Cao *et al.*, *Nature* **619**, 73–77 (2023).
25. M. Stygar *et al.*, *J. Eur. Ceram. Soc.* **40**, 1644–1650 (2020).
26. B. Kombaiah, K. Jin, H. Bei, P. D. Edmondson, Y. Zhang, *Mater. Des.* **160**, 1208–1216 (2018).
27. P. Li *et al.*, *ACS Catal.* **12**, 11667–11674 (2022).
28. A. Sarkar *et al.*, *J. Eur. Ceram. Soc.* **38**, 2318–2327 (2018).
29. S. S. Aamlid, M. Oudah, J. Rottler, A. M. Hallas, *J. Am. Chem. Soc.* **145**, 5991–6006 (2023).
30. J. Hao *et al.*, *Nat. Commun.* **13**, 2662 (2022).
31. J. Dong, X. Feng, X. Hao, W. Kuang, *Scr. Mater.* **204**, 114127 (2021).
32. K. Chen *et al.*, *J. Eur. Ceram. Soc.* **38**, 4161–4164 (2018).
33. K. Yuan *et al.*, *J. Adv. Ceram.* **11**, 882–892 (2022).
34. Y. Yao *et al.*, *Science* **359**, 1489–1494 (2018).
35. A. Abdelhafiz, B. Wang, A. R. Harutyunyan, J. Li, *Adv. Energy Mater.* **12**, 2200742 (2022).
36. A. H. Phakatkar *et al.*, *Langmuir* **37**, 9059–9068 (2021).
37. B. Yang *et al.*, *Nat. Mater.* **21**, 1074–1080 (2022).
38. X. Li *et al.*, *Adv. Funct. Mater.* **34**, 2411216 (2024).
39. Y. Yang *et al.*, *J. Power Sources* **482**, 228959 (2021).
40. T. X. Nguyen *et al.*, *Chem. Eng. J.* **430**, 132658 (2022).
41. A. Sarkar *et al.*, *Nat. Commun.* **9**, 3400 (2018).
42. A. W. Sleight *et al.*, *Acta Chem. Scand.* **20**, 1102–1112 (1966).
43. A. Krella, *Coatings* **10**, 921 (2020).
44. G. Chow, R. S. Bedi, Y. Yan, J. Wang, *Microporous Mesoporous Mater.* **151**, 346–351 (2012).
45. I. P. Roof, M. D. Smith, H.-C. zur Loye, *Solid State Sci.* **12**, 1941–1947 (2010).
46. C. Lin *et al.*, *J. Appl. Phys.* **119**, 045902 (2016).
47. M.-C. Saine, M. Gasperin, J. Jové, A. Cousson, *J. Less Common Met.* **132**, 141–148 (1987).
48. B. Cheng *et al.*, *Mater. Today Adv.* **8**, 100102 (2020).
49. B. Cheng *et al.*, *Commun. Chem.* **2**, 114 (2019).
50. J. L. Musfeldt *et al.*, *Proc. Natl. Acad. Sci. U.S.A.* **121**, e2312571121 (2024).
51. P. Vinet, J. Ferrante, J. H. Rose, J. R. Smith, *J. Geophys. Res.* **92**, 9319–9325 (1987).
52. Y. Akahama, H. Kawamura, *J. Appl. Phys.* **100**, 043516 (2006).

ACKNOWLEDGMENTS

We are grateful to R. Ripani, R. Hrubiak, Y. Meng, and C. Malliakas for help with the experiments. **Funding:** This work was supported by US National Science Foundation (NSF) grants DMR-1729420, DMR-2119308, and DMR-2118020 and by US Department of Energy–National Nuclear Security Administration (DOE-NNSA) cooperative agreement DE-NA-0003975 [Chicago/DOE Alliance Center (CDAC)]. Synchrotron XRD experiments were performed at HPCAT (Sector 16), Advanced Photon Source (APS), Argonne National Laboratory (ANL). HPCAT operations are supported by DOE-NNSA's Office of Experimental Sciences. The APS is a DOE Office of Science User Facility operated for the DOE Office of Science by ANL under contract no. DE-AC02-06CH11357. Synchrotron infrared experiments were performed at the Frontier Infrared Spectroscopy (FIS) at the National Synchrotron Light Source II (NSLS-II), Brookhaven National Laboratory (BNL). FIS is supported by DOE-NNSA (CDAC) and by the NSF grant EAR−2223273 [Synchrotron Earth and Environmental Science (SEES)]. The NSLS-II is a DOE Office of Science User Facility operated by the DOE Office of Science by BNL under contract no. DE-SC0012704. Z.H. acknowledges the support of the Swedish Research Council Formas (2020-00831), the Swedish Research Council (VR, 2022-02939), the Guangdong Basic and Applied Basic Research Foundation (2024B1515020078), the Guangdong Innovative and Entrepreneurial Research Team Program (2023ZT10C139), and the GJYC program of Guangzhou (2024D03J0001). The authors acknowledge the use of the Nanotechnology Core Facility (NCF) and Electron Microscopy Core Facility of UIC's Research Resources Center (RRC) and Northwestern University's NUANCE, IMSERC, and EPIC Centers. **Author contributions:** H.S., P.S., and A.A. synthesized the materials. SEM-EDS was led by H.S. and performed by H.S., S.W., and P.S. RT powder XRD was performed by H.S., J.C., and K.K. H.S. performed in situ high-temperature XRD. P.S. performed TGA, AFM, and chemical testing. H.S. and S.N. performed XPS. H.S. and I.P. performed ICP experiments. I.P. prepared samples for SEM after high-pressure; double-checked synthesis, SEM, XRD, XPS, and AFM results; and helped with outlining the manuscript. A.S.-K. led the work and supervised P.S., H.S., S.N., and I.P. H.F., M.D., M.A., Z.L., and R.J.H. were responsible for the high-pressure experiments, analysis, and text. T.Y., S.Fe., and Z.H. performed 3DED and high-resolution TEM (HRTEM) characterization of crystal structure. S.Fa. performed the DFT calculations and Wulff shape predictions. S.K. supervised S.Fa. A.K. performed nanoindentation characterization. J.W. supervised A.K. All authors contributed to the write-up of the manuscript. **Competing interests:** The authors declare no conflicts of interest, including financial interests or any patents filed related to this work. **Data and materials availability:** All data are available in the main text or the supplementary materials.

License information: Copyright © 2025 the authors, some rights reserved; exclusive licensee American Association for the Advancement of Science. No claim to original US government works. https://www.science.org/about/science-licenses-journal-article-reuse

SUPPLEMENTARY MATERIALS

science.org/doi/10.1126/science.adr5604
Materials and Methods; Supplementary Text; Figs. S1 to S45; Tables S1 to S17; References (*53*–*123*)

Submitted 7 July 2024; accepted 10 April 2025

10.1126/science.adr5604

SOLAR CELLS

Vapor-assisted surface reconstruction enables outdoor-stable perovskite solar modules

Xiangnan Sun[1]†, Wenda Shi[2]†, Tianjun Liu[3], Jinzhan Cheng[1], Xin Wang[4], Peng Xu[1], Wei Zhang[1], Xiaoming Zhao[1]*, Wanlin Guo[1]*

Natural illumination variations in light-dark cycles induce irreversible ion migration in perovskite solar cells, posing substantial challenges to their long-term outdoor operational stability. We addressed this issue by isolating defective octahedra at the perovskite surface using a vapor-deposited polydentate ligand. Surface octahedra isolation suppresses ion migration into the charge transport layer and reduces surface ionic defects, modulating the kinetics of ion migration during light-dark cycles. Our 785-square-centimeter industrial-scale perovskite solar modules achieved a power conversion efficiency (PCE) of 19.6%. Our modules demonstrated enhanced diurnal stability, retaining more than 97% of their initial PCE even after 101 light-dark cycles at 50°C. Our perovskite modules maintained stable power output during 45 days of outdoor operation under severe summer conditions, exhibiting stability comparable with that of the reference silicon cell.

During the past decade, perovskite solar cells (PSCs) have experienced rapid advancements in certified power conversion efficiency (PCE) up to 27%, which approaches the level of commercial silicon-based solar cells (*1*). In terms of fabrication costs, PSCs are projected to be approximately half the cost of crystalline silicon–based solar cells (*2*, *3*). However, their long-term operational stability has yet to meet the necessary requirements for photovoltaic products, presenting challenges for commercialization (*4*–*8*). This issue is particularly pronounced for industrial-scale solar modules, for which achieving scalable stability remains a formidable task. In addition, most studies have focused on the long-term aging behavior of laboratory-scale PSCs under constant indoor light conditions, but addressing the outdoor stability of industrial-scale perovskite solar modules (PSMs) is essential before this technology can be commercialized (*9*).

Under operating conditions, PSCs experience light-dark cycles that result in both reversible and irreversible performance losses during cyclic operation (*10*–*12*). The inherently soft ionic crystal structure of perovskites renders their ionic bonds relatively weak, making them susceptible to the formation of ionic defects within the perovskite lattice. Furthermore, the low activation energy required for ion migration makes these defects prone to movement under operational conditions, ultimately compromising the device's life span (*12*–*14*).

In PSCs, both reversible and irreversible ion migrations occur, with the latter resulting from mobile ions migrating from the perovskite layer into the charge transport layer or electrode under combined aging stressors. This migration can lead to permanent damage to device performance (*15*, *16*). To mitigate irreversible ion migration, the main strategies used in small-area unit cells are passivating surface defects to reduce the number of mobile ionic channels (*5*, *17*) and inserting a barrier layer at interfaces to suppress ionic motion (*16*, *18*). Studies indicate that the $[PbI_6]^{4-}$ octahedra near the perovskite surface are typically more defective than those in the crystal interior, making these regions particularly vulnerable to irreversible halide ion migration (*19*, *20*). For large-area PSCs, ion migration within the perovskite absorption layer must be limited. Isolating the defective octahedra and simultaneously reducing ionic channels through reconstructing the perovskite surface structure would contribute to enhancing the outdoor operational stability of perovskite solar modules.

In this study, we isolated ion migration within the perovskite absorption layer by reconstructing the perovskite surface into a zero-dimensional (0D) structure, in which $[PbI_6]^{4-}$ octahedra are separated by a vapor-deposited polydentate ligand. This modification effectively blocked the migration of iodide ions into the charge transport layer and reduced surface ionic defects, modulating the kinetics of ion migration during light-dark cycles. Additionally, this vapor-phase post-treatment facilitated large-scale stabilization of the perovskite surface. The surface octahedra isolation strategy enabled us to fabricate small-area unit cells (active area = 0.16 cm^2) and large-area PSMs (aperture area = 785 cm^2) with efficiencies of 25.3 and 19.6%, respectively. Our solar modules demonstrated enhanced diurnal stability with projected T_{80} lifetimes (time to 80% of efficiency remaining) of 2478 cycles, which is equivalent to more than 6.7 years under light-dark operation at 25°C. Encouragingly, after 45 days of outdoor operation under real-world conditions, our PSMs exhibited stability comparable with that of a commercial silicon solar cell, underscoring our PSMs' viability for practical applications.

Surface octahedra isolation

The concept of perovskite surface octahedra isolation is illustrated in Fig. 1A. To reconstruct the perovskite surface into a 0D framework in which $[PbI_6]^{4-}$ octahedra are separated from one another, we treated the preformed $FAPbI_3$ perovskite film with vapor-deposited 2,2′:6′,2′-terpyridine (Tpy), a polydentate ligand that forms the 0D framework $(Tpy)_2PbI_6$ when mixed with PbI_2 (fig. S1). We have previously demonstrated that vapor-phase fluoride treatment enables the large-scale stabilization of perovskite films (*9*).

To further enhance the mildness of the reaction and address instrument limitations for practical production, we used vapor deposition of Tpy for large-scale stabilization of the perovskite films (supplementary text 1 and fig. S2). Grazing-incident wide-angle x-ray scattering (GIWAXS) patterns (Fig. 1B) showed a new reflection emerging on $FAPbI_3$ films (referred to as "pristine") after Tpy treatment (referred to as "isolated"), corresponding to the (020) reflections of 0D $(Tpy)_2PbI_6$. Increasing the incident angle of the x-ray beam resulted in a decrease in the relative intensity of this reflection (Fig. 1C), suggesting that the emerging 0D structure preferentially formed on the $FAPbI_3$ surface, which was further verified with transmission electron microscope images that showed 0D $(Tpy)_2PbI_6$ on the surface of $FAPbI_3$ perovskite (fig. S3) (*21*). From scanning electron microscopy (SEM) images (fig. S4), evident pinholes were observed on the surface of the pristine film. After the surface octahedra isolation treatment, these pinholes were nearly eliminated, resulting in a more uniform and dense morphology. The emerging 0D structure at the perovskite surface remained stable under combined light and thermal stressors, showing no substantial changes after 900 hours of aging under 1-sun illumination at 85°C (fig. S5).

We performed x-ray photoemission spectroscopy (XPS) measurements to probe the perovskite surface chemistry after the surface treatment. The Pb 4f (Fig. 1D) and I 3d (fig. S6) peaks both shifted to higher binding energies after the surface octahedra isolation, indicating a

---

[1]Institute for Frontier Science, State Key Laboratory of Mechanics and Control of Mechanical Structures, Key Laboratory for Intelligent Nano Materials and Devices of the Ministry of Education, Nanjing University of Aeronautics and Astronautics, Nanjing, China. [2]School of Chemistry and Chemical Engineering, Northwestern Polytechnical University, Xi'an, China. [3]Department of Physics, Chemistry, and Biology (IFM), Linköping University, Linköping, Sweden. [4]School of Energy and Materials, Shanghai Key Laboratory of Engineering Materials Application and Evaluation, Shanghai Polytechnic University, Shanghai, China. ***Corresponding author. Email: xiaoming.zhao@nuaa.edu.cn (X.Z.); wlguo@nuaa.edu.cn (W.G.)** †These authors contributed equally to this work.

strong interaction between Tpy and $[PbI_6]^{4-}$ that contributed to the increased stability of the octahedra. We used time-resolved photoluminescence (TRPL) to study the charge-carrier dynamics in pristine and isolated perovskite films. The decay lifetime of the perovskite films increased from 133.7 to 532.6 ns after treatment, signifying fewer nonradiative recombination centers in the isolated perovskite films (fig. S7A). Upon depositing an electron transporting layer (ETL), the isolated sample showed a faster decay than that of the pristine sample, suggesting that surface octahedra isolation enhances interfacial charge extraction (fig. S7B) (*22*). Density functional theory (DFT) calculations revealed that the formation energies of most typical defects near the perovskite surface increased after the surface octahedra isolation treatment (fig. S8A). Furthermore, the activation energy of ion migration for the isolated sample (0.68 eV) was substantially higher than that for the pristine sample (0.43 eV), as determined by fitting the temperature-dependent electrical conductivity (Fig. 1E). This experimental result was in good agreement with the findings from the DFT calculations (fig. S8B). These results indicate that ion migration was effectively suppressed in the perovskite films subjected to the surface octahedra isolation treatment.

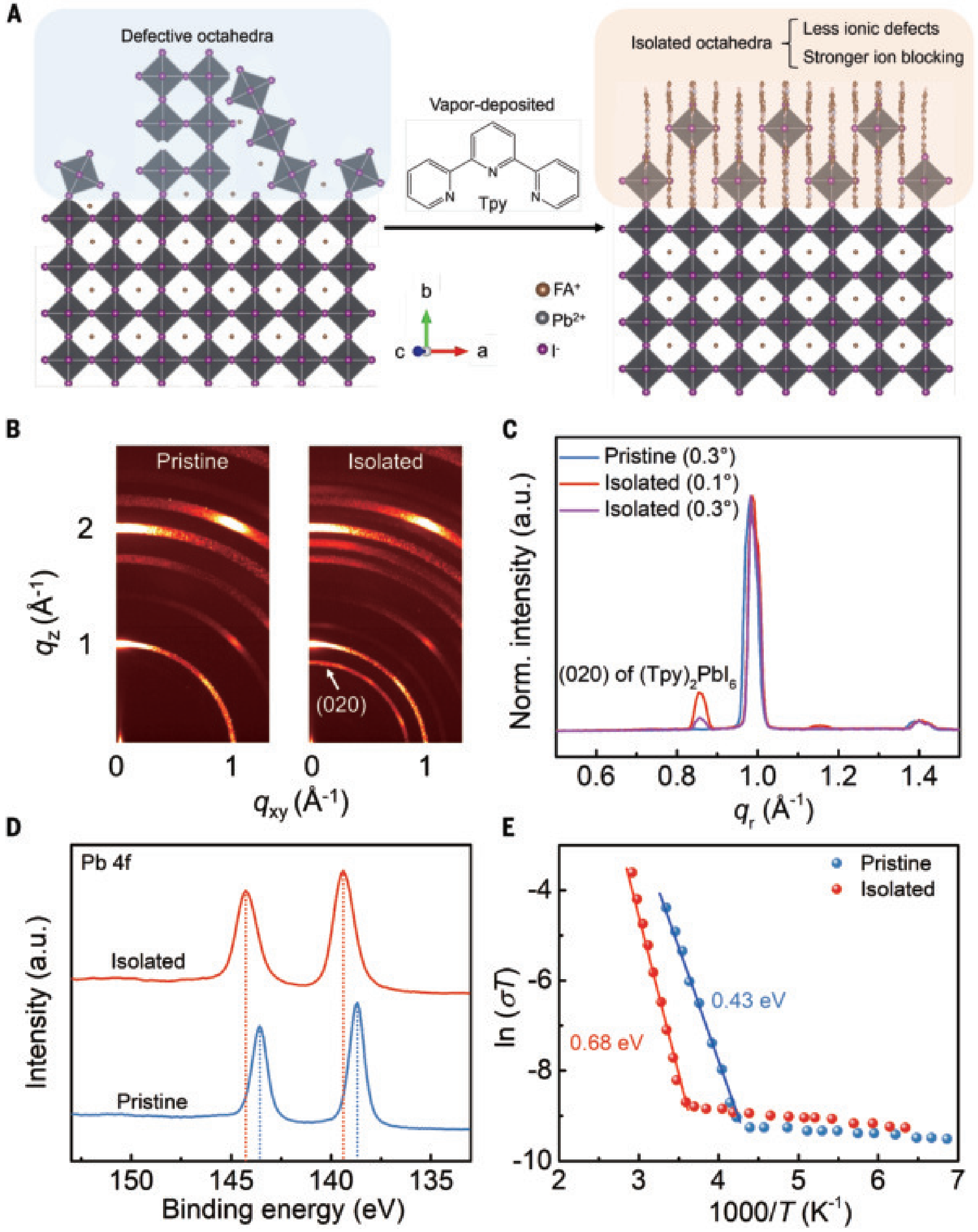

Fig. 1. Perovskite surface octahedra isolation. (**A**) Schematic illustration of surface octahedra isolation. (**B**) GIWAXS patterns of FAPbI$_3$ film ("Pristine") and FAPbI$_3$ film treated with Tpy ("Isolated") taken at an incident angle of 0.10° (surface-sensitive). (**C**) Azimuthally integrated GIWAXS traces collected on pristine and isolated samples at incident angles of 0.10° (more surface-sensitive) and 0.30° (less surface-sensitive). (**D**) XPS Pb 4f spectra and (**E**) temperature-dependent conductivity of pristine and isolated films.

Photovoltaics and stability of the devices

To evaluate the impact of surface treatment on solar cell performance, we fabricated single cells with an active area of 0.16 cm^2 and large-area modules with aperture areas of 186 cm^2 (10 subcells) and 785 cm^2 (46 subcells), respectively. Photovoltaic characterization of representative as-fabricated devices is shown in Fig. 2, A and B, and figs. S9 to S15 and listed in tables S1 and S2, with population statistics shown in figs. S16 to S20. For small-area devices, the champion isolated device achieved a short-circuit current density (J_{SC}) of 25.8 mA cm^{-2}, an open-circuit voltage (V_{OC}) of 1.18 V, and a fill factor (FF) of 0.83, resulting in a PCE of 25.3%, compared with 23.0% for the champion pristine device. The surface treatment enabled reduced ideality factor from 1.66 to 1.21 (fig. S21), decreased density of trap states from 3.74×10^{15} to 1.57×10^{15} cm^{-3} (fig. S22), and greatly lowered shallow defects by an order of magnitude (fig. S23). These results illustrate the beneficial impact of surface octahedra isolation treatment in decreasing defect density and suppressing nonradiative recombination, accounting for the enhanced solar cell performance.

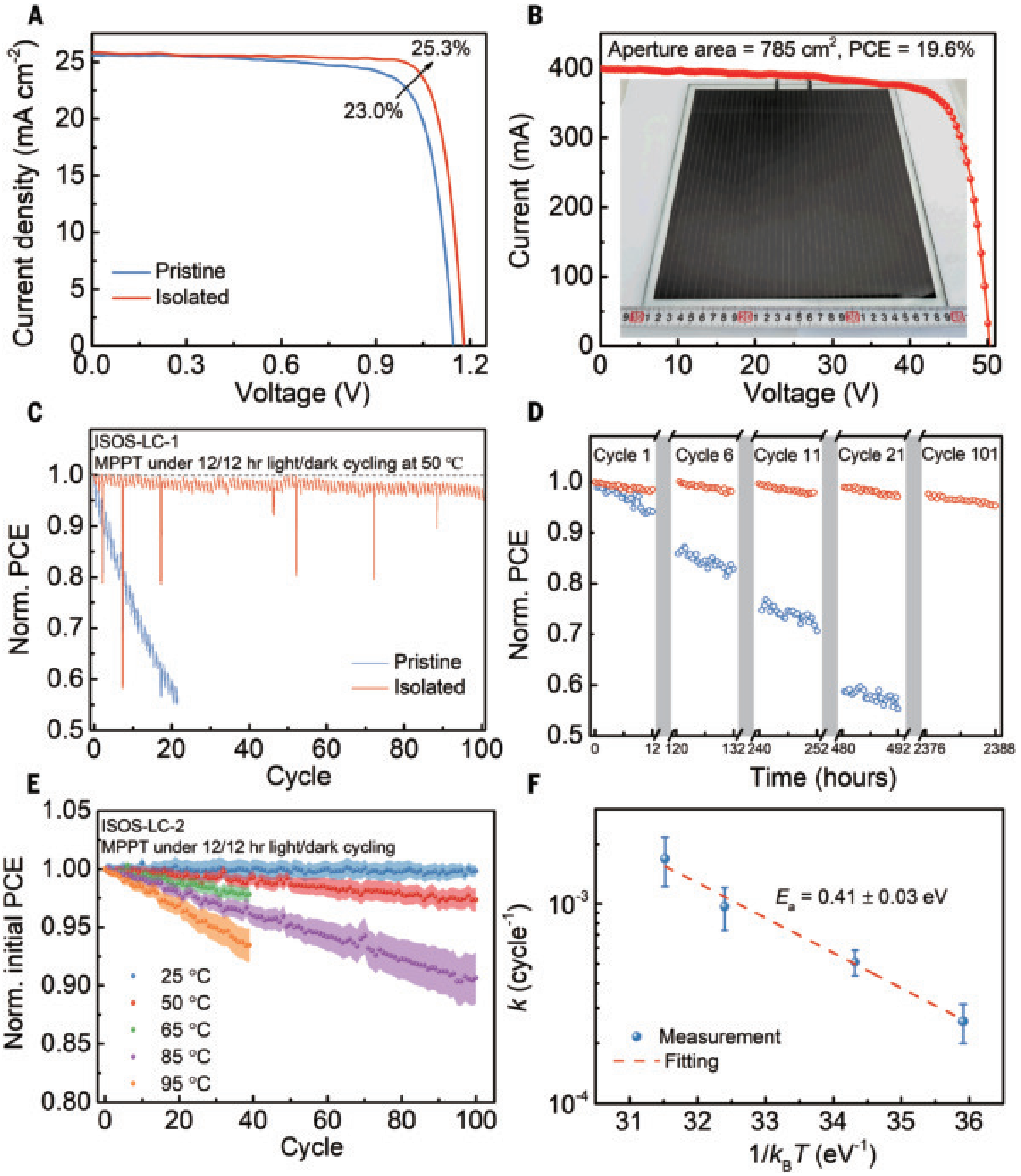

Fig. 2. Device performance and stability. (**A**) *J-V* characteristics of 0.16-cm^2 pristine and isolated solar cells. (**B**) *I-V* characteristics of the champion solar modules with an aperture area of 785 cm^2. (Inset) The module photograph. The substrate dimensions are 30 by 30 cm, which corresponds to a total area of 900 cm^2. The aperture area (illuminated region) is specifically 785 cm^2, whereas the active area (electrically functional portion) measures 730 cm^2. The geometric fill factor (GFF; the ratio between the active area and the aperture area) is calculated to be 0.93. (**C**) Normalized PCE and (**D**) selected cycles of encapsulated pristine and isolated PSMs operating under 12-hour light-dark cycling at 50°C. Data points are derived from one representative device for each condition. (**E**) Normalized initial PCE for each cycle (the starting PCE of each cycle normalized to the starting PCE of the first cycle) for isolated PSMs operating under 12-hour light-dark cycling at temperatures of 25°, 50°, 65°, 85°, and 95°C, respectively. Data points and error bars indicate average values and standard deviations calculated from three devices at each temperature. The PSMs were encapsulated. The relative humidity during these tests was maintained at 45 ± 7%. (**F**) Degradation rate *k* obtained from linear fits to PCE degradation versus $1/k_BT$, where T is the aging temperature and k_B is the Boltzmann constant. The fitted value for the device operating at 25°C was not included because it exhibited no clear degradation trend over the entire 101 cycles.

Vapor-phase treatment facilitated large-scale stabilization of the perovskite surface. The 186-cm^2 isolated modules exhibited a champion aperture-area PCE of 20.2% (fig. S13) with a V_{OC} of 11.3 V, a J_{SC} of 2.29 mA cm^{-2}, and an FF of 0.78, outperforming the pristine module with champion PCE of 17.4% (fig. S14). Current density-voltage (I-V) characteristics and the photograph of as-fabricated 785 cm^2 solar modules are shown in Fig. 2B. We achieved an aperture-area PCE of 19.6% (V_{OC} = 50.1 V, I_{SC} = 399 mA, and FF = 0.77), which corresponds to an active-area PCE of 21.1% (geometric FF = 0.93). This result indicates that our surface treatment strategy is scalable and offers an opportunity for improving the industrial-scale PSMs.

To maximize the simulation of the real-world operational condition, we conducted diurnal cyclic aging (12 hours light and 12 hours dark) at 50°C following the International Summit on Organic PV stability (ISOS) light-dark 1 protocol. As shown in Fig. 2C, the pristine module remained only ~55% of its initial PCE after 20 light-dark cycles, whereas the isolated module exhibited reversible PCE losses and retaining over 97% of its initial PCE even after 101 light-dark cycles at 50°C, which represents one of the most stable PSCs operating under light cycling (fig. S24 and table S3) (*10*, *11*, *23–32*). The stability of the pristine device closely resembles the current state of the art in the literature when fabricated at a small area, with much of the instability in these pristine devices attributed to area scaling (fig. S25 and table S3).

We further performed detailed analysis for PCE evolution in representative cycles (Fig. 2D). In the first cycle, the pristine module showed slight irreversible PCE loss. As the number of cycles increased, the pristine module continued to suffer from more pronounced fatigue behavior. By contrast, the isolated module maintained nearly stable power output throughout the test, implying that the surface octahedra isolation strategy inhibited irreversible degradation during light-dark cycles.

To determine a meaningful lifetime for our isolated PSMs at the standard temperature, we conducted thermally accelerated aging studies following methodologies outlined in previous reports (*4*, *6*, *9*). These PSMs underwent aging at their maximum power point under 1-sun illumination with 12/12-hour light-dark cycling at 25°, 50°, 65°, 85°, and 95°C, respectively. The evolution of the normalized initial PCEs (the starting PCE of each cycle normalized to the starting PCE of the first cycle), averaged from three PSMs at each temperature, is depicted in Fig. 2E. The trends for normalized J_{SC}, V_{OC}, and FF are shown in fig. S26. The initial PCEs of the PSMs are summarized in tables S4 and S5.

The PCE degradation was temperature dependent and was fitted to a linear function, except for the data acquired on modules operating at 25°C, for which no appreciable PCE degradation was observed (Fig. 2E). The temperature-dependent degradation rates were further plotted as a function of the inverse temperature, which we fitted to an Arrhenius temperature-dependence model (Fig. 2F) (*4*, *6*, *33–35*). The degradation rates could be effectively described by a single Arrhenius function across the entire temperature, suggesting that a consistent degradation mechanism operates throughout this range—a prerequisite for a reliable accelerated aging test (*36*). With this analysis, we obtained a degradation activation energy (E_a) of approximately 0.41 eV.

To extract a meaningful degradation rate at standard operating condition, k_{ref}, from the accelerated degradation rate at high temperatures, k_{acc}, we calculated the acceleration factor (AF) (*33*)

$$\mathrm{AF} = \frac{k_{acc}}{k_{ref}} = \exp\left[\frac{E_a}{k_B}\left(\frac{1}{T_{ref}} - \frac{1}{T_{acc}}\right)\right] \quad (1)$$

where T_{acc} and T_{ref} represent the temperatures during aging at accelerated and standard operating conditions, respectively; the latter is defined to be 25°C under 1-sun illumination with 12/12-hour light-dark cycling. The calculated AF is approximately 21 at 95°C.

With this comprehensive dataset, we can extract the T_{80} lifetime for isolated PSMs operating at the standard temperature of 25°C. On the basis of the T_{80} of 118 cycles extrapolated for PSMs operating under 12/12-hour light-dark cycling at 95°C, and with an AF of 21, we estimated an intrinsic T_{80} lifetime of 2478 cycles (equivalent to over 6.7 years) for our isolated PSMs under 12/12-hour light-dark cycling at 25°C.

Outdoor aging tests

Encouraged by the results from diurnal cyclic aging tests, we aimed to evaluate the reliability of our solar modules under real-world outdoor conditions. Collecting outdoor data from multiple climates is an essential step in the commercialization of PSCs because variations in outdoor temperature, relative humidity, solar radiation intensity, and the cycling of these factors substantially affect the stability of the devices. We tracked the power output of our isolated PSMs under real-world conditions, following the ISOS outdoor O-2 protocol. To maximize the resistance of our solar modules to external stressors, we developed a multilayer encapsulation technique, with further details provided in the supplementary materials, materials and methods. A photograph of the encapsulated 785 cm^2 module is provided in Fig. 3A, and the encapsulation schematic is illustrated in Fig. 3B. In Fig. 3, C and D, we present outdoor data recorded on a rooftop test field during a high-irradiance summer period in Suzhou, China, for our modules under tracking. During this field test, a commercial polysilicon solar cell was also studied under the same conditions for comparison.

As shown in Fig. 3, C and D, the encapsulated module maintained a fairly constant power output after being placed in the outdoor environment for more than 45 days during the relatively high-temperature and -humidity summer period. To track outdoor stability, we used the performance ratio (PR) metric, which is the ratio between the produced and expected power over 1 day or cycle (*32*, *37*, *38*). The PR values of the perovskite module were closely comparable with those of the Si reference cells during the 45 days of operation, implying comparable operational stability to the reference Si cell. Using another metric—midday power ratio—produced qualitatively similar results (fig. S27). Temperature-dependent analyses suggest that Si cells exhibited a relatively stronger response to temperature changes as compared with that of perovskite modules (fig. S28). This difference may be attributed to the reported lower temperature coefficient of PSCs compared with Si cells (*32*, *39*).

As shown in Fig. 3, E and F, the daily trends in outdoor PCE ($\mathrm{PCE}_{outdoor}$) remained consistent: It decreased from morning to midday and then slightly recovered from midday to evening, likely owing to the drop in temperature (fig. S28). We observed that the daily decay of $\mathrm{PCE}_{outdoor}$ recovered overnight, as illustrated by trends over 5 selected days (Fig. 3E). Similar photovoltaic parameter recovery has been observed for PSCs (*40*, *41*) and perovskite-Si tandem solar cells (*18*). Our observed pattern mirrored our indoor light cycling studies, which also showed reversible performance degradation over consecutive days caused by overnight recovery.

To evaluate the performance of our perovskite module before and after outdoor operation, we compared its PCE tested under standard test conditions (STC). After 45 days of outdoor exposure, the PCE value (19.5%) was nearly identical to that measured before operation (19.6%) (Fig. 3F). This comparison further confirmed that there was no appreciable degradation of our solar modules after 45 days of outdoor operation. Furthermore, our modules also demonstrated stability comparable with that of Si cells after 18 days of operation in winter conditions (fig. S29).

Stabilization mechanism

To explore the underlying mechanism behind the enhanced stability induced by the isolated octahedra, we analyzed the photoluminescence (PL) evolution in both pristine and isolated perovskite films under a 12/12-hour light-dark cycling regimen (Fig. 4A). During the first cycle, the pristine sample exhibited rapid PL decay during the initial 12 hours of continuous light exposure, whereas the isolated sample demonstrated only a slight decline in PL intensity under the same conditions. The decrease in PL intensity during light-dark cycling has been attributed to illumination-induced ion migration within the perovskite films (*42*). After the dark recovery period, the PL intensity of the isolated sample nearly fully returned to its initial level. By contrast, during the subsequent cycles, the pristine sample exhibited a continuous decrease in PL intensity. This observation indicated that iodide ions underwent irreversible migration toward the perovskite surface as the duration of illumination increased (*10*). By contrast, the isolated sample exhibited negligible PL degradation throughout all the cycles.

We conducted a detailed analysis of the first four cycles (Fig. 4B). In the first cycle, the PL intensity of the pristine sample recovered to >98% of its initial value during the 12-hour dark resting period,

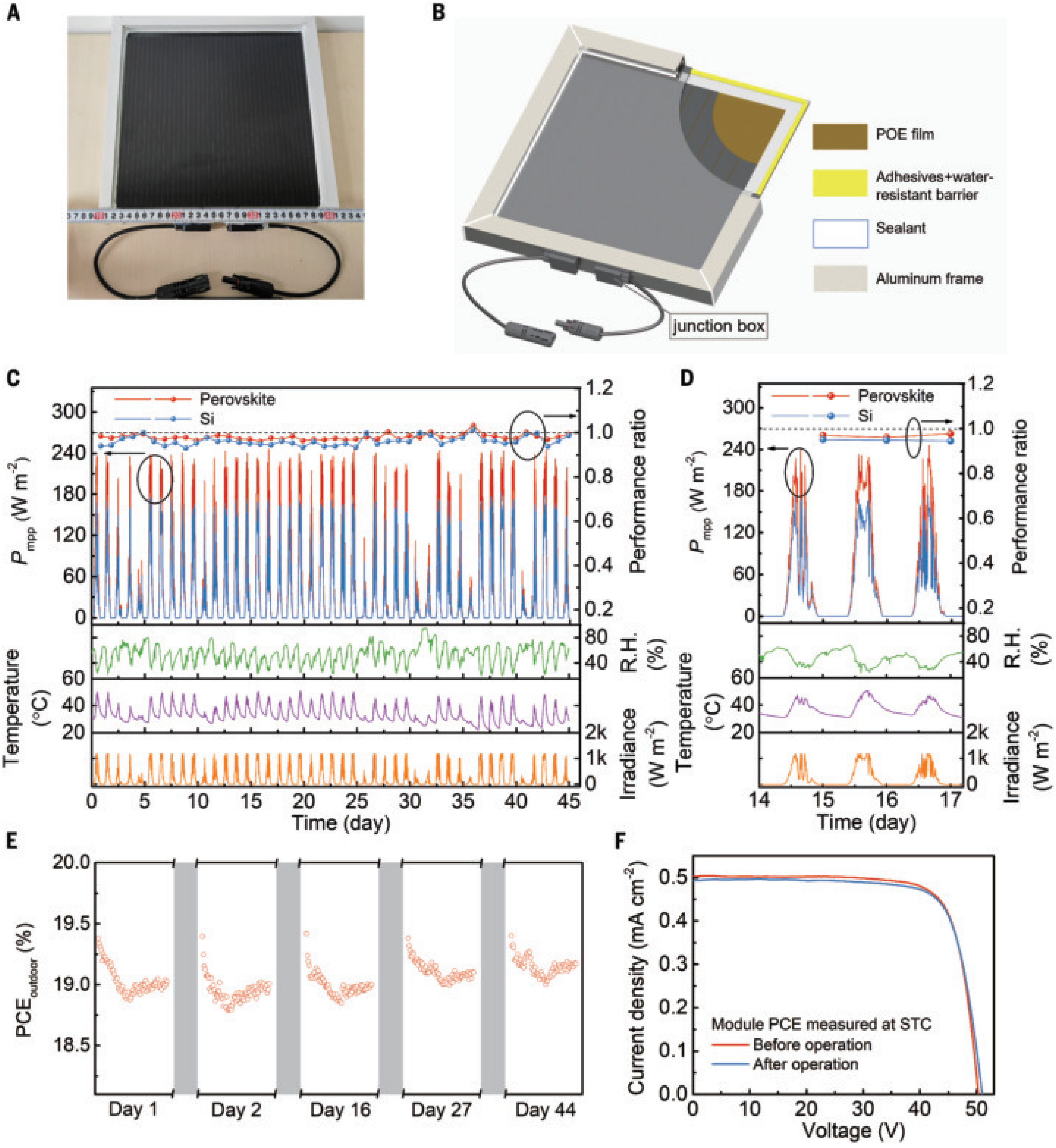

Fig. 3. Long-term outdoor stability. (**A**) Photograph of the encapsulated 785-cm^2 module. (**B**) Schematic representation of the encapsulation. (**C**) Outdoor power output of the encapsulated PSMs and the Si reference cell under real-world conditions (ISOS-O-2), including PR values. The time interval for PR calculation was set to 1 day (for example, the PR value for the first day of exposure is plotted on the *x* axis as 1). Temperature here refers to the measured module temperature. (**D**) Selected data over 3 consecutive days. (**E**) Diurnal variation of PCE$_{outdoor}$ for perovskite modules over 5 days, recorded from 7 a.m. to 7 p.m. (**F**) *J-V* characteristics of the PSM before and after 45 days of outdoor operation. The PCE measurements were conducted under STC.

implying a self-healing behavior associated with reversible ion migration. However, in subsequent cycles, the pristine sample exhibited noticeable fatigue behavior, with residual PL intensities decreasing as the number of cycles increased. The PL intensity of the isolated sample effectively retained its initial value after four cycles.

We further performed time-of-flight secondary-ion mass spectrometry (TOF-SIMS) analysis to investigate the compositional variations of fresh pristine and isolated solar modules before and after dark recovery (figs. S30 and S31). In the transition from the fresh pristine device to the pristine device after operation under light, the I^- ion intensity exhibited a prominent change, with a sharp increase at the ETL-electrode interface and a decrease at the perovskite-ETL interface. This observation implies the migration of iodine species from the perovskite to the ETL. The migration of iodine species and the

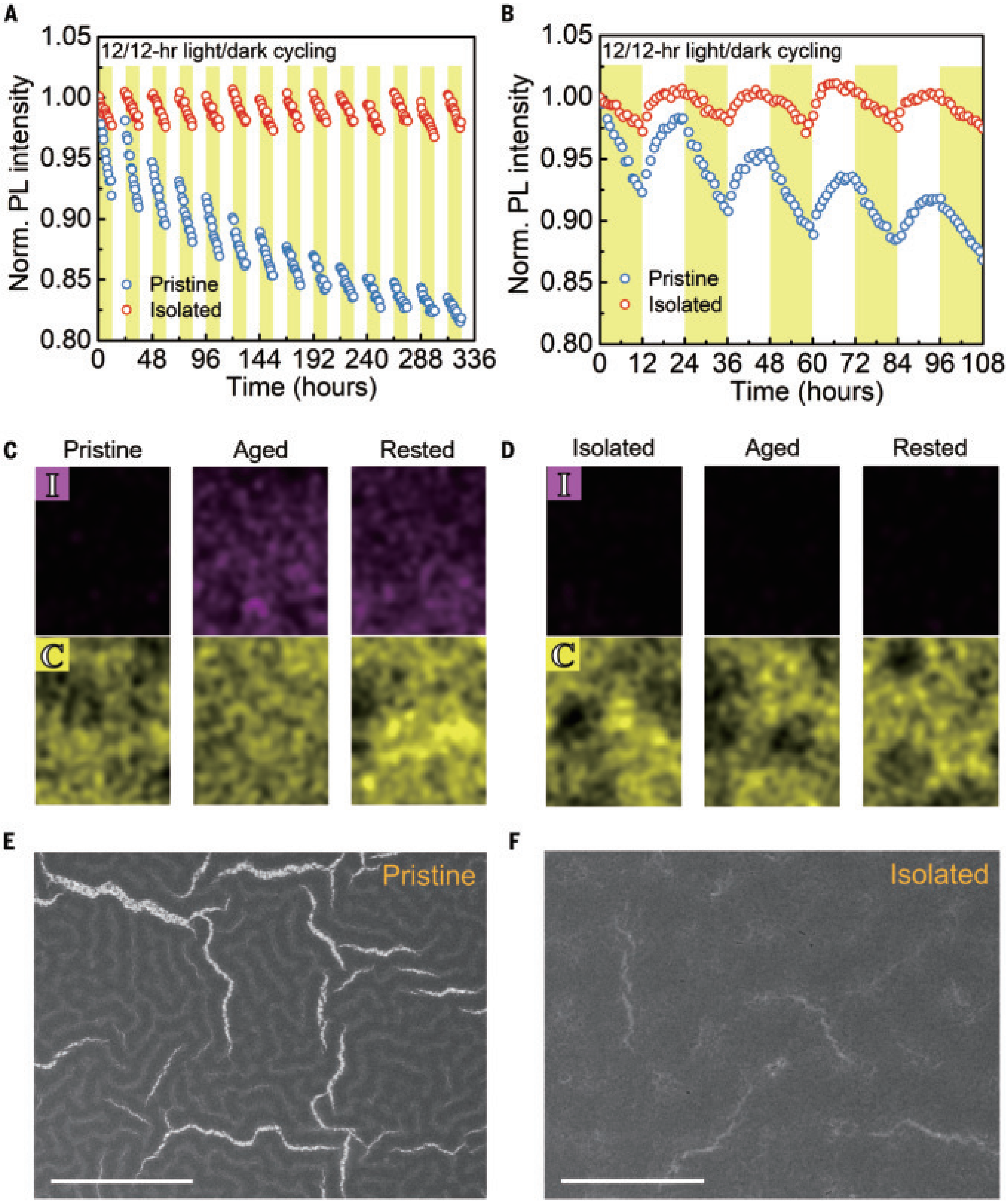

Fig. 4. Degradation mechanism. (**A**) Normalized PL intensity of pristine and isolated perovskite films with time. The samples were aged in nitrogen atmosphere under 12/12-hour light-dark cycles at 50°C. The light intensity is 100 mW cm^{-2}. PL spectra were measured every hour. (**B**) PL degradation and recovery dynamics of four cycles for pristine and isolated perovskite films. (**C** and **D**) STEM-EDX mapping in the ETL layer of fresh, aged (60 cycles of 12/12-hour light-dark cycling at 50°C) and rested (12 hours in dark at 50°C) (C) pristine and (D) isolated devices. (**E** and **F**) SEM images on the ETL layer of rested (E) pristine and (F) isolated devices. Scale bar, 10 μm.

formation of iodide vacancies could induce nonradiative recombination centers, decreasing device performance.

After the dark resting period, the iodine distribution near the ETL-electrode interface showed no substantial changes, whereas the iodine distribution near the ETL-perovskite interface demonstrated a recovery trend toward the original distribution observed in fresh cells. When PSCs are allowed several hours to recover in the dark, the ionic distribution returns to its initial state, making the device appear "fresh" (*10*). These previous findings aligned with our observations regarding iodide distribution near the ETL-perovskite interface, which could account for the reversible loss in our PSCs. However, when iodine migrated into the ETL, these highly corrosive iodine species could react with or dissolve the ETLs and may also interact with the metal electrode to form metal-halide compounds, such as metal iodides (*43*, *44*). Once this reaction occurred, the iodine species could not return to the perovskite layer, which resulted in the irreversible loss in our devices.

We then used scanning transmission electron microscopy with energy-dispersive x-ray spectroscopy (STEM-EDX) to further investigate the I element distribution on the surface of ETL layers by peeling off the electrode from the fresh, aged, and rested devices, respectively. Both fresh pristine and isolated samples detected no I signal (Fig. 4, C and D). After operation, a mass of I^- ions migrated into the ETL for the pristine sample (Fig. 4C). These I signals did not vanish even after the dark resting, implying the occurrence of irreversible I^- ion migration.

From the SEM images, we observed that the pristine sample exhibited obvious cracks and inhomogeneous surface morphology (Fig. 4E). By contrast, there was no obvious I signal on the ETL surface of isolated sample after light aging and dark resting (Fig. 4D). The surface morphology of ETL was still uniform and dense (Fig. 4F), likely because of the substantial suppression of irreversible I^- ion migration. The mobile iodine species are extremely corrosive (*43*) and could react with or dissolve ETL and create pinholes and nonuniformity in the ETL (*44*). These results provided strong evidence that the surface octahedra isolation treatment effectively blocks the migration of iodide ions from the perovskite layer into the ETL, contributing to enhanced stability.

Discussion

We have developed a vapor-assisted surface reconstruction strategy that achieves uniform stabilization of industrial-scale perovskite solar modules. The isolated surface octahedra effectively inhibit the migration of iodide ions into the charge transport layer and reduce surface ionic defects, minimizing irreversible degradation during light cycling. Consequently, we achieved accelerated-aging–projected T_{80} lifetimes exceeding 6.7 years for our isolated solar modules operating under 12/12-hour light-dark cycling at 25°C, although other degradation modes not considered here may emerge with continued testing. Under relatively severe outdoor summer conditions, our isolated modules show reversible performance recovery overnight and exhibit outdoor stability comparable with that of commercial Si solar cells, indicating their potential to meet industrial standards. We anticipate that our findings will not only enhance the mechanistic understanding of mobile ionic defects that lead to irreversible device degradation but also facilitate the advancement of perovskite devices capable of meeting the demands of real-world applications.

REFERENCES AND NOTES

1. National Renewable Energy Laboratory, "Best research-cell efficiencies" (2025); https://www2.nrel.gov/pv/cell-efficiency.
2. L. Meng, J. You, Y. Yang, *Nat. Commun.* **9**, 5265 (2018).
3. Z. Song *et al.*, *Energy Environ. Sci.* **10**, 1297–1305 (2017).
4. X. Zhao *et al.*, *Science* **377**, 307–310 (2022).
5. R. Azmi *et al.*, *Science* **376**, 73–77 (2022).
6. Q. Jiang *et al.*, *Nature* **623**, 313–318 (2023).
7. Y. Jiang *et al.*, *Angew. Chem. Int. Ed.* **63**, e202410721 (2024).
8. J. Zhang *et al.*, *Angew. Chem. Int. Ed.* **64**, e202413303 (2025).
9. X. Zhao *et al.*, *Science* **385**, 433–438 (2024).
10. Y. Zhang *et al.*, *Nat. Photonics* **17**, 1066–1073 (2023).
11. F. Huang *et al.*, *Nano Energy* **27**, 509–514 (2016).
12. K. Domanski *et al.*, *Energy Environ. Sci.* **10**, 604–613 (2017).
13. Z. Shen *et al.*, *Nat. Photonics* **18**, 450–457 (2024).
14. R. Gottesman *et al.*, *J. Phys. Chem. Lett.* **6**, 2332–2338 (2015).
15. C. Besleaga *et al.*, *J. Phys. Chem. Lett.* **7**, 5168–5175 (2016).
16. Y. Wang *et al.*, *Science* **365**, 687–691 (2019).
17. C. Chen *et al.*, *ACS Energy Lett.* **5**, 2560–2568 (2020).
18. M. De Bastiani *et al.*, *ACS Energy Lett.* **6**, 2944–2951 (2021).
19. Z. Ni *et al.*, *Science* **367**, 1352–1358 (2020).
20. Y. Lin *et al.*, *Energy Environ. Sci.* **14**, 1563–1572 (2021).
21. Y. Yuan *et al.*, *RSC Adv.* **11**, 24816–24821 (2021).
22. T. Kirchartz, J. A. Márquez, M. Stolterfoht, T. Unold, *Adv. Energy Mater.* **10**, 1904134 (2020).
23. Y. Shen *et al.*, *Nature* **635**, 882–889 (2024).
24. K. Domanski, E. A. Alharbi, A. Hagfeldt, M. Grätzel, W. Tress, *Nat. Energy* **3**, 61–67 (2018).
25. L. Jiang *et al.*, *Nano Energy* **58**, 687–694 (2019).
26. Y. Cheng *et al.*, *Adv. Mater.* **33**, e2006170 (2021).
27. X. Deng *et al.*, *Matter* **4**, 3301–3312 (2021).
28. F. Li *et al.*, *Adv. Energy Mater.* **12**, 2200186 (2022).
29. Y. Wang *et al.*, *Adv. Mater.* **36**, e2401416 (2024).
30. C. Zhu *et al.*, *Mater. Today Energy* **47**, 101757 (2025).
31. J. Barbé *et al.*, *J. Mater. Chem. C Mater. Opt. Electron. Devices* **8**, 1715–1721 (2020).
32. M. Khenkin *et al.*, *Energy Environ. Sci.* **17**, 602–610 (2024).
33. O. Haillant, D. Dumbleton, A. Zielnik, *Sol. Energy Mater. Sol. Cells* **95**, 1889–1895 (2011).
34. S. Züfle, R. Hansson, E. A. Katz, E. Moons, *Sol. Energy* **183**, 234–239 (2019).
35. Q. Burlingame *et al.*, *Nature* **573**, 394–397 (2019).
36. M. V. Khenkin *et al.*, *Nat. Energy* **5**, 35–49 (2020).
37. Q. Emery *et al.*, *ACS Appl. Mater. Interfaces* **14**, 5159–5167 (2022).
38. J. Li *et al.*, *Adv. Energy Mater.* **13**, 2203898 (2023).
39. M. Jošt *et al.*, *Adv. Energy Mater.* **10**, 2000454 (2020).
40. V. Paraskeva *et al.*, *Energies* **16**, 2608 (2023).
41. M. V. Khenkin *et al.*, *Energy Environ. Sci.* **11**, 739–743 (2018).
42. N. Phung *et al.*, *Adv. Energy Mater.* **10**, 1903735 (2020).
43. J. Carrillo *et al.*, *Adv. Energy Mater.* **6**, 1502246 (2016).
44. Z. Song *et al.*, *Adv. Mater.* **37**, e2410779 (2025).

ACKNOWLEDGMENTS

The authors acknowledge the Center for Microscopy and Analysis of Nanjing University of Aeronautics and Astronautics for characterization support. **Funding:** This work was supported by the National Natural Science Foundation of China (22305119, T2293691, 12204234, and 52303248), Natural Science Foundation of Jiangsu Province (BK20243065 and BK20220878), National Key Research and Development Program of China (2019YFA0705400), the Fundamental Research Funds for the Central Universities (NJ2024001, NC2023001, NJ2023002, and NS2023059), the China Postdoctoral Science Foundation (2022TQ0157 and 2023M741695), and the Fund of Prospective Layout of Scientific Research for NUAA (Nanjing University of Aeronautics and Astronautics). X.W. thanks the Sailing Project from the Science and Technology Commission of Shanghai Municipality (24YF2714200). **Author contributions:** X.Z. and X.S. conceived the idea, initialized the project, and contributed to the fabrication and characterization of films and devices. X.S. performed the majority of experiments and data analysis. W.S. fabricated the large-area module and contributed to the DFT calculations and outdoor stability studies. T.L. contributed to device fabrication and stability studies. J.C. contributed to encapsulation. X.W. and P.X. contributed to device fabrication and discussions. W.Z. contributed to XPS analysis. X.Z. and W.G. directed and supervised the project. X.S., X.Z., and W.G. wrote the manuscript, with inputs from all coauthors. All authors contributed to discussions and to finalizing the manuscript. **Competing interests:** The authors declare no competing interests. **Data and materials availability:** All data needed to evaluate the conclusions in the paper are present in the paper or the supplementary materials. **License information:** Copyright © 2025 the authors, some rights reserved; exclusive licensee American Association for the Advancement of Science. No claim to original US government works. https://www.science.org/about/science-licenses-journal-article-reuse

SUPPLEMENTARY MATERIALS

science.org/doi/10.1126/science.adv4280
Materials and Methods; Supplementary Text; Figs. S1 to S31; Tables S1 to S5; References (*45*–*50*)

Submitted 18 December 2024; accepted 7 April 2025

10.1126/science.adv4280

SOLAR CELLS

C_{60}-based ionic salt electron shuttle for high-performance inverted perovskite solar modules

Shuai You[1]†, Hongwei Zhu[2]†, Zhongjin Shen[3]†, Xiaoming Wang[4], Bingyao Shao[2], Qingxiao Wang[5], Jianxun Lu[2], Youyou Yuan[5], Benjia Dak Dou[6], Erin M. Sanehira[6], Todd Russell[6], Adam Lorenz[6], Yifan Dong[1], Lei Chen[1], Marco Casareto[7], Nicholas Rolston[7], Matthew C. Beard[1], Joseph J. Berry[8,9,10], Marina Freitag[3]*, Yanfa Yan[4]*, Osman M. Bakr[2]*, Kai Zhu[1]*

Although buckminsterfullerene (C_{60}) is usually the electron transport layer (ETL) in inverted perovskite solar cells (PSCs), its molecular nature leads to weak interfaces that result in nonideal interfacial electronic and mechanical degradation. In this study, we synthesized an ionic salt from C_{60}, 4-(1′,5′-dihydro-1′-methyl-2′*H*-[5,6] fullereno-C_{60}-I_h-[1,9-c]pyrrol-2′-yl) phenylmethanaminium chloride (CPMAC), and used it as the electron shuttle in inverted PSCs. The CH_2-NH_3^+ head group in the CPMA cation improved the ETL interface, and the ionic nature enhanced the packing, leading to a ~threefold increase in the interfacial toughness compared with that of C_{60}. Using CPMAC, we obtained ~26% power conversion efficiencies (PCEs) with ~2% degradation after 2100 hours of 1-sun operation at 65°C. For minimodules (four subcells, 6 square centimeters), we achieved a PCE of ~23% with <9% degradation after 2200 hours of operation at 55°C.

Organic-inorganic hybrid metal halide perovskite materials have successfully been used as light absorbers in efficient photovoltaic devices (*1*–*16*). The inverted (p-i-n) perovskite solar cell (PSC) structure is attractive for commercialization because of its easy fabrication, low-temperature processability, and suitability for tandem cells (*17*–*31*). The power conversion efficiency (PCE) of single-junction inverted PSCs has exceeded 26% through advances in solvent engineering, compositional tuning, interface optimization, and defect passivation strategies (*32*–*37*). However, challenges related to scalability and long-term operational stability are obstacles to their commercialization.

Buckminsterfullerene (C_{60}) is almost exclusively used in the electron transport layer (ETL) structure for high-performance inverted PSCs, as C_{60}/bathocuproine or C_{60}/SnO_x (*22*). The latter with the SnO_x (tin oxide) deposited through atomic layer deposition (ALD) has become the preferred approach for better stability and compatibility with tandems. However, the molecular nature of the C_{60} layer leads to a weak interface and loose packing, and in turn, to nonideal interfacial properties and challenges for ALD-SnO_x coating. These issues inevitably limit device performance, especially long-term stability (*38*–*42*).

For example, the ALD-SnO_x precursor is known to be reactive with the perovskite surface or even to penetrate into the bulk material (*43*, *44*). A C_{60} layer of around 20 nm (or thicker) is normally needed to support ALD-SnO_x coating (*32*, *43*, *45*). Efforts have been made to address the C_{60}/perovskite interface challenges, such as interlayer strategies and C_{60} functionalization (*46*–*50*). However, these strategies focus on perovskite surface defect passivation, interfacial energetics adjustment, or both, whereas the ETLs in these studies still rely on C_{60} molecules. Thus, these efforts do not address the fundamental issue of the molecular nature of the C_{60} ETL.

In this study, we used *N*-methylglycine, tert-butyl 4-formylbenzylcarbamate molecules, and hydrochloric acid to react with C_{60} to form an ionic salt, 4-(1′,5′-dihydro-1′-methyl-2′H-[5,6] fullereno-C_{60}-Ih-[1,9-c]pyrrol-2′-yl) phenylmethanaminium chloride (referred to as CPMAC). We further used CPMAC salt as the electron shuttle in inverted PSCs and minimodules. This ionic salt layer fundamentally addressed the disadvantages of the molecular C_{60} layer. Density functional theory (DFT) calculation revealed that it is energetically preferred for the CH_2-NH_3^+ heads in the phenylmethanaminium units to fill in formamidinium (FA) vacancies or replace FA ions on perovskite surfaces, enabling ionic bonding between CPMA and the perovskite surface. The ionic nature of CPMAC strengthens its interface and packing. The strong electron-withdrawing C_{60} unit in the CPMA cation helps ensure that the CPMAC is an effective electron conductor. As a result of these physical and chemical characteristics, a thin CPMAC layer was used to support ALD-SnO_x coating to construct an effective ETL. The corresponding PSCs and minimodules using CPMAC show improved PCE and stability compared with those using the conventional C_{60} layers.

Design concept

An ionic salt layer would need the same electron-withdrawing ability but have enhanced ETL interface properties and packing. In our designed CPMAC compound, the $CPMA^+$ cation contains a CH_2-NH_3^+ head with a structure similar to that of the methylammonium (MA^+) cation. Our DFT calculations showed that CPMAC, reacting with the FA-rich perovskite surface by replacing an FA^+ cation with a $CPMA^+$ cation, lowered the surface energy by 0.375 eV. In comparison, CPMAC reacting with MA^+ would lower the surface energy by 0.181 eV, whereas reacting with Cs^+ would slightly increase the surface energy by 0.003 eV. Thus, FA^+ would be replaced preferably by CPMAC for mixed-cation perovskites.

In comparison with C_{60}, two interactions between CPMAC and perovskite were expected. First, the CH_2-NH_3^+ head could fill a FA^+ vacancy, and the Cl^- anion could occupy an I vacancy, providing double-defect passivation. Second, the $CPMA^+$ cation could replace an FA^+ cation on the surface, as expected from our DFT calculation, and FA^+ and Cl^- would form a FACl molecule, which could escape the perovskite during annealing.

A comparison of C_{60}/perovskite and CPMAC/perovskite interfaces is shown in Fig. 1A. In both cases (filling a FA^+ vacancy or replacing a FA^+ cation), the CH_2-NH_3^+ head in the $CPMA^+$ cation would introduce ionic bonding with the surrounding I anions on the surface. Thus, the ionic nature of CPMAC could strengthen the CPMAC/perovskite interface. It could also enable stronger packing of the CPMAC layer on the perovskite and the use of a thinner CPMAC layer (~10 nm) versus ~20 nm typically used for C_{60}. In addition, the C_{60} unit in $CPMA^+$ facilitates electron transport, making the CPMAC layer both a strong and conducting bridge to transfer electrons from the perovskite to external electrodes in a device.

To synthesize CPMAC, we used the Prato reaction of C_{60} with *N*-methylglycine and tert-butyl 4-formylbenzylcarbamate to form the intermediate (compound **1**), which then reacted with hydrochloric acid

---

[1]Chemistry and Nanoscience Center, National Renewable Energy Laboratory, Golden, CO, USA. [2]Division of Physical Science and Engineering, Center for Renewable Energy and Storage Technologies (CREST), King Abdullah University of Science and Technology, Thuwal, Saudi Arabia. [3]School of Natural and Environmental Sciences, Newcastle University, Newcastle upon Tyne, UK. [4]Department of Physics and Astronomy and Wright Center for Photovoltaics Innovation and Commercialization, The University of Toledo, Toledo, OH, USA. [5]Imaging and Characterization Core Lab, King Abdullah University of Science and Technology, Thuwal, Saudi Arabia. [6]CubicPV, Bedford, MA, USA. [7]School of Electrical, Computer and Energy Engineering, Arizona State University, Tempe, AZ, USA. [8]Materials Science Center, National Renewable Energy Laboratory, Golden, CO, USA. [9]Renewable and Sustainable Energy Institute, University of Colorado Boulder, Boulder, CO, USA. [10]Department of Physics, University of Colorado Boulder, Boulder, CO, USA. ***Corresponding author. Email: kai.zhu@nrel.gov (K.Z.); osman.bakr@kaust.edu.sa (O.M.B.); yanfa.yan@utoledo.edu (Y.Ya.); marina.freitag@newcastle.ac.uk (M.F.)** †These authors contributed equally to this work.

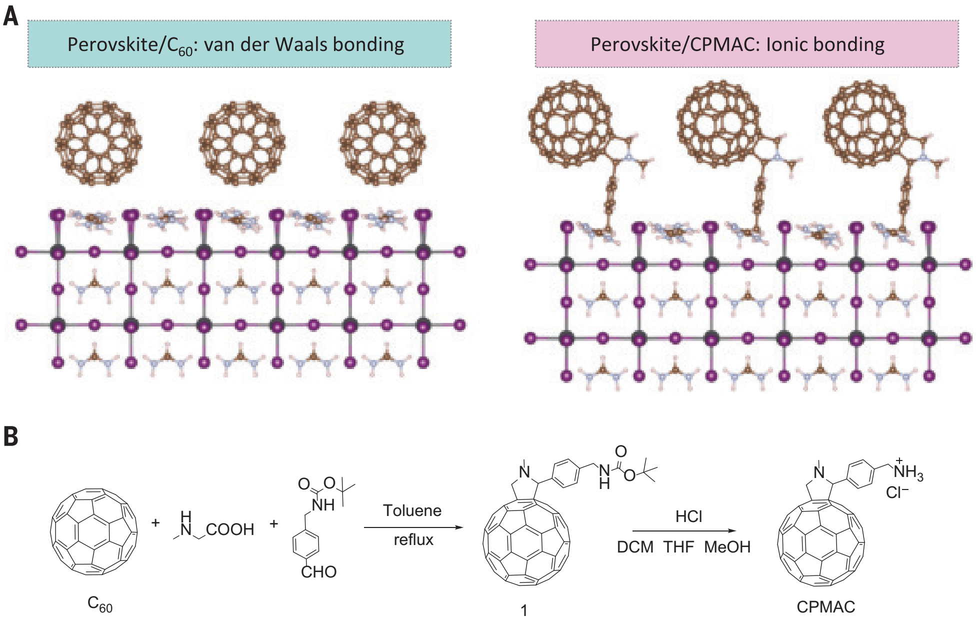
A
Perovskite/C$_{60}$: van der Waals bonding
Perovskite/CPMAC: Ionic bonding
B
COOH
NH
CHO
Toluene
reflux
HCl
DCM THF MeOH
Cl$^-$
NH$_3$
C$_{60}$
1
CPMAC

Fig. 1. Design concept. (**A**) Comparison of C_{60} and 4-(1′,5′-dihydro-1′-methyl-2′*H*-[5,6] fullereno-C_{60}-I_h-[1,9-c]pyrrol-2′-yl)phenylmethanaminium chloride (CPMAC) on their different interactions with the perovskite surface. (**B**) Synthetic route of CPMAC. DCM, dichloromethane; THF, tetrahydrofuran; CHO, aldehyde group.

in a tert-butyl carbamate deprotection reaction to achieve the final CPMAC compound (Fig. 1A and fig. S1). Both **1** and the final CPMAC compound were characterized by ^{1}H nuclear magnetic resonance (NMR), ^{13}C NMR, and high-resolution mass spectrometry (figs. S2 to S5). The ionic interaction between CPMAC and the perovskite surface is consistent with the x-ray photoelectron spectroscopy measurements in which the Pb 4*f* peaks of the treated perovskite film shifted toward a lower binding energy (by about 0.33 eV) compared with the control film (fig. S6).

Structural and optoelectronic properties

We compared the grazing-incident wide-angle x-ray scattering (GIWAXS) studies of the perovskite films without and with CPMAC coating, respectively (fig. S7). No additional Laue rings were observed, indicating that the introduction of CPMAC did not induce perovskite phase change. However, the apparent changes in diffraction intensity and growth orientation of the perovskite from the existing Laue rings indicated interactions between CPMAC and the perovskite components. The one-dimensional (1D) GIWAXS results demonstrated a decreased scattering vector *q*-value, corresponding to an increased lattice *d*-spacing of perovskite (fig. S7). These results were consistent with the chemical interaction between CPMAC and perovskite in the surface region.

Photoluminescence (PL) mapping images of perovskite films without and with CPMAC (Fig. 2, A and B, respectively) showed that the CPMAC-treated perovskite film was more uniform and has a reduced PL intensity compared with the pristine perovskite film. We used Kelvin probe force microscopy (KPFM) to investigate the spatial variations in the surface potential of perovskite films with and without CPMAC. As shown in Fig. 2, C and D, the perovskite/CPMAC film exhibited a more uniform potential distribution than the pristine sample, which suggested that CPMAC effectively mitigates surface defects (*51–54*). In addition, cyclic voltammetry measurements of C_{60} and CPMAC, with ferrocene as the reference, showed lowest unoccupied molecular orbital levels of −4.20 and −4.09 eV against vacuum (fig. S8), respectively. In comparison with C_{60}, the reduced conduction band offset between the CPMAC and perovskite (−3.92 eV) should result in a better energy alignment at this interface and a reduced voltage loss in the corresponding device (fig. S8).

We measured the time-resolved microwave conductivity (TRMC) transients for both C_{60} and CPMAC thin films over a range of excitation intensities. The yield-mobility products were plotted as a function of excitation intensities (Fig. 2E). The mobility in CPMAC was about 30% higher than that in C_{60} measured at the lowest excitation intensity.

We further examined the fracture energy (G_C) of devices with C_{60} or CPMAC by using force-displacement measurements with a double cantilever beam test following a reported methodology (*55*). The fracture path of all samples involved the ETL layer, and the average G_C values changed by about a factor of 3, increasing from about 0.50 ± 0.07 J m^{-2} for C_{60} to 1.43 ± 0.03 J m^{-2} for CPMAC (Fig. 2F). Glow-discharge optical emission spectroscopy of the delaminated samples further supports the improved fracture toughness within the CPMAC layer as compared with C_{60}, as well as improved adhesion at the CPMAC/perovskite interface (fig. S9). These results were consistent with stronger mechanical stability for CPMAC. These values are above the empirical threshold of 1 J m^{-2} that limits the susceptibility of the perovskite device to delaminate in operation (*56*).

To directly visualize the distribution of CPMAC on the perovskite layer, we performed high-angle annular dark-field scanning transmission electron microscopy (HAADF-STEM) measurements. A cryogenic focused ion beam system was used to prepare the STEM specimen without damaging the inherent structures of the perovskite layer. The cross-sectional HAADF-STEM images in Fig. 2G revealed a dark layer sandwiched between the brighter ALD-SnO_x and perovskite layers. This layer corresponded to the CPMAC layer and is discernible because of the contrast in atomic number. The CPMAC layer is ~10 nm thick and is amorphous (fig. S10). To further investigate the elemental distribution, we performed electron energy-loss spectroscopy (EELS) coupled with cryo–high-resolution transmission electron microscopy (cryo-HRTEM) experiments on cross sections of the device (Fig. 2H). The distributions of silver, tin, oxygen, carbon, and iodine were consistent with the distributions of the Ag, ALD-SnO_x, ALD-SnO_x, CPMAC, and perovskite layers. EELS also revealed the uniform and compact presence of the CPMAC layer atop perovskite through the detection of the carbon element.

Device characteristics

The current density–voltage (*J-V*) curves and photovoltaic (PV) performance parameters of the champion devices under standard AM 1.5 G

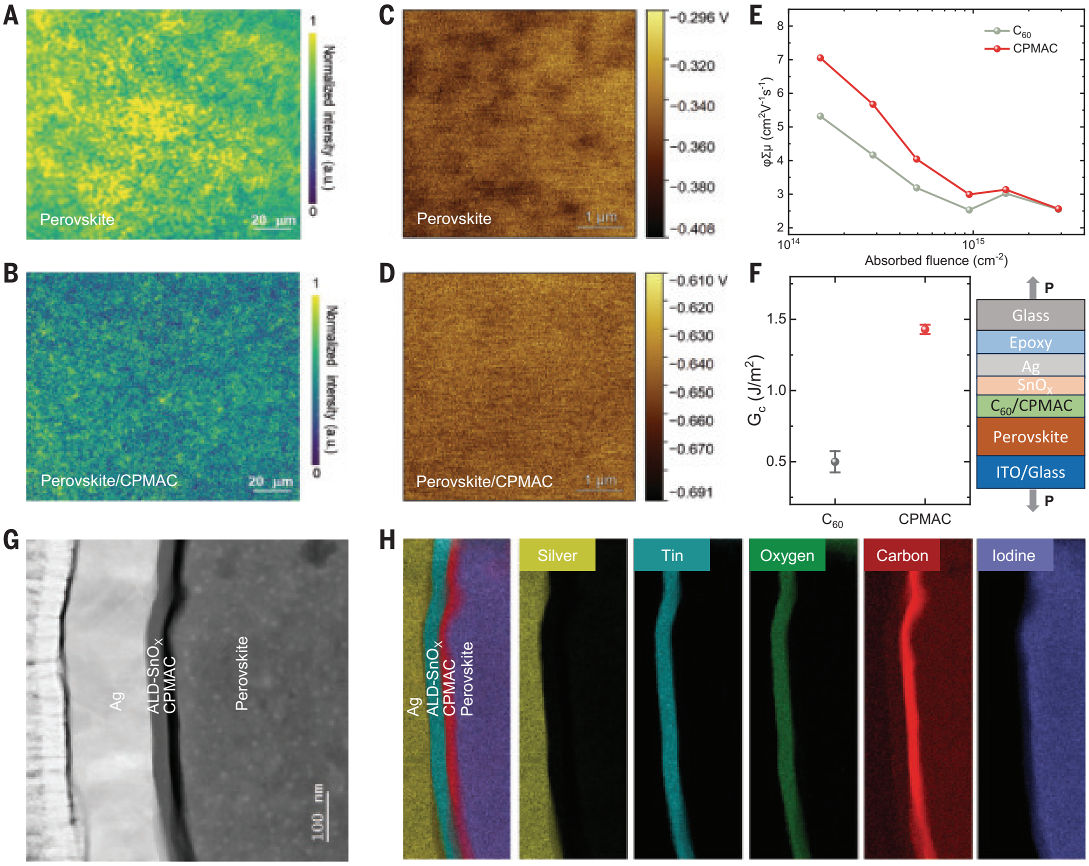

Fig. 2. Structural and optoelectronic properties. PL imaging of perovskite films (**A**) without CPMAC and (**B**) with CPMAC. a.u., arbitrary units. (**C** and **D**) KPFM surface potential images for the control and target perovskite films, respectively. (**E**) Comparison of TRMC of C_{60} films and CPMAC films, respectively. (**F**) Comparison of fracture energy (G_C) of devices to quantify ETL for C_{60} or CPMAC. (**G**) HAADF-STEM images of the Ag/ALD-SnO_x/CPMAC/perovskite configuration. (**H**) EELS analysis of element mapping for silver (Ag), tin (ALD-SnO_x), oxygen (ALD-SnO_x), carbon (CPMAC), and iodine (perovskite).

(where AM is "air mass" and G is "global") illumination are shown in Fig. 3, A and B. The PSC with the configuration of FTO/HTL/perovskite/ALD-SnO_x/Ag (where FTO is fluorine-doped tin oxide and HTL is hole transport layer) showed a negligible PCE of 0.07% (fig. S11), which we ascribed to the degradation of the perovskite layer during the ALD-SnO_x coating (*43*, *44*). The incorporation of a standard C_{60} layer between perovskite and ALD-SnO_x ameliorated this degradation, achieving a PCE of 25.5% (reverse scan) with a short-circuit current density (J_{sc}) of 25.9 mA cm^{-2}, open-circuit voltage (V_{oc}) of 1.16 V, and fill factor (FF) of 84.9% (Fig. 3A). Notably, replacing C_{60} with CPMAC further improved the PV performance to a PCE of 26.1% (reverse scan) with a J_{sc} of 26.0 mA cm^{-2}, V_{oc} of 1.18 V, and FF of 85.5% (Fig. 3B). The increase in V_{oc} for the CPMAC-based PSC is consistent with its higher photoluminescence quantum yield than the C_{60}-based cell (fig. S12). Both C_{60}- and CPMAC-based PSCs exhibited minimal hysteresis between forward and reverse *J-V* scans.

The improved PV parameters achieved by using CPMAC to replace C_{60} were further verified on the basis of statistical results from 20 devices of each device type (fig. S13). All of the PSCs with the CPMAC layer processed over a range of CPMAC solution concentrations exhibited similar PCEs (fig. S14), which would provide a favorable processing window for solution deposition of the CPMAC layer. The measured J_{sc} (26.0 mA cm^{-2}) was consistent with the integrated current density (25.9 mA cm^{-2}) from the external quantum efficiency spectra (fig. S15). It is also noteworthy that CPMAC-based PSCs do not require additional perovskite surface treatment, as is often the case for C_{60}-based PSCs (fig. S16). The ideality factors (n_{id}) of control and target devices were calculated from the dependence of V_{oc} on the light intensity (fig. S17). The n_{id} decreased from 1.77 to 1.41 after substituting the C_{60} layer with CPMAC, which could be attributed to reduced trap-assisted nonradiative recombination (*57*, *58*).

The operational stability of PSCs with C_{60} and CPMAC was evaluated to investigate the impact of CPMAC on device stability (Fig. 3, C and D). The unencapsulated device with CPMAC exhibited only a ~2% efficiency loss after 2100 hours of continuous maximum power point tracking (MPPT) under an N_2 atmosphere at about 65°C with 1-sun illumination. By contrast, the C_{60}-based devices showed a ~6% drop in PCE.

We further tested the operational stability at 85°C. For this test, poly[bis(4-phenyl)(2,4,6-trimethylphenyl)amine] (PTAA) was used as the HTL because as we showed previously, the mixed self-assembled monolayer HTL was prone to degradation at 85°C (*19*). The operational stability at 85°C for the CPMAC-based device was substantially better than the standard C_{60}-based device, maintaining ~95% of its original efficiency over 1500 hours of MPPT under N_2 (Fig. 3D). When tested under damp-heat conditions (85°C and 85% relative humidity), the encapsulated CPMAC-based device retained 94.3% of its initial PCE after 2000 hours, whereas the C_{60}-based device exhibited a 16% PCE loss (fig. S18). Thus, replacing C_{60} with CPMAC increased device stability under various testing conditions. The improved stability with CPMAC is also consistent with the time-of-flight secondary ion mass spectroscopy measurement of aged PSCs (fig. S19).

Furthermore, we fabricated minimodules with four subcells (6 cm^2) by blade-coating the perovskite layer (Fig. 4A and fig. S20). The representative *J-V* curves of perovskite solar minimodules (PSMs) are compared in Fig. 4B. The CPMAC-based PSMs exhibited a PCE

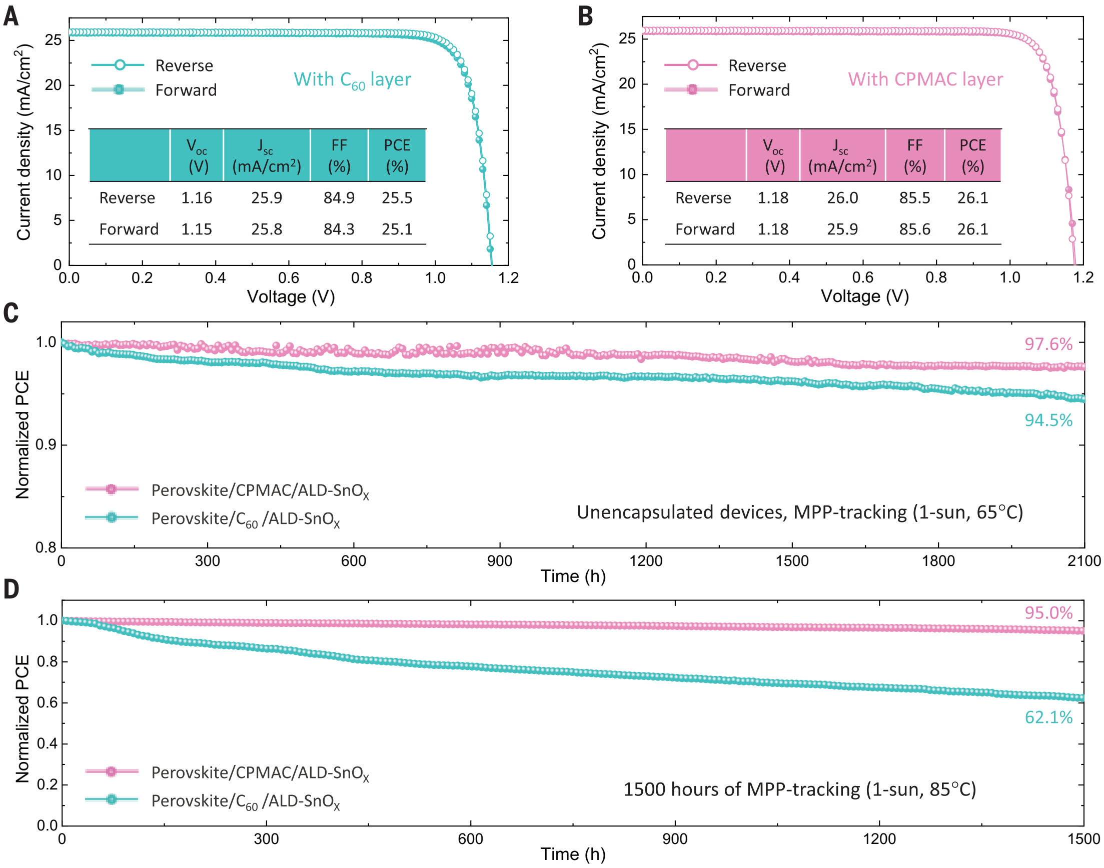

	V_{oc} (V)	J_{sc} (mA/cm^2)	FF (%)	PCE (%)
Reverse	1.16	25.9	84.9	25.5
Forward	1.15	25.8	84.3	25.1

	V_{oc} (V)	J_{sc} (mA/cm^2)	FF (%)	PCE (%)
Reverse	1.18	26.0	85.5	26.1
Forward	1.18	25.9	85.6	26.1

Fig. 3. Perovskite solar cell characteristics. (**A** and **B**) The *J-V* characteristics of the p-i-n perovskite solar cells with various device configurations (including FTO/HTL/perovskite/C_{60}/ALD-SnO_x/Ag (A) and FTO/HTL/perovskite/CPMAC/ALD-SnO_x/Ag (B), and the corresponding photovoltaic parameters under simulated AM 1.5 G illumination (insets). Device areas were 0.059 cm^2, as defined by a metal aperture. (**C**) Comparison of operational stability of devices under 1-sun MPPT following the ISOS-L-1 protocol (65°C, N_2 atmosphere). HTL was a MeO-2PACZ/Me-4PACZ mixture in (A) to (C). The initial PCEs of C_{60}- and CPMAC-based devices were 24.9 and 25.8%, respectively. (**D**) Comparison of operational stability of unencapsulated PSCs measured by MPPT under continuous 1-sun illumination (85°C, N_2 atmosphere). For this test, PTAA was used as the HTL. The initial PCEs of C_{60}- and CPMAC-based devices were 24.3 and 25.5%, respectively.

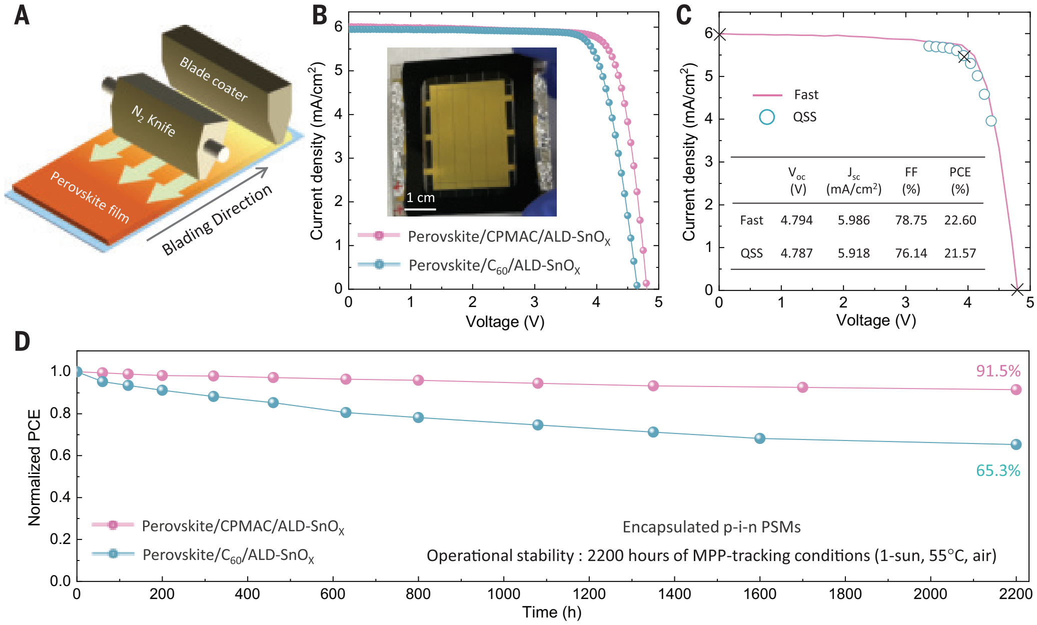

	V_{oc} (V)	J_{sc} (mA/cm^2)	FF (%)	PCE (%)
Fast	4.794	5.986	78.75	22.60
QSS	4.787	5.918	76.14	21.57

Fig. 4. Perovskite solar module characteristics. (**A**) Schematic illustration for blade-coating the perovskite films. (**B**) *J-V* curves of a representative PSM with C_{60} and CPMAC (inset shows a photograph of a typical PSM). (**C**) QSS and *J-V* results of a representative CPMAC-based device measured by the NREL PV Performance Group. (**D**) Operational stability of the encapsulated PSMs under 1-sun MPPT following the ISOS-L-1 protocol at ~55°C in air with 40 to 60% relative humidity. The initial PCEs of C_{60}- and CPMAC-based devices were 20.2 and 21.5%, respectively.

of 23.2% with a J_{sc} of 6.01 mA cm^{-2}, V_{oc} of 4.81 V, and FF of 80.3%. In comparison, C_{60}-based PSMs exhibited a PCE of 21.8%, a V_{oc} of 4.7 V, an FF of 78.6%, and a J_{sc} of 5.95 mA cm^{-2}. No discernible difference (hysteresis) in *J-V* curves under different scanning directions were observed for the CPMAC-based PSMs (fig. S21). The corresponding stabilized PCEs of the PSMs based on C_{60} and CPMAC are 21.2 and 22.7%, respectively (fig. S22).

We provided one such device to an accredited PV laboratory [National Renewable Energy Laboratory (NREL) PV Performance Group], obtaining the certified quasi–steady state (QSS) PCE of 21.6 ± 0.2% with a corresponding backward-scan *J-V* PCE of 22.6% (Fig. 4C and figs. S23 and S24). Notably, the efficient PSMs with CPMAC on blade-coated perovskite demonstrated that CPMAC could effectively integrate with perovskite processed at scale. We also investigated the operational stability of the encapsulated PSM under continuous light illumination at ~55°C in ambient air (Fig. 4D). After 2200 hours, the CPMAC-treated PSM maintained 91.5% of its initial PCE, whereas the control sample lost >30% of its initial PCE. Our results suggest that using CPMAC to replace C_{60} is an effective approach to improve the PCE and operational stability of p-i-n PSCs and PSMs.

Discussion

We showed that an ionic salt, CPMAC, can address the mechanical instability associated with the molecular C_{60} in inverted PSCs. In comparison with C_{60}, the ionic nature associated with CPMAC strengthened the ETL/perovskite interface region. A thin CPMAC layer was sufficient for effective device operation. The use of CPMAC boosted device efficiency and stability. We further demonstrated that CPMAC is suitable for developing minimodules, reaching a PSM efficiency and operational stability that is among the best in the literature. Taken together, our results point to a promising approach to advance perovskite PV technology toward commercialization.

REFERENCES AND NOTES

1. A. Kojima, K. Teshima, Y. Shirai, T. Miyasaka, *J. Am. Chem. Soc.* **131**, 6050–6051 (2009).
2. Y. Yang *et al.*, *Science* **386**, 898–902 (2024).
3. M. Liu, M. B. Johnston, H. J. Snaith, *Nature* **501**, 395–398 (2013).
4. Y. Ding *et al.*, *Science* **386**, 531–538 (2024).
5. X. Li *et al.*, *Nat. Chem.* **7**, 703–711 (2015).
6. T. Duan *et al.*, *Science* **384**, 878–884 (2024).
7. M. Abdi-Jalebi *et al.*, *Nature* **555**, 497–501 (2018).
8. Z. Li *et al.*, *Chem. Mater.* **28**, 284–292 (2016).
9. S. Bai *et al.*, *Nature* **571**, 245–250 (2019).
10. R. He *et al.*, *Nature* **618**, 80–86 (2023).
11. X. Zheng *et al.*, *Nat. Energy* **8**, 462–472 (2023).
12. Q. Cheng *et al.*, *Nano Lett.* **24**, 5308–5316 (2024).
13. S. You *et al.*, *Adv. Mater.* **32**, e2003990 (2020).
14. L. Luo *et al.*, *Nat. Energy* **8**, 294–303 (2023).
15. H. Zhu *et al.*, *Nat. Photonics* **19**, 28–35 (2025).
16. Y. Xiong *et al.*, *Mater. Today Electron.* **7**, 100086 (2024).
17. S. Zhang *et al.*, *ACS Energy Lett.* **7**, 3958–3966 (2022).
18. M. Chen *et al.*, *ACS Energy Lett.* **9**, 2582–2589 (2024).
19. Q. Jiang *et al.*, *Nature* **623**, 313–318 (2023).
20. C. Fei *et al.*, *Science* **384**, 1126–1134 (2024).
21. R. Lin *et al.*, *Nature* **620**, 994–1000 (2023).
22. Q. Jiang, K. Zhu, *Nat. Rev. Mater.* **9**, 399–419 (2024).
23. H. Wang *et al.*, *Nature* **634**, 1091–1095 (2024).
24. P. Zhu *et al.*, *Science* **383**, 524–531 (2024).
25. H. Gao *et al.*, *Science* **383**, 855–859 (2024).
26. S. M. Park *et al.*, *Science* **381**, 209–215 (2023).
27. Y. Chen *et al.*, *Science* **385**, 554–560 (2024).
28. X. Tang *et al.*, *ACS Energy Lett.* **9**, 5679–5687 (2024).
29. S. You *et al.*, *Adv. Mater.* **30**, e1706924 (2018).
30. B. Dong *et al.*, *Nat. Energy* **10**, 342–353 (2025).
31. X. Liu *et al.*, *ACS Energy Lett.* **9**, 2446–2455 (2024).
32. J. Chen *et al.*, *Nat. Photonics* **18**, 464–470 (2024).
33. P. Shi *et al.*, *Nature* **620**, 323–327 (2023).
34. J. Park *et al.*, *Nature* **616**, 724–730 (2023).
35. N. J. Jeon *et al.*, *Nature* **517**, 476–480 (2015).
36. D. Luo *et al.*, *Science* **360**, 1442–1446 (2018).
37. Y.-H. Lin *et al.*, *Science* **369**, 96–102 (2020).
38. S. Pont, F. Foglia, A. M. Higgins, J. R. Durrant, J. T. Cabral, *Adv. Funct. Mater.* **28**, 1802520 (2018).
39. A. Distler *et al.*, *Adv. Energy Mater.* **4**, 1300693 (2014).
40. W. Shen *et al.*, *Adv. Energy Mater.* **14**, 2400582 (2024).
41. J. Warby *et al.*, *Adv. Energy Mater.* **12**, 2103567 (2022).
42. M. Stolterfoht *et al.*, *Nat. Energy* **3**, 847–854 (2018).
43. A. Hultqvist *et al.*, *ACS Appl. Energy Mater.* **4**, 510–522 (2021).
44. A. F. Palmstrom *et al.*, *Adv. Energy Mater.* **8**, 1800591 (2018).
45. S. A. Johnson *et al.*, *Joule* **7**, 2873–2893 (2023).
46. C. Liu *et al.*, *Science* **382**, 810–815 (2023).
47. R. Azmi *et al.*, *Nature* **628**, 93–98 (2024).
48. C. Li *et al.*, *Nat. Energy* **9**, 1388–1396 (2024).
49. X. Li *et al.*, *Science* **375**, 434–437 (2022).
50. J. Zhao *et al.*, *Adv. Mater.* **36**, e2406246 (2024).
51. T. A. S. Doherty *et al.*, *Nature* **580**, 360–366 (2020).
52. P. Chen *et al.*, *Adv. Funct. Mater.* **28**, 1706923 (2018).
53. S. D. Stranks, *ACS Energy Lett.* **2**, 1515–1525 (2017).
54. S. You *et al.*, *Nat. Energy* **8**, 515–525 (2023).
55. Z. Dai *et al.*, *ACS Energy Lett.* **9**, 1880–1887 (2024).
56. M. Casareto, N. Rolston, *Commun. Mater.* **5**, 74 (2024).
57. M. Kim *et al.*, *Science* **375**, 302–306 (2022).
58. J. Jeong *et al.*, *Nature* **592**, 381–385 (2021).

ACKNOWLEDGMENTS

Funding: The work was authored in part by the NREL for the US Department of Energy (DOE) under contract no. DE-AC36-08GO28308. We acknowledge the support on molecule design, first-principles calculations, and transient spectroscopy measurements as part of the Center for Hybrid Organic-Inorganic Semiconductors for Energy (CHOISE), an Energy Frontier Research Center funded by the Office of Basic Energy Sciences, Office of Science within the DOE. The DFT calculations were performed using computational resources sponsored by the DOE Office of Energy Efficiency and Renewable Energy and located at NREL, and the resources of the National Energy Research Scientific Computing Center (NERSC), a DOE Office of Science User Facility located at Lawrence Berkeley National Laboratory, operated under contract no. DE-AC02-05CH11231 using NERSC award BES-ERCAP0032847. We also acknowledge the support on module development from DE-FOA-0002064 and award no. DE-EE0008790; the support on the general perovskite fabrication and characterization from the Perovskite Enabled Tandems program, funded by the DOE, Office of Energy Efficiency and Renewable Energy, Solar Energy Technologies Office award no. 52776; and the support on the mechanical testing from the NSF under grant no. 2339233. M.F. and Z.S. acknowledge the support on CPMAC synthesis by the Royal Society through the University Research Fellowship (URF/R1/191286), Research Grant 2021 (RGS/R1/211321), and UKRI EPSRC Standard Grant EP/W025280/1. The views expressed in the article do not necessarily represent the views of the DOE or the US Government. **Author contributions:** S.Y. and K.Z. conceived the idea. K.Z., O.M.B., M.F., and Y.Ya. supervised the projects and process. S.Y., Z.S., and H.Z. conceptualized and designed the experiments. S.Y. and H.Z. fabricated perovskite solar cells and conducted device efficiency and stability measurements. Z.S. prepared the CPMAC and conducted NMR measurements. X.W. carried out the DFT calculation under the supervision of Y.Ya. B.S. and J.L. conducted the PL mapping measurements and other PL measurements. Q.W. conducted the cryo-HRTEM measurements. Y.Yu. conducted the GIWAXS measurements. B.D.D., E.M.S., T.R., and A.L. provided support on module fabrication and packaging. Y.D. conducted TRMC measurements and analysis under the guidance of M.C.B. M.C. conducted the mechanical measurements and analysis under the guidance of N.R. J.J.B. provided valuable suggestions for experiment planning, analysis, and manuscript preparation. S.Y., H.Z., Z.S., O.M.B., Y.Ya., and K.Z. wrote the manuscript. All authors discussed the results and contributed to the revisions of the manuscript. **Competing interests:** S.Y., Z.S., M.F., and K.Z. are inventors on a provisional patent (US patent application no. 63/669,821) related to the subject matter of this manuscript. **Data and materials availability:** All data needed to evaluate the conclusions in the paper are present in the paper or the supplementary materials. **License information:** Copyright © 2025 the authors, some rights reserved; exclusive licensee American Association for the Advancement of Science. No claim to original US government works. https://www.sciencemag.org/about/science-licenses-journal-article-reuse. The US Government retains and the publisher, by accepting the article for publication, acknowledges that the US Government retains a nonexclusive, paid-up, irrevocable, worldwide license to publish or reproduce the published form of this work, or allow others to do so, for US Government purposes.

SUPPLEMENTARY MATERIALS

science.org/doi/10.1126/science.adv4701
Materials and Methods; Figs. S1 to S24; References (*59*–*68*)

Submitted 19 December 2024; accepted 1 April 2025; published online 17 April 2025
10.1126/science.adv4701

PALEOPROTEOMICS

Enamel proteins reveal biological sex and genetic variability in southern African *Paranthropus*

Palesa P. Madupe[1,2]†, Claire Koenig[3]†, Ioannis Patramanis[1]†, Patrick L. Rüther[3], Nomawethu Hlazo[2,4], Meaghan Mackie[1,3]‡§, Mirriam Tawane[2,5], Johanna Krueger[6], Alberto J. Taurozzi[1], Gaudry Troché[1,3], Job Kibii[7]¶, Robyn Pickering[2,8], Marc R. Dickinson[9], Yonatan Sahle[2,4], Dipuo Kgotleng[10], Charles Musiba[2,11], Fredrick Manthi[2,12], Liam Bell[13], Michelle DuPlessis[13], Catherine Gilbert[14], Bernhard Zipfel[15], Lukas F. K. Kuderna[6]#, Esther Lizano[16,17,18], Frido Welker[1], Pelagia Kyriakidou[19], Jürgen Cox[19,20], Catherine Mollereau[21], Caroline Tokarski[14], Jonathan Blackburn[22], Jazmín Ramos-Madrigal[1], Tomas Marques-Bonet[6,16,23,24], Kirsty Penkman[9], Clément Zanolli[25,15], Lauren Schroeder[2,26], Fernando Racimo[1], Jesper V. Olsen[3]*, Rebecca R. Ackermann[2,4]*, Enrico Cappellini[1]*

Paranthropus robustus is a morphologically well-documented Early Pleistocene hominin species from southern Africa with no genetic evidence reported so far. In this work, we describe the mass spectrometric sequencing of enamel peptides from four ~2 million–year-old dental specimens attributed morphologically to *P. robustus* from the site of Swartkrans in South Africa. The identification of AMELY-specific peptides enabled us to assign two specimens to male individuals, whereas semiquantitative mass spectrometric data analysis attributed the other two to females. A single amino acid polymorphism and the enamel-dentine junction shape variation indicated potential subgroups present within southern African *Paranthropus*. This study demonstrates how palaeoproteomics can help distinguish sexual dimorphism from other sources of variation in African Early Pleistocene hominins.

Although our understanding of the evolution of Middle to Late Pleistocene hominins is becoming increasingly clear in large part because of ancient DNA (aDNA) sequencing data (*1*, *2*), the biological and behavioral variation among earlier Plio-Pleistocene hominins remains poorly understood. The genus *Paranthropus* first appeared in the fossil record around 2.8 million years ago (Ma) and persisted until 1 Ma, coexisting in time and space with a number of other hominins, including *Australopithecus* species and members of the genus *Homo*. Most researchers consider *Paranthropus* to be monophyletic (*3*); however, morphological similarities between *Paranthropus robustus* and *Australopithecus africanus* (*4*, *5*) and between *Paranthropus aethiopicus* and *Australopithecus afarensis* (*6*, *7*) have raised the possibility of paraphyly or even admixture between species (*8*, *9*). Furthermore, analyses of the enamel-dentine junction (EDJ) of southern African *Paranthropus* indicate significant variation, suggesting the possibility of detectable substructure within *P. robustus* (*10*) or even the presence of more than one species of this genus in southern Africa (*11*, *12*). Other researchers have argued that the observed morphological differences stem from sexual dimorphism (*13*). Determining to what extent the variation within and between Plio-Pleistocene hominins is due to evolutionary diversification versus intraspecific variation, of which sexual dimorphism is likely a major contributor, is fundamental to interpreting their evolutionary history.

Although genetic data from the African continent have provided insights of unprecedented resolution into human demography and evolution (*14*, *15*), aDNA has never been successfully recovered from African hominin material older than ~0.02 million years (*15*). As phylogenetically informative ancient protein sequences have been retrieved beyond the limits of aDNA preservation in Eurasia (*16*–*18*), we attempted to recover them to help investigate the causes of Plio-Pleistocene hominin variation in Africa. We used liquid chromatography coupled to high-resolution tandem mass spectrometry (LC-MS/MS) to reconstruct dental enamel protein sequences from four southern African hominin specimens assigned to *P. robustus* (supplementary materials).

The four hominin fossils analyzed (SK 830, 835, 850, and 14132) originated from Swartkrans cave, located approximately 40 km northwest of Johannesburg, in South Africa's Cradle of Humankind World Heritage Site (Fig. 1). The teeth originate from the oldest deposits at Swartkrans, Member 1 (MB1), which is dated to between 1.8 and 2.2 Ma (*19*, *20*). Although Swartkrans has produced the largest collection of specimens attributed to *P. robustus*, the relationships between this material and the *Paranthropus* fossils from other southern African sites have been the subject of various interpretations, summarized by Martin *et al.* (*21*).

Results

To maximize the breadth and depth of amino acid sequence coverage, manual off-line high-pH reversed-phase fractionation was carried out on StageTips. This strategy extends the dynamic range of the less complex fractions for subsequent MS analysis (*22*), increasing peptide identifications in all four *Paranthropus* samples (fig. S1). The number of recovered amino acid positions increased up to 17%, and the number of peptide-spectrum matches increased up to threefold (supplementary materials). Further methodological development was achieved with the creation of an automated and open-source sequence assembly pipeline (fig. S2). A site-based sequence reconstruction approach (*23*) was developed to generate consensus sequences directly from the MaxQuant output tables. This sequence assembly pipeline enables faster, more reproducible, and transparent data analysis processes. The generated outputs can be traced back to the original fragmentation spectra, thereby simplifying manual validation of ambiguous hits.

After successful proteomics analysis on faunal material (fig. S3), dental enamel from four *Paranthropus* specimens was sampled. The combined analysis of the LC-MS/MS data obtained from fractionated

---

[1]Globe Institute, University of Copenhagen, Copenhagen K, Denmark. [2]Human Evolution Research Institute (HERI), University of Cape Town, Cape Town, South Africa. [3]Novo Nordisk Foundation Center for Protein Research, University of Copenhagen, Copenhagen N, Denmark. [4]Department of Archaeology, University of Cape Town, Cape Town, South Africa. [5]National Heritage Council South Africa, Pretoria, South Africa. [6]Institute of Evolutionary Biology (UPF-CSIC), PRBB, Barcelona, Spain. [7]Turkana Basin Institute, Nairobi, Kenya. [8]Department of Geological Sciences, University of Cape Town, Cape Town, South Africa. [9]Department of Chemistry, University of York, York, UK. [10]Palaeo-Research Institute, University of Johannesburg, Johannesburg, South Africa. [11]Department of Evolutionary Anthropology, Duke University, Durham, NC USA. [12]Palaeontology Section, National Museums of Kenya, Nairobi, Kenya. [13]D-CYPHR, Centre for Proteomic and Genomic Research, Cape Town, South Africa. [14]CBMN UMR CNRS 5248, Bordeaux Proteome, University of Bordeaux, Bordeaux, France. [15]Evolutionary Studies Institute, University of the Witwatersrand, Johannesburg, South Africa. [16]Institut Català de Paleontologia Miquel Crusafont (ICP-CERCA), Universitat Autònoma de Barcelona, Edifici ICTA-ICP, Cerdanyola del Vallès, Spain. [17]Unidad de Paleobiología, ICP-CERCA, Unidad Asociada al CSIC por el IBE UPF-CSIC, Cerdanyola del Vallès, Barcelona, Spain. [18]Departament de Medicina i Ciències de la Vida, Institut de Biologia Evolutiva (CSIC-UPF), Universitat Pompeu Fabra, Barcelona, Spain. [19]Computational Systems Biochemistry, Max Planck Institute of Biochemistry, Martinsried, Germany. [20]Department of Biological and Medical Psychology, University of Bergen, Bergen, Norway. [21]Research Center on Animal Cognition (CRCA), University of Toulouse, Toulouse, France. [22]Institute of Infectious Disease and Molecular Medicine, University of Cape Town, Cape Town, South Africa. [23]Catalan Institution of Research and Advanced Studies (ICREA), Barcelona, Spain. [24]CNAG, Centro Nacional de Analisis Genomico, Barcelona, Spain. [25]Univ. Bordeaux, CNRS, MCC, PACEA, UMR 5199, F-33600 Pessac, France. [26]Department of Anthropology, University of Toronto Mississauga, Toronto, ON, Canada. ***Corresponding author. Email: jesper.olsen@cpr.ku.dk (J.V.O.); becky.ackermann@uct.ac.za (R.R.A.); ecappellini@sund.ku.dk (E.C.)** †These authors contributed equally to this work. ‡Present address: University College Dublin, Dublin, Ireland. §Present address: University of Turin, Turin, Italy. ¶Present address: University of the Witwatersrand, Johannesburg, South Africa. #Present address: Illumina Artificial Intelligence Laboratory, Illumina Inc., San Diego, CA, USA.

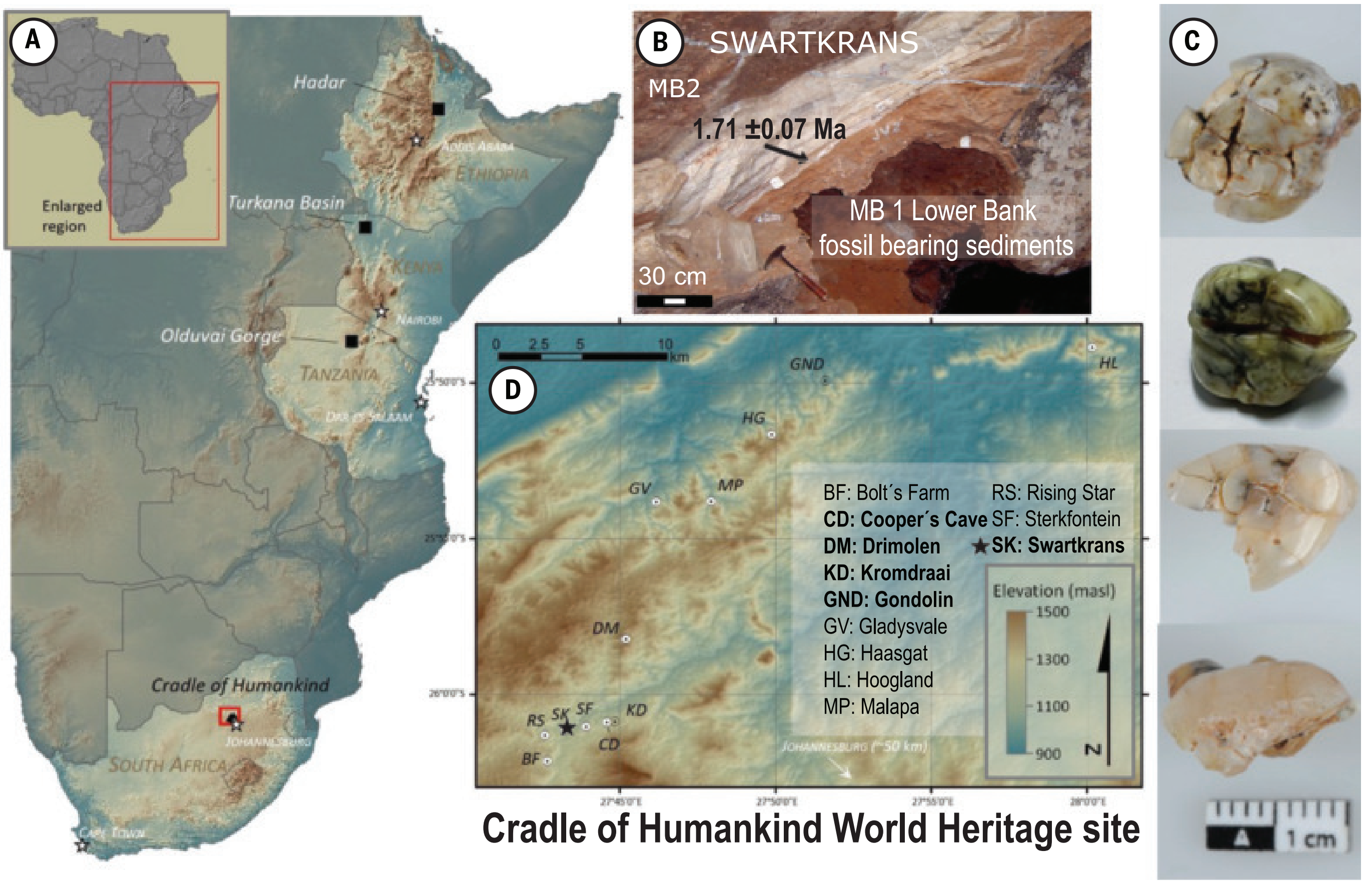
A
Enlarged region
Hadar
ADDIS ABABA
ETHIOPIA
Turkana Basin
KENYA
NAIROBI
Olduvai Gorge
TANZANIA
DAR ES SALAAM
Cradle of Humankind
JOHANNESBURG
SOUTH AFRICA
CAPE TOWN
B
SWARTKRANS
MB2
1.71 ±0.07 Ma
MB 1 Lower Bank
fossil bearing sediments
30 cm
C
1 cm
D
0 2.5 5 10 km
GND
HL
HG
GV
MP
DM
RS
SK
SF
KD
CD
BF
BF: Bolt´s Farm
CD: Cooper´s Cave
DM: Drimolen
KD: Kromdraai
GND: Gondolin
GV: Gladysvale
HG: Haasgat
HL: Hoogland
MP: Malapa
RS: Rising Star
SF: Sterkfontein
SK: Swartkrans
Elevation (masl)
1500
1300
1100
900
N
JOHANNESBURG (~50 km)
25°50'0"S
25°55'0"S
26°0'0"S
27°45'0"E
27°50'0"E
27°55'0"E
28°0'0"E
Cradle of Humankind World Heritage site

Fig. 1. Location and cave structure of the site of Swartkrans, South Africa. A) Topographical map of the African continent (inset) showing the major early hominin fossil–bearing regions. (**B**) Photograph of the *Paranthropus* bearing paleocave Swartkrans, showing the MB1 fossil–bearing sediments and dated flowstone (*19*). (**C**) The occlusal view of *Paranthropus* teeth analyzed, from top to bottom: SK 830, a left P_4; SK 835, a left M^3; SK 850, a right P_3; SK 14132, a fragment of an isolated postcanine tooth (supplementary materials). (**D**) Enlarged view of the Cradle of Humankind World Heritage Site in South Africa [shown in (A)], with *Paranthropus* fossil locality names in bold. Swartkrans is marked with a black star.

and single-shot samples of each individual resulted in 4600 to 8500 peptide spectrum matches (PSMs) covering 540 to 780 amino acid positions from 8 to 10 enamel-associated proteins (*24*–*26*), six of which, i.e., ALB, AMBN, AMELX, COL17A1, ENAM, and MMP20, appeared in all analyzed specimens. A total of 425 amino acid positions were consistently identified in all four *Paranthropus* specimens, indicating that the majority of the covered positions are shared across all the samples (fig. S4). For validation, the MS workflow was successfully replicated in a proteomics laboratory in Cape Town, South Africa (fig. S5; supplementary materials).

The authenticity of the recovered sequences is supported by multiple lines of evidence. Firstly, the relationship between free and bound amino acids and their expected levels of racemization as well as the extent of peptide bond hydrolysis indicate that, in all the samples, the dental enamel is exhibiting behavior consistent with a closed system (fig. S6; supplementary materials). Equally, across all four specimens, no or negligible exogenous contamination was supported by the high similarity of the amino acid composition profiles observed both within our sample set and in comparison to other ancient dental enamel specimens previously investigated (figs. S6 and S7; supplementary materials). Secondly, all samples show advanced rates of diagenetically induced amino acid modifications, such as glutamine and asparagine deamidation and arginine to ornithine conversion, compatible with the age and the geographic origin of the *Paranthropus* specimens (fig. S4). Additionally, we observed extended oxidative modification of histidine, phenylalanine, tyrosine, and tryptophan (fig. S8; supplementary materials). Thirdly, the peptide length distribution is skewed toward shorter amino acid chains compared to modern human dental enamel, as previously observed in other paleoanthropological material and in agreement with the high levels of peptide bond hydrolysis observed in the amino acid analysis (fig. S4; supplementary materials). Altogether, these lines of evidence independently support the authenticity of the ancient amino acid sequences we report. An attempt to detect protein-protein cross-links did not lead to any confident identification (supplementary materials).

Specimens SK 850 and SK 835 were unambiguously identified as male *Paranthropus* individuals based on the observation of multiple overlapping AMELY-specific peptides (Fig. 2A; supplementary materials). No AMELY-specific peptide was detected in SK 830 and SK 14132. This absence alone, however, cannot necessarily lead to a female attribution (*27*, *28*), for it is also consistent with these specimens belonging to male individuals whose signal for the AMELY-specific peptides would not be detectable by MS, or their acquisition would be stochastic. To exclude the latter scenario, we used a site-based semiquantitative approach. Specifically, we defined an AMELX intensity threshold above which AMELY-specific peptides should be consistently detectable if present in the sample. For validation, we applied this approach to 11 modern human enamel specimens, achieving sex attribution with 100% accuracy. Because the AMELX site intensities of both SK 830 and SK 14132 were measured above the defined intensity thresholds as well as above the intensity of SK 835, we inferred that both specimens originated from female individuals (Fig. 2 and fig. S9; supplementary materials).

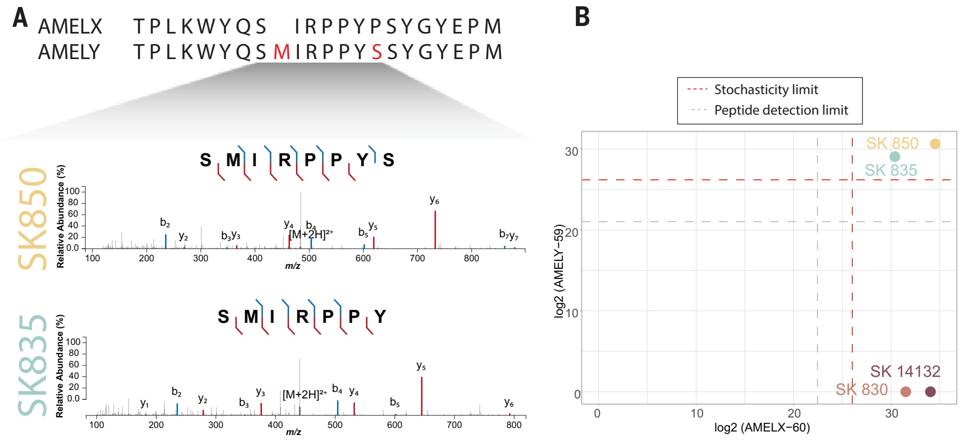

Fig. 2. Sex identification of the four *Paranthropus* specimens. (**A**) MS/MS spectra of AMELY-specific peptides detected in the two male individuals, SK 850 and SK 835. In both spectra, the detection of the methionine in position 59, characteristic of males, is well supported by the fragment ion series. (**B**) Site intensities of AMELY-59 as a function of the site intensities of AMELX-60. Site intensities are calculated as the sum of all precursor intensities covering the given amino acid position. The red dashed lines represent the stochasticity limits inherent to the MS acquisition strategy and setup (supplementary materials). Below the lines, we would expect the acquisition to be stochastic. The gray dashed lines represent the peptide detection limits. They have been assessed as the minimum intensity of a precursor covering the given amino acid position in a male individual for the studied data set. Above the line, precursors can technically and consistently be measured in the MS. Each point represents a different *Paranthropus* specimen. Single-letter abbreviations for the amino acid residues referenced throughout the figures are as follows: T, Thr; P, Pro; L, Leu; K, Lys; W, Trp; Y, Tyr; Q, Gln; M, Met; I, Ile; R, Arg; S, Ser; G, Gly; E, Glu.

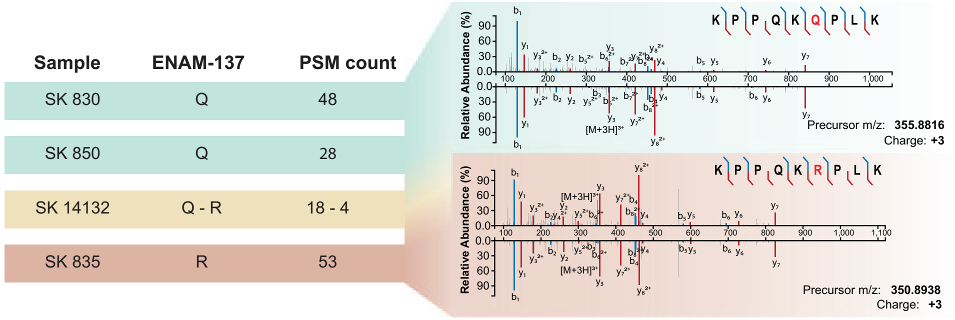

Sample	ENAM-137	PSM count
SK 830	Q	48
SK 850	Q	28
SK 14132	Q - R	18 - 4
SK 835	R	53

Fig. 3. Sequence variation within the *Paranthropus* individuals. Amino acid sequence variation at ENAM-137 in the four *Paranthropus* samples and number of PSMs supporting their detection. The detection of glutamine (Q) and arginine (R) at ENAM-137 was validated with the analysis of synthetic peptides. On the right, the mirror plots represent the MS/MS spectra covering glutamine in peptide KPPQKQPLK and arginine in peptide KPPQKRPLK in the *Paranthropus* samples (top) compared with the MS/MS spectra of the corresponding synthetic peptides (bottom).

We used available buccolingual and mesiodistal measurements of SK 830, SK 835, and SK 850 to compare our molecular-based sex attributions with those based on overall tooth size (supplementary materials). A sample of *A. africanus* is also included for comparison to better assess the extent of size variation in *Paranthropus* (*29*). SK 14132 is not included in the comparison, as its incompleteness precludes reliable measurement (fig. S10). SK 830, which is assigned to a female individual based on molecular evidence, has mesiodistal and buccolingual measurements consistent with specimens previously regarded as female. SK 850, assigned to a male based on AMELY-specific peptides, has a mesiodistal measurement falling within the lower range of size variability seen among specimens previously considered to be males. SK 835, recently suggested to possibly belong to a female individual based on tooth crown dimensions (*30*), is here confidently identified through AMELY-specific peptides as originating from a male. Our results thus indicate that measurements of dental size are not necessarily accurate for correct sex estimation. The protein-based male attribution of SK 835 is consistent with its local strontium isotope signal that previously suggested philopatric male behavior (*31*).

After aligning the amino acid sequences assembled for each *Paranthropus* specimen, we identified a subset of 425 positions that are covered in all four individuals. Among these positions, we detected a variable site in enamelin (ENAM) position 137 (based on *Homo sapiens* canonical Ensembl transcript, ENST00000396073.4). Individuals SK 830 and SK 850 bear a fully deamidated glutamine in that position, whereas SK 835 has an arginine (Fig. 3). Additionally, in SK 14132, the ENAM-137 site appears to be heterozygous, with the glutamine allele covered in 80% of the spectra (18 versus 4 PSMs). The confident identification of the two ENAM-137 alleles is further confirmed by the analysis of synthetic peptides (Fig. 3 and fig. S11).

To assess how unexpected the within-sample variation would be if all four individuals belonged to a single species, we repeatedly sampled four randomly selected individuals from a global sample of present-day humans (supplementary materials). We found it plausible that genetic variants segregating within a given species of equivalent diversity to modern humans could manifest as amino acid differences in a sample of the same size as the one we had for *Paranthropus*. However, we note that the effective population size of humans today most likely differs from that of the *Paranthropus* population we sampled (supplementary materials), leaving any taxonomic conclusion based on this genetic variation alone premature. When we compared the reconstructed protein sequences from the four *Paranthropus* individuals with their orthologs from a panel of extant and extinct hominids (great apes and humans), we detected a total of 16 species-informative single–amino acid polymorphisms (table S1). On the basis of these phylogenetically informative sites, all four *Paranthropus* protein sequences appear closer to those in the *Homo* clade than to any other primate (figs. S12 to S24). Thus, the placement of our *Paranthropus* samples agrees with the consensus view based on morphology (*32*, *33*), further supporting the endogeneity of the protein sequences we retrieved. Given the limited total number of informative sites, conclusive phylogenetic results will require broader sequence coverage. Out of the 16 identified single–amino acid polymorphisms, only two, COL17A1-636 and ENAM-137, showed an allelic state different from that of present-day humans, Neanderthals, and Denisovans. The mapping of these two variants on the primate phylogenetic tree (fig. S12) indicates that although COL17A1-636 is likely an ancestral variant compared to modern humans, the ENAM-137 glutamine is most likely a *Paranthropus*-derived variant.

To integrate the evidence obtained with paleoproteomics and more established morphological approaches (*11*), geometric morphometric analyses of the enamel-dentine junction shape were carried out on

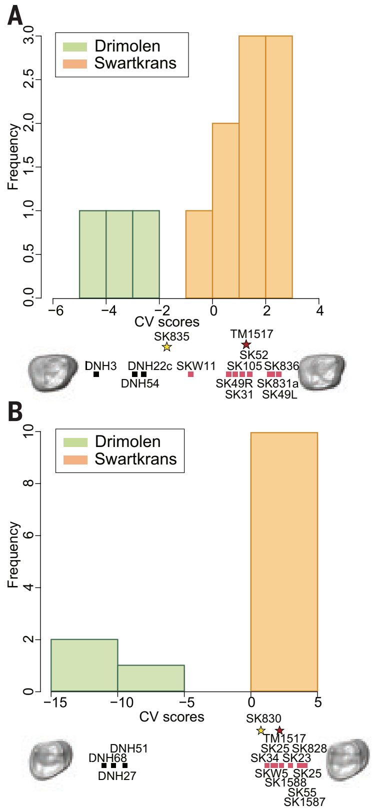

Fig. 4. Geometric morphometric analysis of the enamel-dentine junction. (**A**) Frequency and distribution of canonical variate scores of the Swartkrans (and Kromdraai), and Drimolen M^3s enamel-dentine junction shape analysis. This analysis shows SK 835 as statistically closer to specimens from Drimolen compared with other specimens from Swartkrans and the holotype of *P. robustus* TM 1517 from Kromdraai. (**B**) Same as in (A) but using P_4s, showing that SK 830 is closer to Swartkrans and Kromdraai specimens compared with other specimens from Drimolen.

the two best-preserved specimens (SK 835 and SK 830) (fig. S10). *Paranthropus* M^3 and P_4 had a more asymmetric and taller enamel-dentine junction than those of early *Homo* and, to a lesser extent, than in *Australopithecus*. The results showed that both specimens belong to *Paranthropus* and differ from *Australopithecus* and early *Homo* (supplementary materials). Noticeably, the enamel-dentine junction of SK 835 M^3, bearing ENAM-137R, is statistically more similar to the *Paranthropus* specimens from the site of Drimolen, showing a wider occlusal basin, than to those from the Swartkrans and Kromdraai assemblages, the latter including the holotype of *P. robustus* (TM 1517). The enamel-dentine junction shape of the P_4 SK 830, in contrast, more closely resembles specimens from Swartkrans and Kromdraai and statistically differs from the Drimolen material (Fig. 4).

Discussion and broader implications

We report the recovery of Early Pleistocene hominin partial protein sequences from southern Africa. The four *Paranthropus* specimens we studied were recovered from cave sediments mostly composed of remobilized soil from outside the cave. Sedimentological evidence points to the fossil accumulations resulting from rapid, episodic flash floods, occurring during relatively arid climate conditions (*34*). This, coupled with extensive cementation of the fossil bearing sediments, explains the richness of fossils in the caves and may have also favorably contributed to the preservation of the proteins within the fossil teeth. Whether or not protein preservation would be comparable in other early hominin-bearing deposits, including open-air sites, such as those found elsewhere in Africa, is an open question. Future work must give attention to the feasibility of biomolecular study while minimizing damage to precious African heritage.

The application of manual off-line reversed-phase high-pH fractionation improved the dental enamel protein sequence coverage (fig. S9), revealing the existence of diversity at the protein sequence level within southern African *Paranthropus* individuals. In addition, spectral prediction software and sequenced synthetic peptides helped validate spectra that provided mass spectrometric evidence to confirm this diversity and detect heterozygosity. Mass spectrometry has been previously utilized as a method of choice for the detection of both newly identified genetic variants and heterozygosity in modern human individuals (*35*–*37*). To our knowledge, however, detecting heterozygosity by using MS has never been previously applied in the context of paleoproteomics. Future studies should further explore this aspect.

The molecular identification of both male and female *Paranthropus* individuals demonstrates the limitations of sexing techniques based on tooth size (*30*). This capability has clear implications for our understanding and interpretation of morphological variation in the deep-time hominin fossil record, as it enables us to exclude sexual dimorphism as one of the multiple variables affecting the range of anatomical variation. However, as the method we use is reliant on the identification of AMELY-specific amino acid sequences, male individuals with a deletion of the AMELY gene will not be detected. Deletions of this gene are uncommon but have been recorded both in modern human populations (*38*, *39*) and in one Neanderthal individual (*40*).

Because of a single–amino acid polymorphism (ENAM-137), our reconstructed trees (figs. S13 to S24) suggest that one of the *Paranthropus* individuals (SK 835) might be more distantly related to the other three individuals. Although potentially the result of incomplete lineage sorting, it is also possible that this individual may have belonged to a distinct *Paranthropus* group, which separated from the other individuals relatively recently, a hypothesis compatible with both the paleoproteomics and enamel dentine junction morphology, but microevolution of a single taxon over time (*21*, *41*, *42*) or a large effective population size could also explain the observed genetic and morphological variability. The southern African *Paranthropus* assemblage exhibits considerable size variation, most of which has previously been attributed to sexual dimorphism, possibly reflecting a gorilla-like pattern of extended growth for males, i.e., bimaturation (*13*). However, recent studies have suggested that these morphological differences might indicate either different taxa (*11*, *21*), or site-related diversity within a single species over time, i.e., microevolutionary changes, following a morphocline (*41*, *43*, *44*). The recent description of *P. capensis*, a gracile species of *Paranthropus*, indicates that taxonomic diversity within this genus is currently underestimated and needs to be investigated further (*45*). Regardless, as the small-crowned SK 835 is now confidently assigned to a male, sexual dimorphism is an insufficient explanation for the observed variation within our *Paranthropus* sample set.

The four specimens that we analyzed, along with other fossils from Swartkrans MB1, were not accurately mapped when they were collected; thus, they came from sediments accumulating within a 500-thousand-year time window. Nevertheless, although MB1 sediments potentially cover a long time interval, the fossil-bearing deposits likely accumulated rapidly (*34*). A rapid accumulation would imply that the *Paranthropus* teeth analyzed in this work are penecontemporaneous and, consequently, that the observed variation may more likely result from taxon diversity than from changes of a single taxon over time. Further combined paleoproteomic and morphometric sampling of *Paranthropus* individuals—from Swartkrans and Drimolen, the latter of which hosts samples that are morphologically closer to SK 835—could inform the source of this variation. Given that ENAM-137 was covered with high confidence in all four of our samples, differences in allele frequencies of this single–amino acid polymorphism between specimens from various paleoanthropological sites would consolidate site-specific

Paranthropus variation, whereas more precise and direct dating techniques would help distinguish between microevolution of a single taxon and intrataxonomic diversity.

We show that the analysis of multiple individuals, in conjunction with morphological evidence, can better explore their genetic history and illuminate variation potentially indicative of inter- or intrataxon diversity. Successful protein extraction should be achievable for hominins recovered in other southern African cave sites of similar age and geology, making biological sex identification and intraspecies analysis possible. This study as well as preliminary results recently published (*46*) also raise the possibility of extracting similar data from other African early hominin material, such as *A. africanus* and *A. afarensis* that are represented by a plethora of isolated and fragmentary dental remains. The Cradle of Humankind has yielded an exceptionally large number of hominin fossils, yet the greatest diversity of hominin taxa is currently known from eastern African sites, mainly in the rift valley regions of Ethiopia, Kenya, and Tanzania. Whether and how much of this phyletic diversity is real and not the result of methodological limitations and/or research(er) bias remains a debated topic. The coherent results obtained from this study combining molecular and morphological data have implications for addressing such long-standing controversies surrounding the nature and extent of Plio-Pleistocene hominin diversity (*47*–*49*).

REFERENCES AND NOTES

1. R. E. Green *et al.*, *Science* **328**, 710–722 (2010).
2. D. Reich *et al.*, *Nature* **468**, 1053–1060 (2010).
3. D. S. Strait, F. E. Grine, *J. Hum. Evol.* **47**, 399–452 (2004).
4. T. Harrison, *Int. J. Primatol.* **12**, 85–88 (1991).
5. B. Wood, K. Schroer, "Paranthropus: *Where Do Things Stand?" in Vertebrate Paleobiology and Paleoanthropology* (Springer International Publishing, 2017), pp. 95–107.
6. W. H. Kimbel, T. D. White, *J. Hum. Evol.* **17**, 545–550 (1988).
7. G. Suwa, in *Evolutionary history of the "robust" australopithecines* (Aldine de gruyte, 1988).
8. L. Schroeder, R. R. Ackermann, *J. Hum. Evol.* **174**, 103296 (2023).
9. R. Hall, *J. Hum. Evol.* **6**, 519–531 (1977).
10. J. Braga *et al.*, *J. Hum. Evol.* **130**, 21–35 (2019).
11. C. Zanolli *et al.*, *Proc. Natl. Acad. Sci. U.S.A.* **119**, e2111212119 (2022).
12. M. M. Skinner *et al.*, *Am. J. Phys. Anthropol.* **165**, 254. https://doi.org/10.1002/ajpa.23489.
13. C. A. Lockwood, C. G. Menter, J. Moggi-Cecchi, A. W. Keyser, *Science* **318**, 1443–1446 (2007).
14. P. Skoglund *et al.*, *Cell* **171**, 59–71.e21 (2017).
15. M. Lipson *et al.*, *Nature* **603**, 290–296 (2022).
16. E. Cappellini *et al.*, *Nature* **574**, 103–107 (2019).
17. F. Welker *et al.*, *Nature* **576**, 262–265 (2019).
18. F. Welker *et al.*, *Nature* **580**, 235–238 (2020).
19. R. Pickering, J. D. Kramers, P. J. Hancox, D. J. de Ruiter, J. D. Woodhead, *Earth Planet. Sci. Lett.* **306**, 23–32 (2011).
20. K. Kuman *et al.*, *J. Hum. Evol.* **156**, 103000 (2021).
21. J. M. Martin, A. B. Leece, S. E. Baker, A. I. R. Herries, D. S. Strait, *Evol. Anthropol.* **33**, e22018 (2024).
22. T. S. Batth, C. Francavilla, J. V. Olsen, *J. Proteome Res.* **13**, 6176–6186 (2014).
23. P. L. Rüther *et al.*, *Nat. Commun.* **13**, 2458 (2022).
24. J. P. Simmer, J. C. Hu, *Connect. Tissue Res.* **43**, 441–449 (2002).
25. A. G. Fincham, J. P. Simmer, *Ciba Found. Symp.* **205**, 118–130, discussion 130–134 (1997).
26. J. P. Simmer *et al.*, *J. Struct. Biol.* **213**, 107805 (2021).
27. G. J. Parker *et al.*, *J. Archaeol. Sci.* **101**, 169–180 (2019).
28. T. P. Cleland, S. A. McGuire, J. S. Beatrice, K. S. Moran, C. A. M. France, *J. Archaeol. Sci.* **168**, 106006 (2024).
29. B. Wood, *Koobi Fora Research Project*, vol. 4 of *Hominid Cranial Remains* (Oxford Univ. Press, 1991).
30. C. Dean *et al.*, *Sci. Rep.* **10**, 19053 (2020).
31. S. R. Copeland *et al.*, *Nature* **474**, 76–78 (2011).
32. M. Dembo *et al.*, *J. Hum. Evol.* **97**, 17–26 (2016).
33. C. S. Mongle, D. S. Strait, F. E. Grine, *J. Hum. Evol.* **175**, 103311 (2023).
34. R. Pickering *et al.*, *Nature* **565**, 226–229 (2019).
35. Y. A. Daniel, C. Turner, R. M. Haynes, B. J. Hunt, R. N. Dalton, *Br. J. Haematol.* **130**, 635–643 (2005).
36. K. E. Mason, D. Anex, T. Grey, B. Hart, G. Parker, *Forensic Sci. Int.* **288**, 89–96 (2018).
37. P.-W. Wu *et al.*, *Proteomics* **17**, 1600462 (2017).
38. Q. Pang, Q. Lin, D. Wang, Z. Sun, J. Wang, *Int. J. Legal Med.* **135**, 1351–1358 (2021).
39. R. J. Mitchell, M. Kreskas, E. Baxter, L. Buffalino, R. A. H. Van Oorschot, *Ann. Hum. Biol.* **33**, 227–240 (2009).
40. L. Skov *et al.*, *Nature* **610**, 519–525 (2022).
41. J. M. Martin *et al.*, *Nat. Ecol. Evol.* **5**, 38–45 (2021).
42. A. B. Leece *et al.*, *Am. J. Biol. Anthropol.* **179**, 240–260 (2022).
43. Y. Rak, W. H. Kimbel, J. Moggi-Cecchi, C. A. Lockwood, C. Menter, *J. Hum. Evol.* **151**, 102913 (2021).
44. J. Braga, G. Chinamatira, B. Zipfel, V. Zimmer, *Sci. Rep.* **12**, 13956 (2022).
45. C. Zanolli *et al.*, *J. Hum. Evol.* **200**, 103634 (2025).
46. P. P. Madupe *et al.*, *S. Afr. J. Sci.* **121**, 18571 (2025).
47. Y. Haile-Selassie *et al.*, *Nature* **521**, 483–488 (2015).
48. F. Spoor, M. G. Leakey, P. O'Higgins, *Philos. Trans. R. Soc. Lond. B Biol. Sci.* **371**, 20150231 (2016).
49. T. White, *Curr. Biol.* **23**, R112–R115 (2013).
50. Y. Perez-Riverol *et al.*, *Nucleic Acids Res.* **50**, D543–D552 (2022).
51. P. P. Madupe *et al.*, Data from: Enamel proteins reveal biological sex and genetic variability within southern African *Paranthropus*, Zenodo (2024); https://doi.org/10.5281/zenodo.10843737.

ACKNOWLEDGMENTS

All the *Paranthropus* fossil specimens analyzed for this study are part of the permanent collection of the Ditsong National Museum of Natural History in Pretoria, South Africa. All nonhominin faunal fossil specimens analyzed for this study are part of the permanent collection of the University of the Witwatersrand in Johannesburg, South Africa. Permits for temporary export and sampling were issued by the South African Heritage Resources Agency (SAHRA permit IDs: 2946, 3079, and 3132). Access to these specimens can be requested through Ditsong National Museum (specimen IDs: SK 830, SK 835, SK 850, and SK 14132) and the University of the Witwatersrand (specimen IDs: SKX 37041, SKX 3730, SKX 4996 a, and CD. 5410). We acknowledge R. Fong-Zazueta for creating and providing the protein translations of the "independent" reference dataset. This research contributes toward the output of the Biogeochemistry Research Infrastructure Platform (BIOGRIP), supported by the Department of Science and Innovation, South Africa. **Funding:** European Union (EU)'s Marie Skłodowska-Curie (MS-C) training network "PUSHH" under the Horizon 2020 research and innovation program, grant no. 861389 (P.P.M., C.K., I.P., J.K., C.G., P.K., J.C., K.P., F.R., T.M.B., J.V.O., and E.C.); EU's MS-C training network "TEMPERA" under the Horizon 2020 research and innovation program, grant no. 722606 (P.L.R., E.C., and J.V.O.); European Research Council (ERC) Advanced Grant "BACKWARD," agreement no. 101021361, under the EU's Horizon 2020 program (E.C., P.P.M., I.P., C.Z., L.S., F.R., J.V.O., R.R.A., A.J.T., M.M., and G.T.); ERC PoC Grant "SSPIN," agreement no. 101138962, under the EU's Horizon Europe program (E.C. and I.P.); VILLUM FONDEN grant agreement no. 17649 (E.C., F.W., and J.R.M.); Danish National Research Foundation "PROTEIOS" (M.M.); Danish National Research Foundation "DNRF128" (M.M.); The Novo Nordisk Foundation grant agreement no. NNF14CC0001 (C.K., P.L.R., and J.V.O.); National Research Foundation of South Africa grant agreement no. 117670 (R.R.A. and N.H.); National Research Foundation of South Africa grant agreement no. 136512 (R.R.A. and N.H.); Natural Sciences and Engineering Research Council of Canada Discovery Grant grant agreement no. RGPIN-2020-04159 (L.S.); VILLUM FONDEN grant agreement no. 00025300 (F.R.); Novo Nordisk Foundation Data Science Ascending Investigator Award grant agreement no. NNF22OC0076816 (F.R.); ERC under the European Union's Horizon 2020 grant agreement no. 101077592 (F.R.); ERC under the European Union's Horizon 2020 grant agreement no. 951385 (F.R.); ERC under the European Union's Horizon 2020 grant agreement no. 864203 (T.M.B.); Natural Environment Research Council (NERC) grant agreement no. NE/S010211/1 (M.D. and K.P.); Department of Science and Innovation in South Africa "DIPLOMICS" (L.B. and M.L.P.); French National Research Agency "GenoMorph" grant agreement no. ANR-20-CE12-0018 (C.Z.); IdEx "Investments for the Future" program / GPR "Human Past" (C.Z.). **Author contributions:** Conceptualization: J.V.O., R.R.A., E.C.; Methodology: P.P.M., C.K., I.P., P.L.R., C.Z., L.S., E.C.; Investigation: P.P.M., C.K., P.L.R., N.H., M.M., A.J.T., G.T., M.R.D., F.W.; Formal analysis: P.P.M., C.K., I.P., P.L.R.; Resources: M.T., B.Z.; Visualization: C.K., I.P., J.K., R.P.; Software: P.P.M., C.K., I.P., P.L.R., J.K., C.G., P.K., C.Z., L.S.; Data curation: I.P., J.R.-M., C.Z., L.S.; Funding acquisition: K.P., J.V.O., R.R.A., E.C.; Project administration: R.R.A., E.C.; Supervision: J.C., C.T., J.B., T.M.-B., K.P., F.R., J.V.O., R.R.A., E.C.; Validation: L.B., M.D.; Writing – original draft: P.P.M., C.K., I.P., J.K., R.P., M.R.D., Y.S., D.K., C.M., F.M., C.Z., L.S., R.R.A.; Writing – review & editing: P.P.M., C.K., I.P., P.L.R., M.M., M.T., J.K., A.J.T., J.K., R.P., M.R.D., Y.S., D.K., C.M., F.M., B.Z., L.F.K.K., E.L., F.W., C.M., J.R.-M., T.M.-B., K.P., C.Z., L.S., F.R., J.V.O., R.R.A., E.C. **Competing interests:** The authors declare that they have no competing interests. **Data and materials availability:** The mass spectrometry proteomics data have been deposited to the ProteomeXchange Consortium (http://proteomecentral.proteomexchange.org) through the PRIDE partner repository (*50*) with the dataset identifier PXD040221. Reference Datasets, XML files, and phylogenetic results files are available on Zenodo (*51*) . Custom R-code for sequence assembly is available on GitHub at https://github.com/ClaireKoenig/ProteinSequenceAssembly. Genetic Variation analysis code is available on GitHub at https://github.com/johnpatramanis/Code_for_Genetic_Diversity_Sampling. Commands for the generation of the phylogenetic workflow is available in the supplementary materials. **License information:** Copyright © 2025 the authors, some rights reserved; exclusive licensee American Association for the Advancement of Science. No claim to original US government works. https://www.science.org/about/science-licenses-journal-article-reuse

SUPPLEMENTARY MATERIALS

science.org/doi/10.1126/science.adt9539
Materials and Methods; Supplementary Text; Figs. S1 to S24; Tables S1 to S21; References (*52*–*180*); MDAR Reproducibility Checklist; Data S1 to S4

Submitted 25 October 2024; accepted 3 April 2025

10.1126/science.adt9539

PALEONTOLOGY

Arctic bird nesting traces back to the Cretaceous

Lauren N. Wilson[1,2,3]*, Daniel T. Ksepka[4], John P. Wilson[3], Jacob D. Gardner[5], Gregory M. Erickson[6], Donald Brinkman[7,8], Caleb M. Brown[7,8,9], Jaelyn J. Eberle[10,11], Chris L. Organ[12], Patrick S. Druckenmiller[1,2]*

Polar ecosystems are structured and enriched by birds, which nest there seasonally and serve as keystone ecosystem members. Despite the ecological importance of polar birds, the origins of high-latitude nesting strategies remain obscured by a sparse fossil record. We report an extreme-latitude Arctic avialan assemblage from the Prince Creek Formation of Alaska—the northernmost Late Cretaceous terrestrial ecosystem. Numerous three-dimensionally preserved fossils constitute one of the most taxonomically rich Late Cretaceous avialan assemblages, including members of Hesperornithes, Ichthyornithes, and near-crown or crown birds (Neornithes), recording a previously undocumented interval in avialan evolution. Abundant perinatal fossils represent the oldest evidence of birds nesting at polar latitudes, which demonstrates that birds began using seasonal polar environments for breeding during the Cretaceous, long before their modern descendants.

Using polar ecosystems for breeding offers exceptional benefits and challenges to more than 250 species of modern birds. Certain birds, such as the Arctic tern (*Sterna paradisaea*), migrate more than 80,000 km annually between Antarctica and the Arctic Circle (*1*). By contrast, the Svalbard rock ptarmigan (*Lagopus muta*) is a year-round Arctic resident, having adapted to endure harsh winter conditions, including subfreezing temperatures, snowfall, and several months of continuous winter darkness (*2*, *3*). Polar birds preferentially nest in such challenging environments to exploit seasonally abundant summer food resources, including growing plants, increased invertebrate biomass, and increased fish populations that benefit from seasonal zooplankton blooms (*4*). This trophic richness is fueled by a polar summer light regime with up to 24 hours of daylight that provides relative protection from predation for nesting and newly hatched birds (*5*). Arctic birds make up less than 2% of global avian richness, but some populations are enormous, with monospecific breeding colonies often exceeding 10,000 individuals (*6*). Arctic birds also serve as keystone ecosystem members that pollinate, disperse seeds, and regulate insect and small mammal populations (*7*). It has been hypothesized that over deep time, birds contributed to structuring modern ecosystems by helping plants, invertebrates, and other species rapidly disperse over long distances to colonize remote regions (*8*, *9*). Understanding polar ecosystem structure and evolution, therefore, pivots on elucidating the advent of polar habitat colonization by birds.

Birds are typically undersampled in the fossil record relative to other vertebrates, a bias exacerbated at the poles, where they are even more sparsely represented compared with lower-latitude formations (*10*). The previous oldest evidence of near-polar bird nesting comes from the late Eocene La Meseta Formation of Seymour Island, Antarctica, located just north of the Antarctic Circle at a paleolatitude of 64°S (*11*). It has produced abundant immature penguin fossils, suggesting a nearby breeding colony (*11*). However, the oldest of these fossils date to 40.5 to 46.5 million years ago (Ma) (*12*), which leaves a gap of more than 100 million years after the origin of birds (Avialae) in the Late Jurassic (*13*).

Our understanding of avialan evolution is further hindered by uncertainty surrounding the origin of crown birds (Neornithes). This is a contentious topic, plagued by referrals based on fragmentary material—a problem magnified by the sparse record of the most crownward stem birds (Ornithurae) (Fig. 1A), which, with the exceptions of Hesperornithes (*14*, *15*) and Ichthyornithes (*15*–*17*), are known predominantly from partial, isolated elements. Only two latest Cretaceous (~66.5 Ma) taxa, *Asteriornis* and *Vegavis*, are widely accepted as unambiguous Mesozoic crown birds (*18*, *19*). However, more than 20 million years separate these species from the commonly recovered sister taxon to Neornithes, *Iaceornis* (86.5 Ma) (*20*). Some specimens have been suggested to fill this gap, but they are typically single, isolated elements with little avifaunal context (*21*), which has resulted in a suite of unanswered questions regarding the evolutionary transition to Neornithes.

We report an extreme high-latitude paleo-Arctic avialan assemblage from the late Campanian (~72.8 Ma) (*22*, *23*) Prince Creek Formation of northern Alaska. This formation preserves the northernmost known Late Cretaceous terrestrial vertebrate assemblage (*24*), deposited at a paleolatitude of 80° to 85°N (*24*) (Fig. 1B). Year-round occupants experienced adverse winter conditions, including several months of continuous darkness, and likely periods of freezing winter temperatures, including occasional snowfall (*24*). Correspondingly, the ecosystem benefited from an extreme summer light regime with ~6 months of continuous daylight (*24*) (Fig. 1C). Numerous three-dimensionally preserved elements, representing every skeletal region, record a taxonomically rich ornithurine avialan assemblage, including Hesperornithes, Ichthyornithes, and several species within or closely related to Neornithes. Abundant perinatal bird fossils document the oldest instance of birds nesting in a seasonal polar ecosystem. These fossils likewise represent the first known perinatal Mesozoic euornithines and include evidence of elements expressing ontogenetically early full-skeletal fusion, a hallmark bird feature. We demonstrate that birds have nested in Arctic environments for at least 72.8 million years (*22*, *23*)—nearly half the tenure of birds on Earth (*13*)—and that Arctic bird breeding arose millions of years before the end-Cretaceous mass extinction ignited the neornithine radiation (*25*).

Taxonomic richness

The Prince Creek Formation avialans exhibit features consistent with at least three euornithine clades. Phylogenetic analyses provide a working hypothesis for the relationships of the Prince Creek Formation taxa, which we supplement with extensive morphological comparisons with other Late Cretaceous euornithines (see supplementary text).

At least one species of Ichthyornithes is represented by a craniocaudally compressed distal humerus with a weak intercondylar incisure (Fig. 2E); two radii with very shallow, oval proximal articular facets (Fig. 2B and fig. S5); two distal carpometacarpi that bear ventrally deflected tubercles proximal to the distal metacarpal symphysis (Fig. 2A and fig. S5); and a proximal manual phalanx II-1 that resembles that of *Ichthyornis* (Fig. 2C). A second manual phalanx II-1 preserves a strongly projected internal index process. Although this process is present in some neoavians, it is considered synapomorphic for Ichthyornithines among Cretaceous birds (*16*, *17*) (Fig. 2D).

---

[1]University of Alaska Museum, Fairbanks, AK, USA. [2]Department of Geosciences, University of Alaska Fairbanks, Fairbanks, AK, USA. [3]Department of Geosciences, Princeton University, Princeton, NJ, USA. [4]Bruce Museum, Greenwich, CT, USA. [5]School of Biological Sciences, University of Reading, Reading, UK. [6]Department of Biological Science, Florida State University, Tallahassee, FL, USA. [7]Royal Tyrrell Museum of Palaeontology, Drumheller, AB, Canada. [8]Department of Biological Sciences, University of Alberta, Edmonton, AB, Canada. [9]Department of Earth Sciences, University of Manitoba, Winnipeg, MB, Canada. [10]University of Colorado Museum of Natural History, Boulder, CO, USA. [11]Department of Geological Sciences, University of Colorado, Boulder, CO, USA. [12]Department of Earth Sciences, Montana State University, Bozeman, MT, USA. ***Corresponding author. Email: lauren.wilson@princeton.edu (L.N.W.); psdruckenmiller@alaska.edu (P.S.D.)**

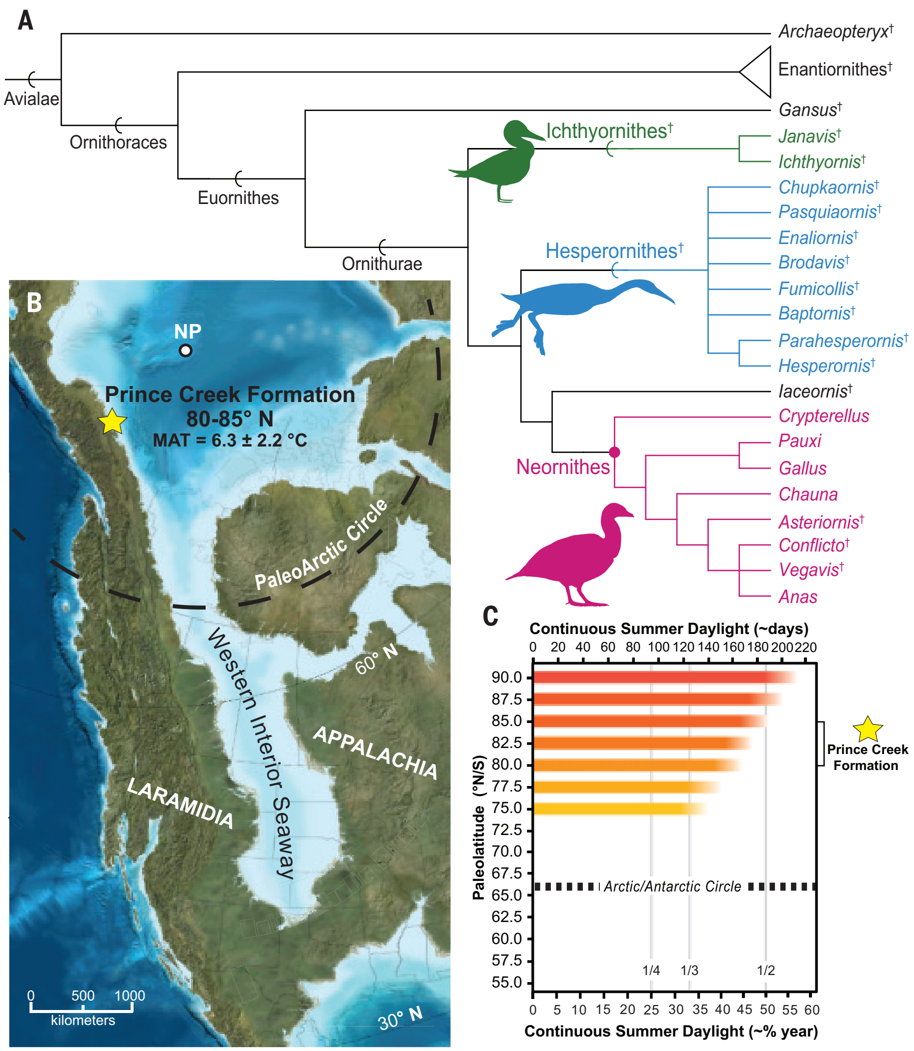

Fig. 1. Key avialan relationships and location and paleoenvironmental conditions of the Prince Creek Formation. (**A**) Simplified cladogram showing key avialan relationships based on Torres *et al*. (*49*) and Benito *et al*. (*16*). Clades with affinities in the Prince Creek Formation are colored and denoted with silhouettes (*Vegavis iaai* by Matt Martyniuk, CC BY 3.0; *Hesperornis regalis* by Scott Hartman, CC BY 3.0; and *Ichthyornis anceps* by Matt Martyniuk, CC BY 3.0). (**B**) North American paleogeography 72 Ma, map by Ron Blakey. Figure modified with permission from Druckenmiller *et al*. (*24*). (**C**) Comparison of polar light regime as approximated by the relative extent of continuous summer daylight by latitude (measured in number of days and percentage of year). Figure modified with permission from Druckenmiller *et al*. (*24*). MAT, mean annual temperature; N, north; NP, North Pole; S, south.

We identify at least one species of Hesperornithes from both adult and immature elements. These include two diagnostic quadrates with shallow intercondylar incisures and otic capituli larger than the squamosal capituli (Fig. 2G and fig. S1), a heterocoelous cervical vertebra with large pleurocoels but lacking pneumatic foramina (Fig. 2H), and a tibiotarsus with a proximally expanded cranial cnemial crest and extremely thickened compacta (Fig. 2F). Two immature distal humeri exhibit the robust shape, arched shaft, and poorly developed intercondylar incisures that characterize those hesperornithines that retain well-developed humeri (Fig. 3C and fig. S4).

We also identify multiple highly derived ornithurine species (crownward of Hesperornithes) based on adult and immature elements. Cranial material attributed to derived birds includes two dorsoventrally deep, broadly rounded, and edentulous premaxillae, which show perinatal texture but complete midline fusion (Fig. 3A and fig. S1), and three edentulous dentaries, two of which preserve broad, bony mandibular symphyses (Fig. 2M and fig. S1), considered a Neornithine synapomorphy by Field *et al.* (*18*). A furcula bears a distinct acrocoracoid articular facet extending from the clavicular ramus (Fig. 2N). Six partial coracoids exhibit humeral articular facets that lie omal to the scapular cotyle (*16*), recovered as synapomorphic of *Iaceornis* and Neornithes by Benito *et al.* (*16*). Two of these coracoids also preserve strongly medially hooked acrocoracoid processes (Fig. 2J and figs. S2 and S3), identified as a synapomorphy of Neornithes by Benito *et al.* (*16*). A partial coracoid bears a pneumatic foramen in the dorsal impression for the insertion of m. sternocoracoidei (Fig. 2O). A pneumatic coracoid is considered synapomorphic of Neornithes (*16*), and the presence of an external foramen is considered the most dependable parameter for determining pneumaticity (*26*). Three partial scapulae bear strongly hemispherical coracoid tubercles but elongate acromion processes (fig. S3), comparable to the condition observed in presbyornithids (*27*). A proximal humerus exhibits a globose humeral head; highly reduced deltopectoral crest; and large, deeply excavated tricipital fossa (Fig. 2P)—a condition more similar to Anseriformes than *Ichthyornis* (*17*, *28*). A second, nearly complete humerus bears a deep, well-defined intercondylar incisure between two globose and cranially located condyles; a particularly deeply excavated olecranon fossa; and a highly reduced deltopectoral crest (Fig. 2I). A proximal carpometacarpus has a grooved capital tubercle (Fig. 2K), to date only observed in *Iaceornis* and crown birds (*17*, *20*). A distal tibiotarsus preserves an ossified supratendinal bridge (Fig. 2L), also observed only in *Iaceornis* and crown birds (*17*, *20*).

Additional partial elements are less diagnostic but preserve morphologies consistent with assignment to Euornithes (figs. S1 to S8 and supplementary text). We note that referral to Enantiornithes can be ruled out for most elements, including many that are highly incomplete. For instance, all coracoids show a concave scapular cotyle, and all scapulae show a convex coracoid tubercle, whereas in enantiornithines, the coracoid instead bears a convexity that fits into a concavity on the scapula. Likewise, all perinatal tarsometatarsi show strong fusion of the metatarsals near their distal ends, whereas the sutures in this region remain distinct late into ontogeny in Enantiornithes.

These taxonomic referrals are broadly supported by phylogenetic positions recovered from parsimony and Bayesian analyses sampling individual specimens (figs. S9 and S10) and support the hypothesis that the Prince Creek Formation avialan assemblage is composed of derived ornithurines. In most cases, strict consensus trees place sampled elements in a polytomy with Ornithurae, in a polytomy with the clade uniting Hesperornithes and Neornithes, or in a polytomy with all sampled Neornithes. The only analyses that result in a placement outside of Ornithurae are the Bayesian analyses for UAMES 51880 (scapula) and UAMES 41764 (quadrate). The placement of the scapula is likely a result of the acromion process that projects anteriorly past the coracoid tubercle—a condition observed in basal taxa, including *Ambiortus* (*29*), but that also occurs in *Iaceornis* (*20*) and in some

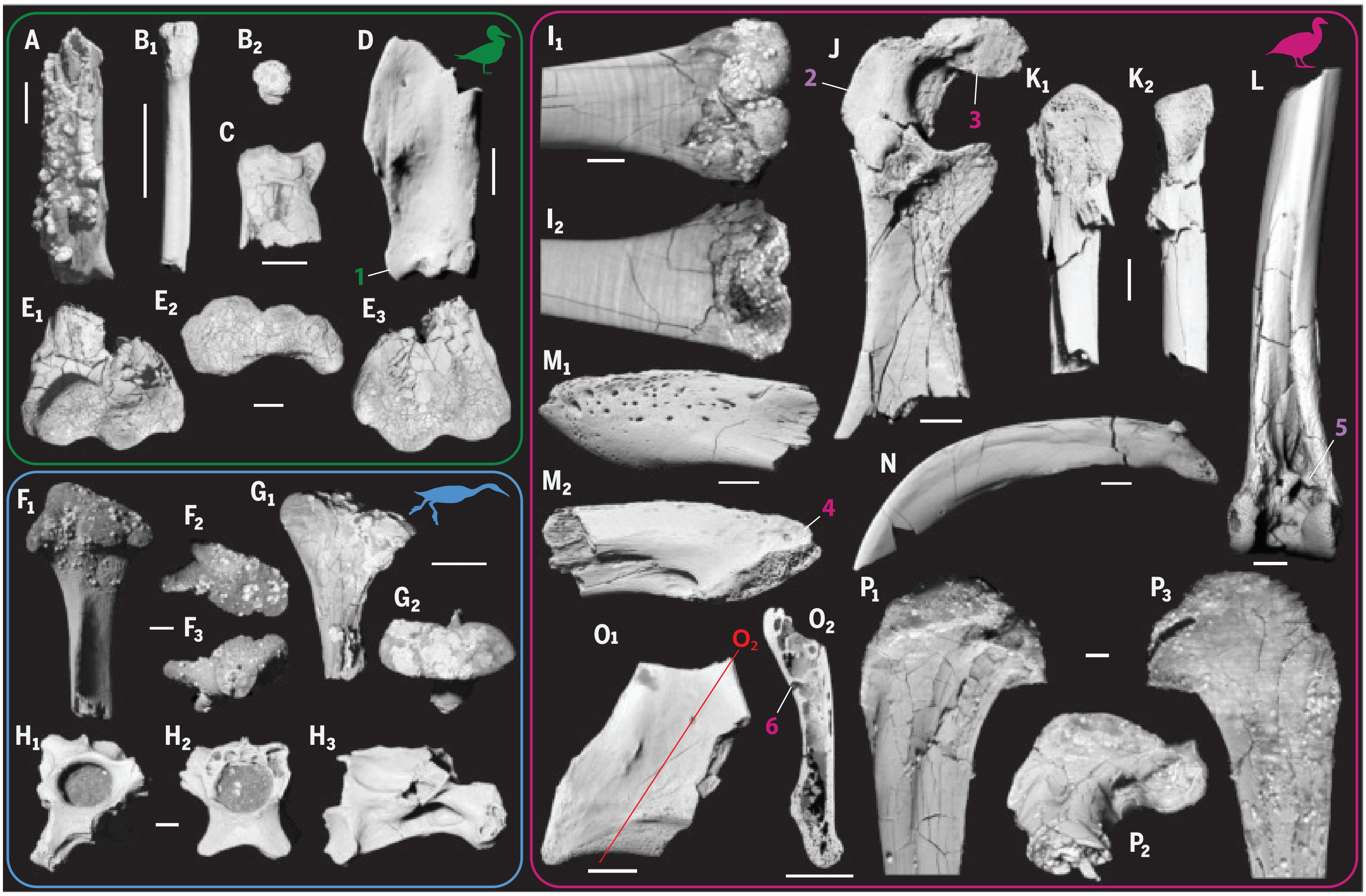

Fig. 2. Select adult elements and their taxonomic affinities. (**A**) UAMES 52854, right carpometacarpus, cranial view. (**B**) UAMES 51909, left radius, caudal (B_1) and proximal (B_2) views. (**C**) UAMES 42806, right manual phalanx II-1, ventral. (**D**) UAMES 36366, right manual phalanx II-1, dorsal. (**E**) UAMES 39671, left humerus, cranial (E_1), distal (E_2), and caudal (E_3). (**F**) UAMES 34561, left tibiotarsus, lateral (F_1), proximal (F_2), and distal (F_3). (**G**) UAMES 41764, right quadrate, medial (G_1) and dorsal (G_2). (**H**) UAMES 41892, cervical vertebra, cranial (H_1), caudal (H_2), and right lateral (H_3). (**I**) UAMES 39672, right humerus, cranial (I_1) and caudal (I_2). (**J**) UAMES 53973, left coracoid, dorsal. (**K**) UAMES 51867, right carpometacarpus, ventral (K_1) and caudal (K_2). (**L**) UAMES 36340, right tibiotarsus, cranial. (**M**) UAMES 51902, left dentary, lateral (M_1) and medial (M_2). (**N**) UAMES 36541, right furcula, lateral. (**O**) UAMES 36364, right coracoid, dorsal (O_1) and cross-sectional (O_2). (**P**) UAMES 52957, left humerus, caudal (P_1), caudodistal (P_2), and cranial (P_3). Key synapomorphies (purple, Neornithes+*Iaceornis*; pink, Neornithes; green, Ichthyornithes): 1, internal index process; 2, humeral articular facet omal to scapular cotyle; 3, medially hooked acrocoracoid; 4, edentulous dentary with bony mandibular symphysis. 5, supratendinal bridge; 6, pneumatic coracoid. All scale bars, 2 mm.

crown birds. The placement for the quadrate is likely a result of the small number of codable characters because comparison of morphological features strongly supports a placement within Hesperornithes (supplementary text).

Perinatal elements

We confidently identify 14 elements as perinatal (embryos or hatchlings) based on extremely porous external bone surface textures, formed from the trapping of incompletely formed primary vascular canals at the periosteal surfaces (*24*, *30*). Computed tomography (CT) data reveal highly vascularized endochondral bone and bulbous osteocyte lacunae (*24*), which support this diagnosis. A humerus and femur are identified as immature but not perinatal on the basis of more developed (though still porous) bone texture (figs. S4 and S5).

Two perinatal premaxillae are distinct among Mesozoic taxa in being rostrally rounded and dorsoventrally deep (Fig. 3A and fig. S1). A complex system of neurovascular foramina is consistent with the presence of a keratinous rhamphotheca (*31*, *32*). These premaxillae have three to four sets of semiregular palatal foramina that, along with external neurovascular foramina, open into canals that communicate with large internal cavities (fig. S8). As in the Cenozoic gastornithid *Omorhamphus*, these likely serve as additional neurovascular foramina that close later in ontogeny (*33*). These premaxillae are tentatively referred to Ornithurae. Whereas loss of premaxillary teeth also occurs in some basal birds and enantiornithines, the combination of being edentulous; the rounded, rather than acutely pointed, rostral margin; and the dorsoventrally deep nature support a placement crownward of Hesperornithes.

A perinatal coracoid with a procoracoid process, a concave and teardrop-shaped scapular cotyle, and an open supracoracoid nerve foramen [compared with Ornithurine E (*34*)] can be confidently assigned to Ornithurae (Fig. 3B). Two immature humeri, one of which is perinatal (Fig. 3C) and one of which is larger with more extensively developed surface texture (fig. S4), exhibit hesperornithine features, including poorly divided distal condyles (though this may be an artifact of the immature status) and dorsally bowed shafts (*14*). Ten perinatal tarsometatarsi show full distal fusion of the metatarsals and strong plantar projection of metatarsal II, consistent with placement within Ornithurae (Fig. 3 and figs. S6 and S7). More basal euornithines, such as *Archaeorhynchus*, do not exhibit such fusion until much later in ontogeny (*35*).

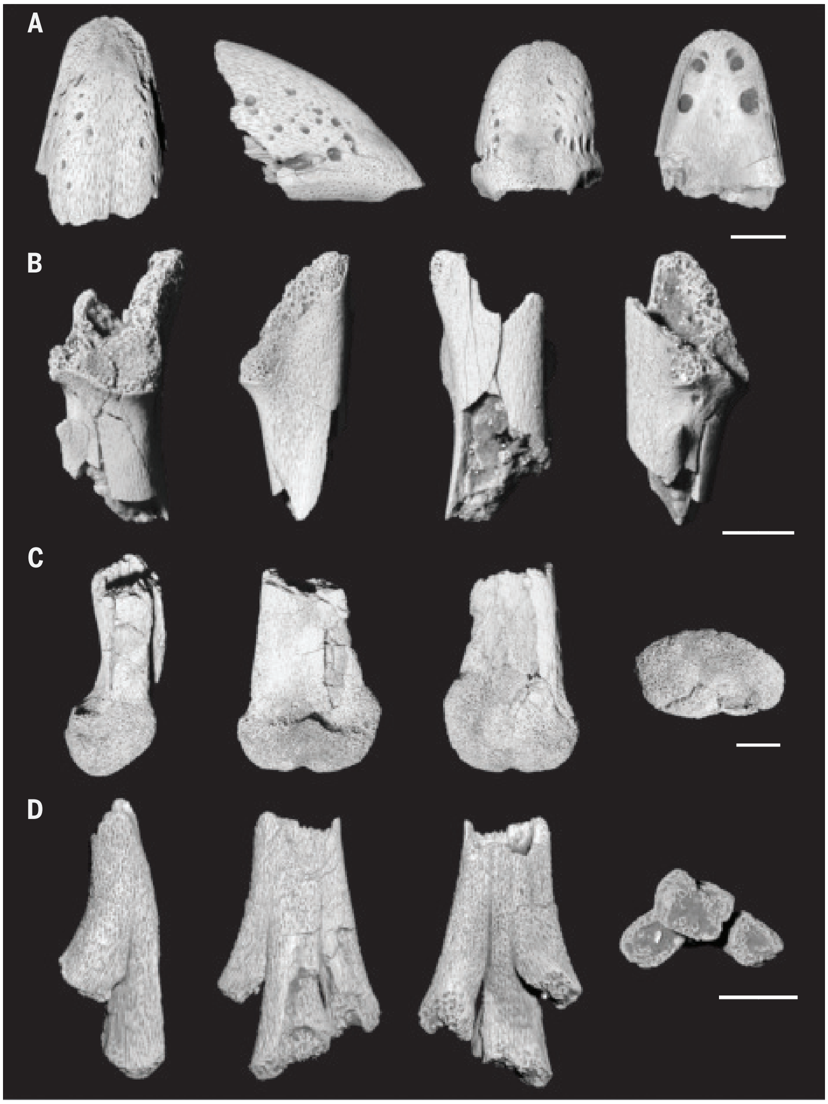

Fig. 3. Select perinatal elements. (**A**) UAMES 42695, paired and fused premaxilla, in dorsal, right lateral, rostral, and palatal views (left to right). (**B**) UAMES 41966, omal end of right coracoid, in dorsal, lateral, ventral, and medial views (left to right). (**C**) UAMES 42694, distal end of left humerus, in dorsal, cranial, caudal, and distal views (left to right). (**D**) UAMES 42700, distal end of left tarsometatarsus, in medial, dorsal, plantar, and distal views (left to right). All scale bars, 2 mm.

Discussion

Adult bird fossils from the Prince Creek Formation make up an exclusively ornithurine fauna, including confident representation of Ichthyornithes and Hesperornithes, filling a key taxonomic and temporal gap along the evolutionary transition to Neornithes. Referrals of specimens exhibiting more derived morphologies are uncertain, although many elements preserve synapomorphies consistent with a near-crown or crown phylogenetic position. Elements consistent with a placement closer to Neornithes than to Hesperornithes include edentulous dentaries with a fused symphysis (Fig. 2M), coracoids with their humeral articular facet omal to the scapular cotyle (Fig. 2J), and a tibiotarsus preserving an ossified supratendinal bridge (Fig. 2L) (*16*). Two additional features are observed only in the Prince Creek Formation fossils and Neornithes: a coracoid preserving a pneumatic foramen (Fig. 2O) and a coracoid with a medially hooked acrocoracoid process (Fig. 2J) (*16*). These features demonstrate that the Prince Creek Formation includes some of the most crownward-known morphologies among Cretaceous birds, many of which are consistent with the presence of one or more early-diverging members of Neornithes. Additionally, these derived elements consistently bear a strong resemblance to extinct and extant species of Anseriformes (supplementary text) (*27*, *28*), consistent with expectations for birds near the base of the crown and a Cretaceous origin for Galloanserae (*18*, *25*). Alternatively, if the Prince Creek Formation birds are exclusively near-crown stem birds, then these characteristics would not exclusively diagnose Neornithes but rather a more inclusive suite of crown and stem species. Further, although early growth stages of the more basally divergent Enantiornithes are well known (*36*, *37*), the Prince Creek Formation documents the ontogenetically earliest-known growth stages for Mesozoic euornithines and ornithurines. Rapid growth rates and full skeletal fusion at early ontogenetic stages are hallmark traits of modern birds that have greatly contributed to their success. Fully fused perinatal premaxillae and tarsometatarsi from the Prince Creek Formation provide the first evidence of this extremely early skeletal fusion in Mesozoic birds (*38*).

Polar ecosystems present some of the most extreme evolutionary and behavioral challenges on the planet. Living far north of the paleo–Arctic Circle at 80° to 85°N, year-round terrestrial inhabitants of the Prince Creek Formation ecosystem are the only Late Cretaceous vertebrates currently known to have endured seasonal polar conditions (*24*). Although not as cold as Arctic conditions today, these environments underwent cold winters with occasional freezing temperatures [cold month mean temperature proxy estimates range from −2.0° ± 3.9°C (*39*) to 2° to 4°C (*40*)] and an extreme seasonal light regime, which impose a distinctive set of adaptive constraints (*24*). The extension of polar nesting back to the late Campanian is important for calibrating the origins of Arctic ecosystem utilization by birds—a strategy that was also used by a diversity of nonavialan dinosaurs (hereafter referred to as dinosaurs). Abundant perinatal material demonstrates that the dinosaurs were year-round residents, as prolonged incubation times would prohibit them from reaching body sizes necessary for long-distance migration (*24*). Just like the dinosaurs, avialans used this Arctic ecosystem for nesting, and they and their hatchlings may have likewise endured these adverse winter conditions; however, unlike their dinosaur counterparts, shorter incubation and maturation times as well as powered flight (with the notable exception of members of Hesperornithes) may have enabled them to migrate to more equable, southerly latitudes. Today, most birds that range above 70°N migrate south before the onset of winter. Most species that overwinter are large bodied, with a few notable exceptions (e.g., chickadees). Thus, it is possible that many of the volant Prince Creek avialans were migratory, potentially serving as dispersal agents and playing an essential role in structuring and enriching their paleo-Arctic ecosystem. Either scenario, overwintering or migrating, would represent the earliest occurrence of such behaviors in birds. The utilization of seasonal polar ecosystems for breeding is a crucial strategy for hundreds of modern bird species, and evidence for its origination before the end-Cretaceous mass extinction reshaped life on Earth is a testament to its adaptive resilience.

The abundance of perinatal dinosaur and ornithurine material from the Prince Creek Formation stands in marked contrast to the conspicuous absence of enantiornithine birds that dominate most other Cretaceous avialan assemblages (*41*). This is consistent with other Cretaceous high-latitude ecosystems, where only euornithine taxa have been recovered thus far (*42*, *43*). Most crown birds directly incubate their eggs, with hatchlings fledging and reaching adult body size within weeks (*44*), and Cretaceous ornithurines may have achieved similarly rapid growth rates (*41*). Enantiornithines are thought to have shown slower incubation times (*41*) and to have laid proportionally smaller eggs, which they partially buried (*45*), typically in warm, humid environments (*46*). They may have been unable to directly incubate their eggs, owing to their adult body mass exceeding egg strength (*47*), and did not rotate their eggs, resulting in longer incubation times (*41*). Although enantiornithines were highly precocial and possibly capable of flight within 24 hours after hatching, they developed slowly, not reaching adult body sizes for several years (*41*). Further, Early Cretaceous enantiornithines are thought to have used intermittent flapping flight styles (*41*), which are energetically expensive (*48*). However, this strategy is restricted to small birds, and the flight styles of larger Late Cretaceous enantiornithines are unknown (*41*). Combined with longer incubation and development times, enantiornithines may have been unable to migrate long distances before the onset of winter.

Enantiornithines also do not appear well adapted to endure harsh winter conditions, and this physiological constraint has been hypothesized to contribute to their demise during the end-Cretaceous mass extinction winter (*41*). For instance, unusual molting patterns would have made enantiornithine juveniles susceptible to sudden decreases in temperatures (*41*), and a lack of gizzard stones may have limited dietary diversity (*41*), especially during winter months. It is possible that the combination of slower developmental times, absence of digestive flexibility, and inefficient plumage rendered enantiornithines both unable to survive harsh winter conditions and poorly suited to undertake long migratory journeys to more favorable conditions at lower latitudes. Although dinosaurs also showed slow incubation and growth to maturity times, rendering them unable to migrate seasonally, they may have been better adapted to the harsh winters. Megaherbivores have been hypothesized to have fasted or sustained themselves with low-quality forage (e.g., bark, ferns, horsetails, or moss), whereas some or all smaller taxa may have hibernated in burrows or other forms of shelter (*24*). Whereas dinosaurs were adapted to overwinter and ornithurines could have used either overwintering or migrating strategies, enantiornithines do not seem particularly well adapted to either, precluding them from colonizing high-latitude ecosystems. Ultimately, although dinosaurs were well adapted enough to survive in this Cretaceous Arctic environment, it was these specifically ornithurine characteristics that proved to be vitally important to their survival of the end-Cretaceous catastrophe— one of natural history's greatest selective filters—and that enabled the subsequent explosive radiation of Neornithes.

REFERENCES AND NOTES

1. C. Egevang *et al.*, *Proc. Natl. Acad. Sci. U.S.A.* **107**, 2078–2081 (2010).
2. Å. Ø. Pedersen, B.-J. Bårdsen, N. G. Yoccoz, N. Lecomte, E. Fuglei, *J. Wildl. Manage.* **76**, 308–316 (2012).
3. W. Arnold *et al.*, *Sci. Rep.* **8**, 14466 (2018).
4. H. Schekkerman, I. Tulp, T. Piersma, G. H. Visser, *Oecologia* **134**, 332–342 (2003).
5. L. McKinnon *et al.*, *Science* **327**, 326–327 (2010).
6. A. J. Gaston, M. L. Mallory, H. G. Gilchrist, *Polar Biol.* **35**, 1221–1232 (2012).
7. C. J. Whelan, Ç. H. Şekercioğlu, D. G. Wenny, *J. Ornithol.* **156**, 227–238 (2015).
8. Á. Lovas-Kiss *et al.*, *Ecography* **42**, 956–967 (2019).
9. D. S. Viana, L. Gangoso, W. Bouten, J. Figuerola, *Proc. R. Soc. B* **283**, 20152406 (2016).
10. L. N. Wilson *et al.*, *Nat. Commun.* **15**, 2864 (2024).
11. P. Jadwiszczak, in *Morphology and Systematics of Fossil Vertebrates*, D. Nowakowski, Ed. (DN Publisher, 2010), pp. 45–51.
12. P. M. J. Douglas *et al.*, *Proc. Natl. Acad. Sci. U.S.A.* **111**, 6582–6587 (2014).
13. S. L. Brusatte, J. K. O'Connor, E. D. Jarvis, *Curr. Biol.* **25**, R888–R898 (2015).
14. A. Bell, L. M. Chiappe, *Life* **10**, 62 (2020).
15. O. C. Marsh, *Am. Nat.* **9**, 625–631 (1875).
16. J. Benito, P.-C. Kuo, K. E. Widrig, J. W. M. Jagt, D. J. Field, *Nature* **612**, 100–105 (2022).
17. J. Benito *et al.*, *PeerJ* **10**, e13919 (2022).
18. D. J. Field, J. Benito, A. Chen, J. W. M. Jagt, D. T. Ksepka, *Nature* **579**, 397–401 (2020).
19. J. A. Clarke, C. P. Tambussi, J. I. Noriega, G. M. Erickson, R. A. Ketcham, *Nature* **433**, 305–308 (2005).
20. J. A. Clarke, *Bull. Am. Mus. Nat. Hist.* **286**, 1–179 (2004).
21. N. R. Longrich, T. Tokaryk, D. J. Field, *Proc. Natl. Acad. Sci. U.S.A.* **108**, 15253–15257 (2011).
22. P. S. Druckenmiller *et al.*, "First U-Pb CA-ID-TIMS age constraints on polar dinosaurs from the Prince Creek Formation, Northern Alaska," paper presented at the 83rd Annual Meeting of the Society of Vertebrate Paleontology, Cincinnati, OH, 18 to 21 October 2023.
23. D. W. Fowler, *PLOS ONE* **12**, e0188426 (2017).
24. P. S. Druckenmiller, G. M. Erickson, D. Brinkman, C. M. Brown, J. J. Eberle, *Curr. Biol.* **31**, 3469–3478.e5 (2021).
25. N. Brocklehurst, D. J. Field, *Proc. R. Soc. B* **291**, 20232618 (2024).
26. S. R. Mohr, J. H. Acorn, G. F. Funston, P. J. Currie, *Can. J. Earth Sci.* **58**, 134–140 (2021).
27. N. V. Zelenkov, *Paleontol. J.* **55**, 323–330 (2021).
28. P. Houde, M. Dickson, D. Camarena, *Diversity* **15**, 233 (2023).
29. J. K. O'Connor, N. V. Zelenkov, *Paleontol. J.* **47**, 1270–1281 (2013).
30. G. M. Erickson, *Annu. Rev. Earth Planet. Sci.* **42**, 675–697 (2014).
31. L. M. Chiappe, S.-A. Ji, Q. Ji, M. A. Norell, *Bull. Am. Mus. Nat. Hist.* **242**, 1–89 (1999).
32. J. Huang *et al.*, *PeerJ* **4**, e1765 (2016).
33. A. Louchart, B.-A. Bhullar, S. Riamon, D. J. Field, *Front. Earth Sci.* **9**, 661699 (2021).
34. N. Longrich, *Cretac. Res.* **30**, 161–177 (2009).
35. M. Wang, Z. Zhou, *J. Syst. Palaeontology* **15**, 1–18 (2016).
36. T. G. Kaye *et al.*, *Sci. Rep.* **9**, 5006 (2019).
37. L. M. Chiappe, J. Shu'an, J. Qiang, *Am. Mus. Novitates* **2007**, 1–46 (2007).
38. J. Watanabe, H. Matsuoka, *Paleontol. Res.* **2013**, 279–306 (2013).
39. R. A. Spicer, A. B. Herman, *Palaeogeogr. Palaeoclimatol. Palaeoecol.* **295**, 423–442 (2010).
40. P. P. Flaig, P. J. McCarthy, A. R. Fiorillo, in *New Frontiers in Paleopedology and Terrestrial Paleoclimatology: Paleosols and Soil Surface Analog Systems*, S. G. Driese, L. C. Nordt, Eds. (SEPM Society for Sedimentary Geology, 2013), pp. 179–230.
41. J. O'Connor, *Curr. Biol.* **32**, R1166–R1172 (2022).
42. R. K. Bono, J. Clarke, J. A. Tarduno, D. Brinkman, *Sci. Rep.* **6**, 38876 (2016).
43. S. Davis *et al.*, *J. S. Am. Earth Sci.* **122**, 104163 (2023).
44. D. J. Varricchio, F. D. Jackson, *Auk* **133**, 654–684 (2016).
45. M. S. Fernández *et al.*, *PLOS ONE* **8**, e61030 (2013).
46. A. M. Bailleul *et al.*, *Nat. Commun.* **10**, 1275 (2019).
47. D. C. Deeming, G. Mayr, *J. Evol. Biol.* **31**, 701–709 (2018).
48. O. Vincze, C. I. Vágási, P. L. Pap, C. Palmer, A. P. Møller, *J. Exp. Biol.* **222**, jeb183517 (2019).
49. C. R. Torres, M. A. Norell, J. A. Clarke, *Sci. Adv.* **7**, eabg7099 (2021).
50. L. Wilson, Arctic bird nesting traces back to the Cretaceous, Data set, Zenodo (2025); https://doi.org/10.5281/zenodo.14714319.

ACKNOWLEDGMENTS

We thank K. May, S. Fowell, K. Anderson, X. Muñoz, Z. Perry, S. Bouta, S. Kula, P. Gignac, T. Hunt, D. Kay, B. Cragun, M. Norell, and C. Griffin. We thank G. Scheiffele and E. Stanley and the Nanoscale Research Service Center at the University of Florida (Gainesville) for assistance with CT data collection. We thank F. Hofmann and the University of Alaska Geochronology Laboratory for assistance with CT data processing. We also thank B. King, M. Kunz, R. Mills, B. Breithaupt, and J. Keeny with the US Bureau of Land Management; R. VanderHoek with the State of Alaska Department of History and Archaeology; the North Slope Borough; ConocoPhillips Alaska Inc.; and Hilcorp for permitting and logistical support. We acknowledge the community of Nuiqsut and the Inupiat on whose ancestral lands our fieldwork occurs. We especially thank all field crews and laboratory volunteers who donated their time to microfossil collection efforts. We also thank the Willi Hennig Society for sponsoring the free use of the program TNT. We thank J. Clarke and three anonymous reviewers for their helpful feedback on an earlier draft of this manuscript. We thank S. Brusatte and an anonymous reviewer for their helpful feedback on the current version of this manuscript. **Funding:** This study was supported by National Science Foundation (NSF) award EAR 1226730 (P.S.D. and G.M.E.); NSF award EAR 1736515 (P.S.D., G.M.E., and J.J.E.); NSF award DEB 1655736 (D.T.K.); Alaska EPSCoR Travel Award and NSF award OIA-1757348 (L.N.W.); the Otto William Geist Fund (L.N.W.); and a Winifred Goldring Award (L.N.W.). **Author contributions:** Conceptualization: L.N.W., P.S.D.; CT data processing: L.N.W.; Identification of elements: L.N.W., D.T.K., J.P.W., G.M.E., P.S.D.; Oversight of field collection: P.S.D., G.M.E.; Phylogenetic analyses: L.N.W., J.D.G.; Supervision: P.S.D.; Writing – original draft: L.N.W.; Writing – review & editing: All authors. **Competing interests:** The authors declare that they have no competing interests. **Data and materials availability:** All specimens are reposited in the University of Alaska Museum of the North Earth Sciences Collection (UAMES). CT scan data for all elements are housed at MorphoSource (https://www.morphosource.org/projects/000671593). A complete list of specimens and files needed to reproduce phylogenetic analyses and all phylogenetic trees are deposited at Zenodo (*50*). **License information:** Copyright © 2025 the authors, some rights reserved; exclusive licensee American Association for the Advancement of Science. No claim to original US government works. https://www.science.org/about/science-licenses-journal-article-reuse

SUPPLEMENTARY MATERIALS

science.org/doi/10.1126/science.adt5189
Materials and Methods; Supplementary Text; Figs. S1 to S10; Tables S1 to S16; References (*51*–*83*); MDAR Reproducibility Checklist

Submitted 29 September 2024; accepted 4 February 2025

10.1126/science.adt5189

GLACIERS

Glacier preservation doubled by limiting warming to 1.5°C versus 2.7°C

Harry Zekollari[1,2,3]*†, Lilian Schuster[4]*†, Fabien Maussion[5], Regine Hock[6,7], Ben Marzeion[8,9], David R. Rounce[10], Loris Compagno[2,11,12], Koji Fujita[13], Matthias Huss[2,11,14], Megan James[15], Philip D. A. Kraaijenbrink[16], William H. Lipscomb[17], Samar Minallah[17], Moritz Oberrauch[18,19], Lander Van Tricht[2,11,1], Nicolas Champollion[20], Tamsin Edwards[15], Daniel Farinotti[2,11], Walter Immerzeel[16], Gunter Leguy[17], Akiko Sakai[13]

Glaciers adapt slowly to changing climatic conditions, with long-term implications for sea-level rise and water supply. Using eight glacier models, we simulated global glacier evolution over multicentennial timescales, allowing glaciers to equilibrate with climate under various constant global temperature scenarios. We estimate that glaciers globally will lose 39 (range, 15 to 55)% of their mass relative to 2020, corresponding to a global mean sea-level rise of 113 (range, 43 to 204) mm even if temperatures stabilized at present-day conditions. Under the +1.5°C Paris Agreement goal, more than twice as much global glacier mass remains at equilibration (53% versus 24%) compared with the warming level resulting from current policies (+2.7°C by 2100 above preindustrial). Our findings stress the need for stringent mitigation policies to ensure the long-term preservation of glaciers.

Global-scale glacier mass loss profoundly affects our society and the natural environment, contributing to sea-level rise (*1*–*3*), influencing downstream water resources (*4*), affecting biodiversity and ecosystems (*5*), exacerbating natural hazards (*6*), and having a negative effect on the tourism industry (*7*). Recent projections of all glaciers outside of the Antarctic and Greenland ice sheets, based on a range of transient climate scenarios, estimate mass losses of ~20 to 50% between 2015 and 2100 depending on emissions scenarios (*8*–*11*). However, even if the current climate were to stabilize, then glaciers would be expected to continue losing mass over extended time periods (*12*–*14*). Glaciers may vanish entirely or, if the new climatic conditions permit, retreat until they reach a steady state in which glacier mass and glacier geometry remain approximately stable (*15*). This continued loss after climate stabilization is due to the slow adjustment of a glacier's geometry, driven by the gradual flow of ice from high to low elevations (*16*, *17*). Additionally, the lag between the climatic forcing and glacier response is influenced by feedback mechanisms involving elevation and mass balance (*18*), as well as albedo and mass balance (*19*).

Observational and modeling studies suggest that the time needed for glaciers to reach a new steady state after a climate perturbation can range from decades to multiple centuries (*20*–*22*). However, the mass losses that are committed but not yet realized in response to long-term climate stabilization remain largely unquantified, with insights primarily derived from only two exploratory studies. Mernild *et al.* (*23*) used observed ratios of accumulation to total glacier area to estimate present-day committed global mass losses, and Marzeion *et al.* (*13*) used a glacier evolution model based on volume-area scaling to project committed losses across various global mean temperature scenarios. Both studies agree on the estimate that ~35 to 40% of glacier mass will be lost under early 21st-century climatic conditions. However, Marzeion *et al.* (*13*) did not account for glaciers in the Greenland Periphery and the Subantarctic & Antarctic Islands. Moreover, both studies relied on limited observations to constrain and evaluate their methods, possibly affecting the precision and reliability of their methods and conclusions.

Here, we used eight state-of-the-art glacier evolution models to simulate long-term glacier mass loss of all glaciers outside of the ice sheets for 80 constant-climate scenarios. These constant-climate scenarios were derived by repeating eight different 20-year periods between 1850 and 2100 from various climate models forced by Shared Socioeconomic Pathways (fig. S1 and materials and methods). Our diverse scenarios form an ensemble of global and regional climates, each of which is associated with a change in global mean temperature compared with preindustrial. The glacier models are run for several thousand years to ensure that the glaciers have sufficient time to equilibrate with the new climate. These long-term simulations thus enable the quantification of the committed glacier mass loss at regional and global scales under diverse policy-relevant global warming levels.

Committed glacier mass changes under present-day climate

Our model simulations project that if current (2014 to 2023) climatic conditions [global mean temperature change (ΔT) = 1.2°C above preindustrial (*24*)] were to persist, glaciers would eventually lose 39% (range, 15 to 55%) of their global glacier mass relative to 2020 [the 17th to 83rd percentiles are the International Panel on Climate Change's (*25*) "likely range"; Fig. 1 and table S1]. This already committed, but not yet fully realized, glacier mass loss is projected to contribute 113 mm (range, 43 to 204 mm) to global mean sea-level rise, irrespective of any future warming. This substantial present-day committed mass loss highlights that today's glaciers are strongly out of balance with current climatic conditions due to their long response times. The strong imbalance between glacier geometry and climate is exacerbated by atmospheric warming being particularly pronounced at high elevations (*26*) and high latitudes (*27*) where glaciers are predominantly located. In our ensemble of climate models, the median air temperature increase over glacier areas is 80% higher than the global average, a relationship that is consistent regardless of the future global temperature increase (fig. S2 and materials and methods).

The imbalance between current climate and glacier geometry varies greatly among regions, resulting in sharply contrasting regional present-day committed losses (Figs. 2 and 3 and table S1). Relative losses of some regions are small, such as South Asia West [5% (range, 0 to 30%) under ΔT = 1.2°C], Central Asia [12% (range, 3 to 32%)], and New Zealand [15% (range, 2 to 39%)], whereas other regions are projected to experience substantial losses regardless of further future warming, such as Arctic Canada South [85% (range, 83 to 94%)], Western Canada & US [74% (range, 43 to 93%)], Scandinavia [66% (range, 24 to 85%)], and Russian Arctic [65% (range, 46 to 80%)].

---

[1]Department of Water and Climate, Vrije Universiteit Brussel, Brussels, Belgium. [2]Laboratory of Hydraulics, Hydrology and Glaciology (VAW), ETH Zürich, Zürich, Switzerland. [3]Laboratoire de Glaciologie, Université libre de Bruxelles, Brussels, Belgium. [4]Department of Atmospheric and Cryospheric Sciences (ACINN), Universität Innsbruck, Innsbruck, Austria. [5]Bristol Glaciology Centre, School of Geographical Sciences, University of Bristol, Bristol, UK. [6]Department of Geosciences, University of Oslo, Oslo, Norway. [7]Geophysical Institute, University of Alaska Fairbanks, Fairbanks, AK, USA. [8]Institute of Geography, University of Bremen, Bremen, Germany. [9]MARUM - Center for Marine Environmental Sciences, University of Bremen, Bremen, Germany. [10]Department of Civil and Environmental Engineering, Carnegie Mellon University, Pittsburgh, PA, USA. [11]Swiss Federal Institute for Forest, Snow and Landscape Research (WSL), bâtiment ALPOLE, Sion, Switzerland. [12]Swiss Reinsurance Company Ltd (Swiss Re), Zürich, Switzerland. [13]Graduate School of Environmental Studies, Nagoya University, Nagoya, Japan. [14] Department of Geosciences, University of Fribourg, Fribourg, Switzerland. [15]Department of Geography, King's College London, London, UK. [16]Department of Physical Geography, Utrecht University, Utrecht, Netherlands. [17]NSF National Center for Atmospheric Research, Boulder, CO, USA. [18]WSL-Institute for Snow and Avalanche Research SLF, Davos, Switzerland. [19] Department of Civil, Environmental and Geomatic Engineering, ETH Zürich, Zürich, Switzerland. [20]Institut des Géosciences de l'Environnement (IGE), Université Grenoble Alpes, Grenoble, France. ***Corresponding author. Email: harry.zekollari@vub.be (H.Z.); lilian.schuster@uibk.ac.at (L.S.)** †These authors contributed equally to this work.

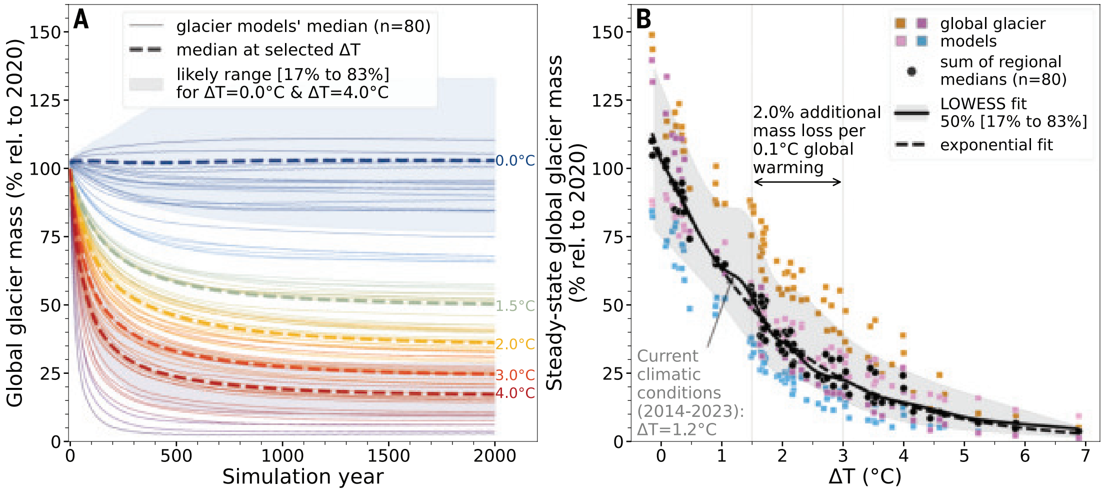

Fig. 1. Projected global glacier mass under constant-climate scenarios. (**A**) Evolution of global glacier mass relative to present day (year 2020; 3-year running mean). Solid lines show the results for all 80 constant-climate scenarios derived from the sum of the regional medians of the glacier model ensemble. Colors indicate corresponding global mean warming levels above preindustrial (ΔT, range from −0.1° to 6.9°C). Dashed lines refer to the mean of the solid lines for select warming levels. Shading marks the multimodel ensemble likely range (shown for $\Delta T = 0.0 \pm 0.2$°C and $\Delta T = 4.0 \pm 0.2$°C). (**B**) Steady-state glacier mass as a function of warming level. Colored dots refer to results for the globally applied glacier models (color coding per glacier model is in Fig. 2). Black dots are obtained by globally summing regional multimodel medians through which a LOWESS fit is added.

These regional differences in relative present-day committed losses are correlated with regional glacier elevation range (the highest correlation among the variables considered, $r = -0.55$; fig. S3 and Fig. 4A). Regions where glaciers span a wide elevation range, typically located at lower latitudes with rugged mountain topography, have a higher potential to adapt to changing climatic conditions, because glaciers can (partly) survive by retreating to higher elevations. Conversely, regions with smaller glacier elevation ranges tend to have higher present-day committed losses. In these regions, glaciers have less potential to retreat to higher elevations, an effect that is particularly pronounced in Arctic Canada South (Fig. 4A). Combined with strong regional warming (2.2 times the global warming; Fig. 2 and fig. S4), Canada South's glaciers are projected to largely disappear in the coming centuries under present-day climatic conditions. Many of this region's large glaciers are relics of past glaciations [e.g., the 6000 km^2 Barnes ice cap, a remnant of the Laurentide ice sheet (*28*, *29*)] and cannot survive.

Committed glacier mass changes under policy-relevant scenarios

If global temperatures stabilize at the limits targeted in the Paris Agreement, then glaciers are projected to eventually lose 47% (range, 20 to 64%) of their global mass relative to 2020 for a +1.5°C scenario and 63% (range, 43 to 76%) for a +2.0°C scenario, contributing 138 mm (range, 59 to 237 mm) and 190 mm (range, 128 to 279 mm) to global mean sea-level rise, respectively (all values at steady state). Under current climate policy pledges, global temperatures are projected to reach 2.7°C above preindustrial levels by 2100 (*30*), which would result in eventually losing 76% (range, 54 to 82%) of glacier mass globally, corresponding to 230 mm (range, 159 to 302 mm) of sea-level rise. Thus, more than twice as much global glacier mass is projected to remain long term under the Paris Agreement +1.5°C goal compared with current climate policies.

Every additional 0.1°C increase between the +1.5°C and +3.0°C scenario eventually results in an additional 2.0% (range, 1.6 to 2.4%) global glacier mass loss, corresponding to 6.5 mm (range, 4.6 to 8.9 mm) of sea-level rise from glaciers alone (Fig. 1B and table S1). Considering the same domain (i.e., without the Subantarctic & Antarctic Islands and the Greenland Periphery), our sensitivity derived from eight glacier models is consistent with that by Marzeion *et al.* (*13*), which was based on a single model (fig. S7). For context, recent glacier projections performed with PyGEM-OGGM (*10*) estimated that a +3.0°C scenario would result in ~8% more global glacier mass loss by 2100 relative to 2015 (34-mm sea-level rise) than the +1.5°C scenario. In their simulations, every 0.1°C increase leads to an additional ~0.6% mass loss and 2.3-mm sea-level rise over the period 2015 to 2100. The glacier mass loss sensitivity to temperature increase revealed by our experiments based on long-term equilibrated glacier masses is three times larger (2.0% per 0.1°C) when considering all models, or about two times larger (1.4% per 0.1°C) when considering PyGEM-OGGM alone (fig. S5), indicating that substantial mass losses resulting from current climate policies will manifest after 2100.

The committed mass loss sensitivity to climate policies varies considerably across regions. Regions currently closest to balance with their climatic conditions, i.e., those with the smallest committed loss under present-day conditions, are the most sensitive to future warming (Fig. 4B and table S1). These regions include South Asia West [3.4% (range, 2.0 to 3.6%) per +0.1°C for $\Delta T = 1.5$ to 3.0°C], Central Asia [3.0% (range, 2.2 to 3.2%) per +0.1°C], the Low Latitudes [3.0% (range, 2.1 to 3.7%) per +0.1°C], and New Zealand [2.9% (range, 2.7 to 2.9%) per +0.1°C]. Therefore, although these regions are projected to experience less relative mass loss under present-day climatic conditions than others, they will be the most affected by future warming levels from current climate policies.

At higher warming levels, the relation between committed global glacier losses and warming levels becomes nonlinear. At +3.0°C, glaciers are projected to lose 77% (range, 60 to 85%) of their global mass, with all 19 regions losing more than two-thirds of their present-day mass and nine of those regions losing more than 90% (table S1). Consequently, in many regions, additional warming above +3.0°C leads to less additional glacier mass loss, because there is little mass left to lose, thereby reducing the sensitivity of global glacier mass loss to temperature change (Fig. 1B). In a 4°C warmer world, glaciers are projected to lose 86% (range, 74 to 93%) of their present-day mass globally, with most midlatitude regions deglaciating (<5% of mass remaining). In an extreme 5°C warmer world corresponding to the upper range of warming projected by 2100 under SSP5-8.5, 91% (range, 82 to 96%) of global glacier mass is lost in the long term, contributing about 282 mm (range, 242 to 352 mm) to sea-level rise.

Conversely, preserving the present-day global glacier mass would require a return to preindustrial temperatures (1850 to 1900; $\Delta T = +0.0$°C; Fig. 1A). Glaciers were substantially larger than today in the second half of the 19th century due to colder and/or wetter climatic conditions in the 18th and early 19th centuries (*22*, *31*–*33*). The retreat of glaciers in the early 20th century was a response to this imbalance, which has more recently been amplified and overtaken by human-induced warming (*34*, *35*). Without anthropogenic warming, present-day temperatures would be close to preindustrial levels (*25*), and glaciers would be larger than they are now. In this hypothetical case, global glacier mass would today still be declining toward the present-day observed glacier mass, a multicentennial process.

Climate policies and multicentennial glacier evolution: a tale of contrasting timescales

Approximately a millennium is needed for the global glacier mass to fully respond and equilibrate with the most optimistic warming level

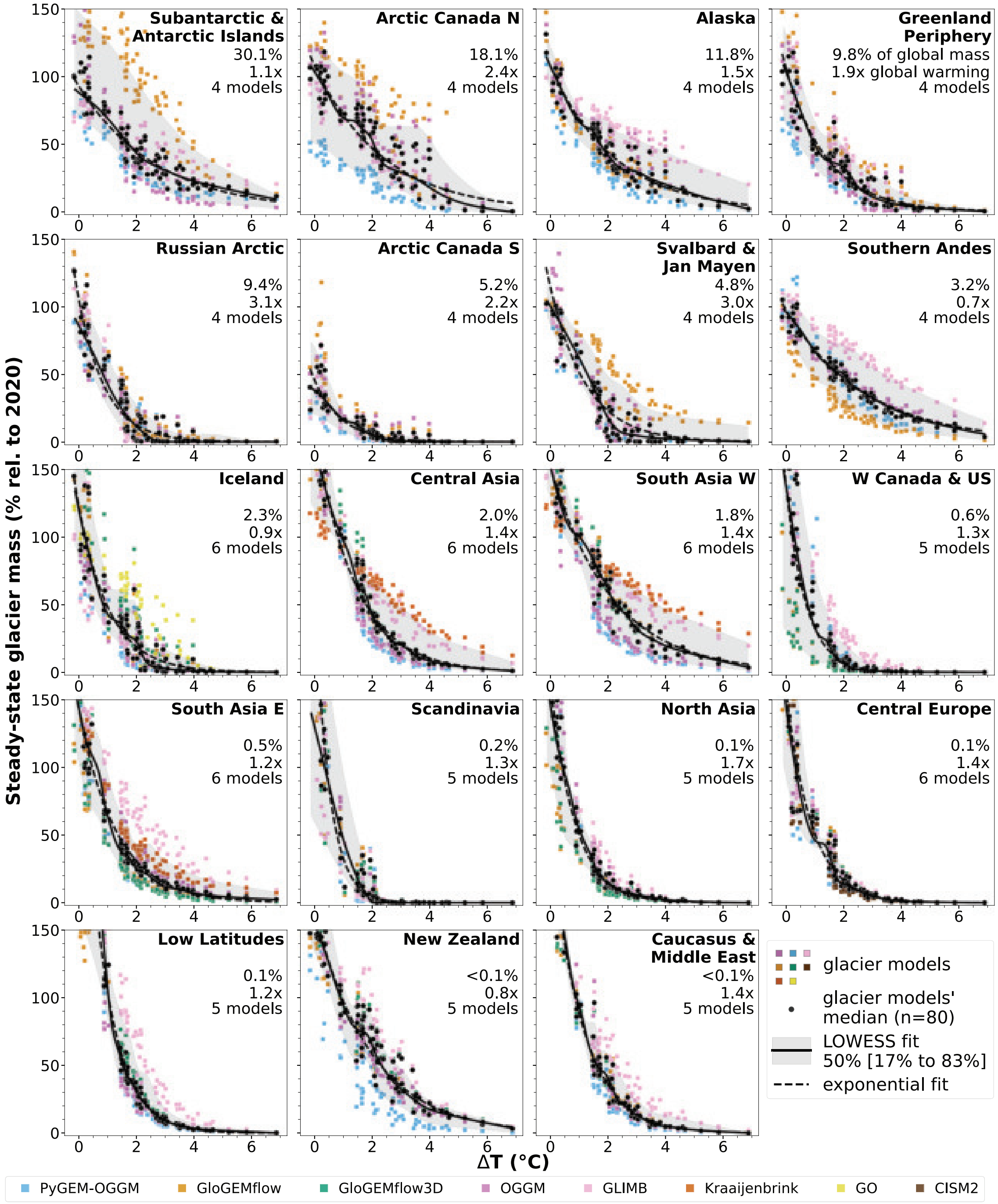

Fig. 2. Regional steady-state glacier masses relative to present day (year 2020) as a function of global warming levels above preindustrial (ΔT). Dots represent individual simulations forced by 80 constant-climate scenarios per glacier model (four to six glacier models per region, color coded). Regions are sorted by descending present-day (2020) glacier mass. For each region, the percentage of global glacier mass in 2020, the warming over the glacierized area relative to the global mean warming (versus 1986 to 2005, median value over 80 climate scenarios; see the materials and methods), and the number of glacier models used are given. For fits with respect to warming levels over each region's glacierized area, see fig. S4; for individual glacier models, see fig. S5; and for regional masses after 100 years, see fig. S6.

outlined in the Paris Agreement (ΔT = +1.5°C; Fig. 1A and fig. S8). This long response time is largely due to high-latitude regions, which contain by far most of the global glacier mass and require multicentury timescales to respond to changing climatic conditions. Most notably, the Subantarctic & Antarctic Islands require more than 800 years for 80% of committed mass loss to occur for a +1.5°C scenario (Fig. 4, C and D). Other regions, such as the Arctic Canada North, Russian Arctic, Greenland Periphery, Iceland, Svalbard, and Arctic Canada South, also respond on long timescales, with 80% changes taking more than 200 years (table S1). These slow-responding regions are characterized by gently sloping glaciers (Fig. 4C and fig. S3), contrasting with regions with steeper glaciers, where most changes occur within a few decades, such

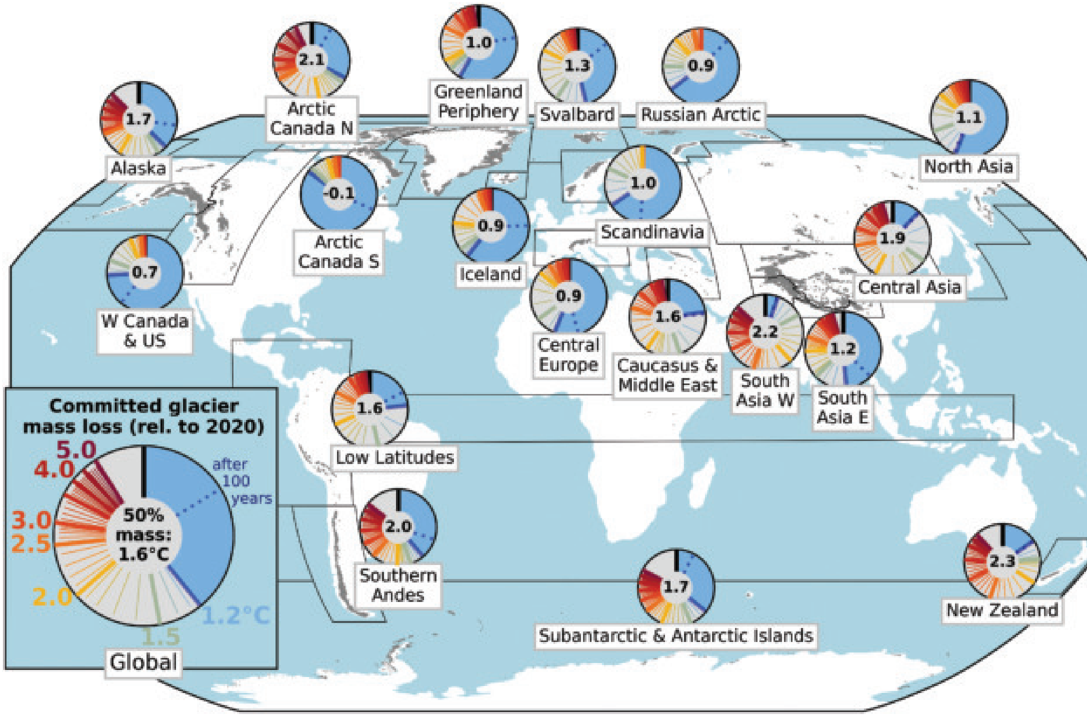

1.7
Alaska
2.1
Arctic Canada N
1.0
Greenland Periphery
1.3
Svalbard
0.9
Russian Arctic
1.1
North Asia
-0.1
Arctic Canada S
0.9
Iceland
1.0
Scandinavia
1.9
Central Asia
0.7
W Canada & US
0.9
Central Europe
1.6
Caucasus & Middle East
2.2
South Asia W
1.2
South Asia E
1.6
Low Latitudes
2.0
Southern Andes
1.7
Subantarctic & Antarctic Islands
2.3
New Zealand
Committed glacier mass loss (rel. to 2020)
5.0
4.0
3.0
2.5
2.0
1.5
1.2°C
after 100 years
50% mass: 1.6°C
Global

Fig. 3. Committed glacier mass loss at different global warming levels above preindustrial (ΔT). In every circle, the colored lines indicate the LOWESS fitted ensemble median estimates of committed mass loss at steady state at different warming levels in the range ΔT = +1.2°C to +5.0°C (increasing in clockwise directions in 0.1°C steps beyond 1.2°C; full circle correspond to 100% committed mass loss). The present-day committed mass loss at steady state (ΔT = +1.2°C) is in light blue, with the loss after 100 simulation years (fig. S6) shown as the dotted line. Numbers in the circle centers are the ΔT at which 50% of the present (year 2020) regional glacier mass is lost.

Fig. 4. Present-day committed glacier mass loss and response timescales globally and for 19 glacier regions. (**A** and **B**) Present-day committed mass losses (ΔT = +1.2°C) as a function of regional mean glacier elevation range, weighted by glacier area (A), and sensitivity of committed glacier mass loss to global mean air temperature change in the range ΔT = +1.5°C to +3.0°C (B) (see the materials and methods). (**C** and **D**) Response timescale, i.e., the year when 80% of the committed mass loss at ΔT =1.5°C $\pm$ 0.2°C has occurred, as a function of glacier-area weighted regional mean surface slope (C) and observed glacier mass change between 2000 and 2019 relative to 2000 (D) (*1*, *37*) (see the materials and methods). *r* is the Spearman's rank correlation coefficient for the 19 regions ($P < 0.02$ in every panel). The coloring of the dots refers to the warming over the glacierized area relative to the global mean warming (versus 1986 to 2005, median value over 80 climate scenarios; Fig. 2). The size of the dots scales with the respective 2020 glacier mass. Slope (C) and observed mass loss (D) data are available in table S3.

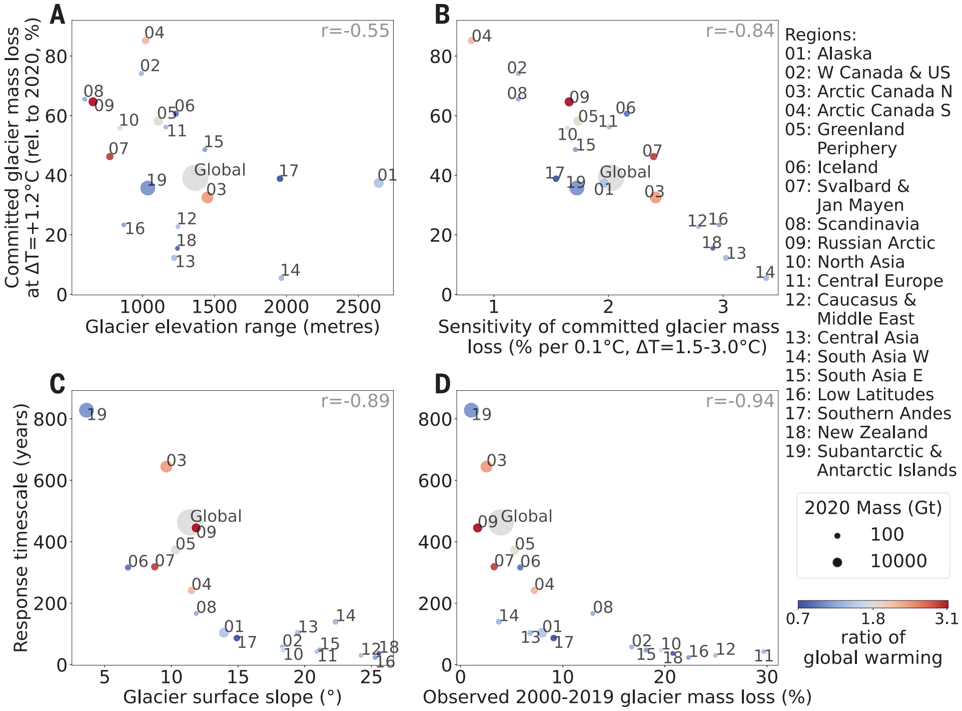

as the Low Latitudes [23 years (range, 14 to 30 years) for 80% change], Caucasus & Middle East [30 years (range, 26 to 56 years)], and New Zealand [36 years (range, 28 to 45 years)]. Under higher warming levels (above +1.5°C), all regions equilibrate faster because they tend to evolve toward a mostly deglaciated state more rapidly (fig. S9B).

The long response timescales result in substantial differences between the glacier states after 100 years and at full equilibration, especially for the slow-responding regions (Fig. 3 and Fig. 2 versus fig. S6). The long-term equilibration experiments thus provide a different and complementary perspective on the vulnerability of glaciated regions compared with previous studies that have focused on transient 21st-century glacier evolution (*10*, *11*). Some regions projected to experience limited mass loss throughout the 21st century, such as the Subantarctic & Antarctic Islands [14% mass loss over 2020 to 2100 for a +2.0°C scenario from an ensemble of three CMIP6-forced glacier evolution models (*11*)], Russian Arctic (22%), and Arctic Canada South (41%), are expected to lose a large part of their mass in the longer term, with committed losses at +2.0°C reaching 56, 88, and 95%, respectively (fig. S10).

Generally, regions modeled to have the longest response timescales are also those with the lowest observed relative mass loss over the past two decades (2000 to 2019), and vice versa ($r = 0.94$; Fig. 4D). For example, the Subantarctic & Antarctic Islands, Arctic Canada North, and Russian Arctic, which each require more than 400 years for 80% of committed changes to occur for a +1.5°C scenario, have lost less than 3% of their mass between 2000 and 2019. By contrast, the fastest responding regions, such as Central Europe, Caucasus & Middle East, Low Latitudes, and New Zealand, need less than five decades for 80% changes to occur and each have lost more than 20% of their mass over the first two decades of the 21st century.

Our results emphasize that the effectiveness of current and near-term climate policies in mitigating short- to mid-term warming will play a decisive role in shaping the future evolution of glaciers, influencing not only immediate glacier changes but also those that will unfold over multicentennial timescales. The findings stress the pivotal role of climate policies in preserving our glaciers, which should be a central focus of the United Nations International Year of Glaciers' Preservation in 2025 (*36*).

REFERENCES AND NOTES

1. R. Hugonnet *et al.*, *Nature* **592**, 726–731 (2021).
2. T. L. Edwards *et al.*, *Nature* **593**, 74–82 (2021).
3. L. Jakob, N. Gourmelen, *Geophys. Res. Lett.* **50**, e2023GL102954 (2023).
4. M. Huss, R. Hock, *Nat. Clim. Chang.* **8**, 135–140 (2018).
5. J. B. Bosson *et al.*, *Nature* **620**, 562–569 (2023).
6. Y. Ding *et al.*, *Earth Sci. Rev.* **213**, 103500 (2021).
7. E. Salim, *Front. Hum. Dyn.* **5**, 1137551 (2023).
8. R. Hock *et al.*, *J. Glaciol.* **65**, 453–467 (2019).
9. B. Marzeion *et al.*, *Earths Futur.* **8**, e2019EF001470 (2020).
10. D. R. Rounce *et al.*, *Science* **379**, 78–83 (2023).
11. H. Zekollari *et al.*, *Cryosphere* **18**, 5045–5066 (2024).
12. J. E. Christian, M. Koutnik, G. Roe, *J. Glaciol.* **64**, 675–688 (2018).
13. B. Marzeion, G. Kaser, F. Maussion, N. Champollion, *Nat. Clim. Chang.* **8**, 305–308 (2018).
14. H. Zekollari, M. Huss, D. Farinotti, *Geophys. Res. Lett.* **47**, e2019GL085578 (2020).
15. J. G. Cogley *et al.*, "Glossary of glacier mass balance and related terms" (IACS Technical Report 86, 2011); https://unesdoc.unesco.org/ark:/48223/pf0000192525.
16. T. Johannesson, C. Raymond, E. Waddington, *J. Glaciol.* **35**, 355–369 (1989).
17. D. B. Bahr, W. T. Pfeffer, C. Sassolas, M. F. Meier, *J. Geophys. Res.* **103**, 9777–9782 (1998).
18. M. Schäfer, M. Möller, T. Zwinger, J. C. Moore, *J. Glaciol.* **61**, 1121–1136 (2015).
19. E. Johnson, S. Rupper, *Front. Earth Sci.* **8**, 8 (2020).
20. G. H. Roe, M. B. Baker, F. Herla, *Nat. Geosci.* **10**, 95–99 (2017).
21. A. Huston, N. Siler, G. H. Roe, E. Pettit, N. J. Steiger, *Cryosphere* **15**, 1645–1662 (2021).
22. O. N. Solomina *et al.*, *Quat. Sci. Rev.* **149**, 61–90 (2016).
23. S. H. Mernild, W. H. Lipscomb, D. B. Bahr, V. Radić, M. Zemp, *Cryosphere* **7**, 1565–1577 (2013).
24. P. M. Forster *et al.*, *Earth Syst. Sci. Data* **16**, 2625–2658 (2024).
25. International Panel on Climate Change, "Climate change 2021: The physical science basis. Contribution of Working Group I to the sixth assessment report of the Intergovernmental Panel on Climate Change" (IPCC, 2021); https://www.ipcc.ch/report/ar6/wg1/.
26. Mountain Research Initiative EDW Working Group, *Nat. Clim. Change* **5**, 424–430 (2015).
27. D. M. Smith *et al.*, *Geosci. Model Dev.* **12**, 1139–1164 (2019).
28. A. Gardner, G. Moholdt, A. Arendt, B. Wouters, *Cryosphere* **6**, 1103–1125 (2012).
29. A. Gilbert *et al.*, *J. Geophys. Res. Earth Surf.* **121**, 1516–1539 (2016).
30. Climate Action Tracker, "The CAT Thermometer" (CAT, 2023); https://climateactiontracker.org/global/cat-thermometer.
31. D. Parkes, B. Marzeion, *Nature* **563**, 551–554 (2018).
32. D. Parkes, H. Goosse, *Cryosphere* **14**, 3135–3153 (2020).
33. F. Paul, T. Bolch, "Glacier changes since the Little Ice Age" in *Geomorphology of Proglacial Systems*, T. Heckmann, D. Morche, Eds. (Springer, 2019), pp. 23–42.
34. G. Roe, J. E. Christian, B. Marzeion, *Cryosphere* **15**, 1889–1905 (2021).
35. B. Marzeion, J. G. Cogley, K. Richter, D. Parkes, *Science* **345**, 919–921 (2014).
36. United Nations, "International year of glaciers' preservation, 2025: revised draft resolution" (UN, 2022); https://digitallibrary.un.org/record/3994297.
37. D. Farinotti *et al.*, *Nat. Geosci.* **12**, 168–173 (2019).
38. Data for: H. Zekollari *et al.*, Glacier preservation doubled by limiting warming to 1.5°C versus 2.7°C, Zenodo (2024); https://doi.org/10.5281/zenodo.14045268.
39. Code for: H. Zekollari *et al.*, Glacier preservation doubled by limiting warming to 1.5°C versus 2.7°C, Zenodo (2024); https://doi.org/10.5281/zenodo.15046031.

ACKNOWLEDGMENTS

We acknowledge the World Climate Research Programme (WCRP) Climate and Cryosphere Project (CliC) for supporting the Glacier Model Intercomparison Project (GlacierMIP). **Funding:** This work was supported by European Union's Horizon 2020 research and innovation program (PROTECT contribution number 158, grant 869304 to H.Z., B.M., M.H., M.J., N.C., T.E., and D.F.); European Research Council under the European Union's Horizon Framework research and innovation program (grant 101115565, ICE^3 to H.Z.); Research Foundation – Flanders (FWO) through an Odysseus Type II project (grant G0DCA23N, GlaciersMD to H.Z. and L.V.T.); VUB ZAP Startkrediet, ICEFIELD (H.Z.); the Austrian Academy of Sciences at the Department of Atmospheric and Cryospheric Sciences, Universität Innsbruck (DOC fellowship 25928 to L.S.); European Union's Horizon 2020 research and innovation program (grant 101003687, PROVIDE to L.S. and F.M.); Norwegian Research Council (project 324131 to R.H.); European Research Council ERC-2022-ADG (grant 01096057 GLACMASS to R.H.); National Aeronautics and Space Administration (grants 80NSSC20K1296 and 80NSSC20K1595 to R.H. and D.R.); Swiss National Science Foundation (grant 200021_184634 to L.C.); Dutch Research Council (NWO) Talent Programme Veni, GREENPEAKS (VI.Veni.222.019 to P.K.); and the NSF National Center for Atmospheric Research, a major facility sponsored by the US National Science Foundation (cooperative agreement 1852977 to W.L., S.M., and G.L.). Computing and data storage resources for CISM simulations were supported by the Derecho system (doi:10.5065/qx9a-pg09) provided by the NSF National Center for Atmospheric Research (NCAR), sponsored by the National Science Foundation (W.L., S.M., and G.L.); GRICAD infrastructure (N.C.); European Research Council under the European Union's Horizon Framework research and innovation program (grant 101142123, DROP, to W.I.); and the World Climate Research Programme (WCRP) Climate and Cryosphere Project (CliC), which funded GlacierMIP workshops. **Author contributions:** H.Z. and L.S. contributed equally to this work and share first authorship. H.Z. was the main project coordinator of the study, which initiated from original ideas by B.M. H.Z., L.S., F.M., R.H., and B.M. designed the GlacierMIP3 experiments, protocol, and methods. F.M., R.H., B.M., and H.Z. acquired funding for data analyses and GlacierMIP3 activities. F.M. did exploratory simulations and analyses to guide the GlacierMIP3 experimental design choices. L.S. preprocessed the climatic input data for the model experiment in close collaboration with F.M. F.M., L.S., and H.Z. created test files and example workflows and guided the data submission process. L.C., K.F., M.H., M.J., P.K., W.L., F.M., S.M., M.O., D.R., L.S., L.V.T., and H.Z. performed the GlacierMIP3 model experiments with contributions in form of supervision and feedback by T.E., D.F., W.I., G.L., and A.S. L.S. performed all data analyses, including pre- and postprocessing of the submitted model simulations and made the figures in close collaboration with H.Z. and F.M. with additional input from R.H., B.M., and D.R. L.S. curated and validated data with input from F.M. B.M. provided resources for computation and data storage. H.Z. and L.S. interpreted the results with input from F.M., R.H., and B.M. H.Z. wrote the original manuscript with major contributions from R.H. and L.S. F.M., D.R., and B.M. provided extensive text reviews and edits, with additional contributions from N.C., L.C., K.F., W.I., P.K., W.L., S.M., L.V.T., and particularly M.H. and D.F. **Competing interests:** The authors declare no competing interests. **Data and materials availability:** The submitted data from the glacier model groups and the code to reproduce the figures is available from (*38*,*39*).

License information: Copyright © 2025 the authors, some rights reserved; exclusive licensee American Association for the Advancement of Science. No claim to original US government works. https://www.science.org/about/science-licenses-journal-article-reuse

SUPPLEMENTARY MATERIALS

science.org/doi/10.1126/science.adu4675
Materials and Methods; Figs. S1 to S15; Tables S1 to S3; References (*40*–*66*)

Submitted 8 November 2024; accepted 2 April 2025

10.1126/science.adu4675

CARBON CYCLING

Thermal acclimation of stem respiration implies a weaker carbon-climate feedback

Han Zhang[1], Han Wang[1]*, Ian J. Wright[2,3,4], I. Colin Prentice[1,5], Sandy P. Harrison[1,6], Nicholas G. Smith[7], Andrea C. Westerband[8], Lucy Rowland[9], Lenka Plavcová[10], Hugh Morris[11], Peter B. Reich[2,12,13], Steven Jansen[14], Trevor Keenan[15,16], Ngoc Bao Nguyen[15]

The efflux of carbon dioxide (CO_2) from woody stems, a proxy for stem respiration, is a critical carbon flux from ecosystems to the atmosphere, which increases with temperature on short timescales. However, plants acclimate their respiratory response to temperature on longer timescales, potentially weakening the carbon-climate feedback. The magnitude of this acclimation is uncertain despite its importance for predicting future climate change. We develop an optimality-based theory dynamically linking stem respiration with leaf water supply to predict its thermal acclimation. We show that the theory accurately reproduces observations of spatial and seasonal change. We estimate the global value for current annual stem CO_2 efflux as 27.4 ± 5.9 PgC. By 2100, incorporating thermal acclimation reduces projected stem respiration without considering acclimation by 24 to 46%, thus reducing land ecosystem carbon emissions.

Plant respiration represents about half of the annual carbon flux globally from terrestrial ecosystems to the atmosphere, approximately six times more than anthropogenic carbon emissions (*1*, *2*). The contribution of respiration by stems is not well quantified (*3*–*5*), but current models estimate it as around a quarter of total plant respiration (fig. S1). Plants respire their photosynthetic products to support physiological processes and growth (*6*, *7*). As an enzyme-mediated process, respiration increases nearly exponentially with increasing temperature on time frames of minutes to hours (*8*). Additional respiratory carbon release is thus widely expected in a warming world, leading to even more warming (*9*, *10*).

In principle, plant respiration is controlled by substrate availability and oxygen supply and demand for respiratory products. Plants modulate their respiratory response to temperature on timescales of weeks to years as a result of changes in these driving forces (*11*–*13*). This behavior could weaken the positive feedback between climate warming and carbon emissions from plants. Plants exposed to warmer conditions show a reduced respiration rate at a standardized measurement temperature and/or a decreased sensitivity to temperature (indicated by a smaller increase in respiratory rate per unit increase in temperature over the short term) compared with plants that have experienced cooler temperatures (*11*–*16*). These adjustments are called “thermal acclimation”; the more pronounced the thermal acclimation of respiration globally, the weaker the positive feedback between climate warming and carbon emissions.

The mechanisms and magnitude of thermal acclimation are still unclear. This is particularly true for stem respiration. Empirical evidence shows that stem respiration scales with nitrogen concentration, similar to leaves and roots, reflecting its enzyme requirements (*17*, *18*). However, the nature of thermal acclimation may differ between tissues. Leaves coordinate their respiratory acclimation with photosynthetic acclimation and have multiple mechanisms for thermal and physiological regulation (*14*, *16*, *19*). Presumably this is not the case for stems and roots, which likely also have higher thermal inertia than leaves (*20*). There have been a number of studies on the environmental controls of stem respiration, but no overarching principles have emerged (*21*–*26*). The lack of a theoretical basis has precluded any global analysis of the impact of thermal acclimation of stem respiration.

The representation of respiration in Earth System Models (ESMs) is simplistic and largely untested. Many ESMs do not implement time-dependent acclimation of plant respiration rates to warming (*27*, *28*). Models that do consider plant acclimation use empirical approaches and either ignore stem respiration acclimation or assume that stems acclimate the same way as leaves (*29*–*32*), presumably due to the paucity of information about stem respiration. Improved understanding of the magnitude of stem respiration and its acclimation is needed for reliable predictions of the global carbon-climate feedback (*33*).

Eco-evolutionary optimality (EEO) principles have been shown to provide parameter-sparse predictions of many different plant processes (*14*, *34*–*37*). EEO hypotheses identify trade-offs between plant resource demand and acquisition that can be expressed mathematically (*34*). The previous success of EEO in predicting plant ecophysiological processes suggests that this approach is also useful for investigating the magnitude of thermal acclimation in stems. Accordingly, this study addresses the following two questions: (i) Is thermal acclimation of stem respiration effectively described by EEO theory? (ii) How does thermal acclimation affect the global carbon cycle? We first propose an EEO-based model for the thermal sensitivity of stem respiration, which we test both spatially, using a global dataset, and temporally, using seasonal measurements and a warming experiment. We then apply the resulting model to test the impact of thermal acclimation on the global carbon cycle under future climate conditions.

Theoretical background

Under the assumption that a primary function of sapwood is maintaining the hydraulic continuum as determined by the canopy water demand, we assumed that the cost of doing so—whole-plant stem respiration—is proportional to transpiration from the canopy on a timescale of days to weeks [supplementary materials (SM) section 2.1]. This coupling ensures that total stem respiration—including both maintenance and growth components—is neither more (which would result in nonproductive carbon consumption) nor less (which would threaten hydraulic integrity) than that required to support the stem hydraulic continuum. Although long-distance water transport through the xylem is largely driven passively, maintenance of the hydraulic continuum is effectively used here as a proxy for associated energy-requiring processes, including the maintenance of stem water storage capacity and stem water potential, new xylem production, defense and resilience to disturbance (SM section 1.3) (*38*–*42*). We combine this hypothesis with physical principles influencing the manner in which respiration

---

[1]Department of Earth System Science, Ministry of Education Key Laboratory for Earth System Modeling, Institute for Global Change Studies, Tsinghua University, Beijing, China. [2]Hawkesbury Institute for the Environment, Western Sydney University, Sydney, Australia. [3]School of Natural Sciences, Macquarie University, Australia. [4]ARC Centre for Plant Success in Nature & Agriculture, Western Sydney University, Richmond, Australia. [5]Department of Life Sciences, Imperial College London, Silwood Park Campus, Buckhurst Road, UK. [6]School of Archaeology, Geography and Environmental Science (SAGES), University of Reading, Reading, UK. [7]Department of Biological Sciences, Texas Tech University, Lubbock, TX, USA. [8]Department of Biology, University of Louisiana, Lafayette, LA, USA. [9]Faculty of Environment, Science and Economy, University of Exeter, Exeter, UK. [10]Faculty of Forestry and Wood Sciences, Czech University of Life Sciences, Prague, Czech Republic. [11]Department of Integrated Land Management, SRUC, Barony, Parkgate, Dumfries, UK. [12]Institute for Global Change Biology and School for Environment and Sustainability, University of Michigan, Ann Arbor, Michigan, MI, USA. [13]Department of Forest Resources, University of Minnesota, St. Paul, Minnesota, MN, USA. [14]Institute of Botany, Ulm University, Ulm, Germany. [15]Department of Environmental Science, Policy and Management, University of California Berkeley, Berkeley, CA, USA. [16]Climate and Ecosystem Sciences Division, Lawrence Berkeley National Laboratory, Berkeley, CA, USA. ***Corresponding author. Email: wang_han@tsinghua.edu.cn**

and transpiration are coupled and use this relationship to predict the spatial and temporal thermal acclimation of stem respiration. First, we assume that whole-plant stem respiration (R_s, nmol C s^{-1}) is proportional to canopy transpiration (E, nmol H_2O s^{-1}) with a cost factor representing the respiration rate required to maintain a unit of transpiration rate (*43*). In principle, this cost factor should be influenced by temperature: Water has a reduced dynamic viscosity as temperature increases, meaning that there is less hydraulic resistance to water transport to the leaves and thus the cost incurred for supporting a given transpiration rate would be lower. Given that R_s is a product of mass-based respiration rate over time (r_s, nmol C g^{-1} s^{-1}) and total sapwood mass (M_s, g C), we expect that r_s and M_s also co-vary with E and the respiration cost of transpiration. At a global scale, where spatial variation in both r_s and M_s is large, we assume that r_s and M_s track variation in the cost factor and E, respectively (SM eq. 20). Therefore, the thermal response of the cost factor as largely determined by the hydraulic resistance and xylem sap viscosity is the primary control of the variation in r_s along geographic temperature gradients. For temporal changes at a weekly scale, in which the change in M_s is small compared with changes in transpiration, we expect only r_s to be coordinated with temporal variation in both E and the cost factor (SM eq. 19). Therefore, the response of r_s to temperature that emerges over time, dominated by acclimation, should be mathematically the same as that emerging across space, dominated by adaptation.

To generate empirically testable predictions for the adjustment of stem respiration to temperature, we calculated r_s at growth temperature ($r_{s.gt}$, nmol C g^{-1} s^{-1}) and r_s at a standard temperature of 25°C (r_{s25}, nmol C g^{-1} s^{-1}), applying a constant Q_{10} temperature coefficient. $r_{s.gt}$ provides a measure of respiration rate under temperature conditions experienced by plants growing under natural conditions whereas r_{s25} allows for a standardized comparison of respiratory capacity (and associated investment in mitochondrial proteins) across sites and species (*44*). Our model specifically predicts that $r_{s.gt}$ acclimates to increasing temperature by −2.3% K^{-1} (Fig. 1B, SM eq. 22), due

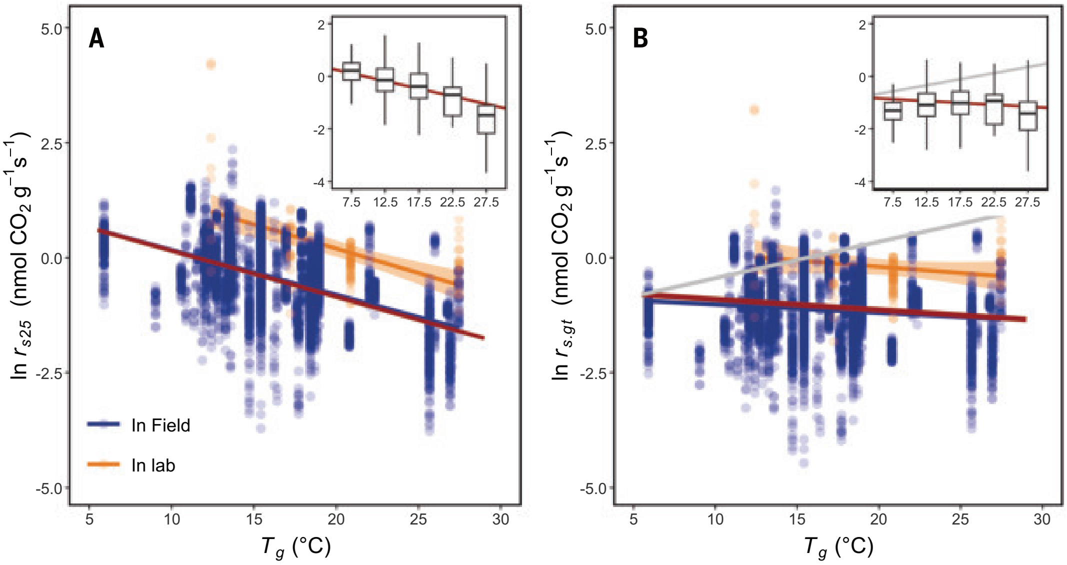

Fig. 1. Global trends of stem respiration at reference temperature (r_{s25}) and at growth temperature ($r_{s.gt}$) in relation to growth temperature (the mean temperature during the thermal growing season when daily temperature above 5°C, T_g). (**A**) Stem respiration was measured in the laboratory (orange dots) and in the field (blue dots). r_{s25} represents stem respiration standardized to the reference temperature of 25°C. Solid fitted lines are shown for the laboratory and field data separately (orange and blue lines, respectively; mathematical details are provided in Table 1). The shaded area represents 95% CI. The solid red line is the theoretical prediction of thermal sensitivity, whose slope is −10.1% K^{-1}. The inset figure presents an overview of all the main figure data aggregated into temperature bins. Horizontal and vertical coordinates are the same as that in the main figure. (**B**) $r_{s.gt}$ represents stem respiration standardized to growth temperature, using the same color coding as in (A). The solid red line is the theoretical prediction of thermal sensitivity of $r_{s.gt}$, whose slope is −2.3% K^{-1}. The instantaneous thermal response is also shown, based on a fixed-Q_{10} function (gray line).

Table 1. Global trends of stem respiration in relation to temperature. Statistical output using the global dataset shown in Fig. 1. r_{s25} represents stem respiration standardized to the reference temperature of 25°C; $r_{s.gt}$ represents stem respiration standardized to growth temperature. Error in Variables regression analysis was performed for field-based and lab-based data separately and also performed using all data. The table provides confidence intervals, R-squared values (R2), *P*-values (*P*), and degrees of freedom (df) associated with each regression model.

Quantity	Theoretical prediction	Measurements	Fitted coefficient	Confidence intervals		Intercept (mean ± SE)	R^2	*P*	df
				2.50%	97.50%				
r_{s25}	−0.101	In lab	−0.110	−0.143	−0.078	2.41 ± 0.74	0.27	<0.01	79
		In field	−0.101	−0.104	−0.099	1.20 ± 0.04	0.28	<0.001	4544
		All data	−0.098	−0.100	−0.095	1.16 ± 0.04	0.26	<0.001	4625
$r_{s.gt}$	−0.023	In lab	−0.028	−0.061	0.005	−0.37 ± 0.74	0.02	0.39	79
		In field	−0.019	−0.022	−0.017	−0.82 ± 0.04	0.01	<0.001	4544
		All data	−0.015	−0.018	−0.013	−0.86 ± 0.04	0.01	<0.001	4625

to the decline in the viscosity of water. A steeper decline of –10.1% K^{-1}, is expected for r_{s25} adjusting to temperature (Fig. 1A, SM eq. 20) because of the greater catalytic rates of respiratory enzymes at higher temperatures. The trend in the thermal response when considering that acclimation is opposite to the instantaneous response due to enzyme kinetics (+7.9% K^{-1}) (SM eq. 7), which means that warming in the short term will increase respiration steeply and exponentially. Therefore, with acclimation to warming in the long term, respiration at a given temperature (r_{s25}) is reduced, reflecting reduction in respiratory capacity.

We evaluated the thermal response of stem respiration through empirical analyses using a new Global Stem Respiration Dataset (GSRD) (fig. S2 and tables S1 and S2) and data from five species measured from a glasshouse warming experiment. GSRD includes data from 187 species sampled at 68 field sites spanning all climate zones (including laboratory measurements from excised branches for 74 species from four sites and plus 8701 measurements made directly on trunks of 114 species from 64 field sites, including 4155 seasonal measurements for three species from one site that were used in our temporal test).

Results

A linear regression of r_{s25} against T_g (mean temperature during the thermal growing season, defined as the period when daily temperatures are above 5°C) showed a strong negative response to higher temperatures across all sites globally: r_{s25} decreased by 9.8 ± 0.3% K^{-1} with warmer temperatures, statistically indistinguishable from our theoretical prediction (10.1% K^{-1}) (Fig. 1A, Table 1, and table S3). Measurements made in the field and laboratory showed a similar thermal response for r_{s25} (field measurements: –10.1 ± 0.3% K^{-1}; laboratory measurements: –11.0 ± 3.3% K^{-1}). Note that the absolute values of the laboratory measurements, 2.97 ± 1.16 nmol CO_2 g^{-1} s^{-1}, were generally larger than that of the field measurements, 0.87 ± 0.012 nmol CO_2 g^{-1} s^{-1}, possibly reflecting differences in the nature of the sample material; e.g., smaller branches might have been used for lab measurements and if so, these might have a higher proportion of living cells (*45*), or reflecting removal of CO_2 diffusion limitations or CO_2 loss to the transpiration stream when measuring CO_2 efflux on excised tissues under laboratory conditions (Fig. 1A and table S6). Comparisons using site-mean values, to minimize the potential impact of over-representation of individual sites with much larger sample sizes, showed that r_{s25} decreased by 8.1 ± 1.8% K^{-1} with warmer temperatures (fig. S3 and table S4). Calculating r_{s25} from measurements made at temperatures other than 25°C assumed a standard, fixed thermal sensitivity of respiration (SM section 1.1.3). To minimize potential effects of that assumption, we also restricted analyses to sites where respiration rate was measured at 25 ± 1°C; these data showed a similar thermal response in r_{s25} (site-mean: –10.1 ± 3.8% K^{-1}, all individuals: –15.5 ± 0.7% K^{-1}) (fig. S4 and table S5). Thus, the observed response of r_{s25} against T_g, considered multiple ways, was in the range of approximately –8% K^{-1} to –15% K^{-1}. Next, we quantified temperature-related trends in $r_{s.gt}$—that is, stem respiration rates estimated under typical thermal growing conditions as opposed to at a standard, set temperature. Again, both observations and theory showed a significant negative response of $r_{s.gt}$ to temperature (data: –1.5 ± 0.3% K^{-1}, theory: –2.3% K^{-1}), opposite in trend from that expected from enzyme kinetics alone (Fig. 1B and Table 1).

Although the global patterns are consistent with an acclimation response to temperature, they may also reflect species replacement along geographic temperature gradients (fig. S5). However, measurements of seasonal variation and a warming experiment are also consistent with our theoretical predictions. A single boreal site provided continuous data on r_s of three species throughout the growing season. We estimated daily transpiration (nmol m^{-2} s^{-1}) with an EEO-based Penman-Monteith model accounting for canopy stomatal regulation driven by radiation, temperature, vapor pressure deficit, atmospheric pressure, and leaf area index (*36*). The best predictions of the temporal variation in r_{s25}, indicated by variance inflation factor, root mean square error, and R^2, were given by a 6-day time window for temperature and a 13-day period for transpiration, although alternative periods around 1 to 2 weeks generated similar predictions (fig. S6 and table S7). Multiple regression showed that r_{s25} declines with acclimated temperature by 10.6 ± 0.5% K^{-1} and increases almost proportionally to transpiration (103.8 ± 1.8%), consistent with the theoretical predictions (temperature: –10.1% K^{-1}, transpiration: 100%, Fig. 2). When evaluated at the acclimated temperature, $r_{s.gt}$ also showed significant responses to temperature (–4.7 ± 0.5% K^{-1}) and to transpiration (111.7 ± 1.8%), both similar but higher than the theoretical values (temperature: –2.3% K^{-1}, transpiration: 100%) (fig. S7). These small differences between the theoretical and empirical values likely reflect uncertainties in the two predictors or the influence of other potential explanatory variables such as soil moisture (see below). The five species measured in the warming experiment showed a consistent decrease in r_{s25} of 10.6 ± 1.6% K^{-1}, close to our theoretical prediction of 10.1% (Fig. 3). Individual species show similar trends (Fig. 3 and table S8). The *Pinus* species in this experiment showed a somewhat stronger thermal acclimation response than *Pinus* species in the global analysis (–8.4 ± 0.4% K^{-1}), possibly reflecting differences in the temperature range sampled (fig. S5 and table S9).

Based on the agreement between theory and observations, we developed a simple model to estimate the global carbon flux from stem respiration and its contribution to the global carbon cycle (SM section 3.2.1). In this model, total stem respiration rate per unit land area is predicted as the product of sapwood mass and mass-based respiration rate under growth temperature ($r_{s.gt}$), on an annual timestep. Sapwood mass is estimated from total above-ground stem biomass and allometric equations describing the shape of the stem, and sapwood depth (SM eq. 35) (*46*, *47*). We simulated $r_{s.gt}$ with a single global parameter (table S10) and T_g to represent the annual thermal growth environment for woody species. The model predicts an annual global carbon release by stem respiration of 27.4 ± 5.9 Pg C in 2010 (Fig. 4A) (*48*, *49*). This is comparable to estimates from most TRENDY models (fig. S8). Modeled stem respiration from forests alone (excluding shrublands

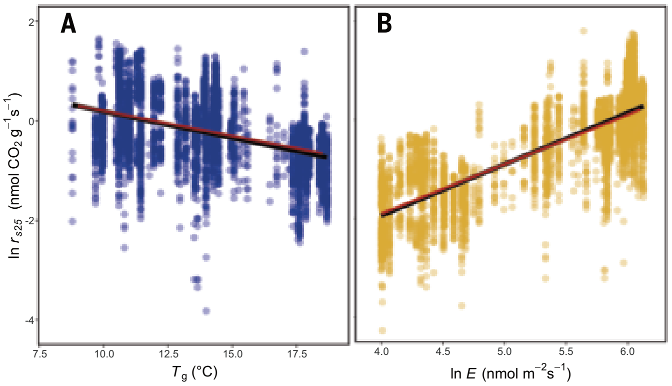

Fig. 2. Partial residual plots showing the relationship between stem respiration and temperature and transpiration when other factors are held constant. (**A**) Growth temperature (T_g) is an average of the 6 days before stem respiration was measured. r_{s25} is stem respiration, natural-log transformed, at the reference temperature of 25°C. (**B**) Transpiration (E) is an average of the 13 days before measurement and was natural-log transformed. The solid black line is the relationship fitted through multiple regression ($\ln r_{s25} \sim (-0.106 \pm 0.005) \times T_g + (1.04 \pm 0.018) \times \ln E$, $R^2 = 0.49$, VIF = 2.01, $P < 0.001$). The red solid line is the theoretical prediction, with a coefficient of –10.1% K^{-1} and 100% (nmol H_2O m^{-2} s^{-1})$^{-1}$ for temperature and natural-log transformed transpiration, respectively.

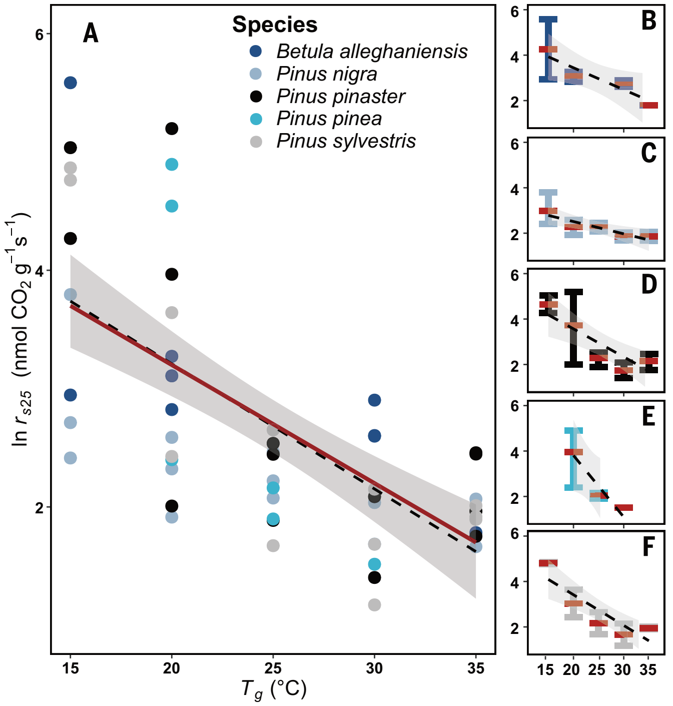

Fig. 3. Relationship between stem respiration and growing temperature derived from a warming experiment. The warming experiment was conducted using five species: *Betula alleghaniensis*, *P. nigra*, *P. pinaster*, *P. pinea*, and *P. sylvestris*. (**A**) r_{s25} is stem respiration, natural-log transformed, at the reference temperature of 25°C. Growth temperature (T_g) is the temperature at which individual species were grown. Different colored points represent different species. The dashed line was fitted ($\ln r_{s25} = 0.106 \pm 0.007 \times T_g$, $R^2 = 0.44$) using linear regression analysis on all the data. The red solid line is the theoretical prediction, with a coefficient of −10.1% K^{-1}. (**B** to **F**) Box plots representing different species, with colors consistent with those in (A). The short horizontal lines represent the maximum and minimum values and the short red horizontal lines represent the average value under each T_g. The dashed/fitted lines with shaded areas represent the 95% confidence intervals (CI). Mathematical details are provided in table S8.

and savannas) is 15.3 ± 3.2 Pg C, higher than a previous empirical estimate (6.7 ± 0.5 Pg C) (*25*), with the difference presumably reflecting different methods of estimation. Global variation in stem respiration was largely controlled by total stem biomass: regions with higher biomass had higher respiration. The highest stem respiration occurred in tropical forests and in the humid temperate forests of eastern North America, eastern Asia, and Europe.

We applied this modeling scheme using different climate change scenarios to assess the influence of thermal acclimation on the carbon flux from stem respiration over the 21st century. The results showed that implementing thermal acclimation led to a reduction in predicted stem respiration of 24 and 46% by 2100 under the weakest (SSP126) and strongest (SSP585) warming scenarios, respectively, and reduced predicted land ecosystem carbon emissions by 10.8 and 24.0 Pg C (Fig. 4B). Some land surface models, including CLM5, CABLE, and QUINCY, consider the thermal acclimation of stem respiration but treat it identically to leaf respiration (*27*, *30*, *32*, *44*). In those models, r_{s25} is predicted to decrease with temperature by 1.83% K^{-1}, an order of magnitude less than that shown by our empirical analyses. This underestimation of the thermal acclimation of stem respiration led to a higher carbon emission from terrestrial ecosystems, resulting in an overestimation of 4.9 and 11.9 PgC in 2100 under the SSP126 and SSP585 scenarios, respectively (SM section 3.2.5).

Discussion and conclusions

We considered several sources of uncertainty inherent in stem respiration observations from assumptions about mean stem diameter values and the allometric equation for deriving mass-based estimates of respiration from stem surface area-based measurements (SM section 1.1.4). Stem size shows a further significant negative effect on stem respiration (tables S11), probably reflecting size-related variation in the proportion of living cells and likely contributing to the difference between lab and field observations. Uneven geographic coverage of observations, with relatively few sites from the tropics and southern hemisphere, may have introduced further biases. Nevertheless, the trends are consistent across the range of temperatures, including boreal and tropical sites. A remaining uncertainty concerns the use of stem CO$_2$ efflux as a proxy for stem respiration, as there can be other processes affecting stem CO$_2$ efflux such as CO$_2$ refixation in bark and dissolution of CO$_2$ in xylem sap (*50*–*52*). Nevertheless, the congruence of the results across different sources and subsets of the data (Figs. 1 to 3, figs. S3 to S5, S7, S9, S10, Table 1, and tables S3 to S5, S7 to S9, and S12) and

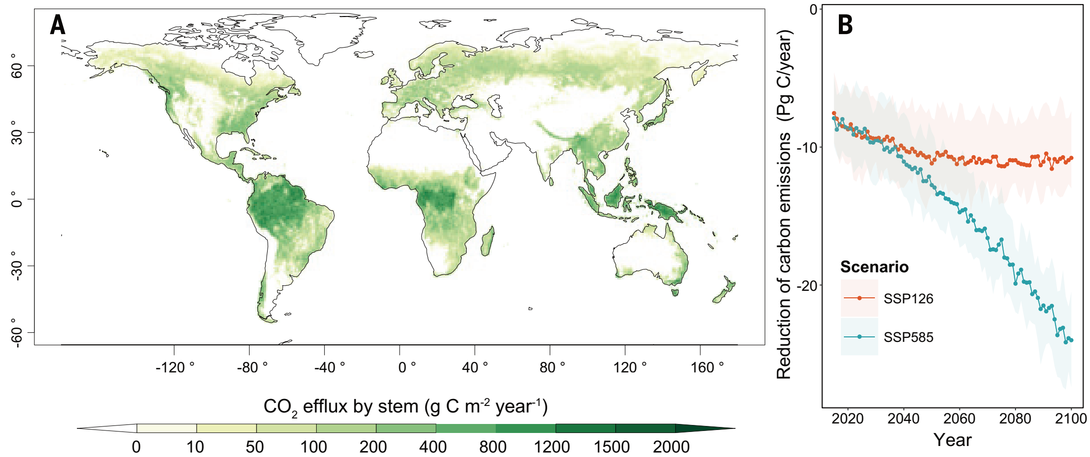

Fig. 4. Predicted global stem respiration under present conditions and in response to future warming. (**A**) Stem respiration calculated at the global scale under recent CO$_2$ levels (see details in SM section 3.2). (**B**) Simulated reduction in carbon emissions due to considering thermal acclimation of stem respiration over the 21st century in two different scenarios (SSP126 and SSP585). The temperature was derived from an ensemble of four future climate simulations [the land surface model is specified in parentheses: ACCESS–ESM1–5 (CABLE), CESM2 (CLM5), IPSL–CM6A–LR (ORCHIDEE) and UKESM1–0 (JULES). The solid dotted line is the mean ensemble value (orange: under SSP126, blue: under SSP585) and the shaded area represents the range of the model ensemble.

the similarity between the observed and predicted relationships suggests that our conclusions about the thermal response of stem respiration are robust. Data limitations preclude further analysis of the sensitivity of respiration to other environmental factors, such as soil moisture (*24*, *53*) or CO_2 concentration. However, we note that vapor pressure deficit had a positive influence on r_{s25}, in line with our theoretical prediction (SM section 2.2, figs. S11 to S12 and table S13). Short-term thermal sensitivity (i.e., Q_{10} temperature coefficient) might itself also acclimate to warming and modify the estimates of r_{s25} and $r_{s.gt}$ (*9*). However, our sensitivity analyses applying a range of Q_{10} values (table S14) and without temperature standardization (fig. S4 and table S5) show that variation in Q_{10} has a minor influence on the agreement between the theoretical prediction and empirical observations. Overall, stem respiration, as our hypothesis predicts, appears to show a much stronger thermal acclimation than leaf respiration, which indicates a weak but positive response to warming (*16*). This disparity potentially reflects their different driving processes and thermal conditions. In particular, leaf respiration tracks the maximum capacity of carboxylation, phloem-loading of photosynthates, and turnover of photosynthetic proteins (*6*, *14*, *16*). Acclimated carboxylation capacity increases with temperature, compensating for enhanced photorespiration under warmer conditions, implying a positive thermal response in leaf respiratory acclimation (*16*). This is probably not the case for woody tissues. Furthermore, leaves are more likely to be sun-exposed and do not have the insulating properties of bark tissue (*20*, *54*). Experimental studies will be needed to reveal the mechanisms controlling the acclimation of stem and leaf respiration.

We have demonstrated that the application of EEO principles provides a simple way to predict stem respiration and its thermal acclimation, consistent with empirical evidence. This approach could and should be implemented in ESMs. The acclimation response to growth temperature in stem respiration is much stronger than that in leaf respiration. This suggests the potential for enhanced carbon use efficiency in a warming world, a subject still hotly debated (*55*–*57*). Enhanced carbon use efficiency would, in turn, substantially weaken the expected positive climate-carbon feedback, enhancing the degree to which ecosystems globally slow the rate of climate change.

REFERENCES AND NOTES

1. P. Ciais *et al.*, Climate Change 2013: The Physical Science Basis (Cambridge Univ. Press, 2014), pp. 465–570.
2. P. Friedlingstein *et al.*, *Earth Syst. Sci. Data* **15**, 5301–5369 (2023).
3. M. Campioli *et al.*, *Nat. Commun.* **7**, 13717 (2016).
4. D.-X. Guan *et al.*, *Agric. For. Meteorol.* **137**, 138–149 (2006).
5. Y. Malhi *et al.*, *Glob. Change Biol.* **15**, 1255–1274 (2009).
6. J. S. Amthor, *Ann. Bot.* **86**, 1–20 (2000).
7. F. Vries, *Ann. Bot.* **39**, 77–92 (1975).
8. M. A. Heskel *et al.*, *Proc. Natl. Acad. Sci. U.S.A.* **113**, 3832–3837 (2016).
9. P. M. Cox, R. A. Betts, C. D. Jones, S. A. Spall, I. J. Totterdell, *Nature* **408**, 184–187 (2000).
10. C. Huntingford *et al.*, *Nat. Geosci.* **6**, 268–273 (2013).
11. O. K. Atkin, M. G. Tjoelker, *Trends Plant Sci.* **8**, 343–351 (2003).
12. K. Y. Crous, J. Uddling, M. G. De Kauwe, *New Phytol.* **234**, 353–374 (2022).
13. P. B. Reich, *et al.*, *Nature* **531**, 633–636 (2016).
14. Y. Ren *et al.*, *New Phytol.* **241**, 578–591 (2024).
15. N. G. Smith, G. Li, J. S. Dukes, *AoB Plants* **11**, plz064 (2019).
16. H. Wang *et al.*, *Glob. Change Biol.* **26**, 2573–2583 (2020).
17. P. B. Reich *et al.*, *Ecol. Lett.* **11**, 793–801 (2008).
18. A. C. Westerband *et al.*, *Ann. Bot.* **129**, 633–646 (2022).
19. B. C. Posch *et al.*, *Proc. Natl. Acad. Sci. U.S.A.* **121**, e2408583121 (2024).
20. Q. Yang, M. Xu, Y. Chi, Y. Zheng, *Acta Ecol. Sin.* **36**, 229–235 (2016).
21. J. Q. Chambers *et al.*, *Ecol. Appl.* **14**, 72–88 (2004).
22. D. Gansert, K. Backes, T. Ozaki, Y. Kakubari, *Flora* **197**, 186–202 (2002).
23. M. B. Lavigne, M. G. Ryan, *Tree Physiol.* **17**, 543–551 (1997).
24. L. Rowland *et al.*, *New Phytol.* **218**, 1393–1405 (2018).
25. J. Yang, Y. He, D. P. Aubrey, Q. Zhuang, R. O. Teskey, *Glob. Change Biol.* **22**, 1433–1444 (2016).
26. A. Zach, V. Horna, C. Leuschner, *Trees* **24**, 285–296 (2010).
27. G. Krinner *et al.*, *Global Biogeochem. Cycles* **19**, GB1015 (2005).
28. G. Y. Niu *et al.*, *J. Geophys. Res.* **116**, D12109 (2011).
29. D. B. Clark *et al.*, *Geosci. Model Dev.* **4**, 701–722 (2011).
30. V. Haverd *et al.*, *Geosci. Model Dev.* **11**, 2995–3026 (2018).
31. D. M. Lawrence *et al.*, *J. Adv. Model. Earth Syst.* **11**, 4245–4287 (2019).
32. T. Thum *et al.*, *Geosci. Model Dev.* **12**, 4781–4802 (2019).
33. D. L. Lombardozzi, G. B. Bonan, N. G. Smith, J. S. Dukes, R. A. Fisher, *Geophys. Res. Lett.* **42**, 8624–8631 (2015).
34. S. P. Harrison *et al.*, *New Phytol.* **231**, 2125–2141 (2021).
35. B. D. Stocker *et al.*, *New Phytol.* **245**, 49–68 (2025).
36. S. Tan *et al.*, *Agric. For. Meteorol.* **336**, 109478 (2023).
37. H. Wang *et al.*, *Nat. Plants* **3**, 734–741 (2017).
38. A. Gauthey *et al.*, *Plant Cell Environ.* **45**, 1216–1228 (2022).
39. S. Martorell, A. Diaz-Espejo, H. Medrano, M. C. Ball, B. Choat, *Plant Cell Environ.* **37**, 617–626 (2014).
40. H. Morris *et al.*, *New Phytol.* **209**, 1553–1565 (2016).
41. M. Tomasella, E. Petrussa, F. Petruzzellis, A. Nardini, V. Casolo, *Int. J. Mol. Sci.* **21**, 144 (2019).
42. M. J. B. Zeppel *et al.*, *Ecol. Evol.* **9**, 5348–5361 (2019).
43. I. C. Prentice, N. Dong, S. M. Gleason, V. Maire, I. J. Wright, *Ecol. Lett.* **17**, 82–91 (2014).
44. O. K. Atkin *et al.*, *New Phytol.* **206**, 614–636 (2015).
45. M. A. Cavaleri, S. F. Oberbauer, M. G. Ryan, *Glob. Change Biol.* **12**, 2442–2458 (2006).
46. M. Santoro *et al.*, *Earth Syst. Sci. Data* **13**, 3927–3950 (2021).
47. M. Thurner *et al.*, *Glob. Ecol. Biogeogr.* **28**, 640–660 (2019).
48. C. Huntingford *et al.*, *Nat. Commun.* **8**, 1602 (2017).
49. M. Jung *et al.*, *J. Geophys. Res. Biogeosci.* **116**, G00J07 (2011).
50. R. L. Salomón, L. De Roo, J. Oleksyn, D. J. W. De Pauw, K. Steppe, *New Phytol.* **225**, 2214–2230 (2020).
51. R. L. Salomón *et al.*, *Tree Physiol.* **44**, tpad157 (2024).
52. R. O. Teskey, A. Saveyn, K. Steppe, M. A. McGuire, *New Phytol.* **177**, 17–32 (2008).
53. C. W. Huang *et al.*, *New Phytol.* **213**, 1093–1106 (2017).
54. N. L. Harris, C. A. S. Hall, A. E. Lugo, *Ecol. Modell.* **216**, 253–264 (2008).
55. M. Campioli *et al.*, *Nat. Geosci.* **8**, 843–846 (2015).
56. A. Collalti *et al.*, *Nat. Commun.* **11**, 5322 (2020).
57. S. Manzoni *et al.*, *Biogeosciences* **15**, 5929–5949 (2018).
58. H. Zhang *et al.*, Global Stem Respiration Dataset (GSRD), version 1 (Science Data Bank, 2024); https://doi.org/10.57760/sciencedb.ecodb.00170.

ACKNOWLEDGMENTS

We thank M. E. Olson and C. Körner for comments on the preprint of this paper and acknowledge A. Eller for her contribution to data collection in Australia. We thank the editor and reviewers for valuable comments and suggestions. **Funding:** This project is supported by National Natural Science Foundation of China 42361144875, National Key Research and Development Program of China 2023YFF1305500, the National Natural Science Foundation of China 72140005, Hainan Institute of National Park Research Program KY-23ZK01, and Tsinghua University Initiative Scientific Research Program 20223080041 (to H.W.); Schmidt Sciences (to H.W., I.C.P., S.P.H., N.G.S., and T.K.); Australian Research Council DP170103410 (to I.C.P. and I.J.W.); Australian Research Council DP220102547 (to I.J.W. and H.W.); Australian Research Council CE200100015 (to I.J.W.); the United States National Science Foundation DEB-2045968 (to N.G.S.); the United States National Science Foundation DBI-2021898 (to P.B.R.); the RUBISCO SFA, sponsored by the Regional and Global Model Analysis Program in the US Department of Energy (DOE) Office of Science and DOE Early Career Research award (to DE-SC0021023) (to T.F.K.). **Author contributions:** Theory: H.Z., H.W., I.C.P., I.J.W., and S.P.H. Data: H.Z., I.J.W., A.C.W., N.S., P.R., L.R., H.M., L.P. and S.J. Investigation: H.Z., H.W., I.C.P., S.P.H., I.J.W., T.K., and N.B.N. Visualization: H.Z. and N.B.N. Writing: original draft: H.Z., H.W., and S.P.H. Writing, review & editing: All. **Competing interests:** Authors declare that they have no competing interests. **Data and materials availability:** Data used in this study and original R code (version 4.0.2) used to analyze results have been deposited as a public archived databases (*58*) and are also available in the SM. **License information:** Copyright © 2025 the authors, some rights reserved; exclusive licensee American Association for the Advancement of Science. No claim to original US government works. https://www.science.org/about/science-licenses-journal-article-reuse

SUPPLEMENTARY MATERIALS

science.org/doi/10.1126/science.adr9978
Materials and Methods; Figs. S1 to S12; Tables S1 to S14; References (*59*–*134*);
MDAR Reproducibility Checklist

Submitted 23 July 2024; accepted 21 March 2025

10.1126/science.adr9978

Moupali Das

Yvette Raphael

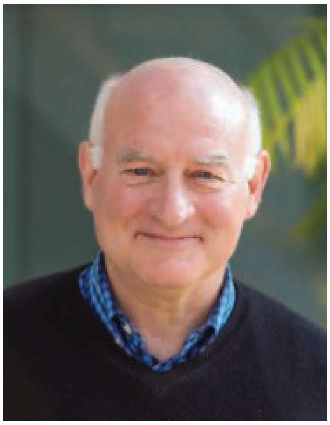
Wesley Sundquist

PHOTOS (FROM LEFT): MOUPALI DAS: ERIK ESPERA, A SHOT IN THE ARM MEDIA; RACHEL MERRILL/UNIVERSITY OF UTAH HEALTH

The road to lenacapavir, a breakthrough HIV treatment

Three individuals have been awarded the AAAS Mani L. Bhaumik Breakthrough of the Year Award for their work on the drug **MEAGAN PHELAN**

In the hunt for a remedy, when the baton is passed from dedicated academic scientists to an innovative company to trusted community advocates, outcomes for society can be especially powerful. Today, thanks to that sequence of contributions, the first HIV drug to offer long-lasting protection from infection—eliminating the need for people to take a daily pill—exists. For their role in ensuring that drug, lenacapavir, came to life and to market, the AAAS Mani L. Bhaumik Breakthrough of the Year Award is being awarded to Wesley Sundquist, chair of the University of Utah Department of Biochemistry; Moupali Das, vice president, clinical development, HIV prevention and pediatrics, at Gilead Sciences; and Yvette Raphael, cofounder and executive director of Advocacy for Prevention of HIV and AIDS in Africa.

"These individuals represent the three arms of what is necessary to create new science and then translate it for the world in a way that is really able to make a difference," said Megan Ranney, dean of the Yale School of Public Health and part of the committee—convened by *Science* journals' Editor-in-Chief Holden Thorp—that selected the winners.

"I was excited about how these three tell the story of the journey required to bring a drug into existence," said committee member William Powderly, codirector of the Division of Infectious Diseases at Washington University School of Medicine. "It takes multiple people, skillsets, and partners."

As of 2023, 39.9 million people globally were living with HIV, newly infecting more than 1 million people a year.

Even after decades of research, there is no cure for the disease HIV causes, AIDS. But lenacapavir, born out of research on HIV's cone-shaped capsid protein, gets close, almost completely preventing new HIV infections from occurring. The drug protects people for 6 months with each shot.

"This drug is extraordinary—the closest thing to a vaccine that we have," said Ranney. She explained that she and many of her peers in the public health community entered the field at the height of the AIDS pandemic, in the 1980s and 1990s. "This medication is beyond the wildest dreams of what many of us could have imagined."

Recognizing the people behind such significant scientific developments is a central philosophy for donor Mani L. Bhaumik, PhD—a physicist with myriad contributions to the development of high-powered lasers—as well as for AAAS and the *Science* family of journals.

"Studying intractable parts of the physical world, like a virus capsid, is critical to scientific innovation," said Bhaumik. "And persisting to ensure that insights from basic research can be applied and that they are trusted by those who they will serve is critical—now more than ever. I'm delighted to see this year's recognition go to people across sectors whose thorough approach made such a valuable contribution."

The Mani L. Bhaumik Breakthrough of the Year Award was established in 2022 with a $11.4 million pledge from Bhaumik: the largest in the organization's history. The award supports a $250,000 cash prize annually for up to three scientists or researchers whose work best underpins the *Science* Breakthrough of the Year, the journal's choice of the top research advance of the year. In 2024, *Science* named lenacapavir the latest Breakthrough.

Mapping HIV's capsid

Sundquist, who moved to the University of Utah as an assistant professor in 1992, played a key role in the development of the drug, though his work was not immediately recognized. "Sundquist spent countless hours in the lab, made a critical discovery, and then watched it sit on the shelf for a while, which can happen in basic science," said Ranney.

His contribution—which he embarked upon as he started his Utah-based lab—was elucidating the structure and functions of the HIV capsid protein. Sundquist focused on the capsid because he was aware that HIV deaths were increasing globally and that most scientists studying HIV treatments were looking at the virus's enzymes. "We wanted to work on an aspect of the problem that was unique," he said, "and we were drawn to the unusual cone shape of the capsid."

Until Sundquist's work, scientists thought the capsid, which encloses the virus's genetic material, was largely a structural element. They did not see it as a particularly "druggable" target, especially compared to enzymes, in part because it was thought to be highly stable.

In 1996, working with a team, Sundquist published a paper in *Science* that defined the capsid's architecture. That laid the groundwork for a study in 2003 in the *Journal of Virology*, in which he and colleagues showed that if the HIV capsid was disrupted, even in minor ways, viral replication was disrupted, too.

"That was unexpected," said Sundquist.

Clinical trials purposefully designed

Even as these critical discoveries were made, however, it wasn't obvious that the capsid would be easily turned into a drug target. For his part, though, Sundquist didn't feel that it was very long after he and his colleagues published their 2003 results that Gilead Sciences contacted them.

Tomas Cihlář, a virologist at the company, visited Sundquist's labs. Impressed with his discoveries, Cihlář took them back to his colleagues. The Gilead team wanted to see if they could use Sundquist's insights about how to hinder viral replication to design HIV drugs with longer acting power for people living with HIV; while the standard-of-care treatment—combination antiretroviral therapy—worked well, it required daily medication.

A dedicated group of scientists at Gilead Sciences showed perseverance as it took more than a decade (beginning around 2006) to develop a drug based on Sundquist's findings. To do so, John Link, then–vice president of medicinal chemistry at Gilead, and his colleagues screened thousands of molecules to identify an effective capsid inhibitor.

"We sometimes think about industry as not having staying power," said Ranney. "But it was something like 15 years here—fits and starts—and Gilead as an institution kept supporting capsid inhibitors."

The molecule's properties meant its effects could be extended over 6 months, a promising option for patients who struggled with daily medications.

Gilead ran the first trial for people with HIV involving an injectable version of lenacapavir in 2018. "I was a medical monitor for the first phase 1 trial," said Das, a winner of this year's Bhaumik Breakthrough of the Year prize on behalf of the many Gilead Sciences team members working on lenacapavir. This meant that Das, a trained physician, provided expert guidance to confirm the safety of trial participants.

At that time, Gilead was focused on evaluating lenacapavir for treatment of HIV. But the reality was that there were already effective treatments, like antiretrovirals. Meanwhile, there were still many people in the world at high risk of acquiring HIV.

"I remember seeing results from the first lenacapavir treatment study and thinking this drug—because of its molecular properties—might be very good for prevention, too." Das said, "I was immediately thinking: how could we use this for prevention?"

The next step forward was figuring out the best way to evaluate this drug for preventing HIV.

"Gilead had already established the company as leaders in the use of oral antiretroviral agents as pre-exposure prophylaxis" said Myron Cohen, director of the Institute of Global Health and Infectious Diseases at the University of North Carolina at Chapel Hill, who also sat on the committee who selected the winners. "But many people found it difficult to maintain usage of daily oral pills. Development of long-acting agents, especially injectable agents, became an important goal."

When Gilead Sciences made this decision, Das played a crucial role. "She was the pivotal person who created studies to garner proof that it worked for prevention, too," said Powderly.

Her leadership was essential in designing the clinical trials, known as PURPOSE 1 and PURPOSE 2, which began in 2021 and are among the most comprehensive HIV prevention trial programs ever conducted. The trials were carefully shaped to include people most in need of preventative care — and people most underserved by past trials. This involved establishing trial sites in locations where infections were happening most.

"There were lots of times where we had to change hearts and minds in designing this trial program because we did a lot differently," she said. Much of this related to the novel design and lenacapavir itself, but also to who was included. Das recalled a story of a young African adolescent woman who was pregnant and who came to a stakeholder meeting in Kigali, Rwanda. That meeting, organized by Gilead, included community advocates, government officials, regulators, ethicists, site staff, and pre-exposure prophylaxis (PrEP) clinical trial investigators whom Gilead had convened to discuss how best to design and implement PrEP trials in cisgender women. "'Make sure people like me have a chance in the trials,' this woman had said to us. I'll never forget her."

Das firmly believes better science happens when everyone is included. "It's not charity," she said. "It's good science."

The PURPOSE 1 trial evaluated lenacapavir in cisgender women and in adolescent girls in sub-Saharan Africa and Uganda, where stigma means some women have challenges using daily oral PrEP products. Some of the women in the trial became pregnant. Results from PURPOSE 1, published in July 2024, showed that twice-yearly lenacapavir led to 100% efficacy in preventing infections, a tremendous result. "It was so exciting to have the first results for lenacapavir for HIV prevention be in women," said Das.

For PURPOSE 2, Das and her team recruited participants from places disproportionately affected by HIV and underrepresented in past HIV clinical trials, including parts of the United States, Brazil, Thailand, South Africa, Peru, Argentina, and Mexico. The trial evaluated lenacapavir for prevention of HIV in a diverse range of cisgender men and gender-diverse people. Results, published in November 2024, showed that the drug reduced new infections by 96%.

Powderly said that years-long work from researchers at Gilead Sciences leading up to Das's efforts was critical, "and without her enthusiasm and drive, that final hurdle—the studies and trials for prevention—would have been much harder."

"The human voice matters"

Keeping the people most in need of HIV drugs at the center of the PURPOSE trials, as Das did, was possible because of a key partner—another winner of this year's Bhaumik Breakthrough of the Year Award: Yvette Raphael.

Das and Raphael met in Kigali, Rwanda, in 2019, 2 years before the PURPOSE trials started, at the same stakeholder meeting where Das and the group convened by Gilead heard from the young pregnant African woman about including people like her in the trials. "Yvette really wanted to know what we were going to do differently," said Das.

Raphael, an HIV prevention advocate and community leader living with HIV, had previously engaged in trials of HIV drugs. "We knew past trials had made mistakes," she said.

"Raphael was well-recognized as a tireless and thoughtful advocate for the development of HIV prevention strategies for women," said Cohen. "Her involvement in the development of lenacapavir—in trusted communication with Gilead and

It's important to fund basic research, as we never know what is going to be the next world-changing discovery.

Megan Ranney Dean of the Yale School of Public Health

trial participants and their communities—was a critical requirement for the success of these studies."

Raphael fought to make sure people affected by HIV had access to information about new treatment options, including long-acting treatments that could improve quality of life. In Africa, especially among African women, problems with HIV preventative strategies—largely in the form of daily pills—were ongoing. Drugs that worked in men were not working in women in part because it was harder, for social reasons, for women to take a pill every day.

"An injection would have been better for women," said Powderly. "But community trust and involvement were critical."

Raphael, who served as chair of the PURPOSE 1 Advisory Board from 2019 to 2024, told Gilead about the major challenges in the African community.

"For lenacapavir trials, we wanted young people to be part so that the drug could be approved for them from the start," said Raphael. Since young people need parental consent, she helped advise parents considering whether their adolescent children could participate.

"It was also very important for pregnant women to be included," said Raphael. "We wanted to be sure that once this drug was approved, pregnant women could get it, too."

Their efforts paid off, and the PURPOSE 1 trial came together, including women, pregnant women, and adolescents.

"The clinical trials would never have been as successful as they were had it not been for Raphael," said Thorp.

"The human voice matters as much as the science to get to translation in the real world," said Ranney. "Yvette's leadership is a gorgeous exemplar of how great science is done."

For her part, Raphael said her collaboration with Das, where they both learned from and pushed each other, was critical.

"I'd like to recognize Moupali's fearlessness for creating greater participation from the community," said Raphael. "We called her the 'Das-rupter'…I've been participating in HIV prevention trials for 25 years, and every time, we said we'd do better. I think with Moupali, this is the best we have done."

Ensuring that the people most impacted by a drug are part of trials provides another benefit that comes later. "We can discover drugs and see they are successful in trials," said Raphael, "but the next outcomes won't be as good if there's nobody to 'own' these innovations, and to advocate for them to be affordable and accessible. We did not want this drug to sit on a shelf."

For Raphael, the outcome of the trials has been nothing short of a miracle. "It's amazing that you need injections just twice a year." She said the biggest surprise to her was the 100% efficacy in PURPOSE 1. "It was also surprising that it was such a short trial." In 2024, the trial was stopped early because of success it had already shown, which meant the drug could become available sooner. "When that news broke," she said, "Africa stood still."

"The PURPOSE 1 and 2 trials are exemplars for how to do a better job making sure people who will one day want to use the medication have a voice," said Ranney. "This will speed the implementation of the drug on the other side."

Raphael knows the research that made this life-changing drug a reality started decades ago, in Sundquist's lab, with studies of a viral capsid.

"This work changed how people think about viral capsids," said Sundquist. "It meant that other people could think about capsids as drug targets."

The future of life-changing basic research

Today, however, as funding cuts to basic research are happening across the US, there is growing concern. "If there's a weakness in the pipeline and people don't know what to target," said Sundquist, "then drugs don't get developed."

"My worry as we watch funding to science get cut," said Ranney, "is we won't fully feel the ripple effects for 10 or 20 years because it can take that long for discoveries to make their way into lives of families and individuals."

Raphael is concerned that cuts mean "life-saving drugs will fall out the window." While lenacapavir is likened to a vaccine for HIV, it is not one. "This is not the last breakthrough for HIV prevention. Without continuous funding for prevention and advocacy, we won't have tomorrow's breakthroughs," she said.

Programs like the President's Emergency Plan for AIDS Relief, or PEPFAR—which has been a key component of global health since it was founded by President George W. Bush in 2003—are critical to supporting HIV prevention. A study published in *Annals of Internal Medicine* in February of this year reported that eliminating PEPFAR would lead to 601,000 HIV-related deaths and 565,000 new HIV infections in South Africa alone over 10 years.

As of 30 April, 2025, PEPFAR's current short-term authorization has expired. "The logical funding for distributing lenacapavir in the developing world would come from PEPFAR, a program that has been very successful, saving so many lives, but is now basically on life support," said Sundquist. "This means lenacapavir is really at risk of not being broadly distributed in the places that need it the most."

Ranney said her hope is that the selection of winners for this year's prize serves to remind science funders of the importance of all stages of scientific innovation and of giving freedom to science to pursue great ideas. "It's important to fund basic research, as we never know what is going to be the next world-changing discovery." □

Individual Development Plan

myIDP ScienceCareers
INDIVIDUAL DEVELOPMENT PLAN

Features in myIDP include:

- Exercises to help you examine your skills, interests, and values.
- 20 career paths with a prediction of which ones best fit your skills and interests.
- A tool for setting strategic goals with optional reminders to keep you on track.
- Articles and resources to guide you through the process.
- Options to save materials online and print them for further review and discussion.
- A certificate of completion for users that finish myIDP.

Start planning your future today!
myIDP.sciencecareers.org

In partnership with:

FASEB Federation of American Societies for Experimental Biology
UMASS University of Massachusetts Medical School
UCSF University of California San Francisco
UIC
BURROUGHS WELLCOME FUND

Duke 100 CENTENNIAL | YEARS & BEYOND DukeNUS Medical School | NUS120 CELEBRATING THE PAST, SHAPING THE FUTURE

We're hiring: Tenure Track and Tenured Faculty Positions (All Ranks) in Singapore!

Duke-NUS Medical School, Singapore's only graduate-entry medical school, invites applications from outstanding scientists and physician-scientists for tenure-track and tenured faculty positions at all ranks. A strategic partnership between Duke University (USA) and National University of Singapore (NUS), Duke-NUS is globally recognized for its impactful research, innovative education, and strong translational outcomes.

As we mark our 20th year anniversary, we are launching the next phase of Faculty growth aligned with Singapore's national biomedical priorities. We are particularly interested in individuals whose work aligns with the following strategic areas:

- **Precision Medicine and Next Generation Therapeutics (including RNA)**
- **Population Health**
- **Healthy Longevity and Aging**
- **Mental Health and Resilience**
- **Climate Change and Health**
- **Artificial Intelligence and Data Science**

What We Offer

- Competitive salary and full faculty benefits
- Generous start-up package and dedicated research space
- State-of-the-art infrastructure and core facilities
- Access to Singapore's strong R&D ecosystem
- Opportunities for joint appointments with SingHealth institutions
- A diverse, collaborative, and internationally engaged faculty culture

We seek passionate investigators (PhD, MD, or MD/PhD) with internationally competitive records and a collaborative spirit. Candidates with translational, innovation, or commercialization experience are especially encouraged to apply.

Our close partnership with SingHealth, Singapore's largest healthcare group, enables rich opportunities for translational and clinical research. As part of the SingHealth Duke-NUS Academic Medical Centre, our researchers are empowered to turn science into solutions that impact health systems and communities. Selected candidates may also be eligible for joint appointments with SingHealth.

Why Now?

Duke-NUS offers a unique opportunity for faculty seeking global relevance, research freedom, and long-term stability in a supportive environment. Our location in Singapore—Asia's innovation hub—makes this an ideal time to consider a move that allows you to do bold, meaningful work that transcends borders.

To Apply

Please submit your CV, a statement of research interests, and names of three referees to:
Chair, Faculty Search Committee
Email: hr@duke-nus.edu.sg

Applications will be reviewed on a rolling basis.
Interviews begin June 2025.
More information: www.duke-nus.edu.sg/research

SingHealth DukeNUS
ACADEMIC MEDICAL CENTRE

Finding strength in sensitivity

Nemanja Stanojević

I remember the moment my mentor in medical school told me she wouldn't be writing me a letter of recommendation for my Ph.D. application—my planned next step. "You're too sensitive," she said. As if something at the core of who I was—something I couldn't change—disqualified me from the future I had worked so hard for. At the time, I was devastated. Honestly, 4 years later, I still am. It felt like a punch to the gut, delivered by someone I respected and trusted. That moment planted a doubt I've carried ever since. But it also ignited a spark that led me to realize what others see as a weakness is ultimately a strength, albeit one that comes with daily challenges.

After six intense years of medical school, my mental health had slowly deteriorated without anyone, including myself, noticing. Right after graduating, I jumped into a Ph.D. program abroad, intending to pursue a career that would combine medicine and research, satisfying both my altruistic side and my fascination with human physiology and disease. That period was full of firsts: first time on a plane, first time living away from my family and boyfriend, first time stepping into the unknown of academic research.

Things quickly unraveled. I was anxious, constantly distracted, and overwhelmed by tasks others seemed to do with ease—such as pipetting, or handling animals during experiments. I'd wake up in the middle of the night convinced I'd left the cell incubator open, even though I'd checked it several times. The stress built up until I reached a breaking point. I switched labs, effectively starting over, and finally began to take my mental health seriously. In the second year of my Ph.D., I saw a psychiatrist and received a diagnosis: bipolar II disorder.

Living with bipolar disorder as a Ph.D. student means sensitivity isn't optional—it's part of how I move through the world. Science is meant to be thrilling, but for me, every new experiment brought waves of stress and doubt. I'd dive deep into the research, trying to eliminate every unknown—sometimes so much that I'd miss deadlines. People saw this as procrastination, and I kept hearing the same message: "Toughen up." So, I learned to hide my struggles, even if it meant pretending I was fine when I wasn't. But once I began treatment, I began to feel I was finding some stability for the first time.

Then, in October 2023, conflict came to Israel, where I was studying. With air raid sirens and drones overhead, I made the hard decision to return home to Serbia. But coming back brought its own pain. As a queer person, I didn't feel safe or seen in my home country. My newfound stability began to unravel, and I knew I couldn't stay. I left again, this time for Denmark—to start my Ph.D. anew in a place where I could live more freely.

Since arriving here, I've figured out ways to make this journey more sustainable, through trial and error. At the suggestion of a friend, I take pictures and record videos of my experiments, so I don't have to stress about taking perfect notes. I've learned to accept criticism without interpreting it as a personal attack. I take my medication and reach out when I need help. Most of all, I speak up for myself, letting my supervisors know which situations will likely be a challenge for me.

My mentor's comment about sensitivity still echoes in my mind when things get hard. Sometimes I wonder whether she was right. But with time I've come to see my sensitivity as something other than a weakness. It's the source of the empathy that compelled me to become a physician in the first place, and it's what pushes me to do research and learn more about the patients I will one day treat. My own experience with a chronic condition has convinced me that patients need doctors who can combine scientific precision with compassionate practice.

The rigid, high-pressure environment of academia isn't easy for people like me. But I'm stronger for having learned how to protect my well-being while pursuing my passion. My mental health struggles have forced me to check in with myself, respect my limits, and make space for emotion in an environment that treats it as a liability. □

Nemanja Stanojević is a Ph.D. student at Roskilde University. Do you have an interesting career story to share? Send it to SciCareerEditor@aaas.org.

ILLUSTRATION: ROBERT NEUBECKER

CALL FOR PAPERS

SPJ
SCIENCE PARTNER JOURNALS

emdria
EMDR International Association

Journal of EMDR
Practice and Research

The *Journal of EMDR Practice and Research* is a peer-reviewed journal that publishes articles on all aspects of EMDR therapy and Adaptive Information Processing (AIP) theory. It's an online-only, Open Access journal published in affiliation with the EMDR International Association (EMDRIA) and distributed by the American Association for the Advancement of Science (AAAS).

Topics of particular interest include, but are not limited to: empirical research evidence based on EMDR therapy and the AIP model, mechanisms of action and dismantling studies, early EMDR interventions, and EMDR therapy in the framework of psychotherapy integration.

Submit your manuscripts to *Journal of EMDR Research* today!

Learn more: **spj.science.org/jemdr**

The Science Partner Journals (SPJ) program was established by the American Association for the Advancement of Science (AAAS), the non-profit publisher of the Science family of journals. The SPJ program features high-quality, online-only, Open-Access publications produced in collaboration with international research institutions, foundations, funders, and societies. Through these collaborations, AAAS furthers its mission to communicate science broadly and for the benefit of all people by providing top-tier international research organizations with the technology, visibility, and publishing expertise that AAAS is uniquely positioned to offer as the world's largest general science membership society. Visit us at **spj.science.org**

@SPJournals **@SPJournals** **@SPJournals**

OPEN ACCESS

ARTICLE PROCESSING FEES WAIVED THROUGH DECEMBER 2026

INTERNATIONAL PRIZE
“LOMBARDY IS RESEARCH”
2025 EDITION

EARLY DIAGNOSIS AND PREVENTIVE MEDICINE

THE PRIZE
1 MILLION EURO

Applications are open for the 2025 Edition of the Prize funded **by Lombardy Region** (Italy) to recognize outstanding **scientific, pharmacological, and technological innovations and contributions** in a field aimed at enhancing life expectancy and quality of life for citizens.

The Prize can be assigned **to researchers from all over the world**.

In the last three editions, the prestigious scientists who won the Prize were **Alberto Mantovani** in 2024, **Steven Rosenberg** and **Carl H. June** in 2023, **Rosalind Picard** in 2022.

THE THEME

The Prize will be awarded to contributions in one of the following areas of interest:

EARLY DIAGNOSIS

- Timely detection of diseases
- Innovations in radiology, histopathology, and laboratory diagnostics
- Genomic and proteomic advancements in diagnostics
- Artificial intelligence and data analysis

PREVENTIVE MEDICINE

- Personalized screening and preventive interventions
- Vaccination and immunization
- Genetic and molecular approaches to prevention
- Health promotion and disease prevention

Candidates are required to **outline their significant contribution** to the selected disciplinary field of the Prize and **propose a translational research project aimed at strengthening their work**, to be conducted in collaboration with Research Centers in Lombardy (Italy).

SUBMIT YOUR APPLICATION NOW ›

DEADLINE JULY 8th, 2025

For more information and to submit your application, please visit this link
www.openinnovation.regione.lombardia.it/en/international-award

or scan the QR code below

UMBERTO 100 ANNI VERONESI 1925-2025
Fondazione VERONESI
PREMIO INTERNAZIONALE Lombardia è Ricerca
Regione Lombardia